Alma Mater Studiorum – Università di Bologna

DOTTORATO DI RICERCA IN

MECCANICA E SCIENZE AVANZATE DELL'INGEGNERIA

Ciclo 34

Settore Concorsuale: 09/C1 - MACCHINE E SISTEMI PER L'ENERGIA E L'AMBIENTE

Settore Scientifico Disciplinare: ING-IND/08 - MACCHINE A FLUIDO

MODELLING OF ORC COMPONENTS AND SYSTEMS FOR LOW-MEDIUM TEMPERATURE HEAT RECOVERY APPLICATIONS WITH REDUCED ENVIRONMENTAL IMPACT

Presentata da: Noemi Torricelli

Coordinatore Dottorato

Marco Carricato

Supervisore

Andrea De Pascale

Co-supervisore

Michele Bianchi, Lisa Branchini

Esame finale anno 2022

Abstract

About half of the world's energy consumption is wasted as heat due to the limitations of energy conversion processes. In this framework, the adoption of waste heat recovery (WHR) solutions with distributed power generation systems could have a great potential in reducing the demand on the primary fuel (and thus, the CO_2 emissions) in the different energy-intensive applications. The Organic Rankine Cycle (ORC), in particular, is recognized as one of the most suitable technologies for the low to medium temperature WHR for several applications, although it presents open challenges that still prevent its diffusion in the market, which are different depending on the application and the size at stake. Focusing on the micro range power size and low temperature heat sources, the ORC technology is still not mature due to the lack of appropriate machines and working fluids. Considering instead the medium to large size, the technology is already available but the investment is still risky. Thus, it is up to the research to find and investigate new configurations to push the industries to invest on this green solution. Literature on the ORC simulation is consistent, but nevertheless several studies have been conducted on this topic, almost all of them are based on a pure thermodynamic approach assuming constant machines efficiency. This approach is not always appropriated to study such systems, which are instead called to often work at part-load conditions due to the variable nature of the heat source. The intention of this thesis is to address some of the topical themes in the ORC field, paying special attention in the development of reliable models based on realistic data and accounting for the off-design performance of the ORC system and of each of its components. The project was split into two main parts, "ORC for micro-generation" and "ORC for the medium to large scale industrial WHR". Different methodologies and models have been employed for the different applications, supported by experimental data and information provided by manufacturers. Original contribution and main outcomes of the work can be summarized as follow.

Concerning the "Micro-generation" part, this work: i) explores the modelling methodology, the performance and the optimal parameters of reciprocating piston expanders, being this typology not yet properly investigated in the literature: ii) investigates the performance of such expander and of the whole micro-ORC system when using Hydrofluorocarbons as working fluid or their new low Global Warming Potential (GWP) alternatives and mixtures, accounting for both direct and indirect emissions (in particular the substitution of R134a, as performing fluid for low temperature applications, is evaluated); iii) analyzes the innovative ORC reversible architecture (conceived for the energy storage), its optimal regulation strategy and its potential when inserted in typical small industrial frameworks. As first result, coming from a models' comparison, this analysis proved the importance of implementing models more based on physical equations (such as semi-empirical lumped parameters models) rather than only on efficiencies polynomial functions. Indeed, the polynomials model could not be suitable to capture the influence of some phenomena occurring into volumetric expanders, which become important at lower- and higher-pressure ratio values, at the

contrary of a lumped parameters approach. Considering the whole system model, the validation process (performed using the data collected from the Unibo test bench) confirmed the effectiveness of semi-empirical models in predicting part-load behaviour of micro-ORCs, since comparing main output calculated values with measured ones, most of the points come within a 10 % error band. After introducing a new methodology to account for the influence of the working over the components' performance, the semi-empirical model was used to investigate the relative importance of the different losses affecting the expander performance when considering different fluids. This study highlighted that the lower pressure ratio and the lower viscosity of the HydroFluoroOlefines (HFOs), in particular, lead to smaller enthalpy drop at the expander and higher leakage losses at the pump meatus, which penalize the performance of such machines if compared to R134a. As additional results of the model application, it arose that the optimization of the built-in volume ratio could lead to a substantial increase of the expander performance. For the case study of the prototype of the University of Bologna, it was estimated a potential electric power output gain around 42 %. Being HFO fluids not always able to guarantee the same performance of R134a, they would introduce an energy production gap if employed in place of it, which can be compensated with energy sources outside the ORC system, likely employing fossil fuels. Indirect emissions caused using HFOs determine total equivalent total emissions of CO_2 greater than the ones related to R134a use; for the analyzed geothermal application case study, up to + 181 % by employing R1234ze(E). The implemented model was also used to simulate the ORC reversible system in the Carnot battery configuration. The results of the optimal control strategy application proved that in order to reach the maximum efficiency for each boundary conditions' combination, the working fluid mass flow rate and the external circuit water flow rate should be regulated in order to adjust the superheating degree and the pressure ratio inside the ORC system. A preliminary analysis on the system feasibility for micro-size applications shows that reasonable values of the payback period lower than 20 years can be achieved in case the thermal power integration amount overcomes a given threshold value (higher than 20 kW for the case study). The storage size plays an important role in the payback period minimization an its value should be chosen depending on the available thermal power and the process scale as discussed into the results section.

Regarding the "Industrial WHR" part, this thesis examines the WHR opportunity of ORCs, with a focus on the natural gas compressor stations application, given its enormous potential for savings. A software born to simulate complex power plants in both design and off-design condition, i.e. *Thermoflex*, was chosen as simulation tool. A particular attention was paid in the selection of the model parameters chosen in line with the current state of the art of the technologies with the support of data provided by manufacturers such as Turboden and Solar Turbines. This work provides information about all the possible parameters that can influence the optimal sizing, the performance and thus the feasibility of installing an ORC system considering its part load operation, being these aspects rarely considered in the current literature on the topic. In particular, results showed that the investment on the ORC is promoted by: i) station load profiles characterized by a higher number of operative hours (typical of natural gas compressor station rather than storage facilities); ii) prime movers gas turbines regulated by means of variable inlet guide vanes, allowing for a an almost constant exhaust gas temperature also at part-load operation; iii) green incentives, which proved to be strictly correlated with the effective possibility of reducing the greenhouse gas emissions. New WHR configurations are also explored: i) a first one, relying on the replacement of a compressor

prime mover with an ORC; in this case, the optimal re-allocation of the station load between the prime movers and the ORC is discussed; ii) a second one, which consists in the use of a supercritical CO_2 cycle as heat recovery system, not yet deeply examined and compared to ORC. Concerning the first point, the results brought to light an interesting consideration about what a brand-new design of a natural gas compressor station should account for, when considering the introduction of an ORC as WHR system. Namely, a different design of the original plant, employing GT runners of different capacities, can allow a wider margin of regulation and exploitation of the ORC system on site. Concerning the second point instead, results of the energy analysis considering only the pure electric production, highlighted that the ORC exhibits better performance, mainly due to lower relative operating machine consumption (3 % against 30 % of the CO_2 configuration), although the s-CO_2 expander enthalpy drops are considerably higher. Concerning the cogenerative performance, instead, the s-CO_2 system exhibits at the same time higher electric efficiency and thermal efficiency, if compared to ORC system. The ORC lower performance is due to the high condensing pressure value, imposed by the thermal user temperature, not affecting instead the s-CO_2 operating pressures, since the s-CO_2 does not present a condensing phase. From the economic point of view, however, this analysis suggested that higher capital costs are still associated to the CO_2 especially to the high heat exchangers investment cost, related to the design and the selection of materials compatible with the high cycle pressures and the strong corrosive behavior of CO_2 at high temperatures. Considering the plant footprint, it cannot be forgotten that the ORC working fluid expands into the ORC turbine at lower density ranges if compared to the CO_2, leading to larger expander machines, even 4 time greater.

Index

PART I - ORC for the micro-generation

List of contents

Figures

Tables

Nomenclature

Acronyms

CB	Carnot Battery
COP	Coefficient Of Performance
CHP	Combined Heat and Power
CS	Compressor Station
DHT	Direct Heat Transfer
EMG	Electric Motor Generator
GEF	Global Error Function
GHG	Greenhouse Gas
GT	Gas Turbine
GWP	Global warming potential
HE	Heat Exchanger
HFC	Hydrofluorocarbons
HFO	HydroFluoroOlefines
HP	Heat pump
HVAC	Heating Ventilation and Air Conditioning
IHTF	Intermediate Heat Transfer Fluid
LHV	Lower Heating Value
lb	Lower boundary
LR	Leak Rate
MRE	Mean Relative Error
NG	Natural Gas
NGC	Natural Gas Compressor
NPV	Net Present Value
OD	Off Design
OECD	Organization for Economic Co-operation & Development
ORC	Organic Rankine Cycle
PB	Payback Period
PES	Primary Energy Saving
s-CO_2	Supercritical CO_2 cycle
ub	Upper Boundary
VIGV	Variable Inlet Guide Vane
VSS	Variable Shaft Speed
VTIT	Variable Turbine Inlet Temperature
WHR	Waste Heat Recovery

Symbols

A	Area (m^2)
AU	Overall heat transfer coefficient (W/K)
b	Meatus thickness (m)
C	Cost (eur)

corr	Correction factor (-)
c_p	Specific heat at constant pressure (J/kg/K)
ct	constant
D	Diameter (m)
Em	Emission ($kgCO_2$)
E	Energy (kWh)
f	Frequency (Hz)
f	Friction factor (-)
FF	Filling Factor (-)
h	Meatus height (m)
h	Enthalpy (kJ/kg)
k	thermal conductibility (W/m/K)
I	Investment (eur)
l	Meatus width (m)
L	Characteristic length (m)
M	Molecular weight (kg/kmol)
m	Mass (kg)
$\dot{m}$	Mass flow rate (kg/s)
N	Rotational speed (rpm)
n	Number (-)
Nu	Nusselt number (-)
NTU	Number of transfer units (-)
SP	Size Parameter (m)
s	Entropy (kJ/kg/K)
T	Temperature (°C)
t	Time (s)
p	Pressure (bar)
pr	Reduced pressure (-)
Pr	Prandtl number(-)
$\dot{Q}$	Heat flow (W)
q	Discount rate (%)
Ra	Rayleigh number (-)
Re	Reynolds number (-)
R	Linear thermal resistance (m·K/W)
R	Revenues (eur)
r	Radius (m)
r_v	Volumetric ratio (-)
T	Temperature (°C)
s	Entropy (kJ/kg/K)
U	Global heat transfer coefficient ($W/m^2/K$)
V	Volume (m^3)
$\dot{V}$	Volume flow rate (m^3/s)
v	Specific volume (m^3/kg)
w	Velocity (m/s)
$\dot{W}$	Power (W)

X_{tt}	Martinelli parameter (-)
x	Mass fraction (-)

Abbreviations

amb	Ambient
ava	Available
bott	Bottomer cycle
calc	Calculated
cc	Cubic capacity
cd	Condenser
circ	Circuit
cool	Cooling medium
cog	Cogenerative
comp	Compressor/compression
conv	Conversion
des	Design
el	Electric
eng	Engine
ev	Evaporator
ex	Exhaust
exp	Expander/expansion
ext	External
gen	Generator
geo	Geometry
eq	Equivalent
HX	Heat exchanger
in	Inlet
int	Internal
ins	Insulating
is	Isentropic
leak	Leakage
log	Logarithmic
meas	Measured
max	Maximum
min	Minimum
mix	Mixed
ml	Mean logarithmic
nom	Nominal
norm	Normalized
opt	Optimal
out	Outlet
par	Parameter
pp	Pump
rec	Recuperator
recomp	Re-compression

ref	Reference
reg	Regenerative heat exchanger
res	Circuit resistance
req	Required
sc	Subcooling
sh	Superheating
sh	Shaft
su	Supply
s	Swept
sat	Saturation
sf	Secondary fluid
sto	Storage
th	Theoretical
thr	Throat
tot	Total
tp	Two-phase
train	Training data
val	Validation data
0	Clearance
wf	Working Fluid

Greek letters

α	Intake stroke ratio (-)
α	Convective heat transfer coefficient ($W/m^2/K$)
γ	Heat capacity ratio (-)
γ	Void fraction (-)
β	Expansion ratio (-)
β	Emission factor ($kgCO_2/MWh$)
ε	Flow coefficient (-)
λ	Conductive heat transfer coefficient ($W \cdot m/K$)
η	Efficiency (-)
σ	Threshold
Δ	Difference (-)
ρ	Density (kg/m^3)
μ	Viscosity ($Pa \cdot s$)
τ	Thermal efficiency (-)
ν	Variance

Introduction

1 ORC technology state of the art

Summary This chapter introduces the thesis work by examining the context in which the ORC technology could be inserted, its potential and the current challenges that hinder its diffusion on the market. In a following chapter, the structure of the document is presented, highlighting the original contribution of this thesis with respect to current literature and issues.

1.1 ORC potential into the energetic scenario

In a world where the energy demand is constantly increasing, the energy production sector must also face as soon as possible the emergency of the climate changes, reducing the global consumption of fossil fuels and the overall greenhouse gas emissions. This challenge can be accomplished by increasing the use of renewable energies, but also improving efficiency in conventional primary sources exploitation, by means of smarter, renewable oriented, integrated, well-regulated and more distributed energy systems [1]. In particular, power generation from low to medium-grade heat sources is gaining interest among the means to implement the aforementioned solutions. In this context, the Organic Rankine Cycle (ORC) is one of the most suitable technologies for valorizing heat into electricity or mechanical power [2].

The world emits around 50 billion tons of greenhouse gases each year (measured in carbon dioxide equivalents) [3], the 78.5 % of which derive from fossil fuel consumption in the energy and the industry sectors (see Figure 1-1). In its turn an important slice is related to: i) the energy use in buildings (17.5 %), for lighting, appliances etc. and heating, at home and at commercial buildings such as offices, restaurants, and shops; ii) industries such as cement, chemicals, metals and others. In this framework, about 50 % of the world's energy consumption is wasted as heat due to the limitations of energy conversion processes [4]. This heat can derive from a variety of sources such as industrial and household waste heat, gas and steam turbines exhaust heat, internal combustion engines exhaust heat, solar radiation, geothermal heat and biomass heat [4]. Thus, the adoption of waste heat recovery (WHR) solutions with distributed power generation systems could have a great potential in reducing the demand on the primary fuel (and the CO_2 emissions) in the different energy-intensive applications.

Many industries, for example, employ simple cycle Gas Turbines (GTs) as prime movers, offering a great potential margin for low-cost energy savings and carbon reductions through energy efficiency improvements. Indeed, basic industrial GT engines have limited size, ranging up to 50 MW, with low inherent efficiency, typically not above 40 %. A significant amount of fuel energy input is rejected as hot exhaust at relatively high temperatures (400–600 °C) [5]. Figure 1-2 shows estimated data of heat rejected by many commercial GT units covering the range of size of industrial machines.

This wasted energy could be profitably used as a secondary thermal resource in order to increase the efficiency of fuel usage and to mitigate environmental drawbacks. Wasted heat can be firstly utilized to generate additional electric energy to support the industrial process or to be sold to the grid. Moreover, combined heat and power solutions, providing steam or hot water for industrial processes can further improve the primary energy utilization, playing a significant role in achieving economic and environmental benefits.

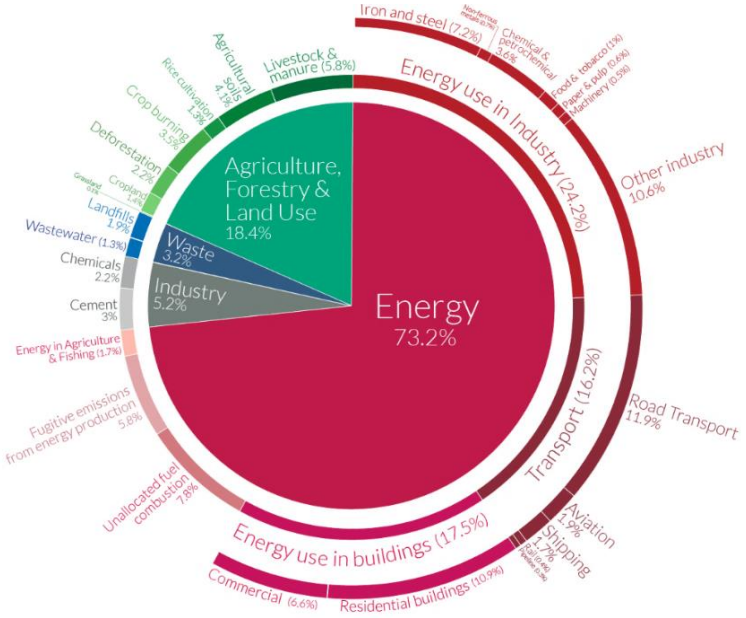

Figure 1-1 - Global greenhouse gas emissions per sector [3].

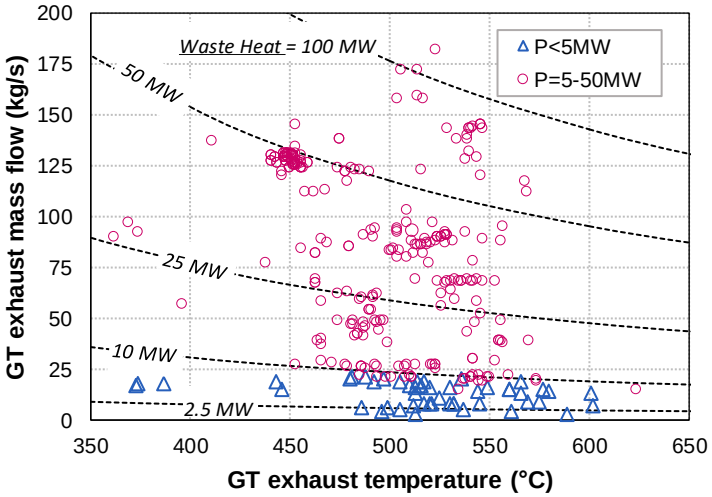

Figure 1-2 - Overview of industrial GTs exhaust temperature, air flow and waste heat ranges*.

* Data from *Thermoflex* industrial gas turbines database [6], obtained considering full load conditions and assuming to cool down to 80°C the exhaust gas.

Statistics also reveal that low-grade waste heat accounts for 50 % or more of the total heat generated in industry [7], thus making also the low-temperature heat recovery of prime importance. Among the low temperature waste heat sources are for example: sewage of residential buildings, hotels, medical-preventive, and other institutions, sewage treatment plants of various types, mine water and ventilation air from mines, waste water from industrial enterprises, heat generating stations, swimming pools and chemical processes in industry [5].

Thanks to its simplicity and its capacity to retrofit existing thermal system, ORC technology is suitable to be employed in several of the aforementioned greenhouse gas emitting sectors, as bottomer cycle of industrial processes but also in the residential/tertiary sector [8]. The potential for savings associated to the ORC introduction in this field is believed to be enormous. For instance, taking into consideration only the cement, steel, glass and gas compressor stations industries, in Europe, the ORC power installation potential is estimated to savings of almost 1.95 billion euro and of over 8.1 million tons of Greenhouse Gas (GHG) emission, a value which represents almost 2 % of the European Industry consumption [9]. An efficient exploitation of small and micro-scale thermal sources, that are in general not valorized and thus wasted to the ambient can represent also a substantial contribution for saving primary sources and emissions [2], in the framework of the micro and distributed generation, providing financial, environmental and security benefits for households, businesses and grid operators [10]. In this case, the exploitable heat sources do not involve only low-value industrial waste heat but also low-enthalpy geothermal sources, solar thermal, biomass, etc.

1.2 Working fluid

1.2.1 Why using an organic fluid?

Whilst the conventional Rankine cycle is suitable for high temperature applications and large centralized systems, it may not be compatible for small and medium scale applications characterized by low-grade enthalpy sources. In these situations, it may occur that the water vapour cannot reach the appropriate superheating degree at the turbine inlet, causing the fluid condensation during the expansion with consequent risk of erosion of the turbine blades. Then, the ORC can be considered as alternative to the traditional water cycle.

An ORC is nothing but a Rankine cycle using an organic fluid as working fluid, featuring higher molecular mass and lower ebullition/critical temperature compared to water. Conceptually it is very similar to a traditional Rankine cycle and since it is based on the same thermodynamic process (see Figure 1-3): a fluid evaporates heated up by an external thermal source, and then goes expanding into an expansion machine to produce work; after the expansion, the fluid is condensed and brought back to the evaporating pressure by means of a pump, and the thermodynamic cycle is closed. However, because of the organic fluids' characteristics, the ORC has the advantage of no needing to excessively superheat the fluid to ensure a dry expansion. In addition, the evaporation process takes place at lower temperature with less needed heat and the pressure ratio are much smaller allowing for a simpler design of the plant. For instance, a one-through boiler can be used for the fluid evaporation in place of different heat exchangers and single stage turbines can be employed.

Possibly, a regenerator can be introduced to increase the efficiency, by pre-heating the fluid entering the evaporator exploiting the expander exhaust vapor residual heat.

Potential ORC working fluids mainly belong to the following categories [11]: Hydrocarbons (HC); Hydrofluorocarbons (HFC), Hydrochlorofluorocarbons (HCFC) and Chlorofluorocarbons (CFC), usually employed as refrigerants; Siloxanes; and mixtures of these fluids (both zeotropic and azeotropic). As can be seen several organic fluids are available on the market and the selection of which one to use as working fluid is not trivial, since it influences different aspects of the system design, as discussed in the following paragraphs.

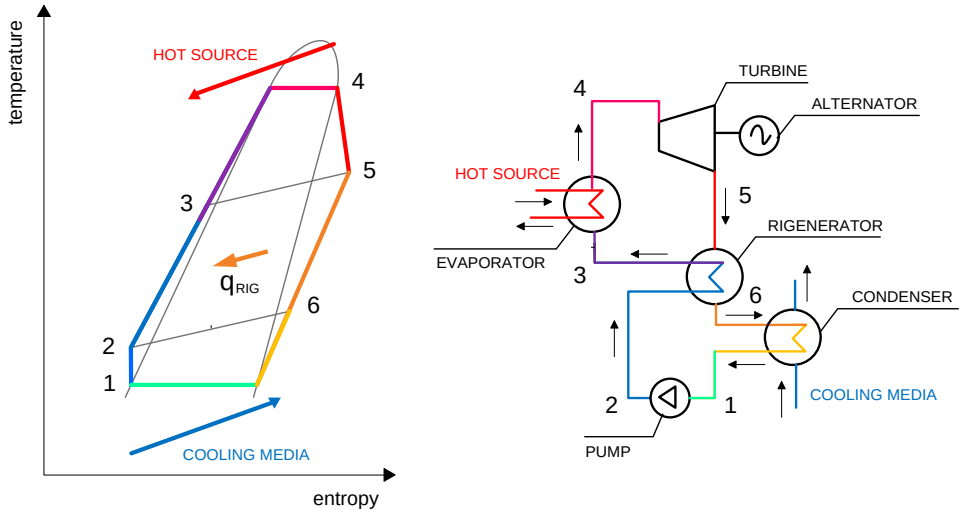

Figure 1-3 - Typical ORC thermodynamic process and layout.

1.2.2 Influence of the thermodynamic properties on the performance

Saturated vapour curve slope

First distinction among the fluids can be made based on the saturated vapour curve slope [12]. Following this distinction criterion, the fluids can be divided into three categories: i) *Wet fluids* characterized by a negative saturated vapour curve slope, ii) *Isentropic fluids* showing a null saturated vapour curve slope and iii) *Dry fluids* with a positive saturated vapour curve slope. Figure 1-4 illustrates the saturation curves and the expansion process for the different fluid categories on the temperature-entropy diagram.

Examples of *Wet* fluids are water (see Figure 1-5) and ammonia. Due to the negative slope of the saturation vapour curve, the turbine outlet stream of these fluids contains a part of condensate liquid in case the expansion starts at saturated vapour state. The presence of liquid droplets inside the turbine affects the isentropic efficiency of the machine and at the same time could represent a cause of damage of the turbine blades. In order to avoid the liquid formation inside the turbine, the minimum vapour quality at the end of the expansion is usually limited at 85 %. A solution to respect this constraint consists in adequately superheating the vapour supplied to the turbine. However, it must be noticed that the heat transfer coefficient decreases significantly in the vapour phase and the heat transfer area requirement and hence the cost of the heat exchanger increase consequently.

Considering instead *Isentropic* and *Dry* fluid types (most of the organic fluids belong to these two categories), since the vapour ideally expands along a vertical line on the T–s diagram, saturated vapour supplied at the turbine inlet will not change of phase throughout the entire expansion process. Consequently, these categories of fluid do not necessitate of a vapour superheater. On the other hand, as the superheating degree at the end of the expansion increases, the cooling load at the condenser also increases. For this reason, a regenerator is usually introduced to exploit the residual heat contained in the exhaust vapour to preheat the liquid before entering the evaporator. Downstream this consideration, it can be concluded that *Isentropic* type fluids represent the ideal working fluids for ORCs, given the features of persistent saturation throughout expansion.

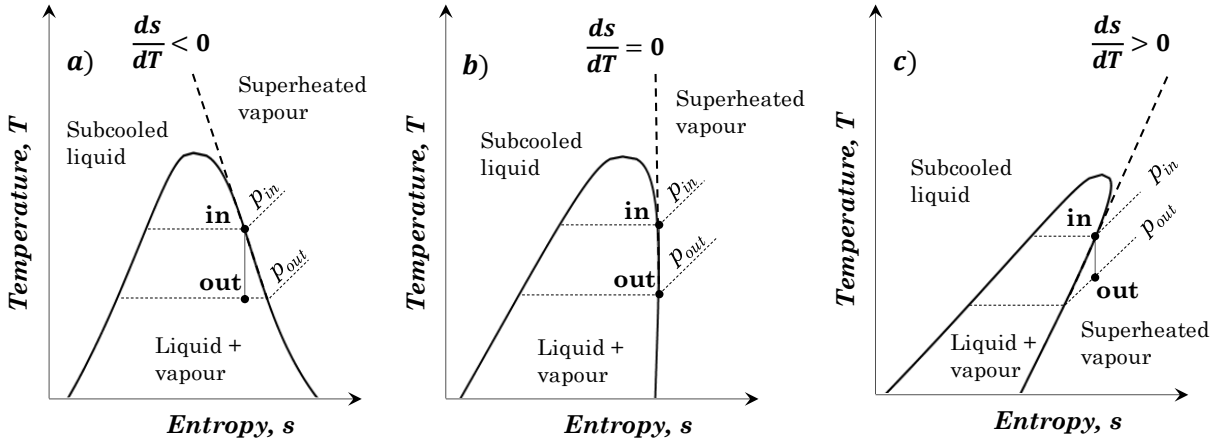

Figure 1-4 - Saturated vapour curve slope classification: a) *Wet* fluid, b) *Isentropic* fluid and c) *Dry* fluid.

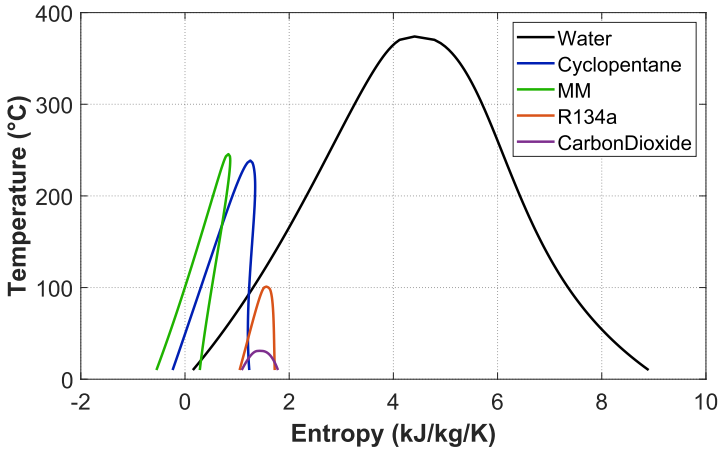

Figure 1-5 - Saturation curves for different categories of fluids.

Vaporization latent heat

Studies in the open literature [12] highlight how the vaporization latent heat magnitude can influence the cycle performance for what concerns both the heat exchangers effectiveness and the expander work output. The first effect of the vaporization latent heat is on the heat transfer process,

as qualitatively illustrated by Figure 1-6a) and b), comparing the heat exchange diagrams of fluids with respectively high and low vaporization latent heat. It can be noticed from Figure 1-6, how higher vaporization latent heat enables most part of the input thermal power to be provided to the working fluid during the phase change process, exploiting high heat transfer coefficient. From literature [12], it could be found that high vaporization enthalpy ratio (the ratio of vaporization latent heat and sensible heat) results in larger unit work production and high cycle efficiency, for defined hot and cold source temperature levels. Even if, fluids with higher vaporization heat, also need higher input thermal power to reach the state of saturated vapour; thus, they may not be always appropriated for low enthalpy sources application. Water, for instance, is considered as a fluid with high vaporization latent heat (as can be deduced from Figure 1-5, by comparing the width of the water bell with the other fluids bell width).

Depending on the heat source nature, organic fluids with lower specific vaporization heat can be preferred in some circumstances. An example is the waste heat recovery application from exhaust gas, which exhibits steep curve slope on the heat exchange diagram. In this case, a low vaporization heat of the working fluid results in a mostly variable temperature heat transfer process in the evaporator, and hence in a temperature profile which better follows the temperature profile of the heating fluid. This leads to reduced temperature differences between fluids in the heat exchanger and irreversibility occurring during the heat transfer process (as highlighted in Figure 1-6).

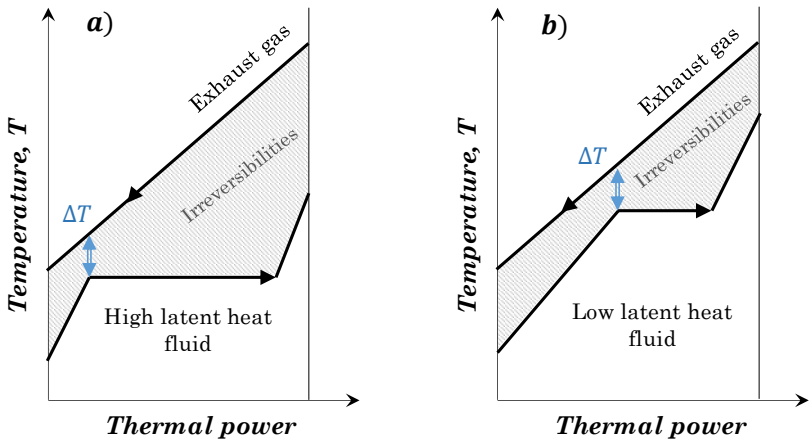

Figure 1-6 - Effect of the vaporization latent heat on the heat transfer irreversibilities.

Critical temperature

The critical temperature of the working fluid has an influence on the system operating conditions, since correlated to the saturated pressure the fluid reaches at a given temperature. In particular, being equal the condensation temperature, higher critical temperatures imply low condensation pressures (as shown in Figure 1-7a, considering a temperature of 20 °C); sometimes even lower than the atmospheric one, which can lead to complications in the plant design and increase the costs. The critical pressure instead remains almost constant with the critical temperature, ranging between 30 and 50 bar, except for the siloxanes that exhibit lower critical pressures, and the water, which instead has a greater critical pressure, equal to 221 bar (see Figure 1-7b). This means that generally higher pressure ratio can be expected when employing fluids with higher critical temperature.

Studies in the literature [12] show that, comparing optimized cycles, fluids characterized by higher critical temperature (and, thus higher pressure ratio and enthalpy drop) allow to achieve higher cycle efficiency. On the other hand, the higher is the involved pressure ratio the higher is the plant complexity and cost, as it is the case of the water Rankine cycle.

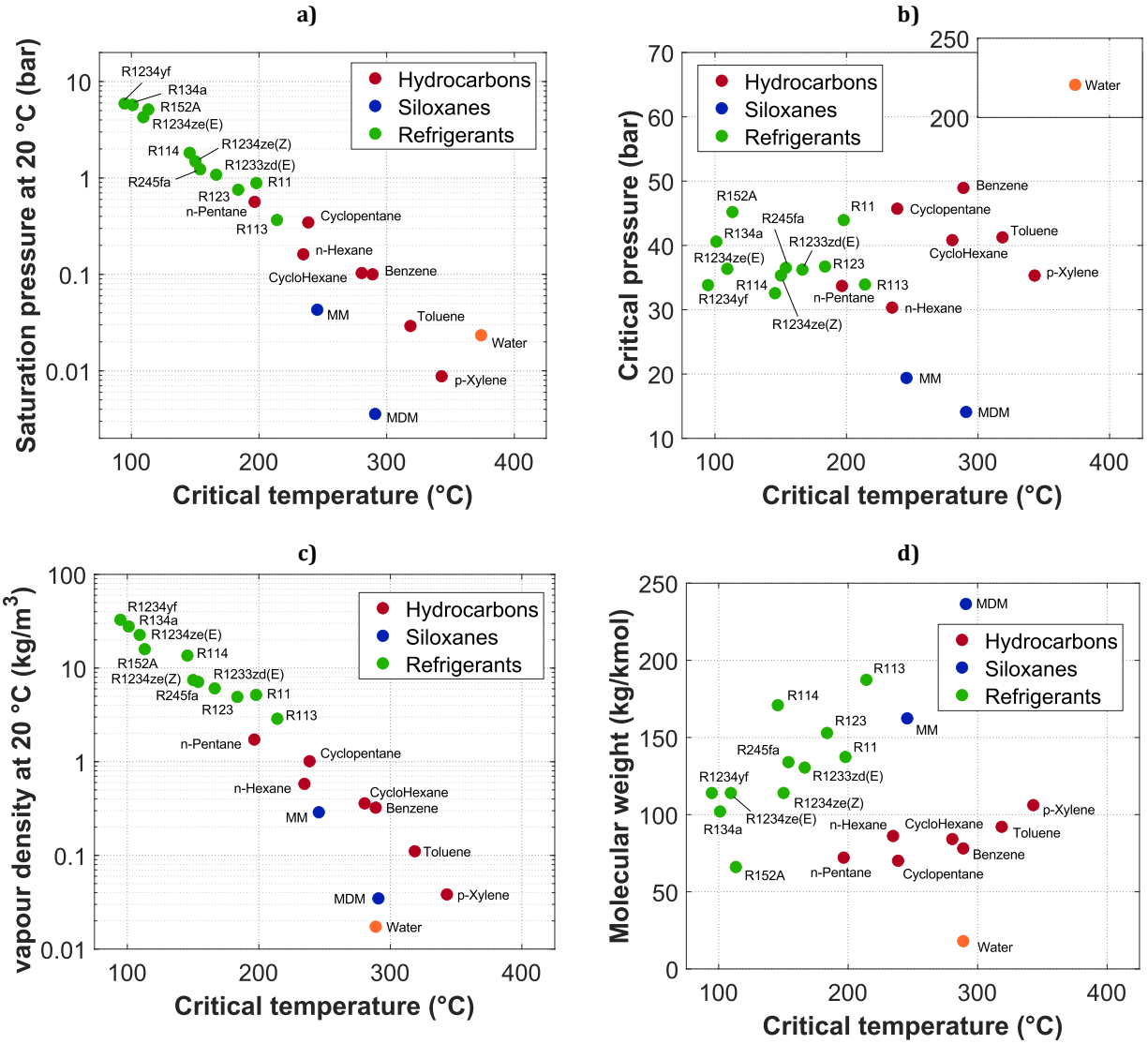

Figure 1-7 - Trend of the: a) saturation pressure, b) critical pressure, c) saturated vapour density and d) molecular weight, as function of the critical temperature†.

Other aspects correlated to the critical temperature, impacting the design and the cost of the system are the vapour density and the molecular weight [12]. In particular, high fluid densities are preferred to limit the volume flow rate and consequently the pressure drops along the heat exchangers and the expander size. As can be seen in Figure 1-7c, the vapour density at the end of the expansion, in general tends to decrease with the critical temperature, thus smaller expander sizes are expected for lower critical temperatures. Conversely, the molecular weight tends to increase

† Data reported for most used fluids for ORC applications (properties calculated by means of CoolProp library [13]).

with the critical temperature, even if different trends can be observed for the different fluid categories. More in specific, hydrocarbons show lower molecular weight than refrigerants and siloxanes. Water is the fluid with the lower molecular weight among the considered ones. Expansion work tends to be in inverse relation to the molecular weight which means that turbines for heavy fluids tend to have a low peripheral speed and a small number of stages [12]. For this reason, high molecular fluids can be preferred for more compact and simple applications.

1.2.3 Environmental impact

The environmental impact of the working fluids it is an aspect to take into account when designing an ORC. This topic – being not very essential in high temperature systems – is quite central for low temperature applications, where high global warming potential (GWP) refrigerants are still adopted as working fluid due to their thermal compatibility with low-grade heat sources. In particular, most common fluids employed for low-temperature applications are refrigerants belonging to HydroFluoroCarbons (HFCs) category, as R245fa, R123 and R134a [12]. Refrigerants appear to be very performing for these applications thank to their low critical temperature. On the other hand, HFCs risk to highly contributing to the greenhouse effect, if released (for example during service operation on the plant), due to their high GWP values and high residence time in the atmosphere.

The GWP index allows to compare the global warming impact of different gases. It evaluates the amount of energy that each gas can absorb causing the earth warming and slowing the rate at which this energy is released outside the atmosphere [14]. Table 1-1 reports the value of the *GWP* indexes for different categories of refrigerants employed for ORC applications, including also data concerning no more used categories of fluids, namely the chlorofluorocarbons (CFC) and the hydrochlorofluorocarbons (HCFC). These families of fluids contain fluorine in addition, whom, if released in the atmosphere, contributes also to the ozone layer depletion. These fluids present thus an ozone depletion potential (OPD) index higher than 0.

Fluids with high ODP already exited the market in the 90s' as a consequence of the Protocol of Montreal, whilst the phase out of GWP refrigerants instead is still underway (see Figure 1-8). According to the EU F-Gas Regulation 517/2014, the quantities of HFCs (expressed in CO_2 equivalent that are placed on the market) will be gradually reduced through the allocation of quotas by the European Commission to producers and importers of bulk HFCs. As a result of the phase-down, HFC consumption should be reduced by 79 % by 2030 and in upcoming years the refrigerants with GWP higher than 150 should not be used in new products [15]. This means that industry needs to make the transition to refrigerants with a lower global warming potential. The regulation refers to all the utilities adopting greenhouse gases as working fluids (including refrigerators, ORC, heat pumps, etc.). One of the challenges for the researchers in this field has been to identify right replacements for HFCs, which comply with low GWP and, at the same time, reproduce similar thermal performance. In particular, for what concerns the refrigeration sector, possible substitutes of HFCs that fulfil these requirements, have been identified in the HydroFluoroOlefines (HFOs) [16], which exhibit *GWP* values close to 1.

Table 1-1 - Values of the GWP and ODP indexes for different categories of refrigerants‡.

Category	Fluid	GWP	ODP
CFC	R11	4660	1
	R113	5820	1
	R114	8590	1
HCFC	R123	79	0.02
HFC	R134a	1300	0
	R227ea	3350	0
	R245fa	858	0
HFO	R1233zd(E)	1	0
	R1234yf	1	0
	R1234ze(E)	1	0
	R1234ze(Z)	1	0

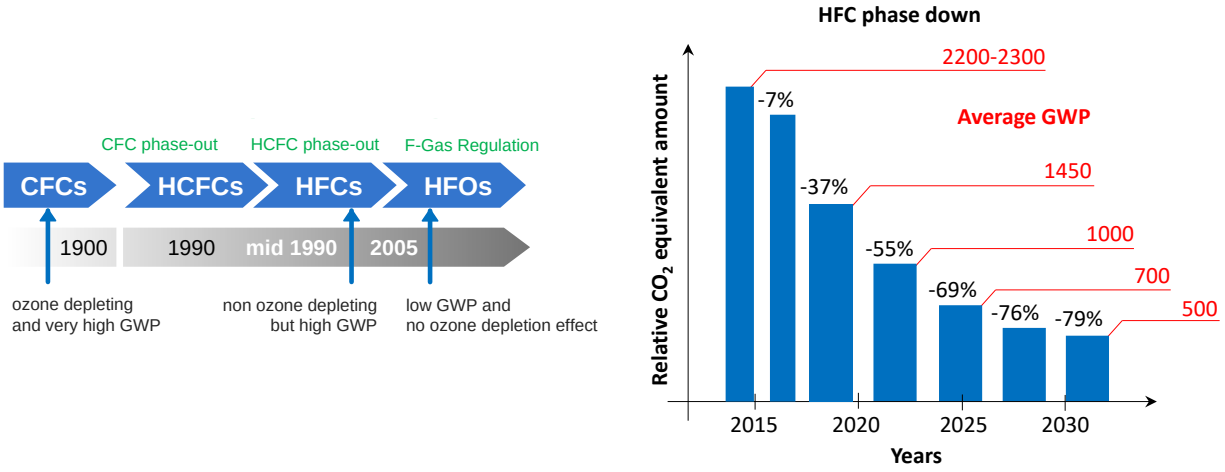

Figure 1-8 - Steps of high ODP and GWP refrigerants phase-down determined by regulation.

1.2.4 Practical guidelines for the selection

The working fluid selection should be done with the aim of achieving the best possible thermodynamic performance considering the influence of all the aspects commented above, whilst limiting the cost. Besides the thermodynamic properties and the environmental impact, others fluid features must be taken into account, namely:

- the thermal and chemical stability limit, which can limit the fluid operating temperature range. Indeed, unlike water, organic fluids usually suffer from chemical deterioration and decomposition at high temperatures.
- the compatibility with materials to avoid corrosion.

‡ properties determined by the 5th Intergovernmental Panel on Climate Change (IPCC) report [17], for most used refrigerants for ORC applications.

- the safety characteristics in terms of toxicity and flammability, provided by the ASHRAE Standard [18].
- The cost and the availability on the market. Fluids already used in refrigeration or in the chemical industry, for example, are easier to obtain and less expensive.

1.3 Components

1.3.1 Expanders

The expander is a crucial component for ORCs, strongly affecting the overall system efficiency. The expansion machines for ORC application can be of two types and the choice of employing one rather than the other is usually made as function of the size. These types are the turbo and the positive displacements type (as illustrated in Figure 1-9), the latter are more appropriate for small-scale ORC units, as characterized by lower flow rates, higher presser ratios and much lower rotational speeds than turbo-machines [1].

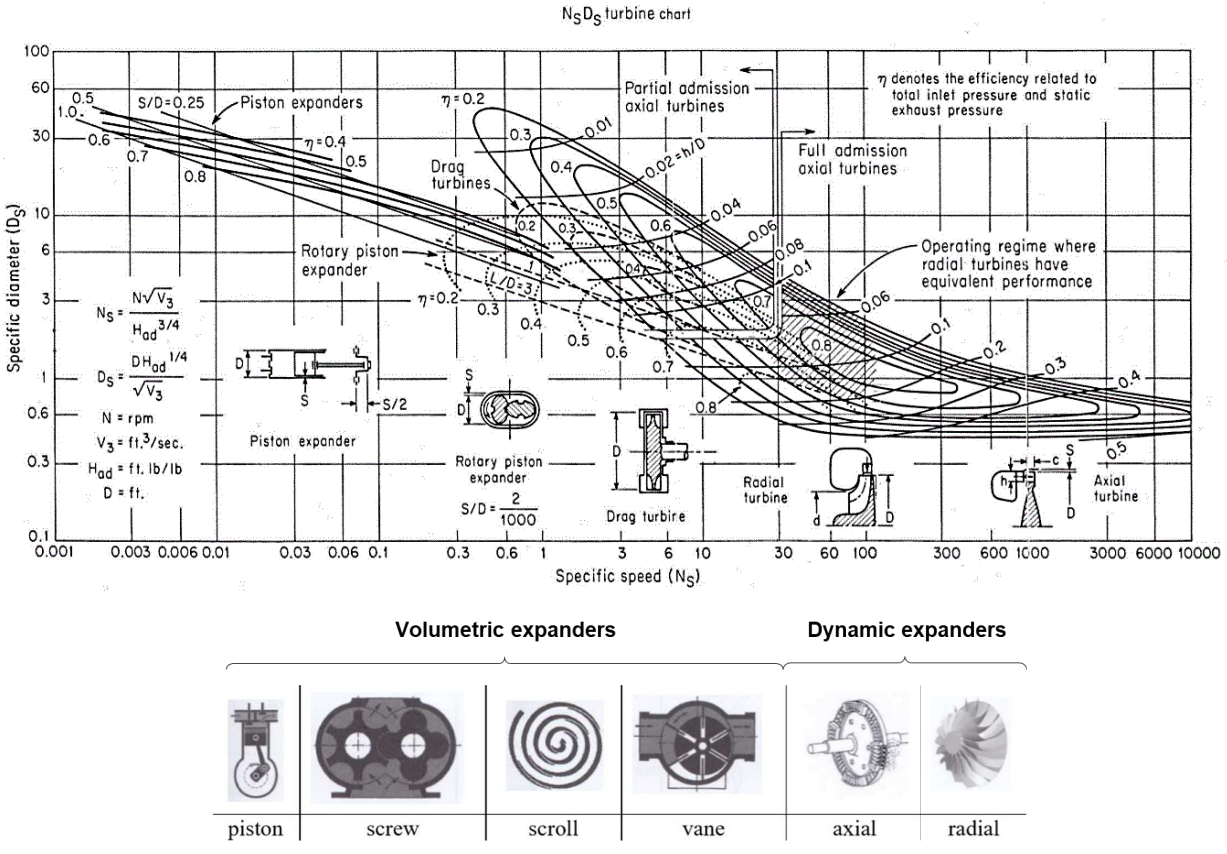

Figure 1-9 - Selection map for expander machines (source [19]).

Non-dimensional parameters, such as specific speed, N_s, and specific diameter, D_s, can be calculated by means of equations in Figure 1-9 and used to provide guidelines for the expander selection [19]; where N is the speed in rpm, D is the diameter in feet, H_{ad} is the adiabatic enthalpy drop through the machine in kJ/kg and V_s is the volume flow rate in ft^3/s. η is the hydraulic efficiency.

The expanders with similar geometry will have the same efficiency for same specific speed irrespective of the difference tip clearance and Reynolds number [20]. Thus, for specific known operating conditions, the specific diameter and specific speed can be estimated and the most performant corresponding expander can be selected as expansion machine according to the map presented in Figure 1-9. Experimental data from prototypes in literature show that the adiabatic efficiency of expanders has an upper quartile at 77 % and a lower quartile at 35 % for an average of 56 %, whatever the expander technology [1].

Turbomachines

Among the turbomachines an additional distinction can be made between axial and radial turbines, where axial turbines are usually preferred to be used in combination with high molecular weight fluids, which present lower enthalpy drop. The design of radial inflow turbines, instead, allows for higher pressure ratios (i.e. higher enthalpy drops) per stage and low working fluid flow rates.

In general, turbomachines employed for ORC application, if compared with the traditional ones, are designed to work with lower enthalpy drop (thus, fewer stages are required) and lower speed of sound. As mentioned before, this kind of machines is not always compatible with small size. The reason is that, due to their typical characteristic, for which their tip speed is approximately constant regardless of the size, the rotating speed would increase proportionally as the diameter decreases, reaching not acceptable values [8].

Volumetric machines

Positive displacement expanders used in ORC are of piston, scroll, screw and vane types. Generally, screw and scroll expander have overall superior performance compared to the rest of the expander, however, piston expander can be preferred since they provide larger expansion ratio [20].

Compared to turbomachines, they present the advantage of working at limited rotating speeds (generally not above 3000 rpm, considering a 50 Hz electrical grid) and of tolerating a two-phase expansion, maintaining a good isentropic efficiency. However, whilst the turbomachines technology is already mature for the medium to large size, it is not for the volumetric machines for the small-scale applications. In most of the cases, positive displacement expanders are prototypes, derived from existing compressors used in the refrigeration industry [1].

In such a machine, the fluid expands progressively with the increase of the expansion chamber volume. In piston expanders, the timing of the suction and the discharge process is determined by the valve opening and closing. Conversely, in rotatory expanders this timing is imposed by the geometry of the machines. An important design parameter, determined by the suction and discharge timing, is the "built-in volume ratio" determined by the ratio between the volume of the chamber at the beginning of the expansion ($V_{exp,beg}$ in Figure 1-10) and the chamber volume at the end ($V_{exp,end}$ in Figure 1-10). This parameter, if not well sized, can be a cause of performance derating, for under/over-expansion losses. The latter can occur when the internal volume ratio is respectively lower/higher than the system specific volume ratio, determined by the ORC operating conditions (as schematized in Figure 1-10a).

Other sources of loss derive from friction, internal leakage, supply pressure drop and heat transfer. The magnitude of the friction and the leakage losses depends on the tolerance between the

moving parts and, in order to limit both these contribution of losses at the same time, volumetric machines, at the contrary of dynamic ones, necessitate of lubrication. Supply pressure drops are caused by the restriction of the cross-section flow at the expander inlet. Heat losses towards the ambient through the expander wall are also not negligible if compared to the power output, for this kind of machines, due to the limited machine size. The sum of all these contributions of losses means that the ideal indicator diagram area is reduced, as in Figure 1-10b, until it becomes equal to the actual indicator diagram area.

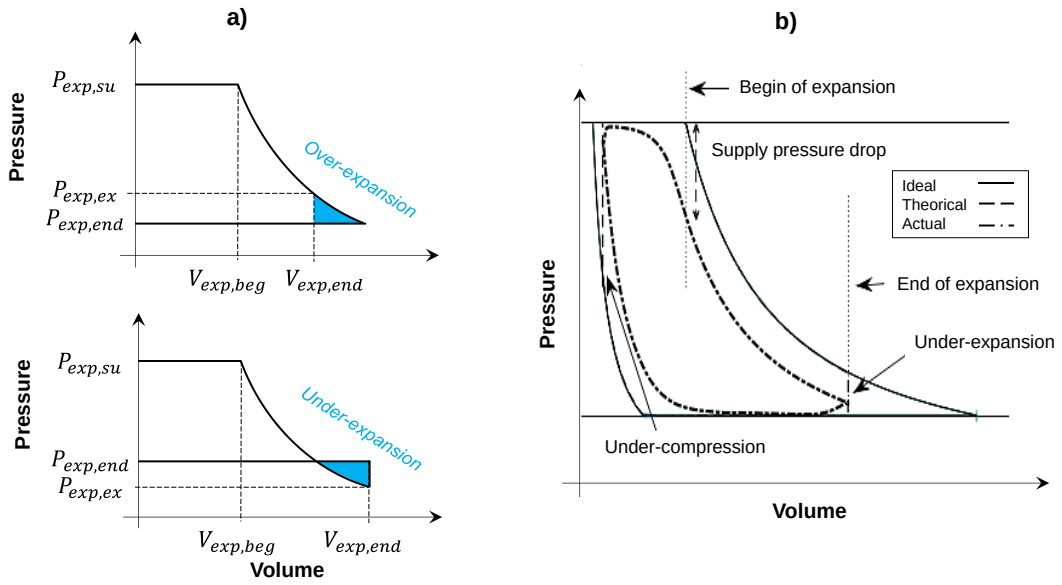

Figure 1-10 - Positive displacement expanders indicator diagram: a) over and under-expansion losses, b) ideal vs real.

1.3.2 Pumps

Similar architectures can be found also in the pump field and similar considerations can be applied. Thus, both centrifugal and volumetric pump types can be used, where the selection criterion is usually dictated by the plant size. Pumps in ORC systems, when of positive displacement type, are used to control the working fluid mass flow rate, since it is roughly proportional to the pump rotational speed. For centrifugal type, instead, the flow rate also depends on the pressure head, imposed by the difference between the evaporating and condensing pressure [1].

It must be noticed that in traditional Rankine cycle, the pump consumption is very low if compared to the power output. This does not apply to ORCs, where the overall efficiency can be strongly affected by the pump consumption also because of the still relatively low efficiency, around the 30 % [21].

1.4 Applications and market share

The choice of substituting water with an organic fluid can be convenient in particular for those applications characterized by limited heat source temperature, i.e. lower than 400 °C, and limited

power plant size, i.e. lower than 10 MW. These applications include renewable sources such as geothermal from high to low temperature, biomass and solar, but also waste heat recovery from energy-intensive industrial processes [8]. Different applications are characterized by different operating temperatures and plant sizes as schematized in Figure 1-11. The market share, divided by heat source and producer, is represented by the pie charts of Figure 1-12, showing how some applications, more than others, have already penetrated the market.

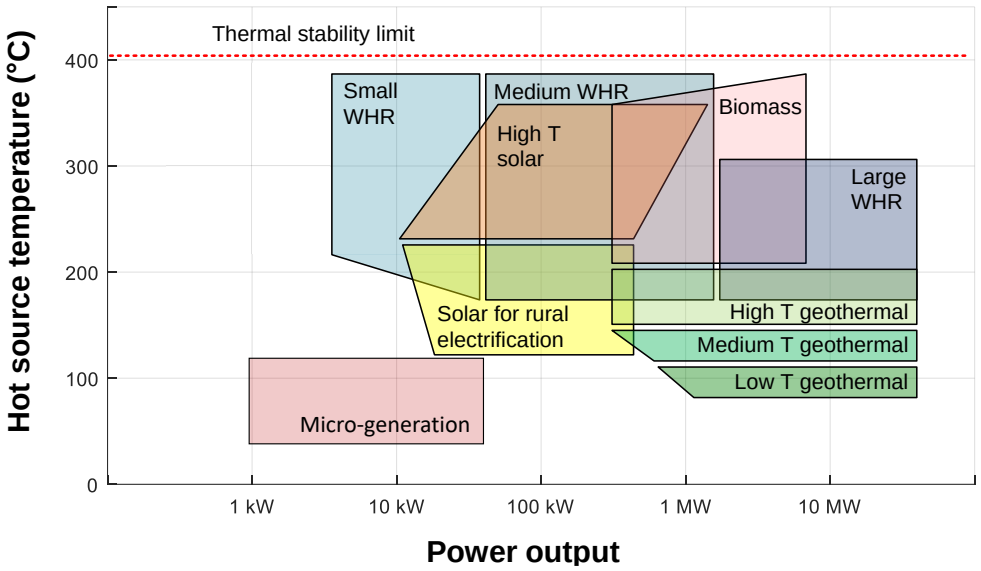

Figure 1-11 - ORC fields of application (data from [8]).

Biomass and geothermal power plants sizes ranges both between 1 to 10 MW, even if characterized by different temperature ranges: not above the 200 °C for the geothermal and above the 200 °C for the biomass. These two applications represent a major part of the market share (see Figure 1-12). The geothermal is predominant over the other applications, since it covers the 76.5 % of the ORC global installed power, followed by th the biomass, which covers the 10.7 %. The WHR application from GTs and engines is ranked third (see Figure 1-12), covering the 8.5 % of the total installed capacity. Other WHR applications cover the 4.2 %, whilst solar only the 0.1 %. In WHR application the waste heat temperatures can go from 200 to 400 °C, with a very variable enthalpy content, influenced by the nature of the heat source and its mass flow rate (see Figure 1-11). Thus, depending on the magnitude of the available thermal power (determining the ORC power output), WHR applications can be distinguished in small WHR, medium WHR and large WHR. Solar power plants size is around 100 kW; the temperatures are limited to 200 °C in solar for rural electrification systems but can reach up to 350 °C in high temperatures solar concentration applications. A more recent and promising application field is the micro-generation, even if not yet significant part of the market share. Micro-generation comprehends those systems conceived to exploit very low-temperature heat sources (lower than 150 °C) with expected power output even under 50 kW, such as low enthalpy industrial waste heat and renewable energy for the self-consumption in the tertiary and residential sector.

Medium to large scale ORCs are yet quite diffused in the market and commonly used to generate power in different industrial heat recovery power plants with more than 340 MW of installed capacity in the world and 18.5 MW of new capacity in construction, even if the current capacity is still scarce compared to its potential [22]. Many of these applications are WHR from gas turbines, mostly installed on compressor stations along gas pipeline [22]. In these configurations, gas turbine operating conditions can often vary following the site demand, leading to fluctuating values of the exhaust temperature and available thermal power, which require flexible WHR solutions. In this context, ORC technology is particularly suitable for flexible and remote operation, thanks to its features, such as: wide part-load regulation range (from 10 to 100 % without problems), simple start-stop procedures, minimum maintenance requirements and compact layout.

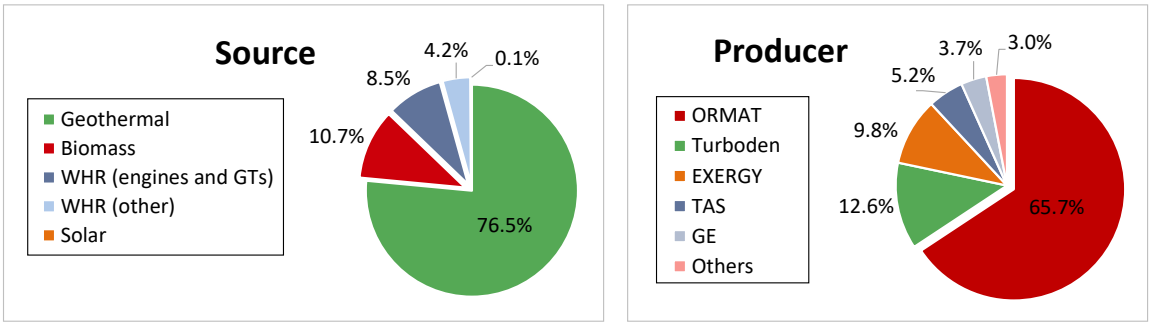

Figure 1-12 - ORC market share (source of data [22]).

Concerning the producers (see Figure 1-12), ORMAT is the world leader for the total installed capacity (65.7 %), followed by the Italian companies Turboden (12.6 %) and Exergy (9.8 %). Within the niche of micro-scale ORC system, some examples of small manufacturers active in the market are: Air Squared (US), Rank (ES), Enogia, Visorc (FI), ElectraTherm (USA) and the Italian Zuccato Energia (IT).

Trends of the technology cost are also reported in Figure 1-13. Available data about the ORC investment cost, provided by Turboden [23], show a negative exponential trend of the ORC cost based on the size, concerning the medium to large scale (see red curve in Figure 1-13). The specific cost decreases with the size, from 4000 to less than 2000 eur/kW, going from a 500 kW to a 20 MW size. For what concerns the micro scale, instead, precise correlations for the specific cost are not yet available. An estimated curve is provided by Air Squared in [24], following almost the same trend of the previous one. According to this trend, for a 1 kW system, the specific cost is around 10000 USdoll (i.e. about 8600 eur).

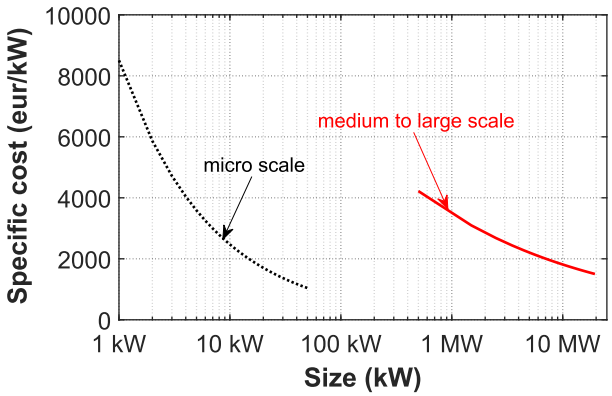

Figure 1-13 - ORC specific investment cost data provided by different literature sources: interpolated curves for the micro scale from [24], for the medium to large scale from [23]).

1.5 Current challenges

1.5.1 Medium to large scale ORCs

Although medium to large scale ORCs are yet quite diffused, this technology is still scarcely exploited compared to its potential [9]. Indeed, barriers that prevent the growth of this market still exists and are in particular the lack of green incentives and long-term paybacks that determine a not negligible risk on the investment. In addition, industrial capital budgets are limited and the industries usually prefer to give priority to safer investments closer to the company's core business [5]. Hence, it is interest of the ORC producers and of the researchers to continue investigating new solutions to make it more attractive for the industries, in particular in those sectors still in the expansion, where important investments are expected in the next years.

It is the case, for example, of the gas distribution networks, which are yet ramified around the world but continue expanding to follow the growing natural gas demand [25]. Natural gas compressor stations, installed along the pipeline, represents a great WHR opportunity. Figure 1-14 gives an idea of the number and the distribution of the natural gas compressor stations considering only the USA and Europe. In these facilities, the ORC could be inserted to produce a surplus of energy to be sold to the grid. For remote applications, in which the energy sell can be discouraged due to lack of grid connections, the ORC can be inserted instead to directly drag a compressor in place of a fuel fed prime mover [26]. In this case, a re-allocation of the station load between the prime movers and the ORC is needed. This solution being barely explored in literature, could incentive the investment on this technology if it demonstrates to be profitable. About this topic, it can be cited the work of Branchini et al. [27] studying the direct coupling between an ORC driver and a gas compressor by a computational fluid dynamic point of view. An ORC axial turbine-based expander is designed to accommodate variable speed operation.

Researchers are increasingly improving the techniques for studying these systems, although in most of the cases, these analyses consider not further than the on-design regime of operation [28]. However, the performance of ORC systems strongly depends on the heat source characteristics and

the system design. In WHR applications, the heat source often undergoes fluctuations and intermittency due to non-uniform production of the industrial process. This can be a crucial aspect to take into account for the evaluation of the system feasibility, even if not commonly considered.

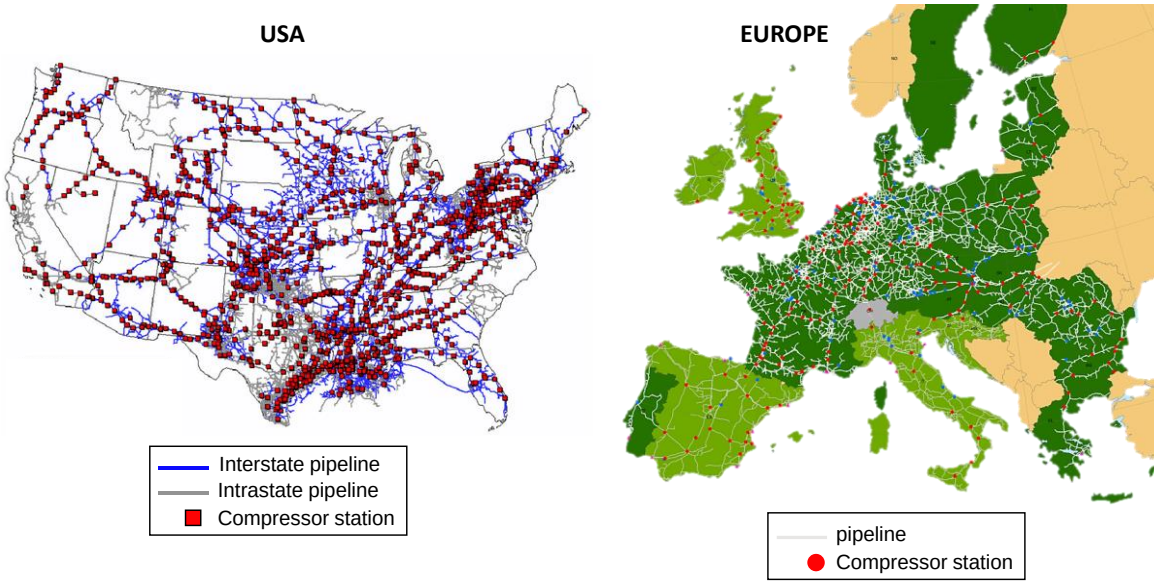

Figure 1-14 - Natural gas compressor stations distribution in USA [29] and Europe [30].

1.5.2 Micro-ORCs

ORC energy systems are an efficient solution for low temperature and small size heat recovery applications [31]. However, the market uptake is still at an early stage, depending on technological issues, such as the selection and design of the system components [32], but also on the structure itself of the electricity generation network, which is mostly of centralized type.

From the analyses of the existing ORC prototypes [33][§] it results that the working efficiency of low temperature micro-ORC is still relatively low (see Figure 1-15), due to the small temperature difference between hot source and cold sink resulting in scarce Carnot efficiency, as well as to the lack of appropriate expander machines in the commercial market and working fluids. Whilst the efficiency reaches up to 25 % for large scales (around 10 MW), for small scales it can decreases below the 5 %.

Expander

In particular, among the different conceived expander technologies, there is not a prevailing solution for micro-ORC (see Figure 1-15) and there is still space for development in this dedicated research field. Experimental data trends related to existing micro-ORC prototypes, suggest that design aspects, among which is the expander built-in volume ratio, should be still optimized. Indeed, most of the conducted experiments present a mismatch between the cycle expansion ratio and

[§] The presented database includes 175 scientific references corresponding to102 unique ORC prototypes.

expander expansion ratio, leading to significant over- and under-expansion losses [34] **. Due to this, isentropic efficiencies of expanders dropped at maximum power output conditions, cycle efficiency does the same as consequence. To optimize the performance of the expander and to minimize under-expansion and over-expansion losses, this built-in volume ratio should match the operating conditions. The volume expansion ratios achieved in Rankine cycle systems are typically larger than those achieved in vapor compression refrigeration systems, thus the development of adapted designs of such expanders, rather than retrofitting existing compressors is necessary. Generally speaking, piston expanders are more appropriate for applications with large expansion ratios because their design allows for higher internal built-in volume ratios. However, this kind of architecture is not yet appropriately investigated in the literature neither in the theoretical nor in the experimental point of view. As shown in Figure 1-15 prototypes using piston expanders are really a few.

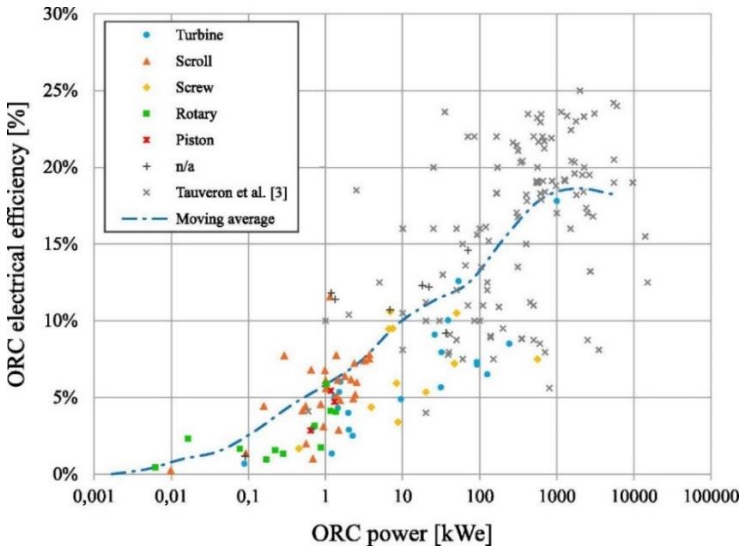

Figure 1-15 - Experimental trend of the ORC electrical efficiency as function of the size (data source [33]).

Working fluid

Concerning the working fluid, the research about new low GWP fluids, in most cases, focuses on how they perform in refrigeration cycles, and on the modifications that has to be done on the hardware for retrofitting existing cooling systems [16]. Indeed, refrigeration plants retrofit with HFOs has been already comprehensively assessed in many studies (see for example the experimental studies by Zilio et al. [35], for air conditioning, by Lee and Jung [36], for car conditioning, by Navarro-Esbrì et al. [37] and Zhao et al. [38], on R134a replacement in compressors), dedicated and extensive tests for ORC applications are still required instead. However, some detailed analyses on olefins performance in ORC systems, both numerical and experimental do exist, even if mostly refer to the replacement of R245fa in application with heat source temperature

** Data collected from scientific works containing or referencing ORC based experimental outcomes scrutinized by availability of the measures of: electrical/mechanical power output from expander, evaporation pressure/temperature and condensation pressure/temperature. Date of publication of the paper: 2018.

between 120 °C and 200 °C. To mention just a few examples, Eyerer et al. [39] and Yang et al. [40] recently performed experimental analyses to evaluate modern HFO fluids substitutes of R245fa in ORC systems, testing also the materials compatibility [39]. On the contrary, studies investigating R134a alternatives for lower temperature applications (lower than 100 °C) are still scarce and mainly numeric type.

Only some early studies, carried out in specific limited conditions, revealed that some low-GWP fluids can be promising alternatives for R134a, even if they could not always guarantee the same performance of HFC fluids. For example Invernizzi et Al. [41] investigated the potential replacement of HFC-134a in an ORC geothermal plant fed with hot water at 150 °C, by new HFOs, observing a decrease in the net power production. Likewise, Boyaghchi et Al. [42] performed a multi-objective optimization of a novel micro combined cooling, heating and power system driven by solar and geothermal for four working fluids including R134a, R423A, R1234ze and R134yf from the energy, exergy and exergoeconomic viewpoints. The multi objective optimization results indicate that the best fluid from the energy and exergy viewpoints is R134a. Other studies have been conducted on the topic, but mainly based on a pure thermodynamic approach, adopting simplified hypothesis such as constant expander and pump efficiency and adiabatic expansion process [43], [44], [45]. Though, it is crucial to properly include into the assessment also the actual influence of the fluid on performance of the key ORC components. Indeed, actual operating conditions of the expander and the pump can strongly depend on fluid properties such as density and viscosity, especially if considering volumetric type machines, as demonstrated in this work of thesis, where these aspects determined in fact a performance degradation. Another important factor of influence when considering the expander real operating conditions is the fluid conductive coefficient, as the expansion process is not strictly adiabatic [46]. All these potential performance change issues require also an environmental investigation.

1.6 Innovative configurations

Innovative configurations for the WHR by means of ORCs are recently proposed in literature and not yet properly explored. Among the most promising architectures, the following have been selected to be further investigated in this work of thesis: i) the supercritical CO_2 cycle for industrial WHR and ii) the ORC in power to heat to power configuration.

1.6.1 Supercritical CO_2 cycle for industrial WHR

A promising and not yet fully explored solution for waste heat recovery from gas turbine exhaust gas is the innovative supercritical CO_2 based Brayton cycle (s-CO_2). The CO_2 cycle is an alternative to the ORC, always relying on an operating fluid with critical temperatures lower than water (see Figure 1-5) having the positive characteristics of: i) the dry expansion; ii) the simple generation of the vapour at the turbine inlet (only a heat exchanger is needed); iii) the possibility to operate with air-cooled condenser. Figure 1-16 compares the different operating range of steam, ORC and s-CO_2 heat to power conversion technologies for WHR applications, highlighting the overlap of the ORC and the s-CO_2 application filed, on the operating range of interest for the medium to large WHR. The s-CO_2 technology, may begin to be considered competitive with the ORC in this area, having also

exclusive feature of using non-toxic, nonflammable, environmentally friendly and widely available working fluid [47].

Whilst ORC systems are already available successfully employed for industrial WHR, conversely, the s-CO_2 cycle is still at an early stage and not yet ready to be introduced in the market. Open problems related to the s-CO_2 design concern: i) the development of compact high pressure heat exchangers at reasonable cost, ii) the reduction of leakage and mechanical losses in turbomachines and iii) the optimal regulation and safe operating conditions of the compressor close to the CO_2 critical point [48]. Nowadays, different research programs are being carried out by both industrial and academic research institutes, to develop prototypes of s-CO_2 and study how to overcome these issues. Among them, it must be cited the "EPS100", proposed by Echogen as the first megawatt topping-class commercial-scale supercritical s-CO_2 heat engine, in phase of validation testing [18], specifically designed for small-scale gas turbines combined cycle (~30 MW total output) applications.

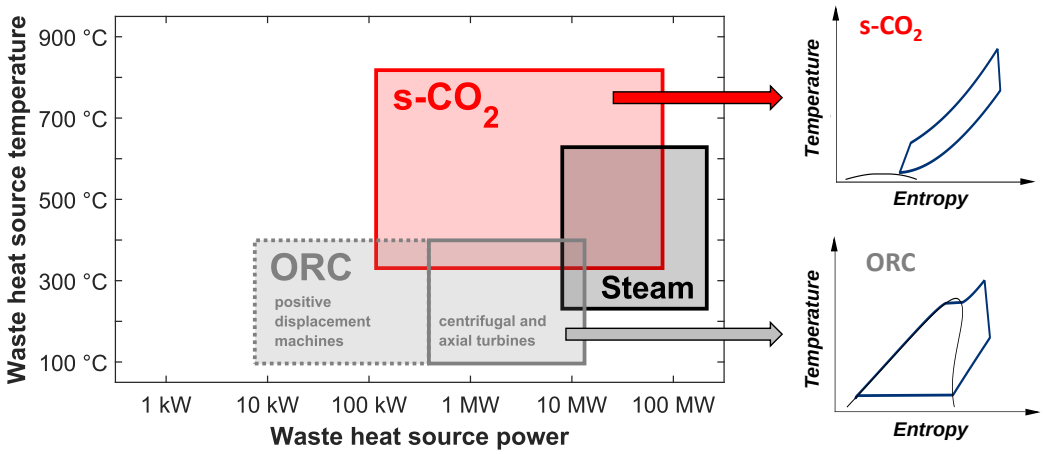

Figure 1-16 - Comparison of steam, ORC and s-CO_2 operating ranges for WHR applications (data source [49]).

However, except for this prototype, the literature on the industrial WHR with s-CO_2 is still scarce, especially considering industrial gas turbines as topper cycle. It can be cited the study proposed by Zhou et al. [50], analyzing a complex combined cycle system for off-shore gas turbines WHR, involving s-CO2 plus a transcritical CO2 cycle. The analysis is applied to the commercial gas turbine model "Solar TITAN 130", demonstrating promising performance and economic gains, for the s- CO_2 application in the oil and gas sector. Several studies investigate instead s-CO_2 potential for high-temperature heat recovery, mostly concerning solar and nuclear applications, and still poorly fossil fuels applications [51]. Some examples are: i) Turchi et al. [52], whom comprehensively analyzed thermodynamic performance of concentrating solar supercritical CO_2 power cycles; ii) Syblik et al. [53], whom focused on design optimization for nuclear and fusion energy sector; iii) Park et Al. [54], whom explore thermodynamic and economic aspects of coal-fired combined power plant with CO_2 based Brayton cycle.

In the current literature, only few studies are dedicated exploring the potential of the s-CO_2 as industrial WHR solutions and compare its performance with the one of the ORC. It can be cited only

the study of Astolfi et al. [55], comparing CO_2 power cycles and ORC, by means of thermodynamic performance maps, as function of different heat sources maximum temperature (200-600 °C) and cooling grades, in which the Authors demonstrated that the most convenient choice sensibly depends on the actual boundary conditions. Then, the analysis, proposed by Yoon et al. [56], which compares off-design performance of ORC and transcritical CO_2 cycle, as bottoming cycle of a micro gas turbine; highlighting how a CO_2 recuperated cycle can be more performant at part-load operations than a simple ORC. In particular, the CO_2 recuperated cycle exhibits a more efficient heat exchange process at the heat recovery unit, due to the presence of the recuperator (however, a more comprehensive analysis including also an ORC recuperated configuration is missing). Except for these examples the literature is poor on the topic and further studies regarding applications of CO_2 based WHR, specifically in industrial likely operating conditions and specific comparison with its main competitor, the ORC, are needed.

1.6.2 Power to heat to power configuration

Small-scale ORCs can be also efficiently employed into a so-called Carnot battery. The Carnot battery is a system that allows to storage surplus of electric energy by converting it into heat and then reuse this heat by converting it back in electric energy when needed [57]. There are different configurations of Carnot batteries, characterized by different heating technologies to charge and discharge the thermal storage. Among the different options there is the reversible heat pump (HP)/ORC power system. In this configuration, the HP and the ORC system are embodied in a single and compact power plant, in which the ORC and the HP share the same volumetric machines, the same heat exchangers and the same working fluid. The system works as an HP in charge mode and as ORC in discharge mode, as illustrated in the scheme of Figure 1-17.

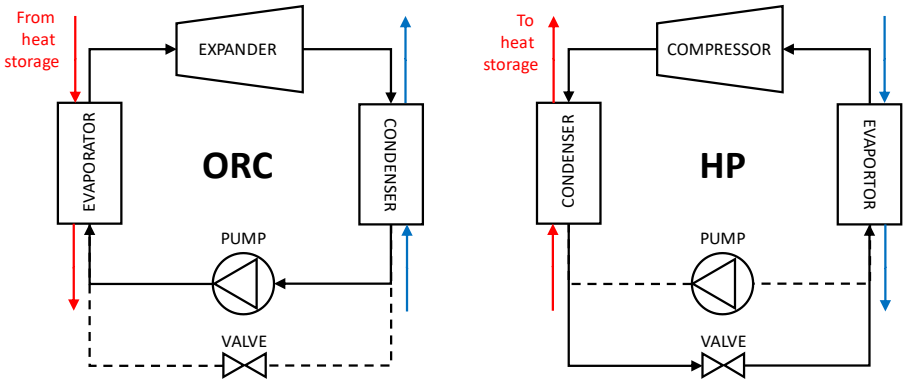

Figure 1-17 - Scheme of the reversible HP/ORC power system.

This type of storage can achieve higher roundtrip efficiency (even higher than 100 %) by adding the contribution of a waste heat source, in a thermally integrated energy storage. In this case, the heat storage configuration uses the heat pump to increase the waste heat temperature. This allows the ORC to increase its efficiency by working with a higher temperature difference as illustrated in Figure 1-18. Thus, this system becomes very interesting in these applications where different energy

fluxes must be handled (both electric and thermal), among which are the automotive sector, data center, stationary engine, supermarkets and Net Zero Energy Buildings [57].

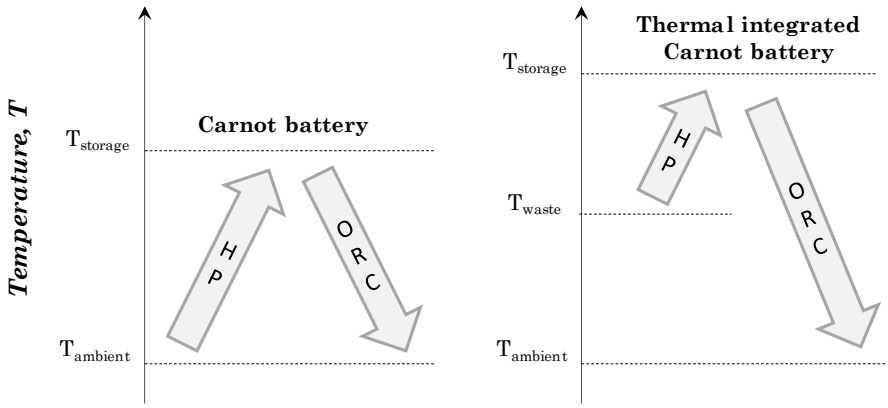

Figure 1-18 - Carnot battery (CB) and thermal integrated Carnot battery (TICB) operating temperatures.

A preliminary comparison with other storage technologies is provided by Dumont et Al. [57], involving: pumped hydro-storage (PHS), fuel cells combined with hydrogen storage (FS), batteries (and flow batteries) (B), compressed air energy storage (CAES), liquid air energy storage (LAES), gravity energy storage (GES). PHS is the most widespread large-scale energy storage technology: the operating principle of PHS is to pump a fluid to a reservoir with a certain elevation when the electricity demand is low. In discharging mode, the fluid converts its potential energy in a turbine to produce electricity. CAES has also been demonstrated at large scale. In CAES, air is compressed in a given hermetic tank or underground reservoir during the charging mode and expanded in the discharge mode. However, they both require specific geological conditions, which significantly decrease the availability of these types of energy storages. Also, their energy density is rather low (see Table 1-2). Flow batteries could possibly become a useful way of storing large quantities of energy due to their large energy density (60 kWh/m^3). However, they suffer from a rather low lifetime and the use of rare (or expensive) materials (Table 1-2). LAES (air compression to store it in its liquid state) and GES (potential energy store by moving a large mass vertically) are not mature technologies and suffer from large energy price and low energy density. Finally, the fuel cells (hydrogen electrolyze), despite their high energy density (Table 1-2) present a relatively low lifetime with a limitation on the number of cycles.

This fast comparison among the available short-time storage technologies shows the interest in developing new energy storage technologies such as the Carnot battery (CB). In this context, the Carnot battery technology becomes interesting due to its long cycle life, no geographical limitations, no need of fossil fuel streams and capability of being integrated into conventional fossil-fueled power plants or with any other type of waste heat source. However, the Carnot battery technology being based on the small-scale ORC one, has not yet reached the technological maturity and it is far to enter the market. The state-of-the-art lacks prototypes demonstrating the performance and the reliability of the system and the storage technology should be also deeper investigated to find out the best solution in terms of be compactness and cheapness.

At the present day, analyzing the state of the art of the technology [57], very few studies are dedicated to this topic. Dumont et al. experimentally investigated a reversible ORC/HP unit designed to be coupled with a passive house [58]. The same authors presented in [59] a part-load model of reversible ORC/HP to analyze the part load performance of the system. Another application is presented by Di Cairano et al. [60] presented a simulation methodology to assess the reversible ORC/HP benefit when integrated in automotive applications.

Table 1-2 - Comparison of the electrical energy storages [57].

Technology	Energy density (kWh/m^3)	Energy price ($/kWh)	Roundtrip efficiency (%)	Lifetime (years)	Specific geographical conditions required
PHS	0.5-1.5	5-100	65-87	30-60	Yes
GES	0.5-1.5	N/A	70-86	30-40	Yes
CAES	3-12	2-200	40-95	20-60	Yes
LAES	50	260-530	40-85	20-40	No
Li-Ion B	300	500-2500	85-95	5-15	No
Flow B	16-60	120-1000	57-85	5-15	No
FS	500-3000	1-10	20-50	5-30	No
CB	0.25-6.9	60	70-80	25-30	No
TICB	0.51-13.9	24	70-200	25-30	No

2 Thesis overview

2.1 Current challenges overview

In this final chapter of introduction, open challenges concerning the ORC technology are summarized to present the related novel contribution made of this thesis. Current challenges that hinder the diffusion of the ORC in the market are different depending on the temperature and the enthalpic content of the heat source. Focusing on the micro range power size and low temperature applications:

- the ORC technology is still not mature and there is still room for improvement especially concerning the expander and the pump design, for which there is not yet a prevailing optimal solution. The design of these two components in particular is proven to strongly affect the micro-ORC efficiency. These components are usually of positive displacement type, since more suitable to be operated with low values of flow rate and expansion ratio and, currently, their design is in many cases derived from the machine used in the HVAC/R industry.
- Another sensitive issue is the selection of the working fluid, which should respect some characteristics in terms of performance and risk of environmental impact. For instance, synthetic refrigerants belonging to HydroFluoroCarbons category are very performant for low-temperature applications thank to their low critical temperature. On the other hand, despite their null ozone depletion potential, HFCs risk to highly contributing to the anthropogenic greenhouse effect, if released, due to their high global warming potential values and high residence time in the atmosphere. Thus, the research, in particular in the refrigeration sector, is currently working on finding valuable alternatives to HFCs, which can guarantee the same performance of typically used fluids, but lower environmental impact at the same time.
- The literature lacks case study of real applications of micro-ORCs considering the thermal storage opportunity, evaluating their integration into already existing realities. In this context, it becomes fundamental to develop optimal control of the reversible ORC system when inserted into a more complex grid.

Focusing instead on the low-to medium size application with temperature even up to 400 °C, the ORC technology is already available but the investment is still risky. In order to promote the investment on this technology, it is up to the research to:

- demonstrate its economic and environmental benefit in different scenarios.
- investigate new solutions for what concerns the coupling between the topper cycle releasing heat and the ORC, and their management during off-design operations.

- Evaluate the convenience of variations of the standard ORC with the aim of finding more performant alternatives.

What they have in common all the aforementioned challenges is the necessity of developing reliable and accurate models to be faced. Literature on the ORC simulation is consistent, but nevertheless several studies have been conducted on this topic, almost all of them are based on a pure thermodynamic approach, adopting simplified hypotheses such as constant expander and pump efficiency and adiabatic expansion process. In general, constant efficiency models are not suitable to evaluate realistic applications of ORCs, which born to operate often under off-design conditions, given the variable nature of the hot source. Concerning in particular micro-ORCs, this approach also risks overlooking the actual influence of the fluid on performance of the component.

2.2 Objectives and structure

This thesis addresses the aforementioned issues touching different themes; in doing so, a particular attention is paid in the development of reliable models based on realistic data and accounting for the off-design performance of the ORC system.

The document is split into two parts, i.e. part I "ORC for micro-generation" and part II "ORC for the medium to large scale industrial WHR".

Part I: ORC for micro-generation

Concerning the "Micro-generation" part, the first aim of this work is to further explore the modelling methodology, the performance and the optimal parameters of reciprocating piston expanders, being this typology not yet properly investigated in the literature. The second objective is to investigate the performance of such expander and of the whole micro-ORC system when using HFC fluids or their new low GWP alternatives and mixtures, accounting for both direct and indirect emissions, in different energetic scenarios. In particular the substitution of R134a, as performing fluid for low temperature applications, is evaluated. As third objective, this thesis intends to analyze the innovative ORC/HP reversible architecture, its optimal regulation strategy and its potential when inserted in typical small industrial realities. The modelling activities on these topics were supported by experimental data collected on two different test benches: the micro-ORC prototype of the University of Bologna, testing a reciprocating piston expander, and the Carnot battery prototype of the University of Liège.

The thesis structure for the "Micro-generation" part is the following:

- Chapter 3 - Experimental data elaboration: this chapter discusses the methodology used to collect reliable data from experimental tests on the test bench of the University of Bologna. This step is fundamental to obtain the data for the calibration and the validation of the models proposed in the next chapters.
- Chapter 4 - Semi-empirical modelling: this chapter presents the implementation and validation of the off-design model of the system, based on a semi-empirical lumped parameters approach with the introduction of a methodology to account for the influence of the change of the working fluid over the components' performance. A focus on the comparison between different literature models for the reciprocating piston expander is proposed.

- Chapter 5 - Influence of the working fluid over the performance and the environmental impact: this chapter analyzes in detail the performance and the optimal operation of the reference expander when working with different working fluids under different boundary conditions. The whole plant performance is also analyzed to comprehensive evaluate the greenhouse impact of the system which can derive from the use of low-GWP fluids, in place of HFCs, and vice versa, accounting not only for direct greenhouse emissions but also for indirect contribution. A comparison of different working fluid and mixtures performance and environmental impact has been performed, analyzing different energetic scenarios.
- Chapter 6 - Optimal management of power to heat to power systems: this chapter presents a model for the Carnot battery prototype of the University of Liège, which consists in the integration of the micro-ORC model discussed in Chapter 3, with a heat pump model, with the necessary adjustments. The model is applied to map the performance of such a system and develop an optimal regulation strategy. Considerations about the optimal storage sizing are made based on the results of the simulations performed for different scenarios.

Part II – ORC for the medium to large scale industrial WHR

Regarding the "Industrial WHR" part, the general objective is to further explore the WHR opportunity of ORCs, with a focus on the natural gas compressor stations application. The intention is to provide information about all the possible parameters that can influence the optimal sizing, the performance and thus the feasibility of such a system, starting with the topper gas turbine model and its part load operation, being these aspects rarely considered in the current literature. This study wants also to take a look to new WHR configurations to investigate their potential advantages. Among the configurations explored in this thesis are, a first one, relying on the replacement of a compressor prime mover with an ORC, into a natural gas compressor station. In this case, the optimal re-allocation of the station load between the prime movers and the ORC must be discussed. A second examined configuration consists in the use of a supercritical CO_2 cycle as heat recovery system, not yet deeply examined and compared to ORC for WHR from industrial applications. The modelling activities on these topics were supported by data provided by ORC and gas turbines manufacturer, within a collaboration with Turboden and Solar Turbines.

The thesis structure for this part is organized in the chapters listed below:

- Chapter 7 - Modelling approach: this chapter describes the building of an off-design gas turbine-ORC combined power plant model using a commercial software dedicated to the simulation of complex energy systems, with the support of technical data provided by Turboden.
- Chapter 8 – Factors of influence on the design of ORC as WHR solution in natural gas compressor stations: this chapter analyses the feasibility, the energetic and the environmental benefit that can apport the ORC into a natural gas compressor station, under several scenarios in terms of demanded energy profile, ambient conditions, prime mover size, regulation strategy, number, etc.
- Chapter 9 - Optimal load Allocation between topper and bottomer system: this chapter discusses the development of an optimal topper system–ORC load allocation strategy, accounting for the part-load operation of the industrial process in which the ORC is inserted. An analysis of a case study of a natural gas compressor station run by Solar models' gas turbines is also proposed.

- Chapter 10 - A comparison between ORC and supercritical CO2 cycles: this chapter proposes a systematic comparison between ORC and s-CO_2 as bottomers of industrial gas turbines in both pure electric and combined heat and power plant configuration. The performance, the components' dimensions and the operating costs are evaluated considering systems specifics in line with the current state-of-the-art products, experience and technological limits.

PART I

ORC for the micro-generation

3 Experimental data elaboration

Summary This chapter describes: i) the micro-ORC prototype of the University of Bologna, subject of analysis of the first part of this thesis, and ii) the methodology used to collect reliable data from the experimental tests on this test bench. More in detail, an algorithm to detect steady-state operating intervals during the tests has been implemented, in order to determine the micro-ORC stable operating points and its performance in these conditions. In this way a large amount of data has been acquired, fundamental for the calibration and the validation of the models proposed in the next chapter. In this regard, a training set of data has been distinguished from the validation set of data, to test both the model interpolation and extrapolation capabilities.

3.1 Test bench of the University of Bologna - experimental setup

The experimental setup of the test bench of the University of Bologna is described in the following paragraphs. For further details about the components and the acquisition system, the lecturer is invited to consult the thesis of Ottaviano [61], dedicated on the design of the test rig and the experimental characterization of the prototype. This work is instead more focused on the data elaboration techniques and its use for the calibration and validation of semi-empirical models.

3.1.1 The ORC system

The reference system consists of a 3 kW nominal scale recuperated ORC with a small footprint, 80x85x253 cm, designed for the residential/small scale industry (see Figure 3-1). It is constituted by the following components:

- Three heat exchangers: two of which are commercial brazed plate heat exchangers ONDA S 202 model, the evaporator, composed by 64 plates, and the recuperator, composed by 16 plates; whilst the other is the condenser, constituted by a shell-and-tube heat exchanger, model ONDA CT 292. More details about the heat exchangers dimensions are reported in Table 3-1
- The key component of the system is the expander, a prototype of reciprocating model developed by the Italian company StarEngine (see patent [62]). Figure 3-2 shows a schematic illustration of the machine architecture. It is made of three cylinders placed radially at 120° with a total displacement of 230 cm^3/rev. The admission and the discharge of the vapor at the expander are executed by rotatory valves, which are placed in correspondence of the cylinder head and are driven by the crankshaft rotation. The expander is directly coupled with the generator, which is connected to an electrical load, made of five pure resistive loads, connected in parallel between them and in delta with the generator output three-phase line. In this configuration, the load does

not allow setting the generator rotational speed nor the load torque, and the expander shaft is free to achieve the equilibrium between the generator torque and the set load resistance. The expander is internally provided with a secondary passage that is used to by-pass the cylinders in cold start-up operations, in order to let the fluid achieving the required superheating conditions and to warm up the expander casing to avoid thermal stresses. The external surface was insulated with a layer of mineral wool to reduce heat losses.

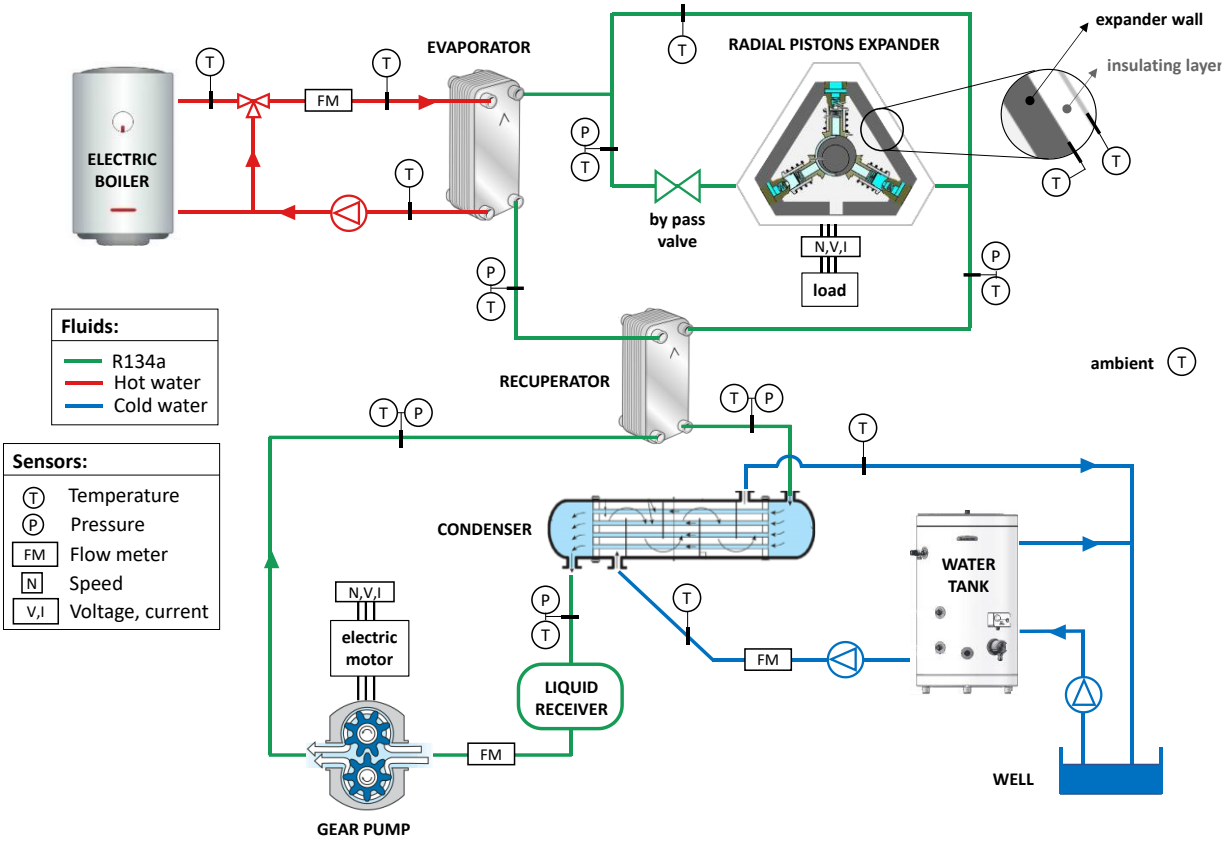

Figure 3-1 - Micro-ORC experimental facility of the University of Bologna.

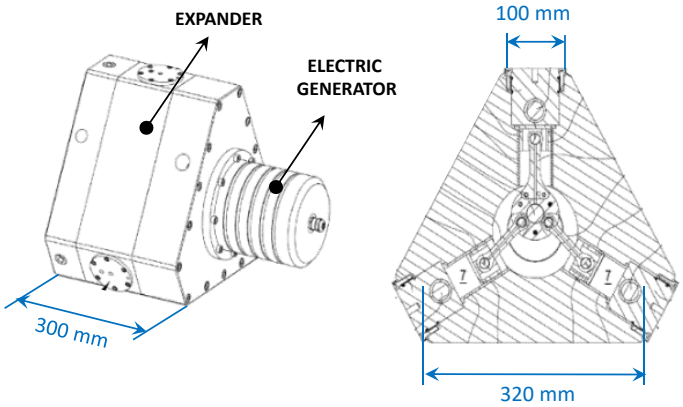

Figure 3-2 - Piston expander prototype [62].

- The feed pump is an external gear type, also provided by the same manufacturer of the expander. The pump is driven by an asynchronous electric motor, to which is coupled through a speed reducer with gear ratio of 1:3. The motor is driven in its turn by a frequency inverter, which allows a proper regulation of the flow rate of the working fluid, since the pump is of positive displacement type. The pump displacement is estimated from the experimental data around 60 cm^3.
- The liquid receiver is a horizontal tank model FrigoMec of volume equal to 0.019 m^3.

3.1.2 Fluid and charge

Since the system is conceived for heat recovery applications from heat sources with temperature below 100 °C, the refrigerant R134a was selected as working fluid, as suitable for working in this range of temperature, given its critical temperature equal to 101 °C and its critical pressure of about 40 bar (R134a thermodynamic characteristics are reported in diagram of Figure 3-3).

The R134a (or Tetrafluoroethane) is a halocarbon of the HFC category with chemical formula $C_2H_2F_4$. It is widely used in automobile air conditioners and household refrigerators, thanks to its great chemical and thermal stability and low toxicity. In addition, it is non-flammable, besides having an excellent compatibility with most materials. As all HFC refrigerants, it doesn't not damage the ozone layer, nevertheless it has a not negligible GWP equal to 1300 [17].

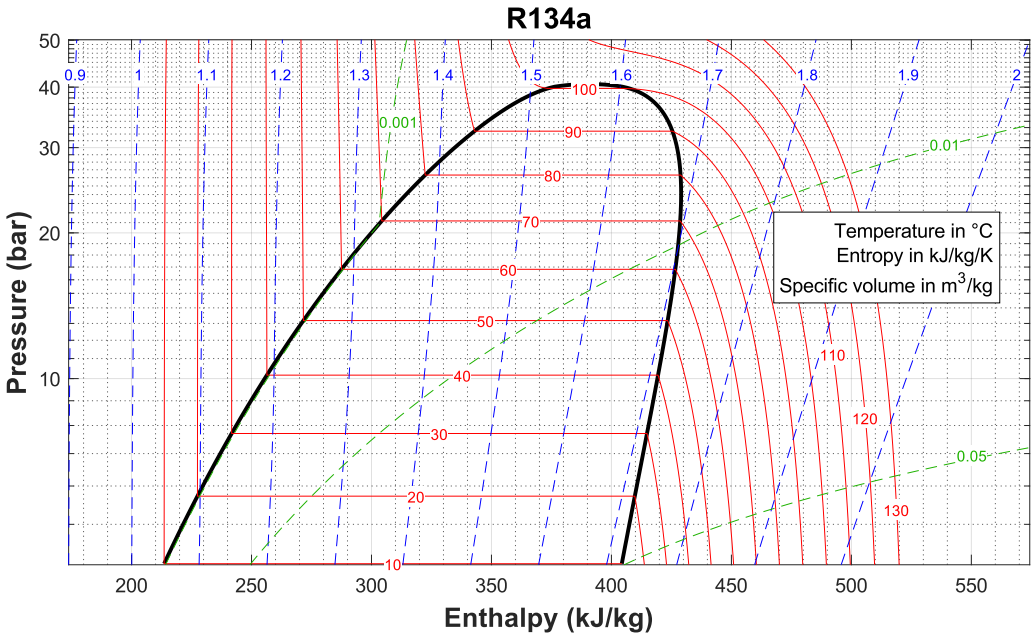

Figure 3-3 - R134a pressure-enthalpy thermodynamic diagram ††.

The amount of fluid charged inside the circuit is for the ORC systems a fundamental parameter affecting the system performance. In particular, an overcharge of fluid can cause at the same time a decrease in the phase change heat transfer area of the heat exchangers and an increase of the fluid

†† Curves obtained by means of the thermodynamic library Refprop [63].

cost (which can be significant in some cases). On the other hand, an insufficient charge of working fluid increases the risk of cavitation of the pump [61]. As it will be detailed into the following chapter, the optimum value of this parameter depends on the temperatures and pressures during the operation and on the involved volume, which can be approximated to the sum of the heat exchangers and the liquid receiver volumes. These parameters are reported in Table 3-1 for the case study. Based on these considerations, for the correct operation of the test bench in exam, the charge is maintained around the 25 kg.

Table 3-1 - ORC circuit main volumes.

Component	Volume (m^3)	Heat transfer surface* (m^2)
Evaporator	0.0085	6.2
Recuperator liquid side	0.0026	1.8
Recuperator vapor side	0.0026	
Condenser	0.034	3.5
Liquid receiver	0.019	/

*estimated

3.1.3 Water circuits

Two external water circuits, representing the hot and the cold source, are included into the test rig in order to characterize the system under variable boundary conditions:

- The hot source is made by an electric water heater with rated power of 42 kW, that allows controlling the water temperature at the evaporator inlet between 50 °C and 100 °C.
- The cold source consists instead in a water well used as heat sink, providing a condenser inlet temperature variable between 13 °C and 28 °C, depending on the ambient conditions.

A pump of centrifugal type, Grundfos Magna1 40-180F model, is inserted in both the water loops to let the fluid circulates.

3.1.4 Sensors and acquisition system

The test bench, then, is fully equipped with an acquisition system, consisting in T-type and K-type thermocouples, absolute pressure transducers and flow meters. Voltage and current transducers are installed on the expander and the pump supply lines for acquiring electrical power and frequency of the two machines. The thermocouples are placed at the inlet and the outlet of each component, plus two additional thermocouples positioned on the expander surfaces, one between the casing wall and the insulating layer and the other on the external surface of the insulator (see the detail on the expander zoom in Figure 3-1), for the heat losses evaluation. The main features of sensors and the acquisition system are reported in Table 3-2.

The signals collected by the sensors are read in real time by means of a National Instrument Compact RIO microcontroller, to be acquired via the acquisition software LabVIEW.

Table 3-2 - Specifics of the acquisition hardware.

Variable	Sensor	Working range	Output signal	COTS accuracy*	Input module
ORC Temperatures	T-type thermocouple	0-90 °C	± 80 mV	±0.5 °C	NI9213-Thermocouple input
Water temperatures	K-type thermocouple	0-90 °C	± 80 mV	±0.5 °C	
ORC Pressures	Pressure transducer Honeywell FP200	0-30 bar	0-5 V	±0.25 % FS	NI9201-Voltage AI
		0-10 bar			
ORC mass flow rate	Coriolis mass flow meter (H+E Promass)	0.05-1.00 kg/s	4-20 mA	±0.3 % RV	NI9203-Current AI
ORC density		10-1300 kg/m^3	4-20 mA	±0.1 kg/m^3	
Hot water flow rate	Magnetic flow meter (H+E Promag)	0-6.4 l/s	4-20 mA	±0.5 % RV	
Cold water flow rate	Magnetic flow meter (H+E Promag)	0-9.8 l/s	4-20 mA	±0.5 % RV	
Electric current and voltage	PCB mounted Hall effect voltage and current transducers	0-400 V 0-5 A	0-4 V	±0.1 % RV ±0.2 % RV	NI9215-Voltage AI

* Component Off-the-Shelf accuracy = instrument accuracy as indicated into the datasheet, before calibration.

3.2 Steady-state detection

3.2.1 Operating principle

A fundamental step to extract realistic and significant data from the experiments is the detection of the steady state operating intervals of the system during the tests. Indeed, performance maps of the system can be traced evaluating its behaviour when working at regime under different boundary conditions (as illustrated in Figure 3-4). Thus, it becomes important to implement rigorous algorithms to detect the steady state operation of the system.

During the tests, the involved variables are measured with a given acquisition frequency, so as to generate a signal composed by an ordered sequence of data in the time. According to the narrow meaning of stationarity, the signal should be considered stationary when its variation over the time is null. However, this definition is not possible to meet when dealing with experimental data. Indeed, the signal deviates from its mean value not only because of perturbations dictated by the variation of the boundary conditions, but also because of the presence of background noise and other kind of disturbances. The noise can be attributed to different events, such as mechanical vibrations, thermal movements, flow turbulence and undesired electrical signals which contaminate the values transmitted to the acquisition system; the disturbances instead derive from dynamic phenomena concerning the sensors. Due to the non-ideality of the process and the presence of errors into the measured signal, it is necessary to relax the concept of stationarity and accept a limited variation of the variables around its mean value, to consider the interval as stationary. Once the steady-state interval is detected, the operating point of the system can be obtained by averaging the values of the variable over the time on the steady-state interval, in order to minimize the influence of the disturbances (as illustrated in Figure 3-4).

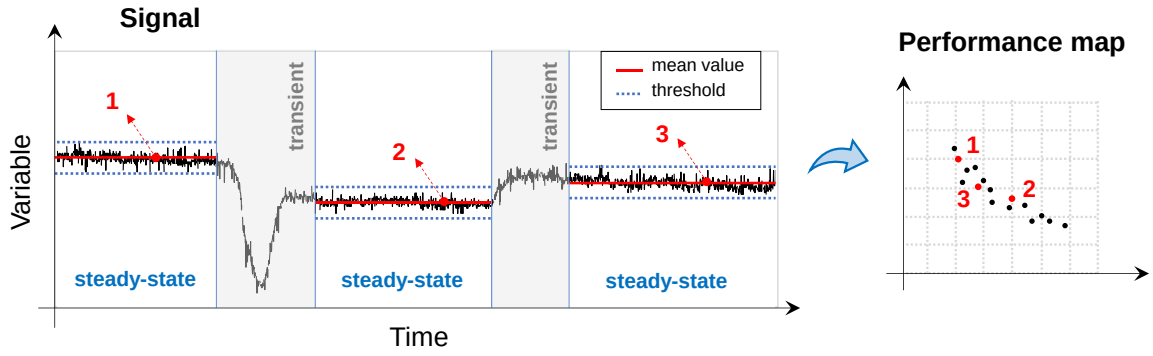

Figure 3-4 - Steady state detection – operating principle.

Different methodologies can be chosen, depending on whether the algorithm must be applied online or in post-processing. An algorithm that should work online requires to not occupy too much memory, in order to not slow down the acquisition process. An example of algorithm for online application is the "R-test" proposed by Cao and Rhinehart [64]: being based on an exponential moving average, it doesn't necessitate to keep in memory all the measures at the previous time steps, but only the one at the last time step. This kind of algorithm can be useful to monitor the test and be sure to achieve the steady-state conditions during the experiment. However, the effectiveness of the algorithm depends on the correct calibration of some parameters (so called filtering factors), whose value is correlated to the characteristic of the process, such as the settling time and the noise around the signal. Thus, the calibration is not always immediate since it should be carefully conducted on the basis of already available data. Algorithms for the post-processing instead have no limits on the memory and can analyze the entire trend of the signal during the experiment. In this case, the advantage is that the acceptable variation around the mean value is no more an implicit input since it does not depend on secondary parameters (such as filtering factors), but it can be directly imposed a priori.

3.2.2 Implemented algorithm

For the case study, a post-processing algorithm similar to the one used by Kim et al. [65], is chosen to elaborate the data coming from the tests. The selected method consists in comparing the value of the variable to its moving mean value. When the variation between the variable and its moving mean falls into an acceptable variation band, the interval can be considered steady state; the concept is illustrated in the example of Figure 3-5. Equations used to implement the algorithm are described more in detail below.

The moving mean, $\bar{x}_k$, at the k-th time step is computed by means of Eq. (3-1):

$$\bar{x}_k = \frac{1}{n} \sum_{i=k-n+1}^{k} x_i \qquad (3\text{-}1)$$

Where x is the generic process variable, and n is the size of the time window over which the average is computed. Basically, according to this equation, at each k-th time step the time window is updated using the n most recent values to compute the average on the next sequence of data, as illustrated by the scheme in Figure 3-6

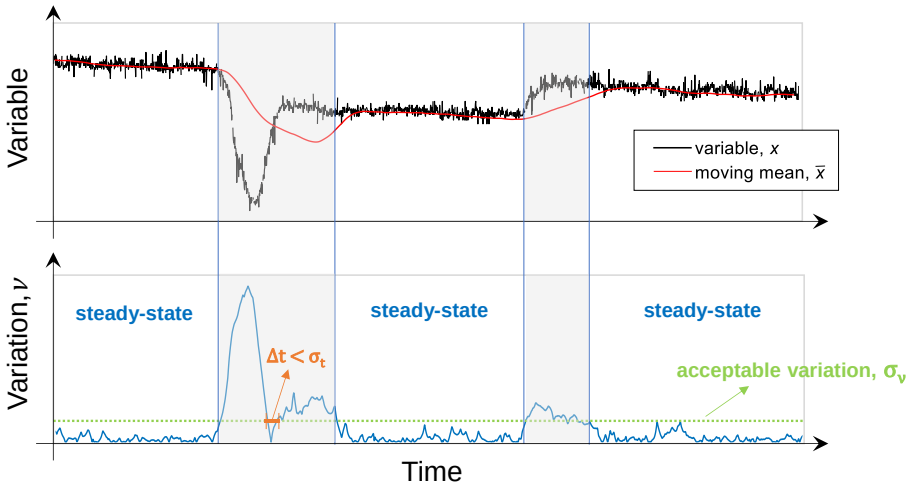

Figure 3-5 - Application of the implemented steady state detection algorithm.

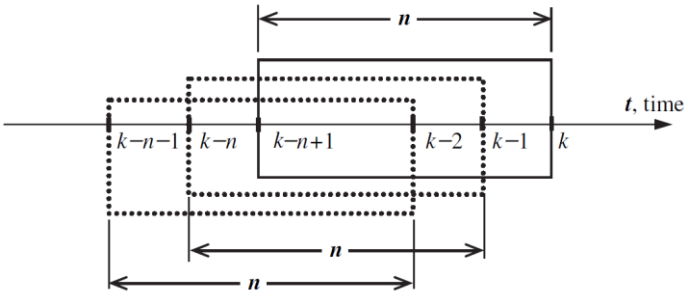

Figure 3-6 - Moving average concept.

The relative variation on the moving window, v_k, is then computed for each time step as the absolute difference between the variable value and its mean over the time window, divided by the mean.

$$v_k = \sum_{i=k-n+1}^{k} \frac{|x_i - \bar{x}_k|}{\bar{x}_k} \tag{3-2}$$

At this point, two constraints must be respected simultaneously to consider the variable as stationary, on the generic time interval which starts at the time step t_{start} and ends at t_{end} (see Eq. (3-3)):

$$\begin{cases} v_k < \sigma_v \quad , \text{ for } k = t_{start} \dots, t_{end} \\ \Delta t = t_{end} - t_{start} > \sigma_t \end{cases} \tag{3-3}$$

First, the relative variation must be lower than the maximum acceptable variation, σ_v, over the entire time interval. Then, the duration of the time interval, Δt, must be higher than the minimum acceptable duration, σ_t. This constraint is necessary to avoid false steady state detection and to have a minimum number of samples to ensure a reliable estimation of the mean value of the variable over

the steady-state interval. The described procedure is applied to all the acquired variables and the system operation is considered steady state only when all its operating variables are stationary at the same time.

The value of σ_v is selected for each variable, based on the characteristic of the signal in terms of inertia and noise, depending on the process in exam and its particular combination with the data acquisition system. It must be highlighted that the smaller is the threshold the more conservatively is the steady-state detection and the more time it takes for the variable to settle within its threshold ranges. Larger thresholds, on the other hand, allow faster data collection but carry a risk of including some transient data. For the case study, the values proposed by [66] (reported in Table 3-3) proved to be effective in most of the cases.

Table 3-3 - Steady-state maximum acceptable variation according Woodland et al. [66].

Variable	Maximum acceptable variation
Temperature	σ_v = 0,5 K (absolute variation)
Pressure	σ_v = 2 %
Flow rate	σ_v = 2 %
Rotational speed	σ_v = 2 %

3.3 Collected data

3.3.1 Characteristic of the conducted tests

A characterization of the reference micro-ORC test bench (described in paragraph 3.1) has been performed in steady state conditions by varying the available control variables for different boundary conditions. These variables are the heat source and the heat sink supply conditions (i.e. temperature and mass flow rate), as well as the pump feed frequency and the expander load resistance. An overview of the conducted experimental tests is given by the map of Figure 3-7. Generally, 5 levels of hot source temperature have been tested, i.e., 65, 70, 75, 80, 84 and 90 °C, varying the pump inverter frequency between 18 and 55 Hz. The cold source temperature changed during the experiments influenced by the ambient conditions, ranging between 8 and 30 °C.

The heat transfer at the heat exchanger and the operating pressures are influenced by the variation of the aforementioned variables as shown in Figure 3-8. Increasing the pump frequency leads to an increasing of the mass flow rate, being the pump of positive displacement type. Increasing the flow rate, a quasi-linear profile of the exchanged thermal power at the heat exchangers, and of the evaporating pressure is observed. The exchanged thermal power tested range goes from 10 to 40 kW, the evaporating pressure from 10 to 23 bar.

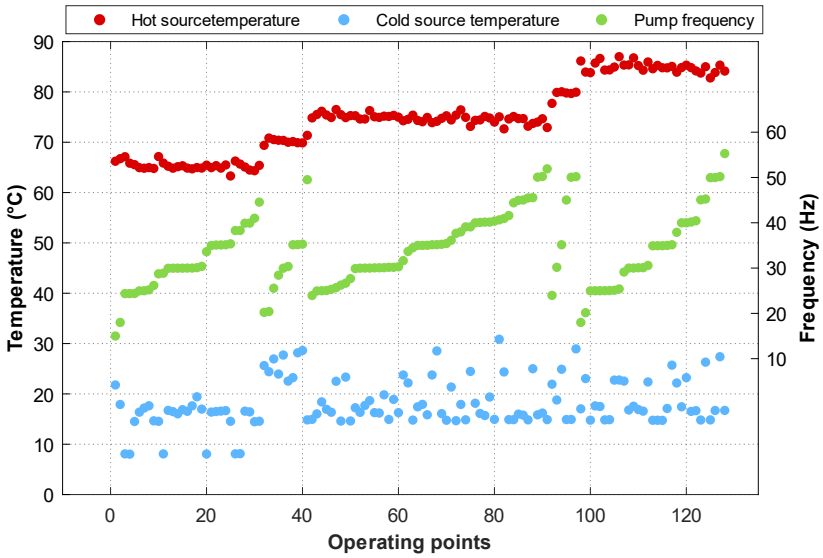

Figure 3-7 - Map of the collected steady-state points – independent variables.

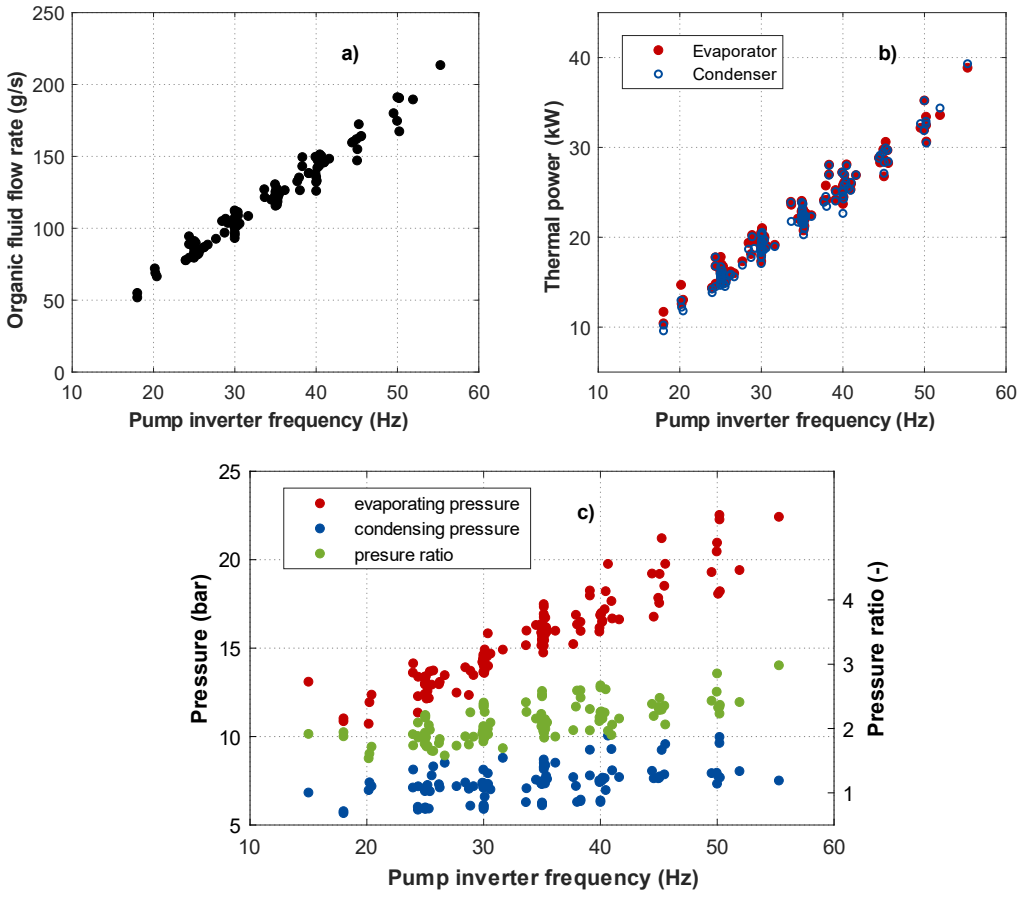

Figure 3-8 - Map of the collected steady-state points - a) organic fluid flow rate, b) heat exchangers thermal power and c) pressures.

The condensing pressure instead keeps barely constant, between 6 and 10 bar, principally depending on the cold water temperature. Consequently, also the expansion ratio linearly increases with the flow rate, going from 1.8 to 2.7.

3.3.2 The "training set" and the "validation set" of data

With the aim of calibrating the semi-empirical models (presented in next chapter, 4) and next validating them, the entire set of data is divided into two subgroups, as proposed by Dumont et al. [67]: a reduced training dataset (used to calibrate the models) and a wider testing dataset (used to validate the models outside of the calibration domain). This approach grants different advantages: it allows to test the model's accuracy also on extrapolated operating conditions and also to reduce the calibration computational cost using a reduced number of experimental data.

Differently from [67] the choice of the "training set" among all the experimental data has been carried out by means of a sort of matrix of experiments, as reported in Table 3-4.

Table 3-4 - Matrix of experiments for the training set selection.

			IV1: T_{max} (°C)	**IV2: $\dot{m}$ (kg/s)**	**IV3: p_{cd} (bar)**
IV1-L1	**IV2-L1**	**IV3-L1**	65	0.08	6
	IV2-L1	**IV3-L2**	65	0.08	7
	IV2-L2	**IV3-L1**	65	0.10	6
	IV2-L2	**IV3-L2**	65	0.10	7
	IV2-L3	**IV3-L1**	65	0.12	6
	IV2-L3	**IV3-L2**	65	0.12	7
IV1-L2	**IV2-L1**	**IV3-L1**	75	0.08	6
	IV2-L1	**IV3-L2**	75	0.08	7
	IV2-L2	**IV3-L1**	75	0.10	6
	IV2-L2	**IV3-L2**	75	0.10	7
	IV2-L3	**IV3-L1**	75	0.12	6
	IV2-L3	**IV3-L2**	75	0.12	7
IV1-L3	**IV2-L1**	**IV3-L1**	85	0.08	6
	IV2-L1	**IV3-L2**	85	0.08	7
	IV2-L2	**IV3-L1**	85	0.10	6
	IV2-L2	**IV3-L2**	85	0.10	7
	IV2-L3	**IV3-L1**	85	0.12	6
	IV2-L3	**IV3-L2**	85	0.12	7

The purpose is to select the most significant points included within a predetermined calibration range. The independent variables (IV columns) controlled during the tests are: the cycle maximum temperature (T_{max} as IV1), the refrigerant mass flow rate ($\dot{m}$ as IV2) and the condensing pressure (p_{cd} as IV3). All the other variables of the ORC circuit implicitly depend from these three variables. Each independent variable assumes discrete values (indicated by L): three for the supply temperature (65 °C; 75 °C; 85 °C) and the mass flow rate (0.08 kg/s; 0.10 kg/s; 0.12 kg/s), two for

the exhaust pressure (6 bar; 7 bar). Therefore, cells of the matrix represent the eighteen possible combinations used for the calibration procedure. Map of Figure 3-9 shows how the training set points are distributed among the entire set of data used in its entirety for the validation.

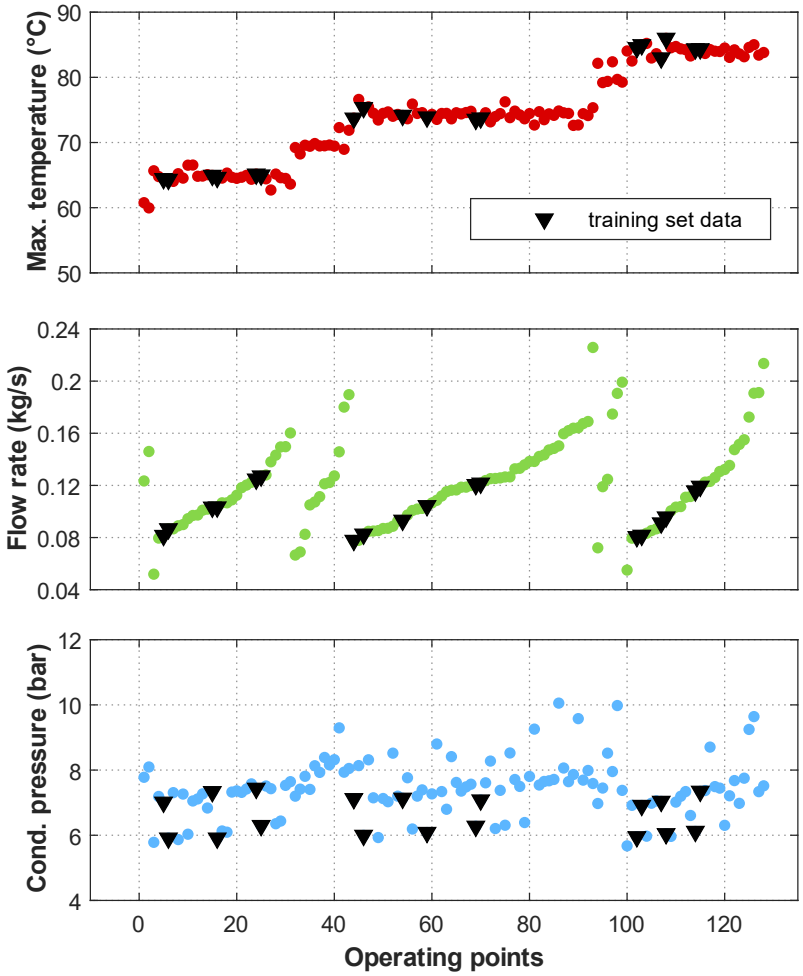

Figure 3-9 - Distribution of the training set points among the entire set of collected points.

4 Semi-empirical modelling

Summary In this chapter, a semi-empirical model for simulating the off-design behavior of micro-ORC systems is proposed. The approach followed to model each component of the plant is first presented in detail, then the connections among them is described in a dedicated section. The calibration and validation procedures of the semi-empirical models is also discussed. Experimental data collected during tests on the test bench of the University of Bologna are used for this purpose.

In particular the first faced challenge is the modelling of the expander, which represents the key component of a micro-ORC system. Different literature models have been compared to understand the advantages, the limits and the criteria of applications of each approach.

The introduction of a methodology to account for the change of the working is also considered to allow the analysis of the fluid influence over the components' performance.

4.1 The semi-empirical modelling approach

The semi-empirical models were born as compromise between the black-box approach and the white-box one. The black-box methodology does not describe the physics of process that takes place inside the box, it is easy to implement but not always so precise in simulating extrapolated conditions: examples of black-box models are constant-efficiency and pure polynomial-based models. The white-box criterion, instead, consists in the implementation of equations describing the physical and chemical phenomena which occur into the system; this approach results to be more accurate but, to be applied, it needs the knowledge of some details of the system which are not always known. The semi-empirical approach is a combination of the two approaches, since it relies both on a set of physically meaningful equations describing the process, and on empirical parameters which simplified the computational process. This is the reason, if correctly implemented, this kind of model can be a good a trade-off among simulation speed, calibration efforts, modelling accuracy and extrapolation capability. The study of Dickes et al. [68] in particular focused exactly on testing and comparing this approach to other types when applied to model micro-ORC systems, demonstrating its effective and its better accuracy rather than constant-efficiency and pure polynomial-based approaches, which are the most diffused models nowadays.

In this work, the semi-empirical model approach was thus chosen to model the off-design behavior of the micro-ORC system. In the following paragraphs (one for each component) the specific methodology used to model the ORC components is presented and discussed.

4.2 A comparison between different approaches to model the reciprocating piston expander

4.2.1 Contribution

Context

Performance prediction of the expander is of utmost importance in a power cycle, as it significantly affects the overall system energy conversion efficiency. Moreover, when implementing an existing expander architecture in a new heat recovery application, it can be interesting to know how the machine will work in this specific condition, that can be different from the original design point considered by the expander manufacturer; in such cases, experimental data on the expander performance in the extended rage of operation can be not always fully available. In this context, the availability of models for performance prediction of the expansion process can help significantly to optimize the design and the operation strategy for the new application of prototypal machines, limiting the need of experiments and thus saving time and costs. If complete information about the internal geometry of the expander is not accessible (especially when using prototypes), as all the geometrical details cannot be fully available, or they are known only by the manufacturer, "semi-empirical" models can be helpful in predicting the expander performance.

This kind of approach has been widely applied to the compressors of refrigeration facilities: for example, Li [69] developed a simplified physical model for hermetic scroll and also reciprocating compressors, with the aim of predicting mass flow rate, absorbed power and discharge temperature, validating the results with experimental data collected from literature. Molinaroli et al. [70] introduced a semi-empirical model of a rolling piston compressor, designed for different applications and working with different refrigerants, validating the results with manufacturer data. D'Amico et al. [71] presented a semi-empirical thermodynamic model of a displacement pump integrated into an ORC experimental unit, where the pump behavior at design and off-design conditions is modeled as a set of thermodynamic processes, whose main geometrical parameters are calibrated using experimental data.

As far as the expanders are concerned, many modelling studies are focused on scroll and screw expanders for ORC systems. For example, Lemort et al. [72] presented the results of an experimental study carried out on a prototype of an open-drive oil-free scroll expander integrated into an ORC working with refrigerant R132, in order to estimate the contribution of the different losses. In the study of Ziviani et al. [73], the authors performed experimental tests on a 5 kW oil-free scroll expander working with R245fa, applying also a semi-empirical model in order to distinguish the different loss terms. Mendoza et al. [74] studied the performance of a scroll compressor modified to work as an expander, characterized by two different setups, using air and ammonia as working fluids. Giuffrida [75] proposed a modelling procedure in order to characterize the performance of a scroll expander for small ORC, when changing the working fluid. Ayachi et al. [76] investigated the performance of a hermetic scroll expander integrated into a Brayton cycle fed with R245fa. Giuffrida [77] improved the performance simulation of a single-screw expander using different approach for modelling mechanical losses and ambient heat losses. A rotatory vane expander, for low to medium power output ORC applications, has been investigated by Vodicka et al. [78], in order to describe the loss term due to delayed contact of vane and stator.

Regarding the reciprocating piston expanders, instead, the open literature is more limited. Among the few available studies, Glavatskaya et al. present and validate a steady-state simulation model for reciprocating piston expanders in [79], where the performance analysis of the expansion machine is carried out. Bouvier et al. [80] performed an experimental study on an oil-free piston expander working with water steam, developing also a semi-empirical model in order to conduct a sensitivity analysis for improving the control strategy.

Contribution

In this paragraph, two semi-empirical literature models (the model by Li [69], originally introduced for compressors, and the model by Glavatskaya [79], for expanders) are elaborated, further extended and used for the case of the reciprocating expander prototype of the case study, which has been experimentally characterized with a dedicated test bench (see chapter 3). The main contributions of this work can be summarized in:

- a more detailed use of the two different models, with respect to the previous introduction, for the specific case of reciprocating piston expander and calibration for a prototype of kW-size, integrated into a micro-ORC system test bench facility for low grade heat recovery application.
- validation of the calibrated models with a different set of experimental data, over a wider range of operation.
- comparison of the calibrated models in predicting the piston expander behavior in an extrapolated range of operation, in order to understand potentialities and limitations and to obtain expander operating maps.

The first selected modelling approach is based on polynomial correlations of the expander efficiencies and it has been extended by introducing a heat losses model based on simple heat transfer coefficient correlations. The heat losses model was added to perform a fair comparison with the other model in exam, which instead already accounts for this contribution of loss, since the heat loss contribution is demonstrated to be not negligible on small size volumetric machines [46].

The second model is based on a lumped parameters approach accounting for key geometrical data of the expander and physical equations to describe the process.

4.2.2 Approach 1: the "polynomial fitting functions" model

Main equations and schematic of the model

Figure 4-1 illustrates in detail the model scheme, which is based on simplified mass and energy balance equations. The main mass and energy flows that pass through the expander are shown in the figure. The model takes into account the supply inlet flow and the exhaust outlet flow (streams indicated as *su* and *ex* in Figure 4-1). The supply stream (with mass flow rate $\dot{m}$) splits in two streams: the main one, with mass flow rate $\dot{m}_{in}$, undergoes the internal ideal expansion (black line); the leakage flow (green line), with mass flow rate $\dot{m}_{leak}$, by-passes the expansion process.

The inputs of the model are the inlet mass flow rate ($\dot{m}$), the inlet or suction pressure (p_{su}), the inlet temperature (T_{su}), the outlet pressure (p_{ex}) and the ambient temperature (T_{amb}). The main output quantities of the model are instead the electric power output ($\dot{W}_{el}$), the rotational speed (N) and the exit temperature (T_{ex}).

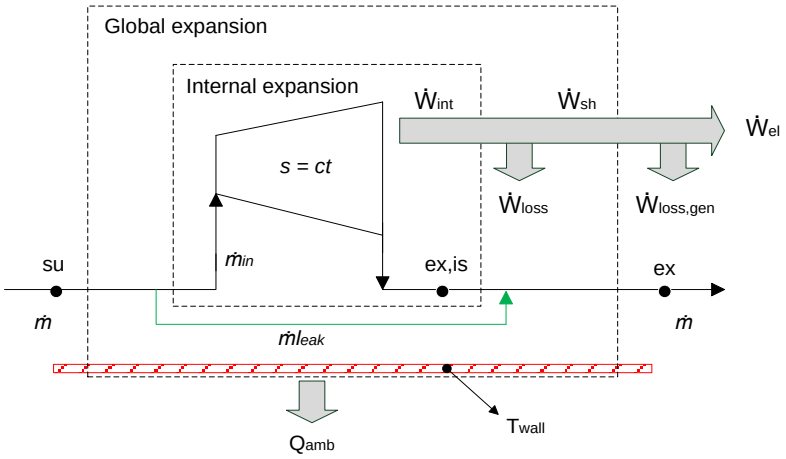

Figure 4-1 - Polynomial fitting functions model scheme.

Following the "polynomial fitting function" approach, the output quantities are calculated basically using two polynomial curves to represent the isentropic efficiency and the volumetric efficiency of the machine. In particular, the isentropic efficiency, η_{is}, can be expressed by a fitting polynomial equation (Eq. (*4-1*)), as function of the expansion pressure ratio, $\frac{p_{su}}{p_{ex}}$:

$$\eta_{is} = a_2 \cdot \left(\frac{p_{su}}{p_{ex}}\right)^2 + a_1 \cdot \left(\frac{p_{su}}{p_{ex}}\right) + a_0 \tag{4-1}$$

where a_2, a_1, a_0 represent empirical parameters to be calibrated by interpolation of experimental data. The volumetric efficiency, η_v, is also calculated through a polynomial function of the expansion pressure ratio:

$$\eta_V = b_2 \cdot \left(\frac{p_{su}}{p_{ex}}\right)^2 + b_1 \cdot \left(\frac{p_{su}}{p_{ex}}\right) + b_0 \tag{4-2}$$

where three additional empirical coefficients of interpolation b_2, b_1 e b_0 are introduced. The isentropic efficiency is used to calculate the shaft power ($\dot{W}_{sh}$) and the electric power output; in particular, the shaft power is function of the isentropic power ($\dot{W}_{is}$):

$$\dot{W}_{sh} = \dot{W}_{is} \cdot \eta_{is} \tag{4-3}$$

The electric power output depends on the shaft power and also on the generator electro-mechanical conversion efficiency (η_{conv}) according to:

$$\dot{W}_{el} = \dot{W}_{sh} \cdot \eta_{conv} \tag{4-4}$$

The isentropic power in Eq. (3) can be calculated, with reference to the expander inlet mass flow rate, as:

$$\dot{W}_{is} = \dot{m} \cdot (h_{su} - h_{ex,is}) \tag{4-5}$$

where h_{su} is the supply enthalpy and $h_{ex,is}$ is the exhaust isentropic enthalpy, corresponding to the exhaust pressure, p_{ex} and the supply entropy, s_{su}:

$$h_{ex,is} = f(p_{ex}, s_{su}) \tag{4-6}$$

It must be highlighted that the isentropic efficiency used in Eq. (4-1) includes both the internal loss due to friction (thermo-mechanical conversion loss) and the loss due to the leakage, depending on the volumetric efficiency.

The volumetric efficiency is used to calculate the expander rotational speed, N, using the following definition:

$$\eta_V = \frac{\dot{m}_{in} \cdot 60}{N \cdot V_s \cdot \rho_{su}} \tag{4-7}$$

Comparing the actually elaborated mass flow rate, $\dot{m}_{in}$, with the theoretical one, given by the product between the expander internal displacement, V_s, is the supply density, ρ_{su}, and the shaft speed. The $\dot{m}_{in}$ value can be derived by the balance equation Eq. (*4-8*), referring to the internal expansion process (see also Figure 4-1):

$$\dot{m}_{in} \cdot (h_{su} - h_{ex,is}) = \dot{W}_{int} = \dot{W}_{sh} + \dot{W}_{loss} \tag{4-8}$$

where $\dot{W}_{int}$ is the internal ideal power (i.e., considering that the internal mass flow undergoes the isentropic process), equal to the sum of the shaft power and of the friction losses contribution ($\dot{W}_{loss}$). In particular, $\dot{W}_{loss}$ is here considered equal to the heat transfer loss through the expander wall to the ambient ($\dot{Q}_{amb}$ in Figure 4-1). The evaluation of this term is discussed in detail in the following paragraph, dealing with the modeling of the heat exchanged with the ambient.

Finally, the exhaust temperature, T_{ex}, is calculated as thermodynamic function of the exhaust pressure and of the exhaust enthalpy, h_{ex}:

$$T_{ex} = f(p_{ex}, h_{ex}) \tag{4-9}$$

where h_{ex} is obtained by the global expansion energy balance, according to:

$$\dot{m} \cdot (h_{su} - h_{ex}) = \dot{W}_{sh} + \dot{Q}_{amb} \tag{4-10}$$

Heat loss to the ambient

For a comprehensive representation of the expansion process, a sub-model was included into the polynomial approach to calculate the heat loss to ambient ($\dot{Q}_{amb}$ in Figure 4-1). The heat transfer term to the ambient is evaluated as:

$$\dot{Q}_{amb} = U \cdot l \cdot (T_{wf} - T_{air}) \tag{4-11}$$

where U is the equivalent linear heat transfer coefficient, l the equivalent length, T_{wf} the equivalent temperature of the organic fluid inside the wall of the expander and T_{air} the external air temperature. The U term and the temperature T_{wf} are calculated considering an equivalent expander geometry

based on a simple model; in particular, the original geometry of the expander (visible in Figure 3-2) is approximated to a cylindrical element, with a circular cross section, as shown in Figure 4-2. The l term represents the equivalent height of the cylinder, where l is calculated so that the overall heat transfer equivalent surface is equal to the total external surface of the real geometry. In this way l considers the heat exchange contribute both through the lateral walls and the triangular faces.

As illustrated in Figure 4-2, the model considers three equivalent layers: the internal fluid, the expander wall and the external insulating layer; these layers correspond to the main domains of the actual expander geometry. The external radius of the three layers are indicated in figure as r_1, r_2 and r_3. The radius values of the equivalent layers are estimated on the basis of few external geometrical sizes of the machine. It must be observed that the proposed approach can be applied also to different external geometries for which not all the internal geometrical details are known.

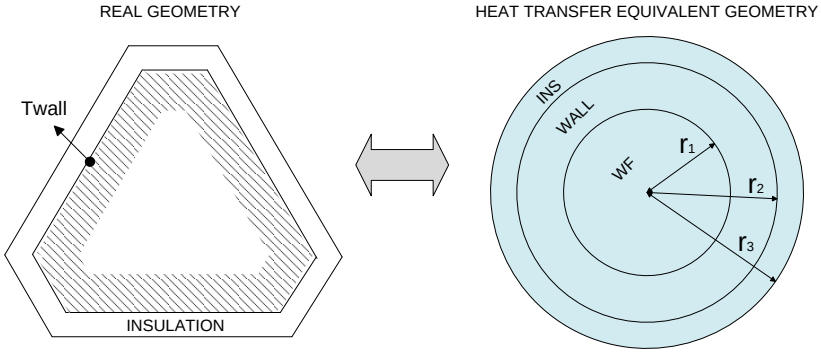

Figure 4-2 - Cross section of the equivalent geometry of the heat transfer model.

The radius r_2 is calculated using the actual external size of the expander (which can be easily measured) and considering an equal external perimeter. The value of r_3 is obtained using the actual thickness of the insulating layer, as thickness of the annular external layer. The internal radius, r_1, is calculated assuming the corresponding internal volume equal to the expander internal displacement volume. Then, the equivalent heat transfer coefficient, U, is calculated as:

$$U = 1/R_{global} \tag{4-12}$$

where the global thermal resistance R_{global}, is expressed as:

$$R_{global} = R_{wf} + R_{wall} + R_{ins} + R_{air} \tag{4-13}$$

where four resistance terms are introduced, namely the convective resistance of the air, R_{air}, the conductivity resistance of the wall material, R_{wall}, the conductivity resistance of the insulation, R_{ins}, and the convective resistance of the fluid, R_{wf}.

The resistance terms of each layer can be calculate using Eq.s (4-14)-(4-17):

$$R_{wf} = 1/(2 \cdot \pi \cdot r_1 \cdot \alpha_{wf}) \tag{4-14}$$

$$R_{wall} = \ln (r_2/r_1)/(2 \cdot \pi \cdot \lambda_{wall}) \tag{4-15}$$

$$R_{ins} = \ln(r_3/r_2)/(2 \cdot \pi \cdot \lambda_{ins}) \quad (4\text{-}16)$$

$$R_{air} = 1/(2 \cdot \pi \cdot r_3 \cdot \alpha_{air}) \quad (4\text{-}17)$$

where λ_{wall} and λ_{ins} are the wall and insulation layers conduction heat transfer coefficients, depending on the materials, while α_{air} and α_{wf} are the convective heat transfer coefficients for the external air and the organic fluid. These convection coefficients α can be calculated through the Nusselt number, Nu, according to:

$$\alpha = Nu \cdot \lambda/D \quad (4\text{-}18)$$

where λ is the thermal conductivity of the fluid, D the corresponding diameter and Nu is calculated with two different correlations. In particular, Nu_{air} is calculated with a correlation assuming natural convection in air [81]:

$$Nu_{air} = 0.59\ (Ra_{air})^{0.25} \quad (4\text{-}19)$$

where Ra_{air} is the fluid Rayleigh number. The Nu_{wf} value for the organic fluid is calculated by means of an experimental correlation based on the Dittus-Boelter formula for turbulent flows [81]:

$$Nu_{wf} = C \cdot (Re_{wf})^a \cdot (Pr_{wf})^b \quad (4\text{-}20)$$

where a, b and C are parameters to be calibrated over the experimental data. The Reynolds number Re_{wf} is calculated using the expander inlet flow conditions and the equivalent diameter $2r_1$. The calibration of the constants that appear into the Nusselt correlation, will compensate, in part, the error committed using a simplified geometry.

4.2.3 Approach 2: the "lumped parameters" model

Schematic of the model

The second modelling approach selected to represent the behavior of the reciprocating piston expander is named here as "lumped parameters" model.

The target output quantities of the model, and the used main input, are the same of the previous model. The approach and the structure of the model equations is instead different, since the lumped parameters model takes into account some key geometrical data of the expander and it introduces additional physical equations, to describe the expansion process, instead of empirical polynomial functions. Nevertheless, also this model introduces additional parameters to be calibrated versus experimental data.

According to this approach, summarized in Figure 4-3, the model accounts for the following thermodynamic steps of the working fluid during the expansion process:

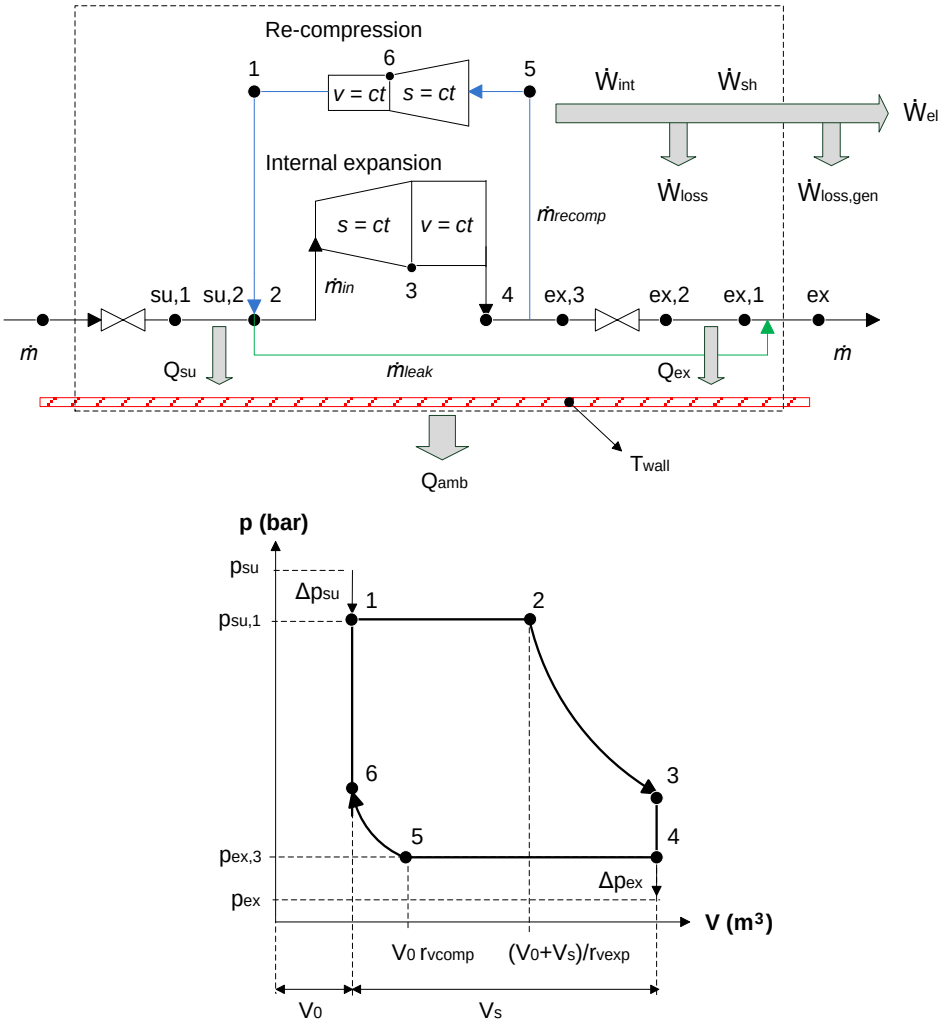

Figure 4-3 - "Lumped parameters" model scheme and the respective p-V diagram representing the internal expansion process.

- an adiabatic pressure drop through the supply valve (*su-su,1*)
- a cooling effect, due to the heat exchange between the fluid and the wall at the suction side (*su,1-su,2*)
- an internal expansion process, modeled as an isentropic (*2-3*) plus a constant volume transformation (*3-4*)
- a partial re-compression of the residual mass of the working fluid trapped into the clearance volume, which undergoes an isentropic (*5-6*) plus a constant volume transformation (*6-1*)
- an adiabatic pressure drop through the discharge valve (*ex,3–ex,2*)
- a heat exchange effect between the wall and the fluid (*ex,2–ex,1*)
- a leakage effect of a fraction of the mass flow rate that by-passes the internal expansion (*su,2-ex*).

Main equations

The main model physical equations are here briefly reported. The supply pressure drop between *su* and *su,1* is modelled as an isentropic expansion through a convergent nozzle, using the flowing equation:

$$\dot{m} = \rho_{su} \cdot A_{su} \cdot \sqrt{2 \cdot (h_{su} - h_{su,1})} \tag{4-21}$$

where the model throat area A_{su} of the supply valve is a model parameter, to be identified by means of the calibration procedure, while $h_{su,1}$ represents the calculated outlet enthalpy, used to obtain the exit pressure, $p_{su,1}$.

The leakage mass flow rate, $\dot{m}_{leak}$, is calculated, using an equation similar to Eq. (4-21), assuming an isentropic flow through a convergent nozzle, with a throat section area equal to the parameter A_{leak}; in this case, the outlet enthalpy is evaluated with the throat critical pressure, assuming chocking conditions, using the following equation:

$$p_{thr} = p_{su,2} \cdot \left(\frac{2}{\gamma_{su,2}+1}\right)^{\frac{\gamma_{su,2}}{\gamma_{su,2}-1}} \tag{4-22}$$

Where γ represents the ratio between the constant pressure and the constant volume specific heat.

The heat exchanged at the supply section, $\dot{Q}_{su}$, required to calculate the fluid thermodynamic state in *su,2*, is obtained in this model by means of the NTU method, according to the following three equations:

$$\dot{Q}_{su} = \varepsilon \cdot c_p \cdot \dot{m} \cdot (T_{su,1} - T_{wall}) \tag{4-23}$$

$$\varepsilon = 1 - e^{-NTU} \tag{4-24}$$

$$NTU = \frac{1}{c_p \cdot \dot{m}} \cdot (AU)_{su,ref} \cdot \left(\frac{\dot{m}}{\dot{m}_{ref}}\right)^{0.8} \tag{4-25}$$

where $\dot{m}_{ref}$ is the reference mass flow rate, evaluated in nominal operating conditions of the expander (assumed equal to 0.16 kg/s), while $(AU)_{su,ref}$ is a calibration parameter of the model.

The expansion and the recompression transformations are modeled using the volumetric expansion ratio, $r_{v,exp}$, and the volumetric compression ratio, $r_{v,comp}$, respectively defined as (see Figure 4-3 for the fluid state numbering):

$$r_{v,exp} = \frac{V_3}{V_2} = \frac{v_3}{v_2} \tag{4-26}$$

$$r_{v,comp} = \frac{V_5}{V_0} = \frac{v_5}{v_6} \tag{4-27}$$

The two volumetric ratios are used to compute the fluid state at the end of the expansion process, after an isentropic and a subsequent isochoric transformation. The isentropic expansion is described by a process for which the product pv^{γ} is maintained constant. The $r_{v,exp}$ and $r_{v,comp}$ parameters are here considered as unknown geometrical data, and they are obtained after calibration versus experimental data.

The mass flow rate that undergoes recompression, $\dot{m}_{recomp}$, responsible for a power loss contribution, is calculated as function of the clearance volume, V_0, according to:

$$\dot{m}_{recomp} = \frac{V_0 \cdot \rho_4 \cdot N}{60} \tag{4-28}$$

where V_0 is a calibration parameter.

The expander shaft power, $\dot{W}_{sh}$, is expressed in the model including the expansion terms, the recompression term and the loss term, as:

$$\dot{W}_{sh} = \dot{m}_{in} \cdot [(h_2 - h_3) + v_3(p_3 - p_4)] - \dot{m}_{recomp} \cdot (h_1 - h_5) - \dot{W}_{loss} \tag{4-29}$$

where $\dot{W}_{loss}$ represents the overall mechanical losses. This term is calculated in the model by accounting for two different contributes: a constant term, $\dot{W}_{loss,ref}$ representing the constant mechanical loss and a second contribute, $\dot{W}_{loss,N}$ proportional to the rotational speed:

$$\dot{W}_{loss} = \dot{W}_{loss,ref} + \dot{W}_{loss,N} \cdot N \tag{4-30}$$

The electric power, $\dot{W}_{el}$, is finally computed as the product between the shaft power and the electro-mechanical conversion efficiency:

$$\dot{W}_{el} = \dot{W}_{sh} \cdot \eta_{conv} \tag{4-31}$$

The rotational speed, N, is obtained as following:

$$N = 60 \cdot \dot{m}_{in} / (\rho_2 \cdot V_2 - \rho_6 \cdot V_6) \tag{4-32}$$

The heat exchanged with the ambient, $\dot{Q}_{amb}$, is computed by Eq. (*4-33*), by means of the ambient heat transfer coefficient AU_{amb}.

$$\dot{Q}_{amb} = (AU)_{amb} \cdot (T_{wall} - T_{amb}) \tag{4-33}$$

where the wall temperature, T_{wall}, is calculated by the energy balance:

$$\dot{Q}_{amb} = \dot{Q}_{su} + \dot{W}_{loss} + \dot{Q}_{ex} \tag{4-34}$$

where the heat exchange at the exhaust section, $\dot{Q}_{ex}$, is described by means of the NTU method, with the nominal heat transfer coefficient $(AU)_{ex,ref}$, applying Eq.s (4-23) - (4-25), to the exhaust section *ex,2*. The exhaust temperature can be finally obtained by the enthalpy mixing balance of the leakage stream and the expansion outlet stream.

4.2.4 Calibration procedure

Models' parameters

Table 4-1 schematically resumes the considered key input and output variables, the constants and the parameters of the two models, which need to be found out through a calibration procedure.

Table 4-1 - Summary of the input, output, constants and empirical parameters of the expander models.

Inputs	
$T_{su}, p_{su}, p_{ex}, T_{amb}, \dot{m}$	
Constants	
V_s = 230 cm^3, η_{conv} = 90 %	
Model parameters	
"polynomial fitting functions" model	**"lumped parameters" model**
a_2, a_1, a_0 — Interpolation coefficients for the isentropic efficiency	$(AU)_{su,ref}$ Supply heat transfer coefficient
b_2, b_1, b_0 — Interpolation coefficients for the volumetric efficiency	$(AU)_{ex,ref}$ Exhaust heat transfer coefficient
a, b, C — Coefficients for the Nusselt correlation	$(AU)_{amb}$ Ambient heat transfer coefficient
	$W_{loss,ref}$ Constant friction losses
	$W_{loss,N}$ Proportional friction losses
	A_{leak} Equivalent leakage area
	A_{su} Supply nozzle equivalent section
	$r_{v,exp}$ Expansion volume ratio
	$r_{v,comp}$ Re-compression volume ratio
	V_0 Clearance volume
Outputs	
$T_{ex}, N, \dot{W}_{el}$	

In both the modeling approaches, the inlet stream conditions (T_{su}, p_{su} and $\dot{m}$), the outlet pressure (p_{ex}) and the ambient temperature (T_{amb}) are input data, representing the key boundary conditions of the expander operation. The swept or displacement volume (V_S), represents the main size fixed data of the machine; the nominal electric generator efficiency (η_{conv}) value is provided by the electric generator manufacturer, and it has been considered constant and equal to 90 %.

The polynomial fitting functions model requires as parameters to be calibrated the interpolation coefficients of the isentropic (a_0, a_1, a_2) and volumetric efficiency functions (b_0, b_1, b_2) and the coefficients of the Nusselt correlation (a, b, C), used for the heat transfer sub-model. The lumped parameters model, based on physical equations, is also characterized by physical calibration parameters, namely the heat transfer coefficients (($AU)_{su,ref}$, $(AU)_{ex,ref}$ and $(AU)_{amb}$), the friction losses coefficients ($W_{loss,ref}, W_{loss,N}$), the equivalent cross sectional areas (A_{leak}, A_{su}), the volume ratio coefficients ($r_{v,exp}, r_{v,comp}$) and the clearance volume (V_0).

It must be observed that in the second model case, the last three parameters are geometrical data that could be available if the expander internal design was completely known before the model

application. Since for the prototypal case study under investigation these parameters were not known; they have been included among the calibration parameters set. It has to be pointed out that the larger is the number of calibration parameters accounted into the model, the higher is the number of experimental data to consider, the higher is the computational cost of calibration, and the more difficult is to obtain an accurate calibration process.

Calibration procedure

In the "polynomial fitting functions" model, the coefficients of the isentropic and the volumetric efficiencies equations (Eq.s (4-1) and (4-2) and Table 4-1) are obtained interpolating the training data set with second degree polynomials. While parameters appearing into the Nusselt correlation (Eq. (4-19) and (4-20)) used to represent the heat exchanged with ambient, have been determined, comparing model outputs and experimental results on two different surface temperatures.

In details, the wall temperatures considered are: $T(r_2)$, the temperature measured by a thermocouple placed between the steel wall and the insulating layer (see Figure 4-2) and $T(r_3)$, the temperature measured by a thermocouple placed on the external surface of the insulating layer. The latter are calculated using the Eq.s (4-35)-(4-37).

$$T(r_1) = T_{wf} - \left({R_{wf}}/{l}\right) \cdot \dot{Q}_{amb} \tag{4-35}$$

$$T(r_2) = T(r_1) - \left({R_{wall}}/{l}\right) \cdot \dot{Q}_{amb} \tag{4-36}$$

$$T(r_3) = T(r_2) - \left({R_{ins}}/{l}\right) \cdot \dot{Q}_{amb} \tag{4-37}$$

The lumped parameter model follows instead a more complicated procedure, due to the strong non-linearity of the correlations between the inputs and the outputs of the model. In these cases, the empirical parameters calibration procedure is a crucial step for the successful implementation of the semi-empirical model. The generic operating principle is schematized in Figure 4-4: it basically consists in finding the value of the empirical parameters that allow minimize the error between the model prediction and the experimental data over the whole data training set. This problem can be approached in different way.

In this work, the calibration problem is addressed as a minimization problem, whose objective function is the global error function, GEF, on the predictions of the model outputs and the variables are the empirical parameters, $\overline{par}$. The global error function is defined as a sort of mean relative error where x_{output} indicates the generic model output variable, the index *i* numerates the different operating points included into the experimental data training set, and the index *j* numerates the different output variables of the model. Where the subscripts *calc* and *meas* distinguish the variables calculated by the model from the one measured during the experimental tests. As explained in paragraph 3.3.2, the function is evaluated over a reduced set of data, i.e. the training set data (n_{train}), accounting for all the model outputs (n_{ouputs}).

$$\begin{cases} min_{\ \overline{par}}\ \ GEF(\overline{par})\ \ \text{, with } \overline{par}_{lb} < \overline{par} < \overline{par}_{ub} \\ GEF = \dfrac{1}{n_{outputs}} \displaystyle\sum_{j=1}^{n_{ouputs}} \sqrt{\dfrac{1}{n_{train}} \sum_{i=1}^{n_{train}} \left(\dfrac{x_{output,calc}(i,j) - x_{output,meas}(i,j)}{x_{output,calc}(i,j)} \right)^2} \\ \bar{x}_{output,calc} = model\left(\bar{x}_{input}\right) \end{cases} \quad (4\text{-}38)$$

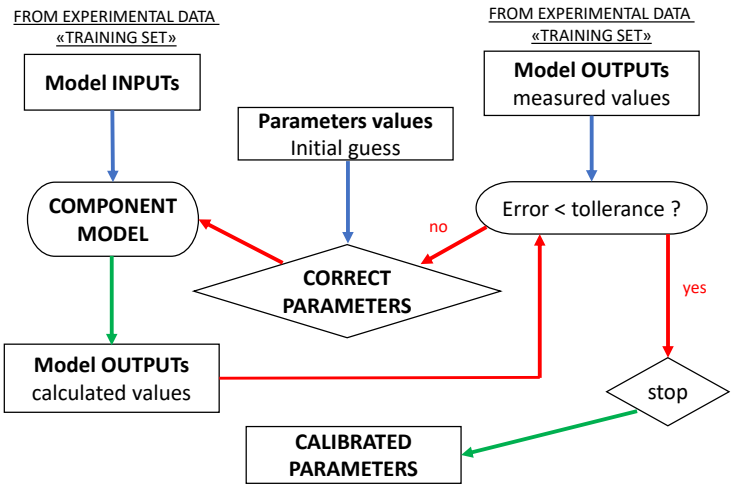

Figure 4-4 - Schematic flow chart of the calibration procedure.

The minimization process has been carried out in two steps:

1. A genetic algorithm routine, available in MATLAB Optimization Toolbox and specifically dedicated to multivariable functions minimization is used to solve the problem.
2. Then the solution is refined by means of a second algorithm, which checks if the solution actually corresponds to the best solution. This algorithm tests how much given variation of the parameters value around the first solution influence the global error, by varying the parameters one by one. If a better solution is detected in the surrounding of the initial solution, so, the solution is updated with the better one. This situation can occur in case that the genetic algorithm is not perfectly set for the application and a local minimum of the objective function is returned instead of the global one.

Results

Results of the calibration process are included in Table 4-2 where the obtained values of the models' parameters are shown. For the "lumped parameters approach" case, a sensitivity analysis of the global error by varying the parameters values around the solution is also reported. Indeed, as anticipated before, optimization algorithm, if not perfectly set, can return a local minimum of the objective function, instead of the global one. So, in order to verify the robustness of the lumped parameters approach calibration procedure and to investigate the influence of each parameter on the global error value this additional analysis has been performed.

The Figure 4-5 shows the response of the model to a variation of calibrated parameters in the range ± 10 %. As highlighted in the figure, the minimum of the *GEF* is obtained with a null variation of the entire set of the calibrated parameters, thus demonstrating that the calibrated parameters identify a global minimum of the objective function. In addition, from the figure, it can be observed that there is a high sensitivity of the model to the expander built in volume ratio ($r_{v,exp}$), followed by the supply heat transfer coefficient ($AU_{su,ref}$) and to the exhaust heat transfer coefficient ($AU_{ex,ref}$).

Table 4-2 - Tuned expander models parameters.

Polynomial fitting functions

Parameter	Value
a_2	-0.2078
a_1	0.9380
a_0	-0.6149
b_2	-0.2906
b_1	1.2297
b_0	-0.9738
a	0.675
b	0.365
C	0.0154

Lumped parameters

Parameter	Value	Unit
A_{su}	1.47e-05	m²
A_{leak}	5.51e-06	m²
$AU_{su,ref}$	5.65e-05	W/K
$AU_{ex,ref}$	9.23e-05	W/K
AU_{amb}	0.96	W/K
$r_{v,exp}$	1.459	-
$r_{v,comp}$	1.25	-
V_0	2.32e-08	m³
$W_{loss,ref}$	0.198	W
$W_{loss,N}$	1.07e-05	W/min

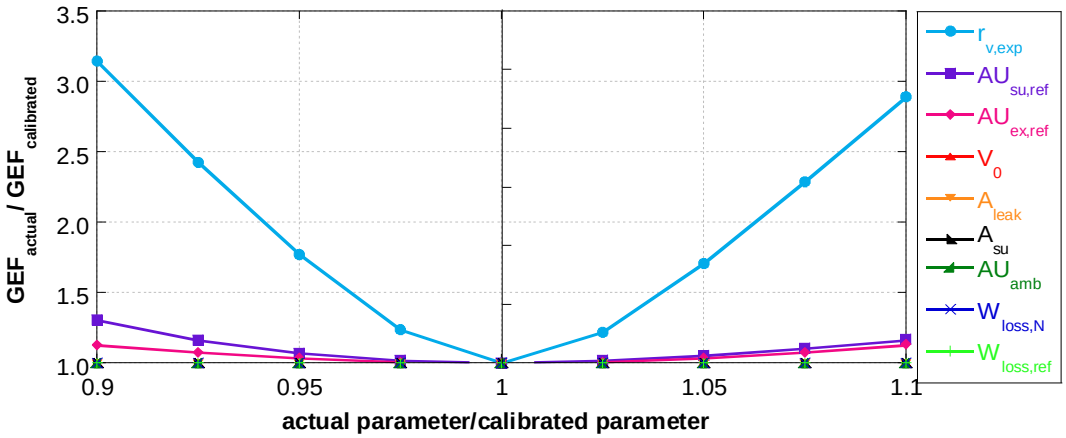

Figure 4-5 - Sensitivity analysis of the *GEF* value to a variation of the model parameters value.

4.2.5 Validation

The models' validation has been carried out making use of the total available experimental data. To prove the effectiveness of the models in predicting the output variables, mean relative errors

(*MRE*) (Eq. (4-39)) and global error function (GEF_{val}) (Eq. (4-40)) have been quantified. It can be noticed that the global error function is nothing but the same global error function used for the calibration process (Eq. (4-38)), but applied over the total available experimental data (n_{val}) instead of over the training set only (n_{train}).

$$MRE(j) = \sqrt{\frac{1}{n_{val}} \sum_{i=1}^{n_{val}} \left(\frac{x_{calculated}(i) - x_{measured}(i)}{x_{calculated}(i)} \right)^2} \tag{4-39}$$

$$GEF_{val} = \frac{1}{n_{outputs}} \sum_{j=1}^{n_{ouputs}} \sqrt{\frac{1}{n_{val}} \sum_{i=1}^{n_{val}} \left(\frac{x_{calculated}(i,j) - x_{measured}(i,j)}{x_{calculated}(i,j)} \right)^2} \tag{4-40}$$

Figure 4-6 focuses on results of the validation procedure, respectively for the polynomial fitting and the lumped model approaches. The parity plots compare the calculated values of the output variables with the measured ones. In the figures, the empty dots show the training set data. The dash lines in figures highlight the mean relative error values (Eq.s (4-39)(4-40)) got on the output variables. Both models show the lowest *MRE* values on the prediction of exhaust temperature, equal to 1 % and 2 % respectively for the polynomial and lumped model (see Figure 4-6a). Maximum relative errors are obtained in the prediction of rotational speed for the polynomial fitting model (equal to 10 % - see Figure 4-6b), and in the electric power output for the lumped approach (equal to 8 % - see Figure 4-6c). The global mean relative error (Eq. (42)) obtained over the overall validation points, is close to 5 % for both the modelling approaches, thus proving that they are suitable to simulate the behavior of the reciprocating expander. In Table 4-3 the values of the errors obtained by the validation process are reported in detail.

The results demonstrate thus a good and similar global accuracy between the two models, both in the interpolated conditions and the extrapolated conditions, considering the available data for the validation.

Table 4-3 - Errors obtained by the validation process of the expander models.

	Polynomial fitting functions	**Lumped parameters**
MRE_{Tex}	2.2 %	1.0 %
MRE_{N}	4.6 %	9.6 %
MRE_{Wel}	7.7 %	4.3 %
GEF_{val}	5.0 %	4.8 %

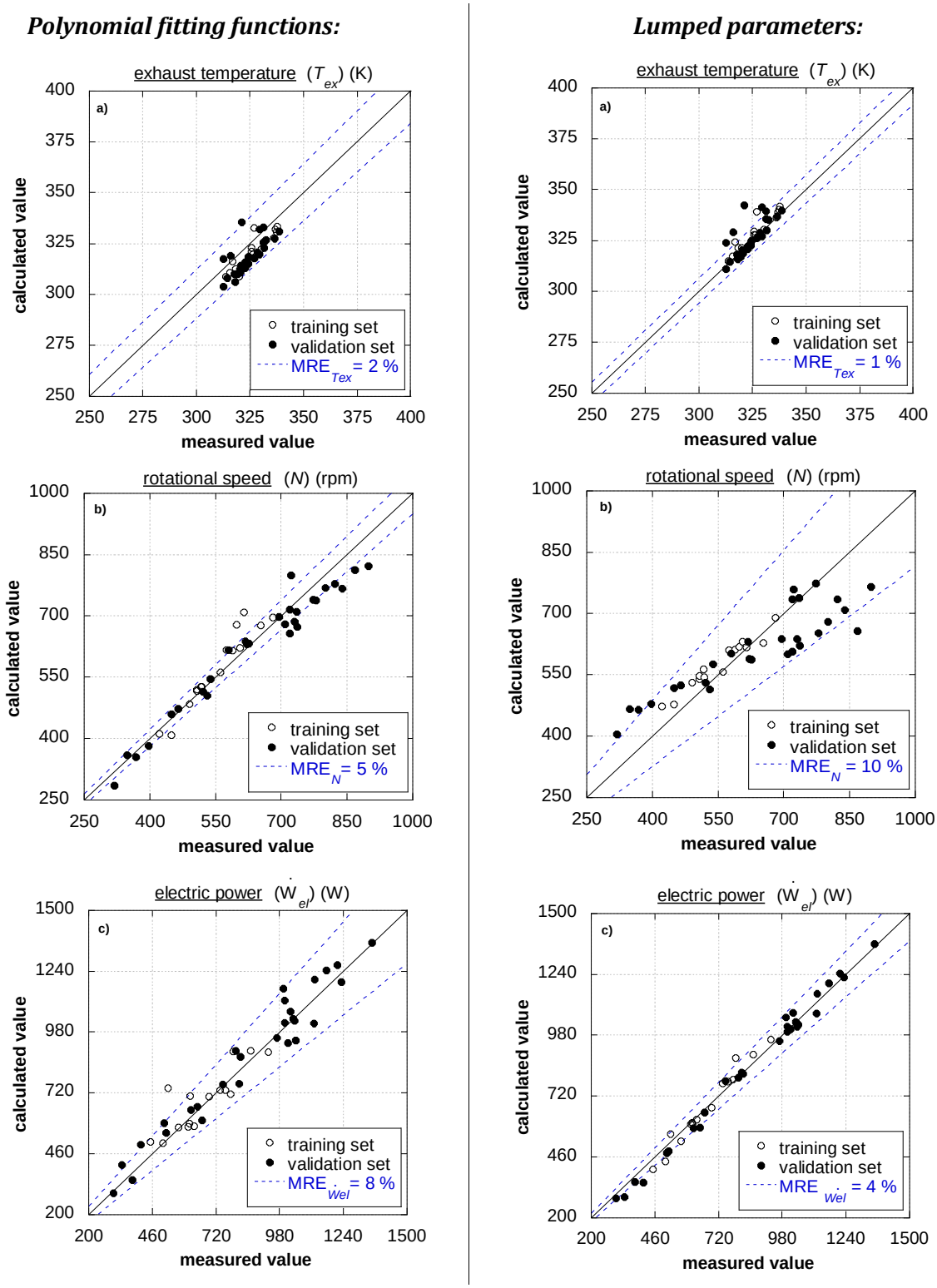

Figure 4-6 - Expander model's parity plots of a) exhaust temperature, b) rotational speed and c) electric power output.

4.2.6 Considerations about the extrapolation capability

The above-described calibrated models can be used to predict the performance maps of the volumetric expander with a good accuracy, as demonstrated by the results of the validation process on the validation data set. However, additional considerations on the extrapolation capability can be done by trying to apply the models under wider unexplored conditions of supply temperature and pressure and flow rate. To this purpose, a parametric analysis has been set as follows: organic fluid mass flow rate variable in the range 0.02-0.24 kg/s, inlet temperature at the expander between 55 °C to 95 °C, expander discharged pressure fixed at 6 bar, expander pressure ratio variable between 1.5 and 5. As mentioned in paragraph 3.3.1, it can be experimentally observed that the evaporating pressure value, i.e. the supply pressure, linearly increases with the mass flow rate in the real operation of the system. Thus, in the maps construction, the supply pressure value has been set variable with the mass flow rate, according to the experimental trend line shown in Figure 3-8, obtained by interpolating the available experimental data. The experimental trend of the pressure ratio as function of the mass flow rate, resulting applying this assumption, is reported in Figure 4-7a.

The maps obtained by the application of the two models are shown and compared in Figure 4-7 and Figure 4-8, where electric power output, electric isentropic efficiency, rotational speed and filling factor results are plotted against fluid mass flow rate or pressure ratio. Where the expander total efficiency, η_{exp}, is calculated as the ratio between the electric power output, $\dot{W}_{el}$, and the isentropic power theoretically available for the expansion process, $\dot{W}_{is}$, i.e. the product between the mass flow rate, $\dot{m}$, and the isentropic enthalpy drop, Δh_{is}:

$$\eta_{exp} = \frac{\dot{W}_{el}}{\dot{W}_{is}} = \frac{\dot{W}_{el}}{\dot{m} \cdot \Delta h_{is}} \tag{4-41}$$

And the filling factor, FF, is computed as the ratio between the elaborated flow rate, $\dot{m}$, and the theorical one, which results from the product between the fluid density, ρ_{su}, the expander swept volume, V_s, and its shaft speed, N.

$$FF = \dot{m} \cdot 60 \,/\, (\rho_{su} \cdot V_s \cdot N) \tag{4-42}$$

Empty dots in figure represents the available experimental data at exhaust pressure, p_{ex}, almost equal to 6 bar ($\pm$5 bar).

It can be immediately noticed that within the calibration range, the semi-empirical models show similar performance results of the aforementioned output variables. Conversely, in most of the cases, when compared outside of the calibration range, prediction maps can substantially differ.

Both models predict an almost linear increase of electric power output with the mass flow rate: best performance is achieved at 95 °C of supply temperature and 0.24 kg/s of mass flow rate. Significant differences among prediction maps can be observed instead looking at the electric isentropic efficiency results: while the polynomial model shows a linear decrease of the efficiency against the pressure ratio value, the lumped approach exhibits a maximum of 40 % of $\eta_{is,el}$ for a pressure ratio close to 1.8. However, the trend of the isentropic electric efficiency as function of the pressure ratio, obtained with the lumped parameters model, is the more realistic one since

consistent with the experimental data in literature, among which is the isentropic efficiency curve for a swashplate piston expander presented by Dumont et Al. [82]. This trend is the expected one for this type of machines: indeed, it exists a pressure ratio value that allows reaching the maximum efficiency; while at lower pressure ratio, the efficiency strongly decreases because of over-expansion losses; at higher pressure ratio, instead, it decreases because of under-expansion phenomenon, pressure drop and mechanical losses. So, the polynomial fitting functions model overestimates the isentropic electric efficiency at low values of the pressure ratio because it is not able to capture the over-expansion losses influence by means of the used isentropic efficiency interpolated curve.

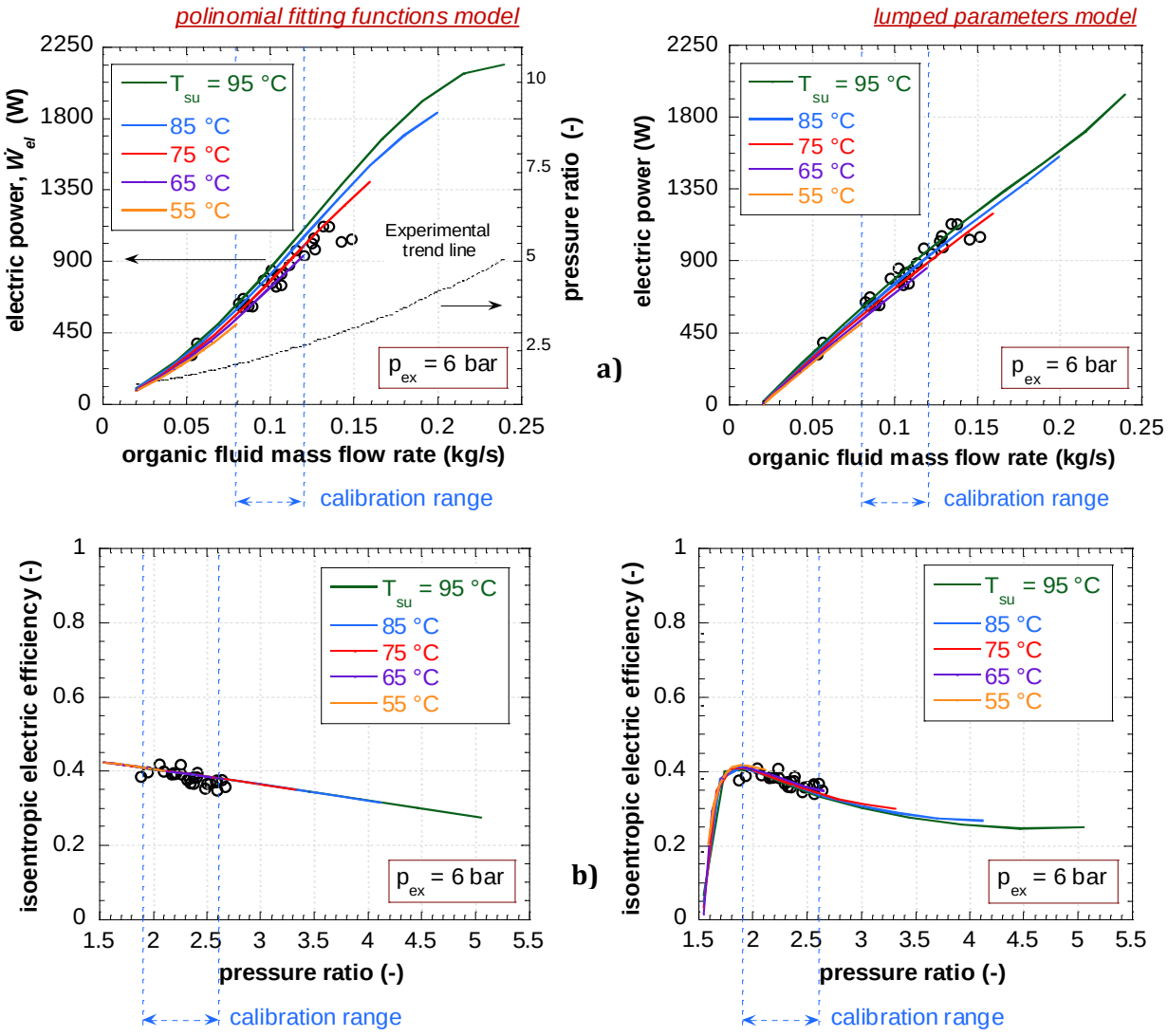

Figure 4-7 - Prediction maps of: a) electric power and b) isentropic efficiency as function of the pressure ratio and the mass flow rate for different values of the supply temperature (experimental data in dots).

The rotational speed trends captured at different supply temperature levels look similar comparing the modelling approaches, however the polynomial model overestimates the values of the rotational speed for pressure ratio values higher than the calibration range. As consequence,

the filling factor results are underestimated compared to the lumped approach, outside of the calibration range. Indeed, the trend calculated with the lumped parameters model is more in line with experiments that can be found in literature, among which is the study of Dumont et al. [83] investigated different volumetric expanders. As shown in this study, the filling factor curve usually reach an asymptote close to 1.

From the comparison it can be concluded that, in the unexplored range of operating conditions, the lumped parameters model shows higher physical soundness in predicting the behavior of the volumetric expander compared to the polynomial fitting model. Thus, the lumped approach can be regarded as the best tool for mapping the performance of the machine in a comprehensive system simulation model or for the design of new reciprocating piston expanders in specific operating conditions.

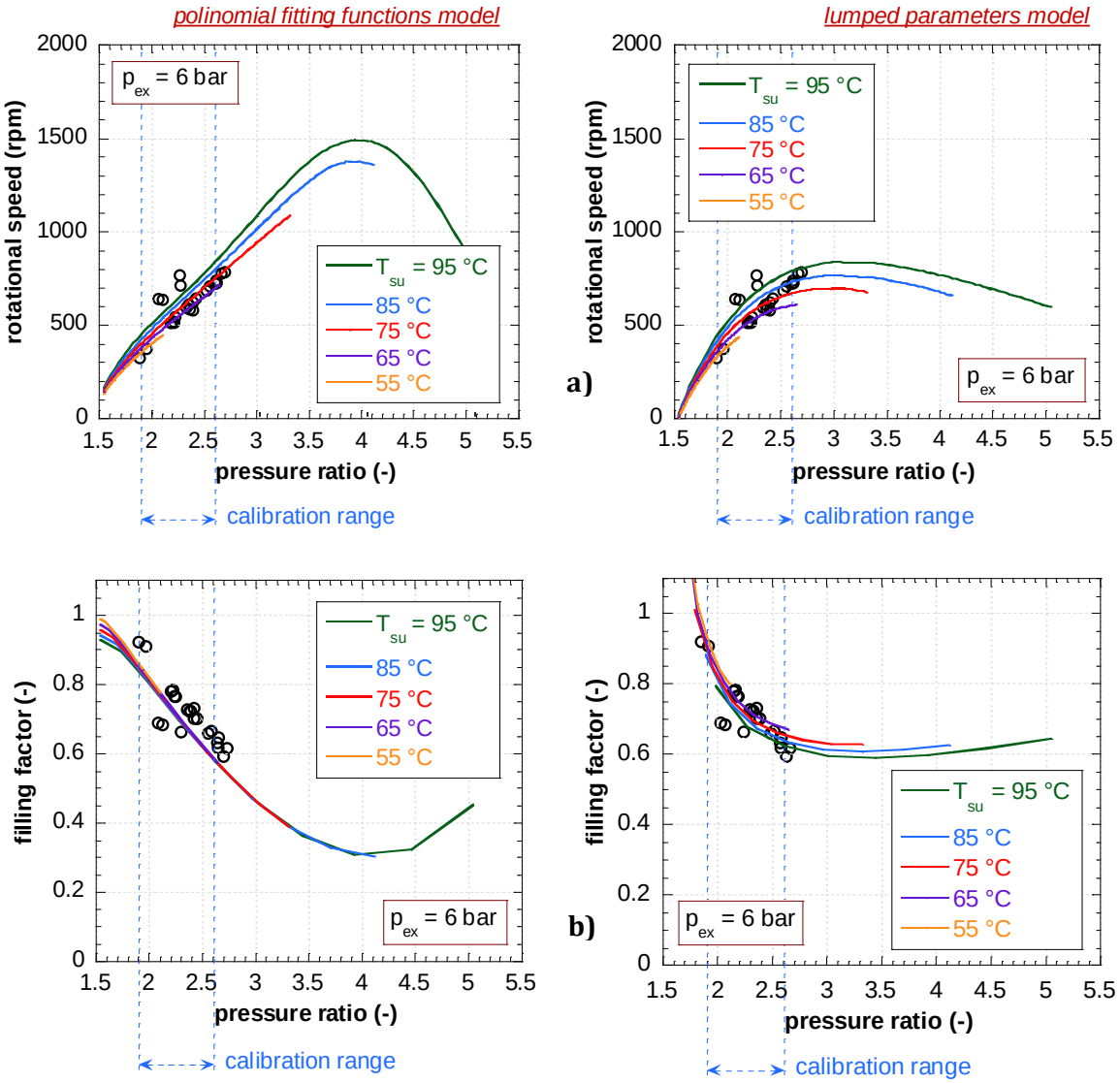

Figure 4-8 - Prediction maps of: a) shaft speed and b) filling factor as function of pressure ratio for different values of the supply temperature (experimental data in dots).

4.2.7 Final comparison

From the comparison between the two different modelling approaches different conclusions can be drawn:

- Starting from the implementation, given its higher complexity the lumped parameters model requires a more complex and sensitive calibration process. An effective calibration of the model requires more computational time and however the risk of a not correct calibration is higher than for the polynomial fitting functions approach.
- Looking at the results, both the models exhibit a good and similar global accuracy, both in the interpolated conditions and in the extrapolated conditions, when considering only the range of the explored operating conditions (i.e. the validation data set). Indeed, the global error on the outputs' prediction do not overcome the 5 % for both the models.
- However, when compared outside of the calibration range, the results obtained by applied a model rather than the other one can differ a lot. In particular, the polynomial model cannot capture the over-expansion and under-expansion phenomena influence which increase at low- and high-pressure ratio values, at the contrary of the lumped parameters approach.

In the view of the above it can be concluded that the polynomial fitting functions model can be suitable to be applied to simulate a volumetric expander into the range of the training data set, with a low effort for its implementation. But, when the aim of the model is to simulate the behavior of the expander under unexplored operating conditions, the best choice is the lumped parameters approach, given its best physical sound in extrapolated conditions. Downstream this analysis, for the purpose of this work, the lumped parameter approach was adopted for the micro-ORC system model.

4.3 Modelling the heat exchangers

4.3.1 The moving boundary approach

The aim of the heat exchangers off-design model is to predict the effective heat transfer between the two involved fluids as function on the fluids' inlet conditions and the component specifics, under different boundary conditions. For the traditional power plants, the direct NTU method is usually implemented to accomplish this task. However, this methodology can't be instead applied to the micro-ORCs case. Indeed, unlike steam power plants (or higher-capacity systems), small scale ORC systems usually employ single once-through heat exchangers to perform the complete vaporization and condensation of the fluid, in place of multiple heat exchangers each one dedicated to work in a single heat transfer region. Thus, several states of fluid can coexist into the component and multiple heat transfer zones can be formed, each one characterized by very different heat transfer properties.

For this reason, for an accurate simulation of the heat exchangers, different heat transfer zones with their spatial distribution should be taken into account. This aspect, in particular, is of outmost importance in the estimation of the mass of fluid enclosed into the heat exchanger volume. As will be seen later, this output is fundamental to evaluate the fluid charge inside the circuit, which is a crucial parameter for the micro-ORC systems [84]. Different approaches are fit for the purpose. For example, imposing a constant pinch point between the temperature profiles can be a simple

approach, but not suitable to simulate off-design conditions. A more accurate but still fast approach is instead the one implemented for the case study, consisting in a one-dimensional moving boundary method [68].

4.3.2 Main equations

Performance of evaporator and the condenser are obtained by means of a three-zone lumped parameters moving boundary model with variable heat transfer coefficients, as schematized in Figure 4-9. According to this approach, the heat exchanger is decomposed into three different heat exchange regions (namely: SC - Subcooled, TP - Two Phase and SH – Superheated, in Figure 4-9), the boundaries of which are defined by the thermodynamic phase change points of the working fluid.

Each zone is characterized by a global heat transfer coefficient U_i and a heat transfer surface area A_i. According to the moving boundary approach, spatial position of each zone and its surface (A_i) are not fixed, but they are determined based on the fluid state. A boundary condition is required to calculate the area of each section. The constraint is that the sum of the single surface areas corresponds to the geometrical surface area of the component, A, which is instead a model parameter.

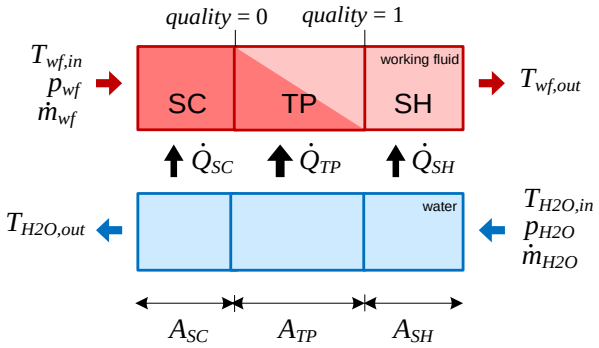

Figure 4-9 - Moving boundary model scheme.

The heat transfer occurring in the i-th zone is given by the product between the global heat transfer coefficient, the surface area and the logarithmic mean temperature difference $\Delta T_{log,i}$ of the zone (Eq.(4-43)).

$$\dot{Q}_i = A_i U_i \cdot \Delta T_{log,i} \tag{4-43}$$

The considered global heat transfer coefficient accounts for the convective coefficient of the working fluid side, α_{wf}, and the convective coefficient of the water side, α_{H2O} (Eq. (4-44)). Conductive heat transfer contribution can be considered negligible, due to high value of steel conductive coefficient and thin wall thickness.

$$U_i = \left(\frac{1}{\alpha_{wf,i}} + \frac{1}{\alpha_{H2O,i}} \right)^{-1} \tag{4-44}$$

4.3.3 Heat transfer coefficients

The heat transfer coefficients are sensitive parameters to estimate when modelling heat exchangers and its determination is not trivial even when experimental data are available. This is because different convective coefficients intervene in the computation of the heat transfer, at least one for each fluid in each zone, and different combination of their values can lead to the exact same heat transfer predictions. Indeed, the same thermal power can be obtained by different profiles of temperatures inside the component, with different zones spatial distribution, determined by the heat transfer coefficients' weight; so more than a solution is possible.

The literature provides several correlations for the estimation of the heat transfer coefficients as function of the fluid properties and the heat exchanger's geometry, for various technologies. However, despite their large availability, even the more employed correlations, when used for the micro-ORC simulations have proved to not perfectly match the experimental observations [84]. Thus, there is not a yet a best practice to apply for the specific case study. A solution can rely on the use of corrected versions of these correlations which involve the introduction of empirical parameters calibrated to fit experimental data. Thus, the latter is the approach chosen for this study.

The water convective coefficients, the working fluid convective coefficients for the subcooling and the superheating zone are determined by means of the Dittus-Boelter correlation:

$$Nu = 0.023 \cdot Re^{4/5} \cdot Pr^{n} \quad , \text{ with } \begin{cases} n = 0.4 & \text{if being heated} \\ n = 0.3 & \text{if being cooled} \end{cases} \tag{4-45}$$

This correlation was selected as well-established correlation to simulate the forced convection of one-phase fluids [85]. The working fluid convective coefficient for the two-phase zone, $\alpha_{wf,TP}$, instead is a more challenging parameter to be predicted in ORC application. For this reason, the estimations of $\alpha_{wf,TP}$, is performed by means of empirical correlations. In particular, correlation used for the evaporator has the form of Eq. (4-46).

$$\alpha_{wf,TP} = \alpha_{wf,TP,ref} \left(\frac{\dot{m}_{wf}}{\dot{m}_{wf,ref}} \right)^{x} \left(\frac{\Delta T_{sat}}{\Delta T_{sat,ref}} \right)^{y} \tag{4-46}$$

where $\alpha_{wf,ref}$ represents the value of the convective coefficient in reference operating conditions. In off-design conditions, $\alpha_{wf,ref}$ is adjusted according to the so called "thermal resistance scaling" method, to account for the dependence of the convective coefficient from the fluid velocity. Following this method, the reference convective heat transfer coefficients, $\alpha_{wf,ref}$, is scaled as function of the ratio between the actual mass flow rate, $\dot{m}_{wf}$, and the one calculated in the reference point, $\dot{m}_{wf,ref}$, to the power of x. The exponent x usually does is close to 0.8, which corresponds to the exponent of the Reynolds number in the Dittus Boelter correlation.

According to empirical observations, an additional correction term accounting for the nucleated boiling phenomenon is introduced to better estimate the variation of the evaporator heat transfer coefficient when the operating conditions differ from the reference one. Assuming a forced convection boiling regime, the nucleated boiling convection weight is proportional to the difference between the working fluid saturation temperature and the secondary fluid temperature, ΔT_{sat} [85]. Thus, the term $\left(\frac{\Delta T_{sat}}{\Delta T_{sat,ref}} \right)^{y}$ in Eq. (4-46) accounts for the modification of ΔT_{sat} with respect to its

reference value $\Delta T_{sat,ref}$ and its influence on the nucleated boiling heat transfer contribution. Both z and y values are obtained by fitting the model outputs with the available experimental data.

Correlation used for the condenser is the same of Eq. (4-46), but assuming pure convective regime, thus, excluding the dependence from ΔT_{sat}. As a result, condenser two-phase working fluid convective coefficient is estimated by means of Eq. (4-47).

$$\alpha_{wf} = \alpha_{wf,ref} \left(\frac{\dot{m}_{wf}}{\dot{m}_{wf,ref}} \right)^{x} \tag{4-47}$$

The recuperator is also modelled on the basis of Eq. (4-43), but considering a single heat exchange zone. The recuperator global heat transfer coefficient is equal to a convective heat transfer coefficient computed my means of Eq. (4-47).

The calibrated parameters of the model, for the heat transfer coefficients are summarized in Table 4-4 reporting also the calibrated value. These values are obtained by interpolation of the available data of the micro-ORC prototype considered as reference.

Table 4-4 - Heat exchanger model calibrated parameters.

Component	Parameters	Value
All	$\dot{m}_{wf,ref}$	0.123 kg/s
	x	0.74
Evaporator and condenser	$\alpha_{wf,ref}$	15.72 kW/m²/K
Evaporator	$\Delta T_{sat,ref}$	20 °C
	y	-0.84
Recuperator	$\alpha_{wf,ref}$	4.79 kW/m²/K

4.4 Modelling the volumetric pump

The pump component is less investigated than the expander, although of fundamental importance, since pump irreversibilities can substantially decrease the ORC cycle overall efficiency [1]. However, semi-empirical models have been successfully applied to volumetric pumps too [71] with the objective of understanding and predicting the behavior when operating at different conditions.

Generally, pump models are described by means of performance maps reporting pressure head versus volumetric flow rate at different rotating speeds. The actual operating point of the pump is then determined by crossing the characteristic curve of the pump with the resistance characteristic of the system in which the pump is inserted. For the case study, the characteristic curve of the pump and the resistance characteristic of the system have been traced by interpolating the experimental data. Figure 4-10 shows the extrapolated pump and circuit characteristic curves that constitute the operating map of the pump in exam. The observed pump volumetric performance is quite reduced at high pressure rise, according to the high slope of the pump characteristic curves of Figure 4-10, probably due to the gears wear out and/or to a non-correct amount of lubricant oil inside the circuit.

For example, at rotational speed corresponding to pump frequency equal to 35 Hz and for a pressure rise equal to 8 bar, the actual volumetric flow is equal to 110 cm³/s while the theoretical volumetric flow is equal to 175 cm³/s (see experimental data in Figure 4-11), corresponding to a volumetric efficiency equal to 63 %.

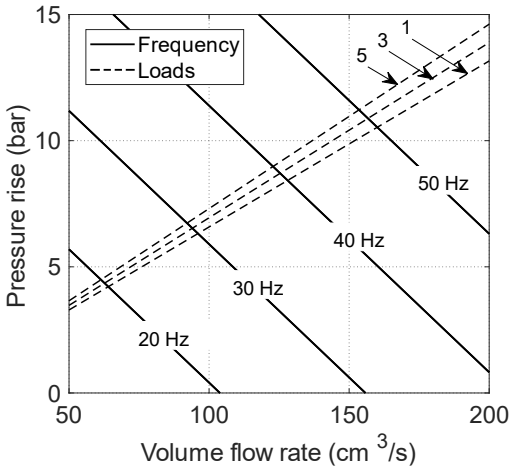

Figure 4-10 - Extrapolated characteristic curves of the pump and circuit resistance.

Data concerning the pump performance have been collected during the experimental campaign conducted over the micro-ORC system (see Figure 4-11).

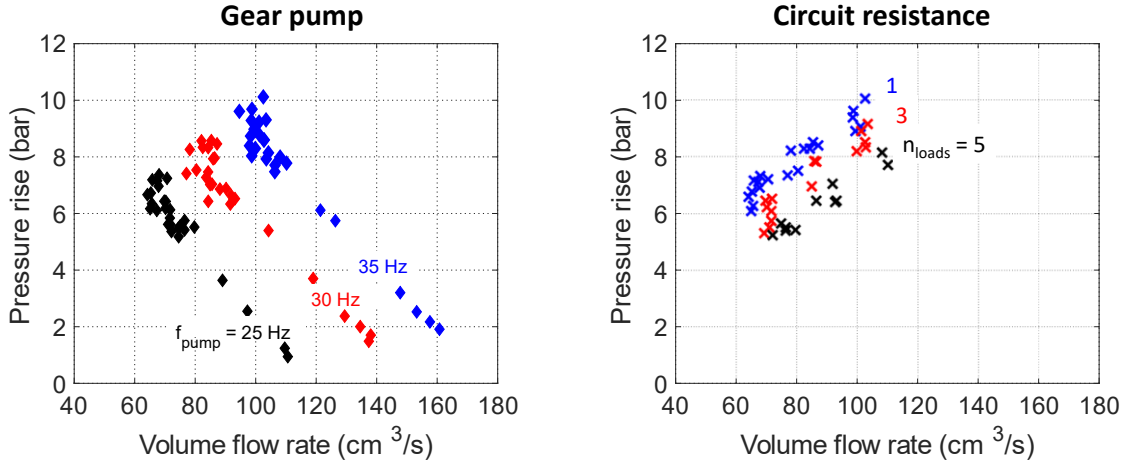

Figure 4-11 - Experimental characteristic of the volumetric pump and the circuit.

Additional tests have been performed with the expander by-passed, with the specific aim of completing the characteristic curves at low pressure head values, which cannot be reached when the expander is running. The procedure consisted in setting a pump frequency and adjusting a valve opening along the circuit to vary the flow rate and increase the circuit resistance. In this way, performance of the volumetric pump has been evaluated over a wider operating range, i.e. pressure rise going from 1 to about 10 bar and volume flow between 60 to 160 cm³/s. This operating map, once integrated into the model, allows to determine the actual pressure rise and the volume flow rate elaborated by the pump, for given conditions of pump frequency (f_{pump}) and number of activated

resistive loads (n_{loads}) (i.e. the point of intersection of the actual pump line and the circuit resistance line). The mass flow rate, input of all the other subcomponents models, is then obtained using the fluid density at the pump inlet, evaluated via Refprop [63] from condensing pressure and pump inlet temperature. The product between the pressure rise, Δp, and the volumetric flow rate, $\dot{V}$, divided by the pump efficiency, η_{pp}, gives the pump absorbed power (Eq. (4-48)).

$$\dot{W}_{pp} = \frac{\dot{V} \cdot \Delta p}{\eta_{pp}} \tag{4-48}$$

The actual resistance of the system is influenced by the number of the activated resistive loads dissipating the electric power generated by the expander. This is because the increase of the expander load determines a greater fluid dynamic resistance of the circuit, resulting in higher values of the pressure rise for given value of volume flow rate (obtainable with higher pump frequency, see Figure 4-10).

4.5 The system model

A schematic of the proposed micro-ORC system model, describing the components sub-models and relationships between them, is shown in Figure 4-12. The micro-ORC simplified layout to which it refers is reported as follow, in Figure 4-13.

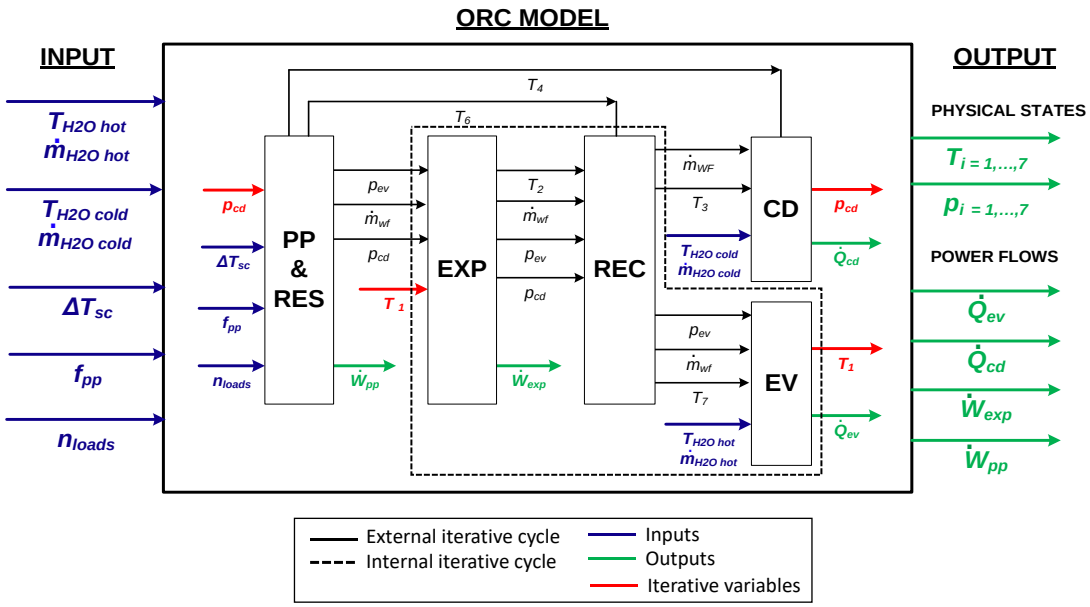

Figure 4-12 - Schematic of the cycle model.

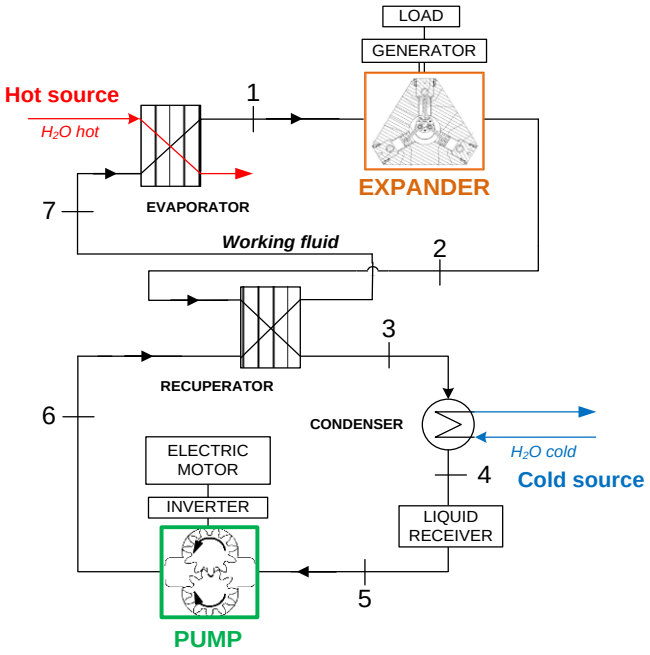

Figure 4-13 - Micro-ORC simplified layout.

The model is based on a lumped parameters approach and it allows to calculate the complete thermodynamic state of the ORC system using as input the boundary conditions only, i.e. the heat source and the heat sink supply conditions (T_{H2Ohot}, $\dot{m}_{H2Ohot}$, $T_{H2Ocold}$ and $\dot{m}_{H2Ocold}$), as well as the pump feed frequency (i.e. f_{pp}) and the expander load resistance (i.e. n_{loads}). Thus, the inputs of the model are the main control variables of the system plus the subcooling level at the condenser outlet, ΔT_{sc}. For the sake of completeness, it must be highlighted that the subcooling degree is not exactly a control variable, but it is implicitly determined by the other control variables and the amount of fluid charged inside in the circuit [84]. Nevertheless, in this study, the fluid charge is considered as an output for two reasons. First of all, the measure of the fluid charge it is difficult to determine with accuracy [84], whilst the value of the temperatures and the pressures necessary to estimate the subcooling degree can be directly measured. This allows to base the model validation on more reliable data. Then, this choice will allow to make some considerations about how the fluid charge could be affected by changing the boundary conditions, as discussed in the next chapters.

Since the ORC model is formulated as an implicit problem, its solution is determined through an iterative process, whose iterative variables are the condensing pressure, p_{cd}, and the expander inlet temperature, T_1. More in detail, the iterative cycle on the expander inlet temperature is nested into the condensing pressure iterative cycle. The outputs of the model are the fluid states in all the point of the thermodynamic cycle and, in particular, indicators, namely, the thermal input provided at the evaporator, $\dot{Q}_{ev}$, the condenser discharged heat, $\dot{Q}_{cd}$, the electric power output, $\dot{W}_{exp}$, and the pump absorbed power, $\dot{W}_{pump}$.

The considered sub-models are the pump and the circuit resistance, the expander, the recuperator, the evaporator and the condenser ones (respectively indicated by the “PP & RES”, “EXP”,

"REC", "EV" and "CD" blocks in Figure 4-12). A detailed description of each sub-model, its parameters and their correction are reported in the following sub-paragraphs.

In this study, experimental data collected during the reference rig experimental tests using R134a have been considered for the model calibration. Sub-models and their empirical parameters requiring calibration are listed in Table 4-5 (see "Nomenclature" and dedicated paragraphs for detailed parameters naming and meaning). It must be highlighted that some empirical parameters are associated only to the components dimensions whilst others depend on the working fluid thermodynamic characteristics. For this reason, parameters related to the working fluid will be corrected to account for the use of fluids different from R134a, as detailed in Paragraph 4.7.

The sub-models have been all implemented in the Matlab environment [86], along with a set of data coming from the experimental campaign. Inside the model, the working fluid thermo-fluid dynamic properties have been evaluated by means of the refpropm function, which is an add-in provided by the Refprop commercial program [63].

Table 4-5 - Micro-ORC model parameters

Component	Parameters
Heat exchangers (EV, CD, REC)	$\alpha_{wf,ref}$, $\dot{m}_{wf,ref}$, $\Delta T_{sat,ref}$, x, y, A
Expander (EXP)	$(AU)_{su,ref}$, $(AU)_{ex,ref}$, $(AU)_{amb}$, $W_{loss,ref}$, $W_{loss,N}$ $r_{v,exp}$, $r_{v,comp}$, V_0, A_{leak}, A_{su}
Pump & Circuit resistance (PP & RES)	c_1, c_2, c_3, c_4, η

4.6 Model validation

Before applying the model to unexplored operating conditions, the model has been tested against experimental data collected during the extensive experimental campaign conducted over the reference test rig [87] using R134a, in order to evaluate the model accuracy. Results are reported in form of parity plots comparing main output calculated values (of evaporator thermal power, expander produced electrical power and pump absorbed electrical power) with measured ones (Figure 4-14).

Dash lines are introduced in figures to highlight the relative prediction error. Results prove the good accuracy of the model. Indeed, Figure 4-14 shows that most of the points come within the 10 % error band. The validation confirms the effectiveness of semi-empirical models in predicting part-load behaviour of micro-ORCs.

4.7 Considering the change of the working fluid

In order to cope with different working fluids, the model can be generalized, by introducing some corrections in the fluid dependent parameters. The procedure applied to generalize the model to simulate fluids other than R134a relies basically on the fluid thermodynamic properties and it is conceived to be applied to simulate fluids quite similar to R134a. For these reasons limited errors

(in lines with the error values shown in case of R134a) could be expected in prediction of their performance in place of R134a.

This kind of fluids are for example the commercial low-GWP alternatives of R134a and fluids with similar critical temperature, which actually are the most indicated fluids to use for micro-ORCs application in the analyzed range of hot source temperature.

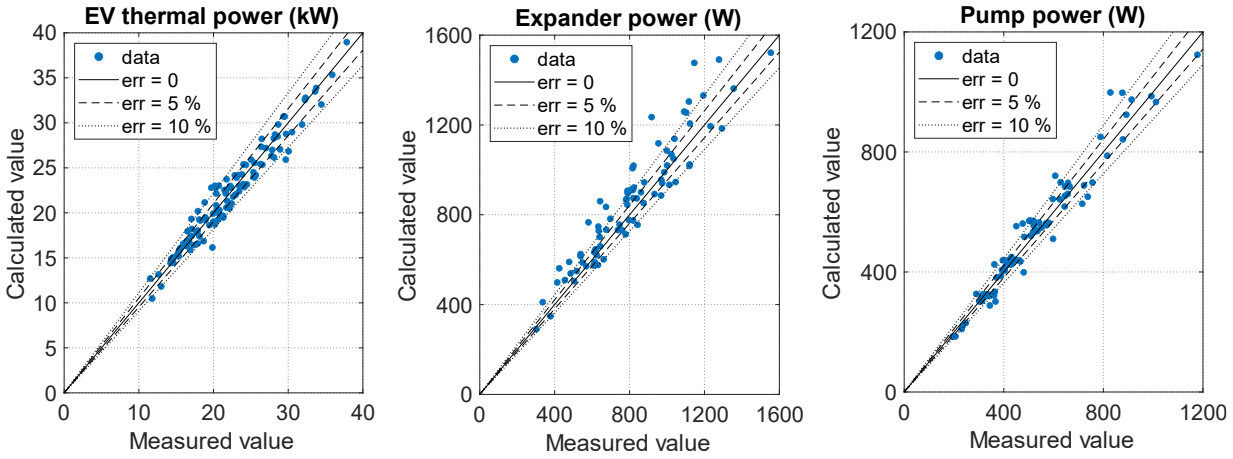

Figure 4-14 - Parity plot comparing output calculated values and measured ones.

4.7.1 Expander and heat exchangers heat transfer coefficients correction

First of all, the global heat transfer coefficients of the heat exchangers models and the expander model must be corrected. In particular, concerning the expander model, the parameters to be corrected are the product of global heat transfer coefficient and heat exchange area in reference conditions of expander inlet and outlet, $(AU)_{su,ref}$ and $(AU)_{ex,ref}$, used to model the heat transfer between the working fluid and the casing, as described by Eqs. (4-23) - (4-25). These parameters have been re-determined adopting the procedure proposed by Giuffrida [77], as reported below.

Thus, the global heat transfer coefficient can be evaluated as:

$$U = \frac{Nu \cdot \lambda}{L} \tag{4-49}$$

where Nu and λ are the Nusselt number and the conductivity, which depend on the fluid thermophysical properties; whilst L is the characteristic length and it is set by the component geometry. Considering estimating the Nusselt number by means of the Dittus-Boelter correlation for turbulent flows. Given that the characteristic length is set and the velocity does not depend on the working fluid (being set the flow passage area and the swept volume), the global heat transfer coefficient for the new fluid, U_{new}, can be determined as function of the reference global heat transfer coefficient, U_{ref}, and the fluids properties, by using Eq. (4-50) .

$$\frac{U_{new}}{U_{ref}} = \frac{Nu_{new} \cdot \lambda_{new}}{Nu_{ref} \cdot \lambda_{ref}} \tag{4-50}$$

Expliciting each terms of Eq. (4-50), the equation for the global heat transfer parameter correction is obtained (Eq. (4-51)).

$$AU_{new} = AU_{ref} \cdot \left(\frac{\rho_{new}}{\rho_{ref}}\right)^{0.8} \cdot \left(\frac{c_{p\,new}}{c_{p\,ref}}\right)^{a} \cdot \left(\frac{\lambda_{new}}{\lambda_{ref}}\right)^{1-a} \cdot \left(\frac{\mu_{fluid}}{\mu_{new}}\right)^{0.8-a} \tag{4-51}$$

where ρ is the fluid density, c_p is the heat capacity at constant pressure and μ the fluid dynamic viscosity; the subscript *new* indicates the quantities related to the new fluid, while the subscript *ref* indicates those referred to the reference case (R134a).

As regards the other expander model parameters listed in Table 4-5, $(AU)_{amb}$ is not dependent on the working fluid, since it describes just the heat losses from the casing to the ambient; thus, it does not require to be corrected when changing the fluid. Same goes for the parameters $r_{v,exp}$, $r_{v,comp}$, V_0, A_{leak} and A_{su}, which are geometrical parameters, characteristic of the specific machine. Eventually, the values of the parameters $W_{loss,ref}$ and $W_{loss,N}$, which take into account the friction losses, are kept equal to the ones obtained for the R134a, according to [77]. Actually, a more detailed modelling approach could include both the Coulomb and the viscous friction terms in the friction losses formulation, which instead would depend on the fluid viscosity. Nevertheless, friction losses represent a limited contribution compared to the other loss sources (as demonstrated later in the results paragraph), thus, the modification of the model friction parameters can be neglected in the model applied in this study.

4.7.2 Pump and circuit characteristics slope correction

Concerning the pump and circuit resistance model, a methodology to account for the change of the working fluid for a volumetric pump is here introduced. The characteristic curves of the pump have been adjusted in order to determine the new operating point of the pump when working with fluids different from R134a, according to the modelling approach described below.

To a first approximation, the volume flow rate actually elaborated by the pump, $\dot{V}$, is equal to the difference between the theoretical volume flow rate that the pump could elaborate ($\dot{V}_{th}$) and the leakage flow rate lost through the meatus ($\dot{V}_{leak}$).

$$\dot{V} = \dot{V}_{th} - \dot{V}_{leak} \tag{4-52}$$

Due to the pressure rise, Δp, between inlet and outlet of the pump, a leakage occurs through its internal clearance, in particular, through the space between the tips of the gear teeth and the cavity wall. Poiseuilles law for laminar flow is here used to evaluate the leakage flow, $\dot{V}_{leak}$, through the meatus, as function of the viscosity of the fluid, μ, of the meatus geometry and of the pressure rise between inlet and outlet, according to the following equation:

$$\dot{V}_{leak} = \frac{b \cdot h^3 \cdot \Delta p}{12 \cdot \mu \cdot l} \tag{4-53}$$

where h is the meatus height, l the length and b the width. The theoretical volume flow rate is equal to the pump cubic capacity (V_{cc}) multiplied by the rotational speed (N_{pump}), which corresponds also to the value of the volume flow rate at null pressure rise.

$$\dot{V}_{th} = V_{cc}\frac{N_{pump}}{60} = \dot{V}(\Delta p = 0) \tag{4-54}$$

The set of equations ((4-52)-(4-54)) define the linear dependence of the pressure rise Δp on the volume flow rate. Indeed, being constant the geometrical quantities, the expression of the pump pressure rise can be written as:

$$\Delta p = (c_1 \cdot N_{pump} - \dot{V} \cdot c_2) \cdot \mu \tag{4-55}$$

where c_1 and c_2 are constant, calculated as:

$$c_1 = \frac{c_2 \cdot V_{cc}}{60} \quad , \quad c_2 = \frac{12 \cdot l}{b \cdot h^3} \cdot c_2 \tag{4-56}$$

c_1 and c_2 are experimentally determined by interpolating the data collected during the test performed on R134a. The parameters values used in equation (4-55) are reported in Table 4-6.

Table 4-6 - Parameters values for the pump model.

Parameter	Value
c_1 (-)	5.29 x 10^2
c_2 (m^{-3})	5.10 x 10^2
V_{cc} (cm^3)	62.3
c_3 ($m^{-1}\cdot s^{-1}$)	1.52
c_4 ($m^{-1}\cdot s^{-1}$)	53.3

According to Eq. (4-55), it can be noticed that being equal the rotational speed, the curve slope varies proportionally with the viscosity of the working fluid, as shown in Figure 4-15.

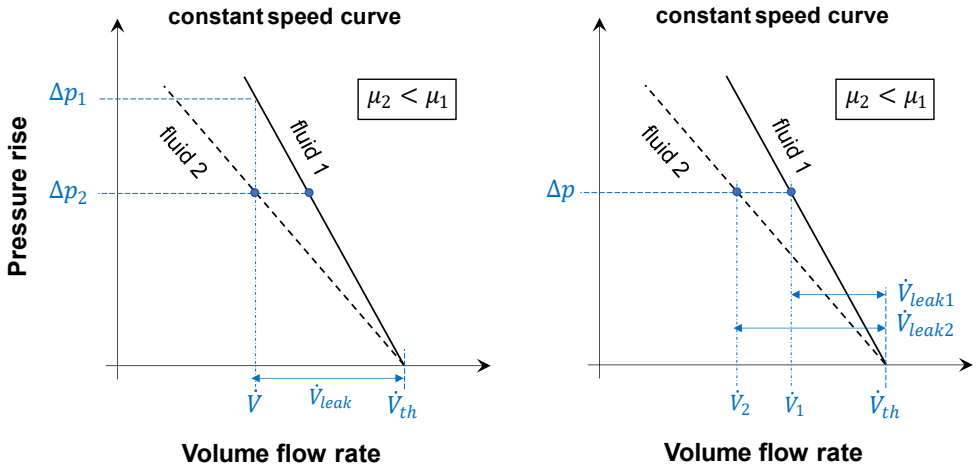

Figure 4-15 - Influence of the change of the fluid on the pump volumetric performance.

In particular, the lower is the viscosity the worst are the pump volumetric performances. Thus, working with a fluid with a lower viscosity:

- being equal the flow rate, the pump can elaborate a lower pressure rise.
- being equal instead the pressure rise, the pump can elaborate a lower volume flow rate, due to the higher leakage losses through the meatus, inversely proportional to the viscosity (see Eq. (4-53)).

Eq. (4-59) represents instead the general formula for evaluating hydraulic circuit pressure head [88], Δp, where ε, is the equivalent flow coefficient, ρ, is the fluid density and w, the fluid velocity:

$$\Delta p = \varepsilon(geo_{circ}, n_{loads}) \cdot \rho \cdot \frac{w^2(geo_{circ}, \dot{V}, \rho)}{2} \tag{4-57}$$

In brackets is implicitly expressed the dependence of ε and w from the circuit geometry, geo_{circ}, the volume flow rate and the density of the fluid. These terms can be indicated in explicit form and rearranged, obtaining a second relationships to determine the Δp, but this time as function of the n_{loads}

$$\Delta p = (c_3 \cdot n_{loads} + c_4) \cdot \dot{V} \cdot \rho \tag{4-58}$$

where c_3 and c_4 coefficients are size dependent constants of the circuit due to the geometry terms geo_{circ}. The result is that the working fluid has an impact on the equations via the fluid density, ρ, influencing the characteristic curves slope. More in specific, the pressure drop along the circuit is proportional to the fluid density.

4.8 Fluid charge estimation

The fluid charge is estimated on the basis of the internal volume of the largest ORC components, i.e. the evaporator, the condenser, the recuperator and the liquid receiver. The amount of working fluid inside expander, pump and in connected pipelines can be considered less relevant. The fluid mass enclosed in the j-th component could be estimated as the product between the j-th component volume, V_j, and the j-th mean fluid density, ρ_j. Mean density inside evaporator and condenser is computed as the weighted average of the densities in relation to the heat exchange regions volumes. The density inside the two-phase region can be calculated using Eq. (4-59).

$$m_j = V_j \cdot (\rho_{liquid,j} \cdot (1 - \gamma_j) + \rho_{gas} \cdot \gamma_j) \tag{4-59}$$

$$X_{tt} = \left(\frac{1-x}{x}\right)^{0.9} \left(\frac{\rho_{gas}}{\rho_{liquid}}\right)^{0.5} \left(\frac{\mu_{gas}}{\mu_{liquid}}\right)^{0.1} \tag{4-60}$$

$$\gamma = (1 + {X_{tt}}^{0.8})^{-0.378}, \quad X_{tt} \leq 10 \tag{4-61}$$

$$\gamma = 0.823 - 0.157 \, ln \, X_{tt}, \quad X_{tt} > 10 \tag{4-62}$$

In particular, the volume vapour fraction γ for a generic component can be derived by the Lockhard-Martinelli model according to Liu et Al. [89], using Eqs. (4-60) - (4-62). X_{tt} is the Martinelli

parameter, x is the fluid quality (considered equal to 0.5), μ, the fluid viscosity, and the subscripts $liquid$ and gas refer to the saturated liquid and saturated vapour fluid state respectively.

5 Influence of the working fluid over the performance and the environmental impact

Summary: This chapter proposes a comprehensive evaluation of the actual greenhouse impact of micro-ORC systems which can derive from the use of low-GWP fluids, in place of HFCs, and vice versa, accounting not only for direct greenhouse emissions (due to refrigerant leakage during the system operation) but also for indirect contribution.

A detailed investigation on the performance of the piston expander working with low-GWP fluids as drop-in replacement to HFCs is conducted; some considerations are also done about pump operation. The aim is to examine how the different thermodynamic characteristics of the fluids could influence the performance at the components level.

The influence of geometrical aspects, such as the built-in volume ratio, over the expander performance is also analyzed. The objective is to: i) confirm the importance of optimizing this parameter for the specific expander operating conditions; ii) explore micro-ORC best achievable performance.

5.1 Contribution

As further discussed also in the introduction chapter, literature suggests that additional experimental and numerical analyses are necessary to assess performance of R134a low GWP alternatives into ORC systems. In the view of the above this study wants to give a contribution to fill this knowledge-gap and to extend the current state of the art. At this scope, different analyses are proposed in the following paragraphs:

1. A first comparative investigation of the performance of the reference reciprocating expander, working with low-GWP fluids as replacement of HFC-134a. Indeed, according to the manufacturer, the expander in exam is designed to work with R134a and fluids with similar properties, as new olefins R1234yf and R1234ze(E) [62], but its performance when working with fluids different from R134a has not yet been tested. The aim was to examine how the different thermodynamic characteristics of the fluids could influence the performance of the volumetric machines at the component level, accounting not only for the influence of the isentropic enthalpy drop, as happen for constant efficiency models. In this analysis, the proposed model has been also used to optimize the built-in volume ratio, modifying the intake

stroke ratio, in order to achieve the best performance of the expander under investigation for all the analyzed working fluids. This result may be used to modify the valve timing in order to improve the performance of the expander.

2. An analysis of the actual greenhouse impact of micro-ORC systems, which can derive from the use of low-GWP fluids, in place of HFCs, for the low-temperature application. A comprehensive evaluation approach is proposed, which accounts not only for direct greenhouse emissions, due to the refrigerant leakage during the system operation, but also for indirect contribution. The indirect emissions term takes into account emissions related to the resulting lack of power production by the ORC, caused by the adoption of a less performing fluid, over a more performing one. The open literature has not yet paid the right attention to the ORC working fluid selection comprehensive greenhouse impact, including not only the direct contribution, but also the indirect one. This term should be an important aspect to evaluate when deciding to substitute the HFC fluid, even if the replacing fluid has a significantly lower GWP value than the replaced one. This analysis, in particular, takes as reference the typical architecture of micro-ORC system, presented in paragraph 3.1. A larger set of fluids is considered in this case, involving not only HFOs pure fluids, but also their mixtures with HFCs and a mixture containing a Hydrocarbon.

The methodology used for these analyses is based on the validated semi-empirical models presented in the previous paragraph, for which adaptations necessary to model low-GWP fluids and blends instead of R134a have been also introduced and discussed. Semi-empirical models are employed to consider actual operating conditions, differently from less realistic constant isentropic efficiency assumptions.

5.2 Analyzed working fluids

The fluids analyzed in this work are selected among the most recent options of low-GWP alternatives to R134a for refrigeration applications, including also intermediate partial mixtures of R134a with pure substitutes and other commercially available mixtures belonging to different fluid categories (i.e. HFs, HFO and Hydrocarbon (HC)). The selected alternative fluids are:

- R1234yf and R1234ze(E) pure fluids;
- mixture of 50 % R134a and 50 % R1234yf in mass, named in this study “R1234yf mix”;
- mixture of 50 % R134a and of 50 % R1234ze(E) in mass, named in this study “R1234ze(E) mix”;
- R515A, which consists in a mixture of 88 % R1234ze(E) and 12 % R227a in mass;
- R430A, which consists in a mixture of 76 % R152a and 24 % R600a (i.e. isobutane) in mass.

In particular, first of all R1234yf and R1234ze(E) are selected for the comparison as the most suitable low-GWP HFOs for heat recovery applications at temperature lower than 100 °C (given their critical temperature close to 100 °C). Indeed, several HFOs organic fluids are now commercially available, but just a few of them are suitable for low temperature heat recovery applications. These fluids present very similar thermodynamic properties compared to R134a (see Table 5-1 and Figure 5-1), nevertheless some small but not negligible differences exist, influencing the performance of the ORC components, especially in case of pump and expander of volumetric type. One of the main

factors of influence over the cycle performance is the expansion pressure ratio, which depends on the pressures at which the fluid evaporates and condenses into the cycle at given temperatures of the hot and cold source respectively. Other properties that can have an impact on performance and internal losses of the volumetric machines are the density and the viscosity of the fluid.

Table 5-1 - Main properties of the substitute fluids compared with R134a.

Properties	**Fluid name and type**						
	R134a	**R1234yf**	**R1234ze(E)**	**R1234yf mix**	**R1234ze(E) mix**	**R515A**	**R430A**
	HFC pure fluid	HFO pure fluid	HFO pure fluid	HFC/HFO mixture	HFC/HFO mixture	HFC/HFO mixture	HFC/HC mixture
$T_{critical}$ **(°C)**	101.1	94.7	109.4	95.3	103.8	108.7	107.0
p_{sat} **(@ 25 °C) (bar)**	6.7	6.8	5.0	7.1	6.0	4.9	6.5
$p_{sat,liquid}$ **(@ 60 °C) (bar)**	16.8	16.4	12.8	17.4	15.2	12.7	15.7
Δh_{sat} **(@ 60 °C) (kJ/kg)**	139.1	110.4	135.5	120.4	135.4	128.8	218.4
$\rho_{sat,liquid}$ **(@ 25 °C) (kg/m³)**	1207	1092	1163	1141	1181	1187	760
$\rho_{sat,gas}$ **(@ 60 °C) (kg/m³)**	87.4	99.8	70.1	99.7	80.7	72.5	50.3
$\mu_{sat,liquid}$ **(@ 25 °C) (Pa·s) x 10⁴**	1.95	1.53	1.90	1.68	1.90	1.94	1.43
GWP (-)	1300	1	1	650.5	650.5	403	106
ASHRAE class	A1 [16]	A2L [90]	A2L [90]	A1 [91]	A1 [91]	A1 [16]	A3 [16]

properties obtained with RefProp [63], GWP values from IPCC AR5 [17]

Beside the GWP issue, another fundamental aspect to consider is the fluid safety and flammability in particular. Most of HFO fluids have the disadvantage of being classified at least as A2L, according to ASHRAE Standard 34 [18], i.e. mildly flammable refrigerant category (this A2L class applies to R1234yf and R1234ze(E), see Table 5-1). This feature may not always be constrictive in the working fluid selection for refrigeration applications, but it should be properly assessed, instead, in the ORC applications, where the operating temperature range rises and flammability risk of the fluid could increase. Options to decrease the flammability risk while containing the GWP issue at the same time, can rely on blending the HFOs with non-flammable fluids with similar thermodynamic properties, such as the basic R134a (classified as A1, i.e. non-flammable, according to ASHRAE). Thus the "R1234yf mix" and "R1234ze(E) mix" cases have been considered in the study, as intermediate mid-term substitute fluid options of the R134a. Moreover, the R515A commercially available HFC/HFO binary mixture (containing high concentration of R1234ze(E) and classified as A1), has been included in the fluid comparison. Eventually, for sake of completeness, also R430A - a mixture indicated in literature as a potential good candidate for R134a replacement in refrigeration application [16] - has been included into the analysis. R430A exhibits several good properties, as highlighted in Table 5-1: i) lower GWP in comparison with R134a and the other mixtures containing

HFCs; ii) lower densities and viscosities compared to the other analysed fluids; iii) higher latent heat of vaporization values at given temperature (see Table 5-1, Δh_{sat}, and Figure 5-1), which influence the heat transfer performance of the evaporator and the condenser heat exchangers. Nevertheless, it should be highlighted that this fluid mixture has a high-flammability classification (A3), as it also contains a HC compound (R600a).

Thus, pure fluids and also binary mixtures are both taken into account for sake of completeness in this study, since it cannot be excluded a priori that optimal or mid-term sub-optimal solutions to limit total carbon emissions could consist in blending current low-GWP fluids with the high performing HFC fluids. In addition, literature still lacks in studies investigating especially the potential of specific mixtures of R134a blended with HFOs, or other potential R134a substitutive mixtures.

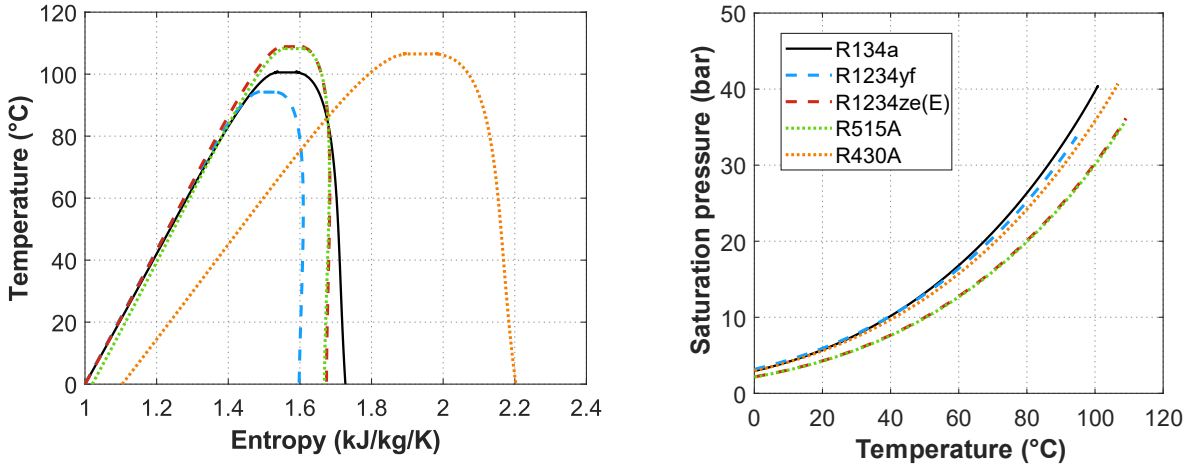

Figure 5-1 -Thermodynamic properties of the analyzed fluids at saturation ‡‡.

5.3 Expander performance and design optimization

Semi-empirical models of the pump and the expander presented in chapter 4 are employed here in order to analyze in detail how the different thermodynamic characteristics of the fluids could influence the performance of the volumetric machines at component level. An integrated expander-pump model has been applied to compare R134a to its low-GWP alternatives, R1234yf and R1234ze(E), for which the expander should be conceived.

Two kinds of analysis have been performed:

- a first one investigates the change in the performance of the expander when varying the working fluid, under following conditions: the temperature levels of the heat source and cold sink and the load connected to the expander generator have been considered the same, while for the feed pump rotating speed different cases have been examined (constant rotating speed, constant superheating degree).

‡‡ Curves obtained by means of the Refprop library [63]

- the second analysis aims at identifying the value of the volumetric expansion ratio that optimizes the electric power generation, for given design conditions.

5.3.1 Simulation approach

Schematic of the expander-pump integrated model

To evaluate the performance of the volumetric machines, a simple model was assembled by the integration of the two semi-empirical models describing the expander and pump (described in Paragraph 4.2.3 and 4.4). In order to focus on the volumetric machines only, the heat exchangers performance influence is neglected. In this way, the problem can be solved directly without iterations on the cycle pressures.

The pump and the expander sub-models have been integrated with the purpose of linking the evaporation pressure and the organic fluid mass flow rate, which are strictly correlated into micro-ORC systems, (as also demonstrated by the experimental trend of expander supply pressure as function of the flow rate presented in Figure 3-8 for the case study). This relationship is defined introducing a pump model that associates pump speed with outlet pressure.

A schematic of the integrated model is shown in Figure 5-2.

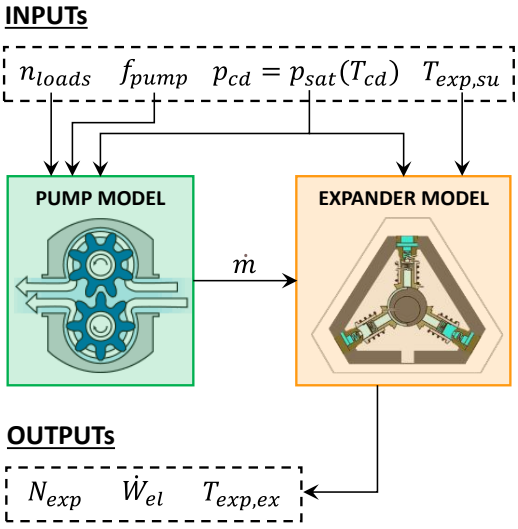

Figure 5-2 - Schematic of the integrated model.

The inputs of the model are the boundary conditions of the system and the thermodynamic cycle (the condensing temperature, T_{cd}, the expander supply temperature, $T_{exp.su}$, the feed pump frequency, f_{pummp}, and the number of resistive loads activated, n_{loads}): this choice allows to perform a fair comparison of the performance of the system when changing the working fluid, considering the same temperature levels, the same pump characteristic and the same system load. The condensing temperature determines the condensing pressure of the cycle, p_{cd}. The organic fluid mass flow rate at the outlet of the pump is equal to the mass flow rate that enters into the expander, in steady-state conditions. The outputs of the expander model coincide with the outputs of the

integrated model and they are the shaft rotational speed of the expander, N_{exp}, the electric power output, $\dot{W}_{el}$, and the expander outlet temperature, T_{ex}. Starting from these outputs it is possible to determine all the expander performance index of interest, evaluated in the following paragraphs.

Correction of the model parameters when changing the working fluid

According to paragraph 4.7, a procedure to simulate a fluid different from the reference one (R134a in this case), used to calibrate the semi-empirical models, is here applied. The parameters depending on the working fluid which need to be corrected are the expander heat transfer coefficients and the pump characteristic curve slope. A representative micro-ORC operating point (see Figure 3-8) is considered as an example, to evaluate how the model parameters vary by changing the working fluid and their influence over the performance of the machines. Results of the correction of the model parameters when changing the working fluid are reported in this paragraph to support the considerations made in the performance results.

Concerning the expander heat transfer parameters at the supply and exhaust pipe, a reference state at a pressure of 15 bar and a temperature of 75 °C was chosen to evaluate $(AU)_{su,ref}$, whilst $(AU)_{ex,ref}$ was evaluated at a pressure of 7 bar and a temperature of 50 °C. These parameters are corrected with respect to their original values (calibrated with R134a) by means of Eq. (4-25) and the results of the correction are reported in Table 5-2.

Table 5-2 - Corrected heat transfer parameters for the expander model.

Parameters	**Fluids**		
	R134a	**R1234yf**	**R1234ze(E)**
$(AU)_{su,ref}$ (W/K x 10^5)	5.65	6.38	6.53
$(AU)_{ex,ref}$ (W/K x 10^5)	9.23	10.19	10.13

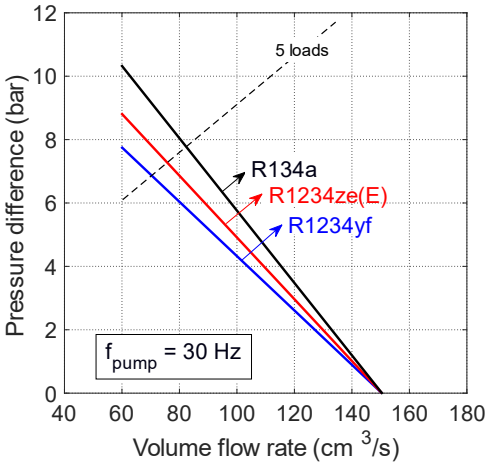

Figure 5-3 - Characteristic curves of the pump, for different working fluids.

Figure 5-3 instead highlight how the change of the working fluid affect the characteristic curves of the pump. The pump curve at a constant pump frequency equal to 30 Hz is reported as example.

The viscosity of the fluid has been evaluated, for all the analyzed fluids, in the reference condition of saturated liquid at 20 °C.

5.3.2 Performance prediction with low-GWP fluids

Analyzed conditions

A parametric analysis has been performed, for each analyzed fluid, setting the conditions of expander supply temperature, condensing temperature and electric load, as indicated in Table 5-3; the feed pump frequency has been varied in the range 25 - 45 Hz.

Table 5-3 - Reference case condition for R134a performance simulation.

Expander inlet temperature (T_{su})	75 °C
Condensation temperature (T_{cd})	15 °C
Activated loads (n_{loads})	5

Feed pump frequency for comparison (f_{pump})	35 Hz
Superheating degree for comparison (ΔT_{sh})	20 °C
Rotational speed for $r_{v,exp}$ optimization (N_{exp})	832 rpm

Then, two particular comparison cases between R134a and the new fluids, when feeding the same circuit, have been investigated, in order to analyze how the performance of the volumetric expander into an ORC circuit can actually depend on the pump regulation strategy and the fluid substitution:

- in one case the same pump frequency value (equal to 35 Hz) has been considered.
- in the second case the same superheating degree value (equal to 20 °C). In the latter case the pump speed is adjusted to reach a target value of superheating degree, which depends, at a given superheating temperature, on the evaporation pressure and thus on the flow rate of the organic fluid.

Feed pump frequency and superheating degree values, for the fluids performance comparison, are chosen (respectively equal to 35 Hz and 20 °C) as the most representative of the regular operation of the micro-ORC system.

Performance maps

The results are shown in the form of performance maps curves of electric power output (Figure 5-4) and expander total efficiency (Figure 5-5), which trend is in line with the performance maps presented and commented in paragraph 4.2.3 for R134a. In Figure 5-4 and in Figure 5-5, operating points at the same pump frequency value are indicated by circular dots, whilst points at the same superheating degree are highlighted by square dots.

The results highlight first of all that R134a proves to be the most performing fluid among the analyzed ones, for all the examined scenarios. However, a best substitute can be identified between the two alternatives depending on the case:

- For given value pressure ratio, the electric power output decreases significantly when using R1234yf (- 24 %) and R1234ze(E) (- 44 %) in comparison with the R134a value. The expander

total efficiency maximum value is obtained with R134a equal to 42 %, lower values of the maximum total efficiency are achieved respectively with R1234yf (37 %) and R1234ze(E) (35 %). It must be noticed that being different the evaporation pressure and the condensation pressure values of the fluids considering the same temperature levels, the peaks of the total efficiency curves are not obtained at the same pressure ratio for the three analyzed fluids, as shown in Figure 5-5.

- for given pump frequency conditions of 35 Hz, the maximum electric power output is achieved with R134a, followed by R1234ze(E) (see circular markers in Figure 5-4). The performance derating of the expander when replacing R134a with low GWP fluids is also shown by the trends of the total efficiency in Figure 5-5. Indeed, the total efficiency achievable with R1234yf also decreases compared to R134a value, the same occurs for R1234ze(E). Even if R1234ze(E) allows to generate a higher value of electric power output compared to R1234yf, the latter achieves higher total efficiency value, in the reference conditions
- when comparing the fluids at the same superheating degree, the pressure ratio value becomes quite similar for all the fluids. The highest electric power output is achieved again with R134a, then by R1234yf instead of R1234ze(E). The same reduction in the expander performance is found in the total efficiency map (in Figure 5-5).

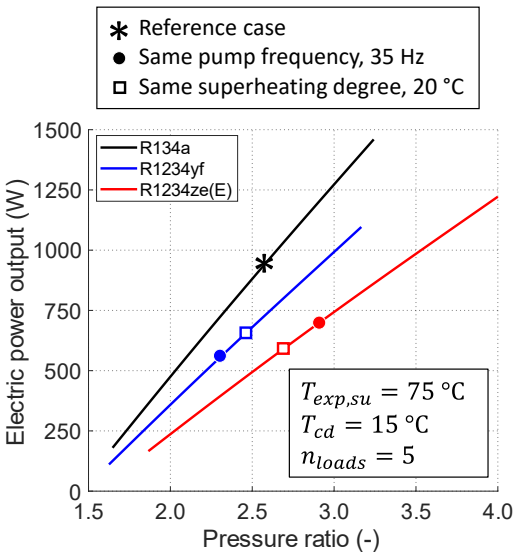

Figure 5-4 - Electric power vs pressure ratio: effect of the fluid variation.

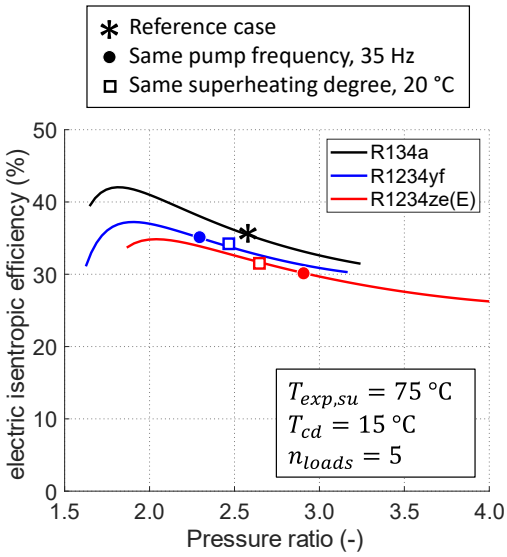

Figure 5-5 - Expander total efficiency vs pressure ratio: effect of the fluid variation.

For sake of completeness, Figure 5-6 and Figure 5-7 relate respectively the pressure ratio and the superheating degree to the pump frequency. As expected, the pressure ratio increases with the pump frequency, since the evaporating pressure increases (see Figure 5-6), while the condensing pressure is constant, equal to the value imposed by the cold source temperature. Being constant the expander supply temperature, the superheating degree instead decreases while the pump frequency increases (Figure 5-7). These data are important to comment more in detail the loss contribution that determine the above presented performance maps trends.

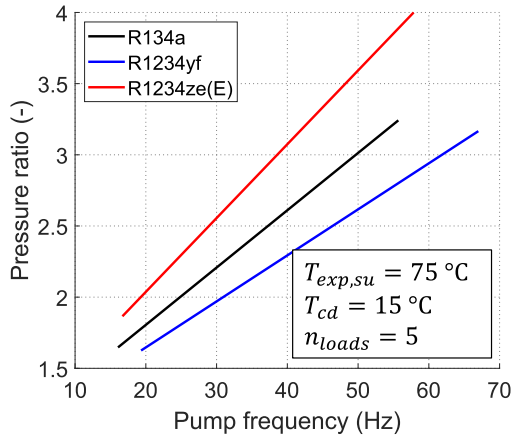

Figure 5-6 - Pressure ratio vs pump frequency: effect of the fluid variation.

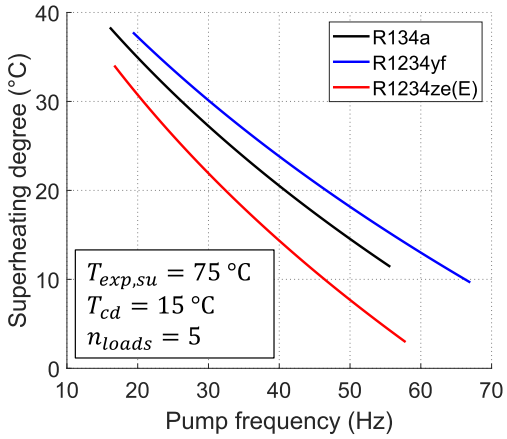

Figure 5-7 - Superheating degree vs pump frequency: effect of the fluid variation.

Contribution of losses

In detail, the main factors that influence the expander performance discussed in this paragraph, and they are:

- the saturation pressure (influencing the enthalpy drop available through the expander).
- the viscosity (mainly affecting the leakage losses at the pump meatus and thus the elaborated mass flow rate).
- the heat transfer coefficients values (influencing the ambient heat loss).
- the vapor density (affecting the leakage losses during the expansion process).

The loss terms affecting the expander performance have been calculated by means of the proposed expander model, which accounts for valve pressure drop, internal leakage, under/ or over-expansion, heat transfer, friction and electro-mechanical conversion losses. The relative importance of the different losses affecting the expander performance, is represented in the pie charts of Figure 5-8, as percentage of the isentropic power theoretically available for the expansion process ($\dot{W}_{is}$). The isentropic power values and other quantities of interest are reported in Table 5-4 for comparison.

The fluids that exhibit higher isentropic enthalpy drop are R134a and R1234ze(E), with quite similar values. However, the fluid that presents the highest expansion isentropic power is R134a (2620 W), due to the highest mass flow rate at the expander inlet. Indeed, R134a is the fluid with the maximum liquid viscosity (2.07 x10^{-4} Pa·s) and thus the minimum leakage loss at the pump meatus affecting volumetric flow (see Figure 5-3).

The heat losses are strongly related to the heat transfer coefficients, which are considered into the model by means of the heat transfer parameters (listed in Table 5-2). As expected, higher ambient heat loss results from higher values of the heat transfer parameters, therefore the percentage heat loss of the low-GWP fluids is higher than that of R134a.

Both internal leakage and pressure drops across the valves depend on the density of the vapour entering the expander, as described in Eq. (4-21). Equation shows the inverse proportionality

correlation between the pressure drop affecting the enthalpy drop, Δh, and the vapour density. The leakage mass flow rate is calculated, using an equation similar to Eq. (4-21). In this case, instead, equation shows the proportionality correlation between the internal leakage and the vapour density. On the basis of these correlations, fluids with higher vapour density (as HFOs, if compared to R134a, see Table 5-1) exhibit lower pressure drop losses, but also higher internal leakages, as shown by the pie charts of Figure 5-8.

The difference between the isentropic power and the sum of all the loss contributions finally corresponds to the electric power output value. The percentage of generated electric power over the total efficiency is equal to the expander total efficiency value.

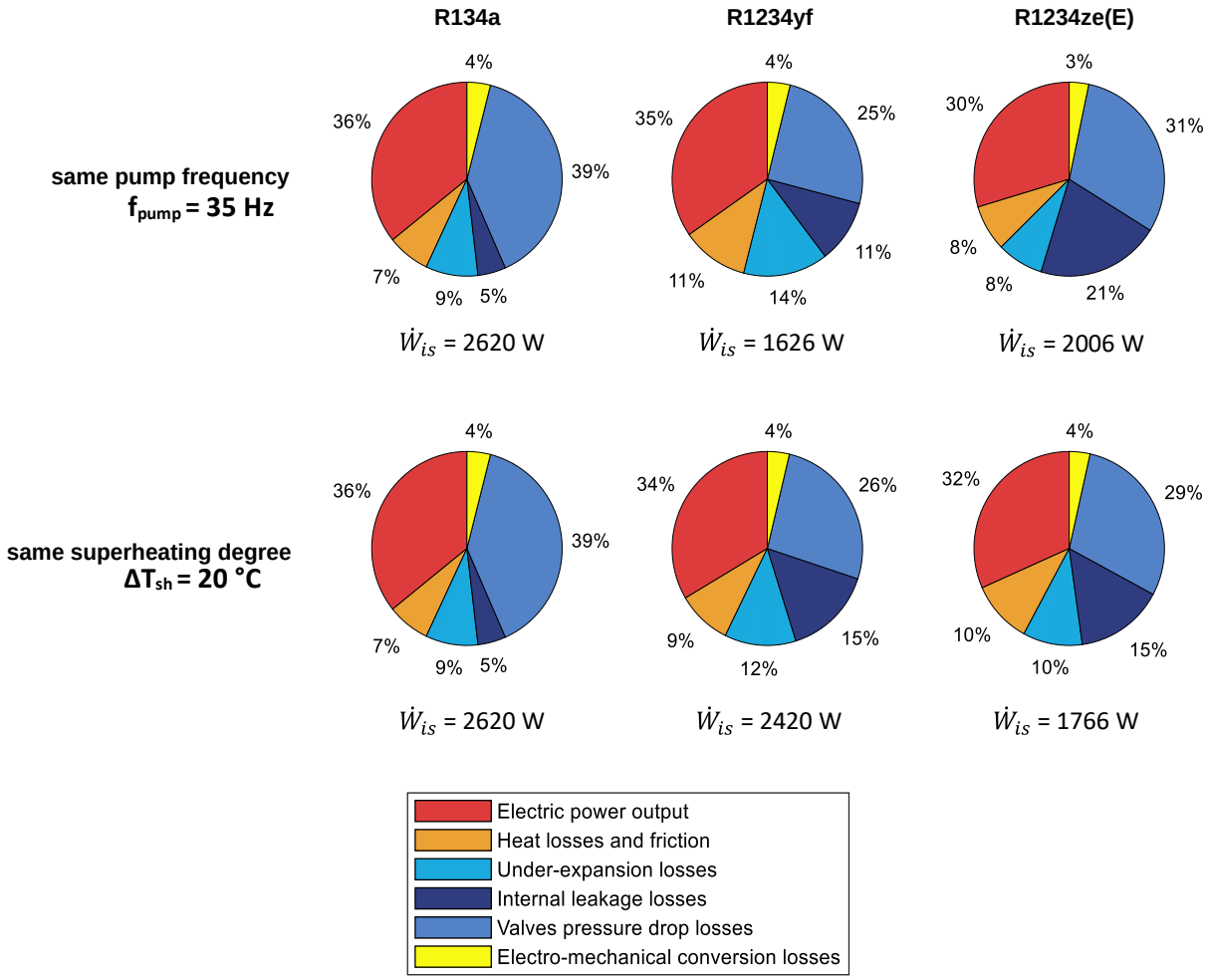

Figure 5-8 - Analysis of loss contributions affecting the expander performance. Values are expressed as percentage of the theorical expansion isentropic power ($\dot{W}_{is}$).

Table 5-4 - Fluids comparison - Percentual variation compared to the reference case in parenthesis.

	Reference case	Same pump frequency comparison		Same superheating degree comparison	
	R134A	**R1234yf**	**R1234ze(E)**	**R1234yf**	**R1234ze(E)**
Pump frequency, f_{pump} (Hz)	35	35	35	40	30
Superheating degree, ΔT_{sh} (°C)	20	23	15	20	20
Evaporation pressure, p_{su} (bar)	14.4	13.6	12.6	14.6	11.2
Condensation pressure, p_{cd} (bar)	5.7	5.9	4.3	5.9	4.3
Isentropic enthalpy drop, Δh_{is} (kJ/kg)	21.3	17.3 (-19 %)	22.2 (+4 %)	18.4 (-14 %)	20.3 (-5 %)
Mass flow rate, $\dot{m}$ (kg/s)	0.123	0.094 (-24 %)	0.109 (-11 %)	0.109 (-11 %)	0.087 (-29 %)
Vapor density (kg/m³)	62.6	66.9	62.0	73.5	53.3
Expansion isentropic power, $\dot{W}_{is}$ (W)	2620	1626 (-38 %)	2420 (-8 %)	2006 (-23 %)	1766 (-33 %)
Heat transfer and friction (W)	183	179	194	181	177
Other losses (W)	1494	878	1500	1143	1024
Total losses (W)	1677	1057	1694	1324	1201
Electric power output, $\dot{W}_{el}$ (W)	943	569 (-40 %)	726 (-23 %)	682 (-28 %)	565 (-40 %)
Expander total efficiency, η_{exp} (%)	36	35	30	34	32
Exhaust expander temperature, T_{ex} (°C)	39.5	47.1	39.2	44.4	43.8
Shaft speed, N_{exp} (rpm)	832	478	750	534	627

The comparative analysis, among R134a substitutes, at the same pump frequency identifies in the R1234ze(E) the best candidate to maximize the electric power output and minimize the environmental impact at the same time; conversely, comparison at the same superheating degree suggests R1234yf as a better choice. This is due to the different evaporation pressure assumed by the fluids, thus affecting the available amount of expansion isentropic power. Indeed, at the same pump frequency, R1234ze(E) presents higher pressure ratio and isentropic power, if compared to R1234yf. At the same superheating degree, the pressure ratio values are very similar, but the isentropic power is higher for R1234yf.

In conclusion, it must be highlighted that R134a presents higher performance than HFO fluids for all the examined conditions, thanks to both the higher isentropic power and the higher total efficiency values. However, whilst the electric power is remarkably higher for R134a compared to the other fluids, the total efficiency among the different fluids is not that different. This is because isentropic power available for most of the HFOs cases is lower than that available for R134a, as well as the total amount of lost power (see Table 5-4). Finally, it should be also highlighted that the expander operates with reduced shaft speed (N_{exp}) values (see Table 5-4) in case of HFOs, in comparison with the reference R134a working condition.

5.3.3 Built-in volume ratio optimization

The built-in volume ratio parameter ($r_{v,exp}$) corresponds to the volumetric expansion ratio of the machine, and it is defined as the ratio between the inlet volume at the end of the expansion and the volume at the end of the admission stroke. For the case study, $r_{v,exp}$ has been optimized for each analyzed fluid, at given reference conditions corresponding to the reference operating point (as indicated in Table 5-3).

The trend of the specific work, the elaborated mass flow rate (Figure 5-9) and the electric power output (Figure 5-10), are plotted against the intake stroke ratio, for a value of the expander shaft speed equal to 832 rpm.

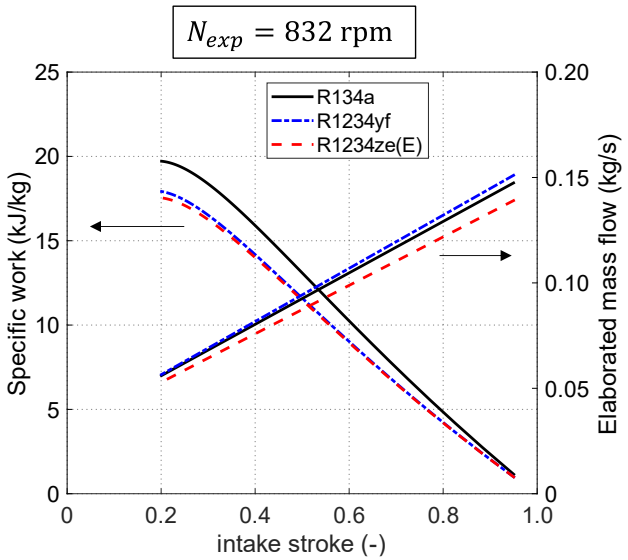

Figure 5-9 - Specific work and mass flow rate elaborated by the expander vs pressure ratio.

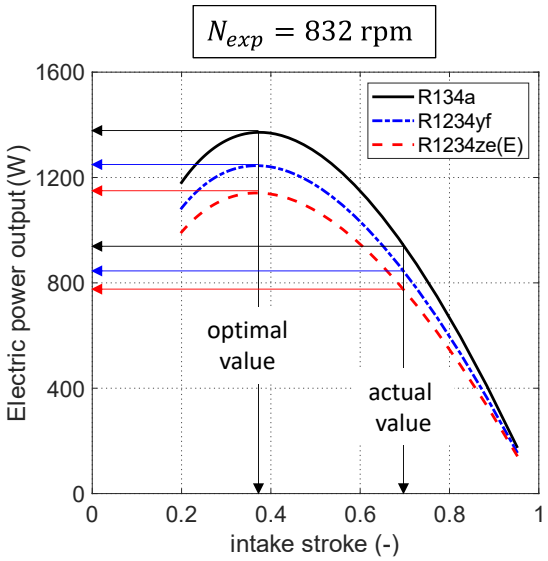

Figure 5-10 - Electric power output vs pressure ratio.

The intake stroke ratio, named α, represents the piston relative swept volume at the moment when the intake valve closes, defined as:

$$\alpha = \frac{V_2 - V_1}{V_s} \tag{5-1}$$

Thus, α can be expressed as a function of $r_{v,exp}$ according to:

$$\alpha = \frac{1}{r_{v,exp}} \cdot \frac{1 - r_{v,exp} \cdot \gamma}{1 - \gamma} \tag{5-2}$$

where γ is a geometrical parameter:

$$\gamma = \frac{V_1}{V_1 + V_s} \tag{5-3}$$

Since the stroke displacement of the expander in study is equal to V_s = 230 cm³ and the clearance volume is equal to $V_1 = V_0 = 2.32 \cdot 10^{-2}$ cm³ (see Table 4-2), the intake stroke ratio α can be approximated as the inverse of the built-in volume ratio, neglecting the clearance volume:

$$\alpha = \frac{1}{r_{v,exp}} \tag{5-4}$$

The bell-shaped curve of the electric power results by the combination of the opposite trends of the specific work and the elaborated mass flow rate, since the electric power output ($\dot{W}_{el}$) is proportional to the product of the two quantities. The specific work decreases when α increases, because of the under-expansion losses; conversely, the elaborated mass flow rate increases with α, because for a longer intake stroke more fluid has time to enters into the cylinder. In this case study, the maximum value of the electric power output is observed for α around 0.37, corresponding to a built-in volume ratio, $r_{v,exp}$ equal to 2.7, very close for all the three considered fluids. On the other hand, the current value of α is close to 0.69, corresponding to a value of $r_{v,exp}$ of 1.46.

The results show that an increase of the built-in volume ratio would lead to the optimal operation of the expander for the considered boundary conditions, typical of low temperature applications. This result could be expected by observing Figure 5-5, which shows that the current isentropic efficiency peak (obtained with the current built-in volume ratio) is shifted towards lower pressure ratio compared to the one associated to the considered boundary conditions. Figure 5-10 shows that the optimization of the built-in volume ratio for the case study could increase significantly the electric power output by 41 % for R134a and by 43 % for R1234yf and R1234ze(E), if compared to the producible electric power of the current configuration.

A comparison between the indicator diagrams obtained with the optimal α value and the one obtained with the reference α value are reported in Figure 5-11, which highlights that reducing the intake stroke significantly decreases the under-expansion losses. Actually, a certain degree of over-expansion is preferred in order to ensure the exploitation of all the available pressure head.

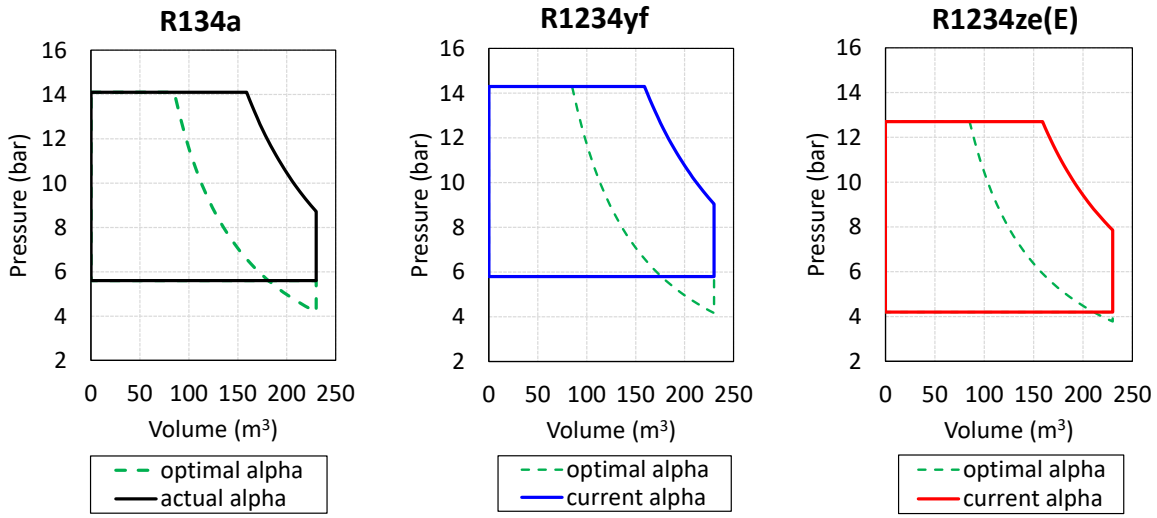

Figure 5-11 - A comparison between the indicator diagrams obtained with the optimal α value and the one obtained with the reference α value.

Finally, in Table 5-5 the main performance results of the optimization of the built-in volume ratio are compared with those related to reference value of $r_{v,exp}$. The percentual increment of the expander efficiency is expected to be higher than the electric power one: indeed, the isentropic power, denominator of the efficiency expression, decreases due to the reduction of the mass flow rate, while the isentropic specific work remains the same, being the inlet and exhaust pressures equal to the reference case. Results of the simulation show potential remarkable efficiency gain of approximately 40 percentage points with respect to the case of $r_{v,exp}$ not optimized, similar for the three fluids. The maximum value is achieved in this case with R1234yf, around 83%. Even if an increase in the expander efficiency is expected, the values of total efficiency, obtained by the α optimization are quite optimistic. Such high values of the expander efficiency are indications that some simplifications are introduced in the expander model. First of all, the supply valve real opening behavior has been modelled in a simplified way: the expander model assumes the instantaneous opening and closing of the valves. Real valve behavior would probably cause a loss of actual mass flow rate elaborated by the expander; indeed, as demonstrated by [92] the valve characteristics play an unneglectable role on the reciprocating machine operation. Nevertheless, the procedure proposed is intended to demonstrate the importance of the optimization of the filling performance of the expander, in order to achieve the best overall performance of the machine. For this purpose, a modification of the valve timing would be required [92][93] in order to optimally exploit the external heat sources, regardless of the working fluid adopted.

Table 5-5 - Results of the built-in volume ratio optimization.

	R134a		**R1234yf**		**R1234ze(E)**	
	Reference α = 0.69	**Optimal α = 0.37**	**Reference α = 0.69**	**Optimal α = 0.37**	**Reference α = 0.69**	**Optimal α = 0.37**
Mass flow, $\dot{m}$ (kg/s)	0.123	0.082	0.126	0.084	0.116	0.078
Isentropic power $\dot{W}_{is}$ (W)	2621	1747	2177	1452	2091	1406
Electric power, $\dot{W}_{el}$ (W)	943	1334	846	1211	775	1111
Expander total efficiency (%)	36	76	39	83	37	79

5.3.4 Conclusions

The purpose of this chapter was to investigate how the performance of a volumetric expander working in a low temperature micro-ORC system, would change when using the R134a low global warming potential alternatives (R1234yf and R1234ze(E)) as working fluids. To this aim, the analysis was conducted on the reference case study of a the three-piston prototype currently installed in a micro-ORC test bench at the University of Bologna.

Two comparison cases between R134a and the new fluids, when feeding the same circuit, have been investigated: the first case considers the same pump frequency, while the second case considers the same superheating degree value. The comparative analysis, at the same pump frequency, identifies in the R1234ze(E) the best candidate to maximize the electric power output and minimize the environmental impact at the same time; conversely, comparison at the same superheating degree suggests R1234yf as better choice. However, R134a proves to be the most

performing fluid among the analyzed ones, for all the examined case. Results of the analysis highlight that the performance of a volumetric expander into an ORC circuit actually depends on the pump regulation strategy and the fluid substitution decision should take into account also this aspect.

In addition, even if the analysis is applied to a reference case study, findings related on how the fluid properties could affect expander and pump performance are generalizable. In particular, this study highlights that the main factors that affect the expander performance, when substituting R134a with its low-GWP alternatives, are: (i) the saturation pressure (influencing the enthalpy drop available through the expander), (ii) the viscosity (mainly affecting the leakage losses at the pump meatus and thus the elaborated mass flow rate), (iii) the heat transfer coefficients values (influencing the ambient heat loss), (iv) the vapor density (affecting the leakage losses during the expansion process). Relative importance of the different losses affecting the expander performance, is discussed.

Semi-empirical model of the expander also allows to account for the influence of geometrical aspects, such as the built-in volume ratio, over the expander performance. Thus, the proposed integrated model has been used to optimize the built-in volume ratio, modifying the intake stroke ratio, in order to achieve the best performance of the expander under investigation for all the analyzed working fluids. With this final step, the intention was to propose a quite simple methodology to identify the optimal intake stroke ratio value; the same procedure is indeed applicable to different displacement expanders for optimizing the volumetric performance, depending on the specific working conditions the machine is required to work with. Results highlight that the optimization of the built-in volume ratio could lead to a substantial increase of the expander performance, with an estimated gain of electric power output around 42 %, similar for the three fluids. Thus, a modification of the valve timing would be required in order to optimally exploit the reference external heat sources, regardless of the working fluid adopted.

5.4 Environmental impact assessment

This paragraph is dedicated to the analysis of the greenhouse impact of micro-ORC systems, which can derive from the use of low-GWP fluids, in place of HFCs, for the low-temperature waste-heat-recovery application. The first step consists in assessing the whole micro-ORC system performance when working with low-GWP substitutes of R134a in a realistic application. Both pure fluids and mixtures, preliminary compared in paragraph 5.2 are considered for the purpose. The performance of the system is evaluated by means of the entire micro-ORC model described in chapter 4.

The second step comprises the simulation of the plant behavior over a typical annual operation, in order to determine the yearly energy production and related greenhouse gas (GHG) emissions. A comprehensive methodology for the environmental impact assessment is here proposed, to account not only for direct greenhouse emissions but also for indirect contribution. More in detail, the examined operating conditions refer to an existing micro-ORC operation, installed at a pool center [94], conceived to exploit a geothermal liquid-dominated well hot source.

5.4.1 Greenhouse gas emissions estimation method

The total GHG emissions from an ORC system can be estimated by taking into account two main terms, namely direct emissions and indirect emissions.

Direct emissions, Em_{direct}, include the environmental impact of leakage of refrigerant, which can occur during system operation and servicing. In particular, the maintenance procedures cause small leakages from the needle valves used for extracting the fluid, from the component that needs to be repaired or replaced. However, despite the F-Gas regulation recommends the verification of all the seals of plant containing refrigerants, phenomena of small leakages also during the plant operation are very difficult to avoid completely, particularly in small scale plants, which usually are not provided with continuous detection systems. Thus, this contribution of emission should not be neglected and can be expressed as:

$$Em_{direct} = m \cdot LR \cdot GWP \tag{5-5}$$

where m is the system's fluid charge estimated by means of equations proposed in paragraph 4.8, LR, the annual leak rate and, GWP, global warming potential of the working fluid.

A second contribution of emission, not yet considered in the analysis of low-GWP fluids potential, is the one related to indirect GHG emissions. In this study, this term is included to compare the fluids. The indirect GHG emissions term ($Em_{indirect}$) considers the energy production gap (E_{gap}) as the effect of operating the micro-ORC with fluids with lower or higher thermodynamic performance than the reference fluid (R134a). Considering a constant request electric power, the energy gap needs to be supplied by a different energy system, or it must be purchased from the electric grid. This amount of supplied energy is in general associated to an additional contribution to CO_2 emission, which depends on the emission factor (β, expressed in kilograms of CO_2 per megawatt hour of energy produced) related to the technology employed to produce the energy gap. In case the electricity is purchased from the grid, β corresponds to the average emission of the fleet of machines in the considered area of the world. Ultimately, the indirect emissions, $Em_{indirect}$, are calculated as the product between the energy gap, E_{gap}, and the emission factor, β, associated to the alternative energy provider:

$$Em_{indirect} = E_{gap} \cdot \beta \tag{5-6}$$

where E_{gap} is given by the difference between the energy produced by using the most performant fluid (E_{max}) and the energy produced by using the fluid in exam (E).

$$E_{gap} = E_{max} - E \tag{5-7}$$

With the aim of evaluating the ORC annual operation, all the energy terms are calculated on the yearly basis.

5.4.2 Case study

The investigation on the micro-ORC system performance and its related GHG impact has been carried out under given boundary conditions, considering a certain scenario, as defined below, in terms of: i) hot source temperature and flow rate annual profiles; ii) cold source temperature and flow rate annual profiles; iii) leak rate and reference emission factor parameters. Different operating fluids have been applied to the given scenario.

The case study of a real geothermal application at a swimming pool center [94] has been investigated in this study; even if the same approach can be applied to ORC operated with different heat sources, profiles and time horizons. The heat source consists in a geothermal well which supplies liquid water at a barely constant temperature close to 60 °C with a volume flow rate of 22 m^3/h. The cold water sink is the swimming pool heating circuit, with inlet water temperature nearly equal to 18 °C an average volume flow rate of 25 m^3/h; because of the negligible dependency of the water temperature on the ambient conditions, the latter is considered constant during the year.

The ORC pump feed frequency value (thus, the pump speed value) is considered adjusted to reach the evaporating pressure that leads to the best ORC performance (best net power output) at the given boundary conditions. A minimum superheating degree of 3 °C is imposed as constraint. Thus, a different optimal pump frequency value is considered for the ORC when using different fluids. The subcooling degree is chosen equal to 4 ° C, according to the subcooling degree value observed during operation of the micro-ORC system.

Finally, 5 activated loads absorbing the expander power output are considered, to receive electric power until 3 kW. The expander built-in volume ratio is assumed equal to its optimized value identified in paragraph 5.3.3.

5.4.3 Results: performance

The representative working point of the ORC operation during the year is examined, to discuss the performance when using different fluids. Main indexes of interest for the analysis are compared by means of the radar plot in Figure 5-12; they comprise: i) the expander electric power output ($\dot{W}_{exp}$); ii) the pump absorbed electric power ($\dot{W}_{pp}$); iii) the evaporator input thermal power ($\dot{Q}_{ev}$); iv) the ORC net efficiency (η_{net}); v) and the fluid global warming potential (GWP). Other operating conditions, such as the pump feed frequency, the working fluid flow rate, the superheating degree, the evaporating and condensing pressure and their ratio are reported in Table 5-6.

When comparing R134a with the other fluids containing HFOs, results show that the most performing fluid is the reference fluid, R134a (see Figure 5-12a). Indeed, it provides the maximum power production (1485 W) and the best net efficiency (7.5 %). R1234yf is the closest pure fluid to R134a; nevertheless, it exhibits a lower electric power output (-22 %) but similar pump power consumption (about 390 W). Main factors determining the performance drop introduced using HFO fluids can be identified in: (i) the lower pressure ratio (leading to smaller enthalpy drop available through the expander); (ii) the lower viscosity (mainly affecting the leakage losses at the pump meatus and thus the elaborated mass flow rate), as analyzed in detail in the previous paragraph 5.3.2.

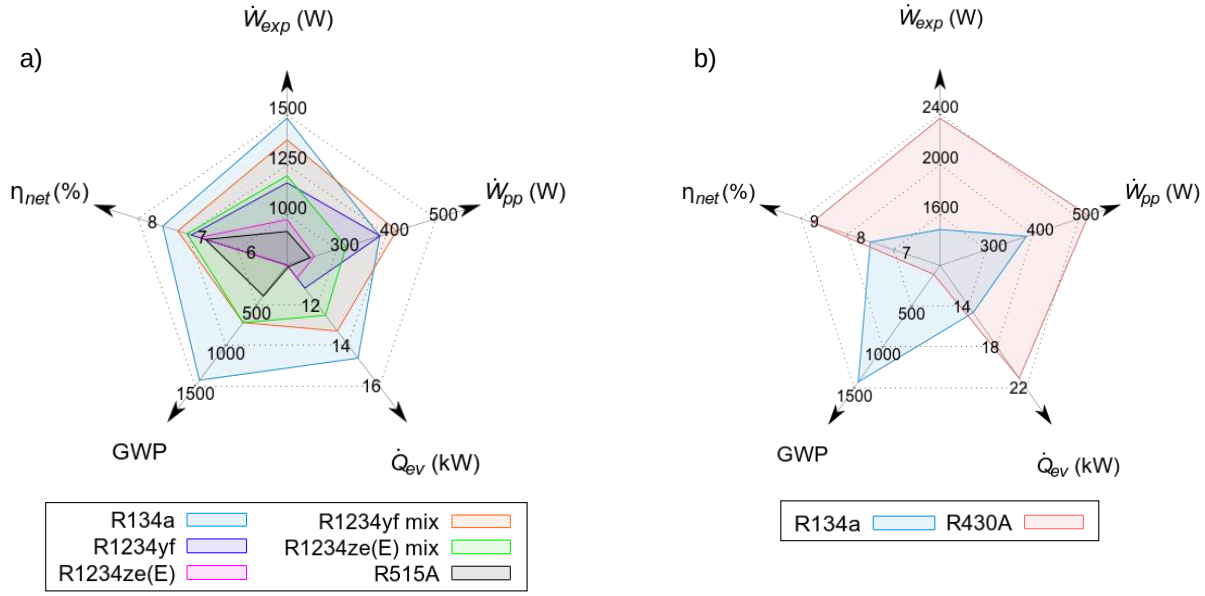

Figure 5-12 - Micro-ORC system and components performance: a) comparison of R134a with HFO-based fluids; b) comparison of R134a with R430A.

Table 5-6 - Micro-ORC system thermodynamic operating conditions – fluids comparison.

Parameters \ Fluids	**R134a**	**R1234yf**	**R1234ze(E)**	**R1234yf mix**	**R1234ze(E) mix**	**R515A**	**R430A**
Pump feed frequency, f_{pp} (Hz)	28	31	22	31	25	21	37
Working fluid flow rate, $\dot{m}_{wf}$ (g/s)	91.4	86.1	70.0	92.8	80.5	69.5	82.9
Superheating degree (°C)	3	3	3	3	3	3	3
Evaporating pressure (bar)	15.6	15.3	11.8	16.2	13.9	14.6	11.7
Condensing pressure (bar)	7.5	7.7	6.5	7.8	7.0	7.4	6.4
Pressure ratio (-)	2.08	1.98	1.82	2.09	2.00	1.96	1.82

The fluid providing highest departure from R134a performance is R515A, showing both lower power (-38 %) and lower pump consumption, but also lower net efficiency (a reduction equal to about 1 percentage point occurs). The energy performances of R1234ze(E) are comparable to the ones of R515A, given to their very similar composition. However, it must be taken into account that, from the environmental point of view, R1234ze(E) shows very low GWP values (6 vs 387 for R515A), but, on the other hand, also a higher flammability risk than R515A. The overall performance obtained with R1234yf mix and R1234ze(E) mix are intermediate between the ones of the two

composing pure fluids; in comparison with R515A, these two HFO/HFC mixtures provide higher efficiency values but also higher GWP values.

Comparison between R430A and R134a (see Figure 5-12b), shows instead a benefit achievable with the substitute fluid in terms of energy performance. The net electric efficiency value increases of more than one percentage point, while the calculated electric power output significantly rises (up to almost 2.4 kW), in comparison with the reference R134a value (equal to 1.5 kW). This is mainly imputable to the higher enthalpy drop available at the expander (21 kJ/kg against 15 kJ/kg), but also to the better heat transfer properties of the R430A, which allows to recover a larger amount of heat at the evaporator for a given available hot source temperature and flow rate and given the ORC components size (see thermodynamic diagram in Figure 5-13). Indeed, the calculated $\dot{Q}_{ev}$ value in case of R430A is almost 3/2 of the reference value (it is equal to 21 kW vs 15 kW in case of R134a case). Similar organic fluid flow rate values for R430A and R134a cases (83 g/s and 91 g/s, respectively, see Table 5-6) have been determined, as function of the operating pressure and densities and the geometric characteristics of the circuit, according to the model described in the previous paragraphs. The comparison shows that this high performing R430A solution provides approximately a 1/10 reduction in GWP, but unfortunately also a high flammability risk (it is the only considered fluid with A3 classification), which makes it not equally compatible, as the other selected options, with this ORC application.

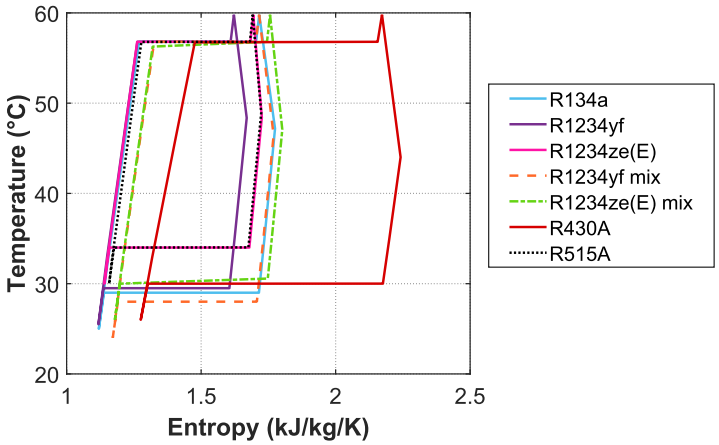

Figure 5-13 - Thermodynamic cycles by varying the working fluids.

The resulting yearly electric energy production in the considered operating scenario is provided in Table 5-7, for the different assessed fluids. Indirect and direct GHG emissions (via Eqs. (5-5) and (5-6)) are affected by two key calculated quantities of the micro-ORC system also shown in Table 5-7, namely: the yearly electric energy gap and the system fluid charge.

The R134a base case fluid shows a yearly net electric energy production value (9621 kWh) larger than the values obtained by the HFO/HFC blends; a decrease occurs of about 13 % and 20 %, respectively for the R1234yf mix and the R1234ze(E) mix; an additional decrease of almost 12 %, 18 % and 24 % is obtained respectively with R1234yf, R1234ze(E) and R515A. R134a yearly energy production has been considered as reference (E_{R134a}), when applying Eq. (5-7), in order to compute

the E_{gap} value. The highest E_{gap} value is calculated in case of R515A. On the contrary, R430A presents a negative E_{gap} value, because of its better performance with respect to the R134a case.

The calculated value of the fluid charge, for the ORC operating with R134a, is equal to 28.8 kg, which is in line with experimental experience over the reference test bench. Fluid charge values for the other fluids are slightly different, because of the different ORC thermodynamic setup (see Table 5-7) and due to different values of density of the fluids (see Table 5-1).

Table 5-7 - ORC energy performance and fluid charge, affecting GHG emissions assessment – fluids comparison.

Parameters \ Fluids	**R134a**	**R1234yf**	**R1234ze(E)**	**R1234yf mix**	**R1234ze(E) mix**	**R515A**	**R430A**
Yearly net electric energy, E (kWh)	9621	6777	6323	8378	7684	5876	16182
Yearly electric energy gap, E_{gap} (kWh) $(E_{gap} = E_{R134a} - E_{fluid})$	0	2843	3298	1243	1937	3745	-6562
Working fluid charge, m (kg)	28.8	27.4	27.1	28.9	28.5	27.1	20.5

5.4.4 Results: environmental impact assessment

The environmental impact of the micro-ORC system is firstly evaluated for a reference case study, assuming:

- A leak rate equal to 2 % as characteristic value provided for Residential and Commercial A/C, including Heat Pumps, by IPCC Good Practice Guidelines and Uncertainty Management in National Greenhouse Gas Inventories (2000) [95];
- An emission factor of the substitute energy provider (β) equal to 460 $kgCO_2/MWh$, which corresponds to the average EU-27 emission factor for electricity consumption, provided by EU 2017 technical report about default emission factors [96].

However, since detailed data are not available for *LR* in micro-ORC applications, for sake of completeness, parametric analysis by varying the leak rate and also the emission factor values are proposed, to include different possible scenarios. Then, an additional sensitivity analysis concerning the influence of the concentration of R134a into the R134a/HFO mixtures is presented. Results of the GHG impact assessment are presented in terms of specific direct, indirect and total yearly equivalent CO_2 emissions. Specific emissions are here expressed per unit of produced electric energy (E).

The calculated specific emissions of the micro-ORC system, when working with the different fluids, are provided in the bar plot of Figure 5-14. As first important result, it must be observed that surprisingly, Figure 5-14 reveals that HFOs and their mixtures do not reduce the overall CO_2 equivalent emissions, even if the direct emission contribution related with GWP is reduced. Actually, the use of R1234yf increases the total specific emission by 148 % and R1234ze(E) even by 208 %.

The two mixtures with HFOs and R134a exhibit intermediate values of total emission, compared to the pure fluids composing the mixtures. Total emissions related to the use of pure R134a are associated to only direct emissions, equal to 78 $kgCO_2$/MWh. Conversely, total emissions related to the use of pure HFOs are basically due to the indirect emission term, since the direct emissions contribution is limited (about 0.08 $kgCO_2$/MWh) due to the associated low GWP values.

The R515A case leads to the highest specific emission, up to 330 $kgCO_2$/MWh, due to remarkable indirect term and not negligible direct term, given both the low energy performance of the micro-ORC and still relatively high GWP of the fluid. For sake of comparison, specific emissions associated to the flammable R430A case are provided in the same figure, even if this fluid has been excluded in the further investigation, for the safety issue. As shown in Figure 5-14, the HFC/HC R430A mixture would provide at the same time: i) a limited direct GHG emission term, due to the reduced GWP in comparison with R134a, and ii) a negative indirect emission term, due to improved energy performance (negative energy gap), resulting in a net gain in total equivalent CO_2 emission.

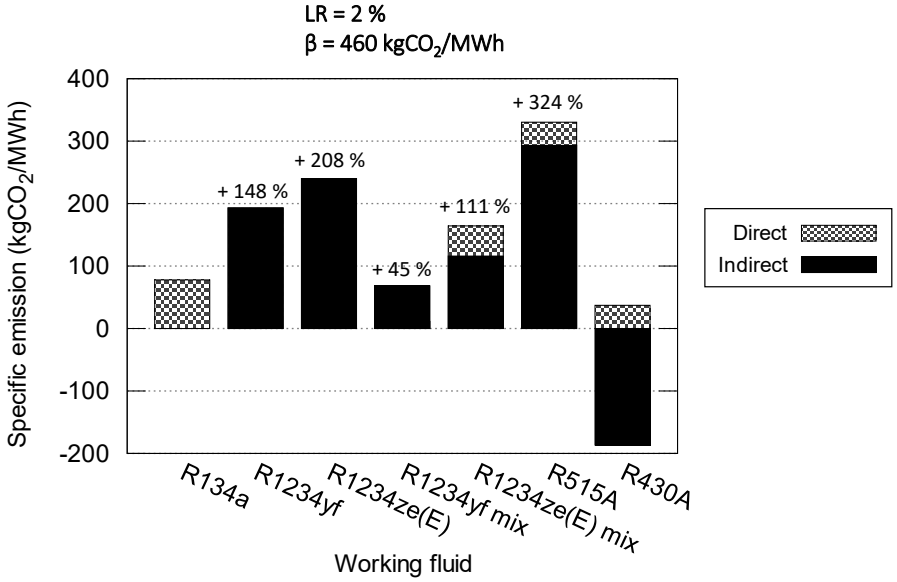

Figure 5-14 - CO_2 equivalent emissions – fluids comparison (percentage values are related to R134a total emissions).

Although this conclusion can be valid when considering an annual leak rate equal to 2 %, things can change in case of higher leak rate. Indeed, direct emissions scale up proportionally to the leak rate, and at higher *LR* values the direct contribution becomes more decisive than the indirect one. Values of the leak rate up to 15% have been explored; higher leak rate instead would not be realistic since representative of large centralized systems (17 % for example represents the typical annual leak rate associated to Centralized Supermarket Refrigeration Systems [95]). Parametric analysis demonstrates that emissions are quite sensitive to the leak rate (see Figure 5-15) and the sensitivity (i.e. the curve slope) increases in particular with the fluid GWP. For instance, for the R134a case, specific emission at *LR* = 15 % are more than seven times the specific emission at *LR* = 2%. On the other hand, specific emissions for the HFOs pure fluids remain almost constant by varying the leak rate, because the direct contribution does not change significantly. It must be noticed that, in most

of the cases, the R134a specific emission curve crosses the HFOs' curve around a leak rate value of 5 %, which can represent a so called "inversion point". Above the inversion point, the R134a specific emission becomes higher than the HFO's ones and the considerations made for LR = 2 % are no more valid. For what concerns R515A, this "inversion point" is shifted at around LR = 14 %. In general terms, knowing the actual annual leak rate of the system is of utmost importance in order to perform a correct evaluation of the global warming impact of the micro-ORC.

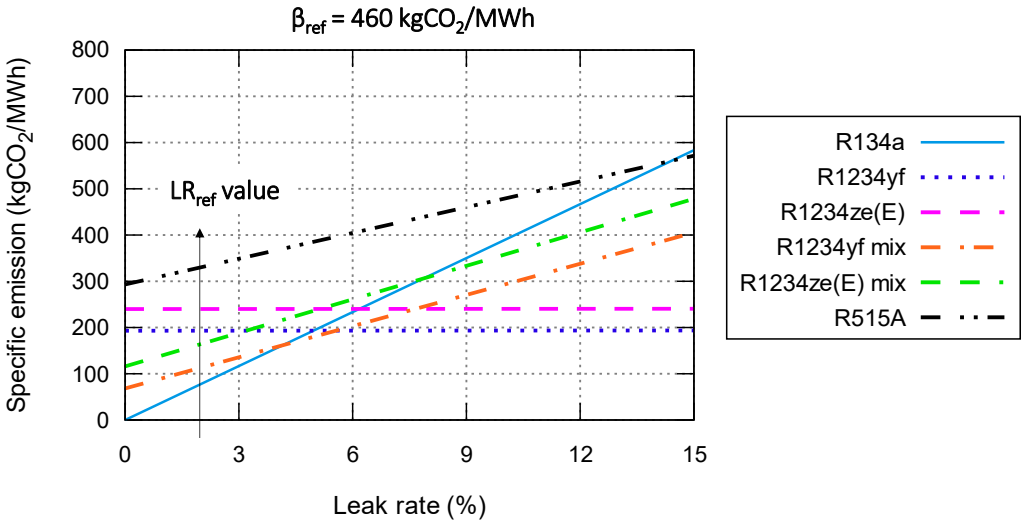

Figure 5-15 - CO_2 equivalent emissions as function of the leak rate – fluids comparison.

Another factor of influence is the reference emission factor β (see Eq. (5-6)), which depends on the energy mix providing the energy gap. A parametric study has been performed (Figure 5-16), exploring β values ranging between the lowest (23 $kgCO_2/MWh$ - Sweden) and the highest (1191 $kgCO_2/MWh$ - Poland) emission factor values documented among the EU-27 countries [96]. It must be noticed that over almost all the explored β range, the specific emissions are higher for all the analyzed fluids compared to R134a pure fluid, as shown in Figure 5-16. In particular higher β values lead to higher indirect emissions and could discourage the use of low-GWP fluids and mixtures even more, as alternatives of R134a. It can be observed that in this sensitivity analysis the R134a specific emission remain constant versus β, whilst the emissions for the fluids containing HFOs vary proportionally to β, with a curve slope determined by the E_{gap} value. The relative deviation from the reference value of β (shown in the figure) ranges between -88 % to +159 % for the HFOs pure fluids.

Coming back to the reference case (β = 460 $kgCO_2/MWh$ and LR = 2%), a further discussion is finally proposed, investigating the effect of R134a fraction within mixtures based on HFOs. In particular, Figure 5-17a shows the influence of the R134a concentration on the total specific GHG micro-ORC emissions, in variable mixtures of R1234yf with R134a, and mixtures of R1234ze(E) with R134a. The extreme conditions with R134a concentration equal 0 % and 100 % indicate respectively, HFO and R134a pure fluid. Among the possible mixtures it must be cited the commercial mixture R513A [90] (composed by 44 % of R134a and 56 % R1234yf) highlighted for convenience in Figure 5-17b.

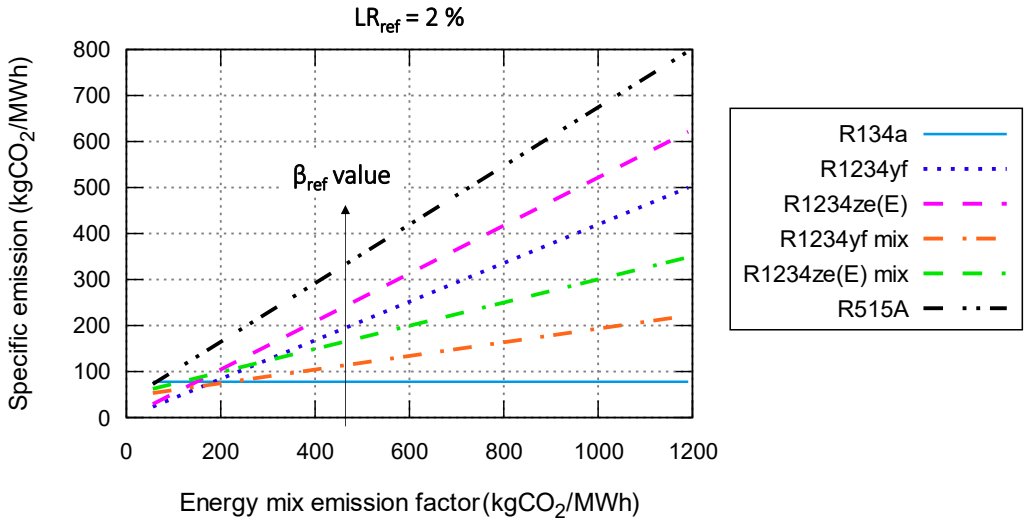

Figure 5-16 - CO_2 equivalent emissions as function of the energy mix emission factor.

The Em_{direct} term increases almost linearly with R134a amount in the mixture, due to the higher GWP of R134a than HFOs. The trend is not strictly linear because of the different required fluid charge, influencing the actual annual fluid leakage. Trends for R1234yf mixture and R1234ze(E) mixture are very similar because of the similar GWP of R1234yf and R1234ze(E) pure fluids. The $Em_{indirect}$ term exhibits a trend opposite to the Em_{direct} term. Indeed, increasing the R134a concentration leads to better performance of the micro-ORC systems and thus to lower need of energy integration and to lower $Em_{indirect}$. In particular, the mixture of R134a with R1234yf shows better performance than the mixture of R134a with R1234ze(E), thus lower $Em_{indirect}$ at given R134a concentration. The sum of the direct and indirect emissions contributions gives the total emission trend reported in Figure 5-17b.

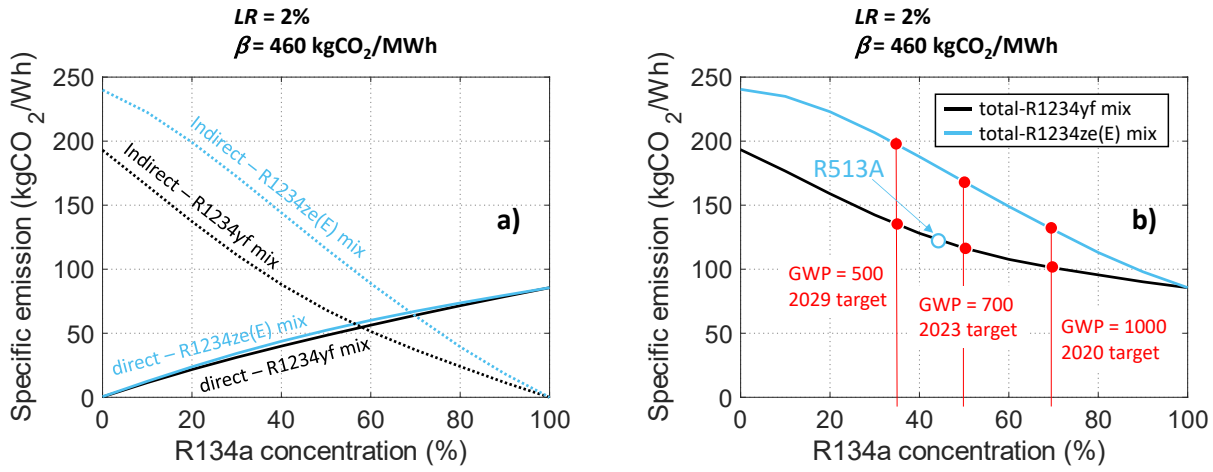

Figure 5-17 - CO_2 Specific emission as function of R134a concentration in the mixture: a) direct and indirect contributions; b) total specific emission.

Maps of the specific emission as function of the emission factor and of the R134a concentration are reported in Figure 5-18. Dot line in Figure 5-18 indicates the reference total emission observed

using R134a pure fluid (equal to 86 $kgCO_2/MWh$ (see Figure 5-17a)) considering the reference emission factor equal to 460 $kgCO_2/MWh$.

On the basis of the expected HFCs phase-down timeline, average GWP of refrigerants on the market should gradually reduce in next years (as indicated in Figure 1-8). As a consequence, R134a should exit the market starting from year 2020, and the R134a concentration in the mixtures of R134a and HFOs should decrease in the following years (as indicated Figure 5-17b). Maps of Figure 5-18 gives an indication on how the emission factor should be reduced hand-in-hand with the R134a reduction in the mixtures, in order to not increase total emission, compared to the reference emission observed using R134a pure fluid. Results show that energy mix emission factor should decrease from 460 $kgCO_2/MWh$ to less than 200 $kgCO_2/MWh$ in about ten years. A similar reduction could be achieved only in the case where the countries energy mix will be overturned. Indeed, nowadays, just a few European countries fall under emission factor below 200 $kgCO_2/MWh$, among which are France (56 $kgCO_2/MWh$) and Sweden (23 $kgCO_2/MWh$) mainly thanks to their large nuclear fleet [97].

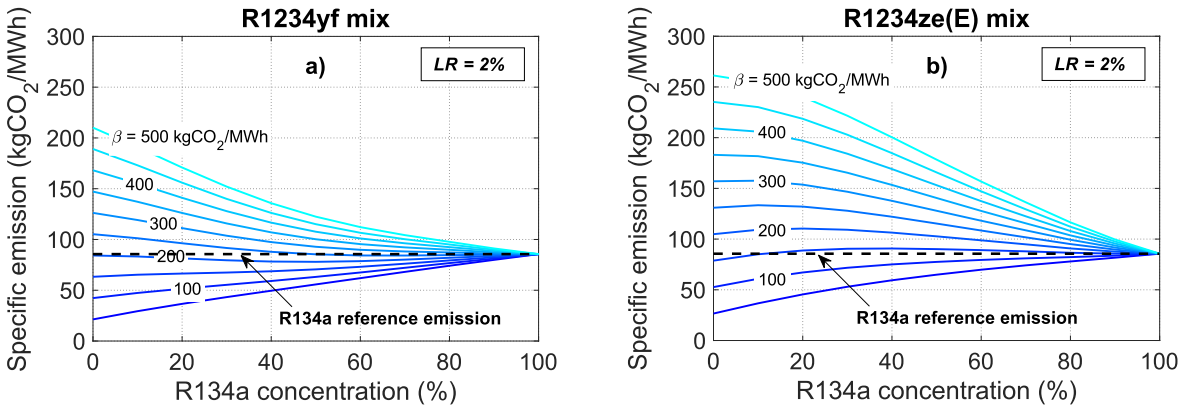

Figure 5-18 - Maps of the specific emission as function of the emission factor and the R134a concentration, for: a) mixture of R134a and R1234yf; b) mixture of R134a and R1234ze(E).

This final analysis intends to highlight how combined actions could be requested in order to effectively reduce emissions related to systems using refrigerants as working fluids, such as micro-ORC: i) the decrease of working fluids GWP, to limit direct emissions; ii) a not negligible reduction of the energy mix emission factor, in order to contain possible indirect emissions. With a view to move towards a greener energy mix, emissions factors are expected to decrease in next years and the use of low GWP fluids could help to effectively reduce GHG emissions. Meanwhile, in this transition period, blends of R134a and HFOs could help to maintain limited indirect emissions, while respecting new regulation concerning high GWP refrigerants, thanks to their intermediate emissions values compared to pure fluids forming the mixture (see Figure 5-14).

5.4.5 Conclusion

In conclusion, a method to comprehensively analyze GHG annual impact of an ORC system is discussed. The aim was to establish the real potential of low GWP fluids and their blends with R134a, in reducing the GHG release compared to conventional HFCs. The intention was to propose a new point of view, considering not only direct emissions due to refrigerant leakage but also indirect emissions. For this purpose, a robust semi-empirical model of a micro-ORC system is chosen to account for actual operating conditions of the volumetric machines and not only for the only thermodynamic process. Adaptations necessary to modelling low GWP fluids and blend instead of R134a has been also discussed and introduced to the aforementioned model.

The proposed analysis reveals that HFO fluids cannot always guarantee the same performance of commonly used fluid R134a, even if they exhibit very lower GWP. Thus, HFOs and their mixtures introduce an energy production gap, which can be compensated with energy sources outside the ORC system, likely employing fossil fuels. If considering a leak rate equal to 2%, indirect emissions caused using HFOs determine total equivalent emissions of CO_2 greater than the ones related to R134a use, up to + 181 % by employing R1234ze(E). More performant and environmental fluids can be identified among the hydrofluorocarbons and their mixtures, such as the R430A, even if their higher flammability risk make not practical to employ them into a residential ORC system.

Parametric study by varying the leak rate highlights that the emissions are quite sensitive to the leak rate. Thus, knowing the actual annual leak rate of the system is important in order to perform a correct evaluation of the greenhouse impact. Unfortunately, specific data for small scale ORC are scarce and not available. Further research could be dedicated to collect data concerning annual leak rate of this kind of plants. Another factor of influence is the emission factor of the energy mix considered to provide the energy production gap. It must be noticed, indeed, that higher emissions factors lead to higher indirect emissions and could discourage the use of low GWP as alternatives of R134a. Anyway, recent energy targets intend to push toward greener energy mix, emissions factors are expected to decrease and the use of low GWP fluids may help to effectively reduce greenhouse gas emissions. At least, blends exhibit, as expected, intermediate emissions compared to pure fluids forming the mixture, and also intermediate performance. Hence, in this transition period, they could help to maintain a good trade-off between performance and greenhouse impact.

In conclusion, this study turns the attention on how combined actions are requested in order to effectively reduce emissions related to systems using refrigerants as working fluids, such as micro-ORC. The decrease of working fluids GWP, to limit direct emissions must be accompanied by also a not negligible reduction of the energy mix emission factor, in order to contain possible indirect emissions.

6 Optimal management of power to heat to power systems

Summary: This chapter is focused on the off-design modelling of the reversible HP/ORC Carnot battery configuration with the aim of employing the model to simulate the performance of such system and discuss its optimal management under different boundary conditions. To this purpose, the ORC model proposed in the previous chapters is here coupled with a semi-empirical lumped parameters model of the heat pump, based on a similar approach. The reversible HP/ORC prototype installed at the University of Liège is considered as reference: experimental data provided by the university are used for the model calibration and validation. The performances of the integrated system are analyzed as function of the most influencing factors: the hot/cold source temperature, its glide through the heat exchangers and the refrigerant flow rate, determined by the pump or the compressor rotational speed. The last two variables are decisive parameters to regulate, so as to achieve the best possible performance from the Carnot battery system under different boundary conditions. Eventually, once the regulation strategy is set, some considerations are done on the optimal size of the storage and the feasibility of the Carnot battery for a given scenario.

6.1 Contribution

As mentioned in paragraph 1.6.2, at the present day very few studies are dedicated to investigating the potential of reversible ORC/HP systems. Some prototype [58], [59] and some numerical studies [59], [60] already exist, but the literature on the topic remains scarce, in particular concerning the management strategy of such a system.

With the aim of contributing to the existent literature, in this chapter a Carnot battery model is proposed, which involves not only the performance prediction of the reversible ORC/HP system but also the optimal Carnot battery regulation strategy, considering the thermal storage inertia. This study was conducted in collaboration with the University of Liège, which provided the experimental data for the calibration of the Carnot battery model, based on the experimental campaign conducted on its prototype [59].

6.2 The reference test bench

6.2.1 Experimental setup

The considerations made in this chapter take as reference the reversible HP/ORC prototype installed at the University of Liège [59] here presented. The hydraulic scheme comprehending all the components and sensors is illustrated in Figure 6-1. The green loop is the main one; it is the refrigerant loop composed of a high-pressure (HP) heat exchanger, a scroll volumetric machine able to work as a compressor or as an expander, a low-pressure (LP) heat exchanger, and two parallel branches with an expansion valve and a pump to work alternatively in heat pump mode and ORC mode. The refrigerant circulates clockwise when working in ORC mode and counterclockwise in heat pump mode. The test bench is provided with other two external circuits (blue loops) where circulates water, simulating the hot and the cold source, feeding respectively the HP and the LP heat exchanger. The hot source loop has two storages in order to operate with a perfect stratification between the hot zone and cold zone, where a pump provides the necessary flow to move the water from the hot water tank to the cold one in ORC mode and vice versa in HP mode by using a four-way valve. The same reversible layout is repeated for the cold source but no storage is present. In order to simulate different temperature levels, both the hot and the cold side are provided with an external heat source.

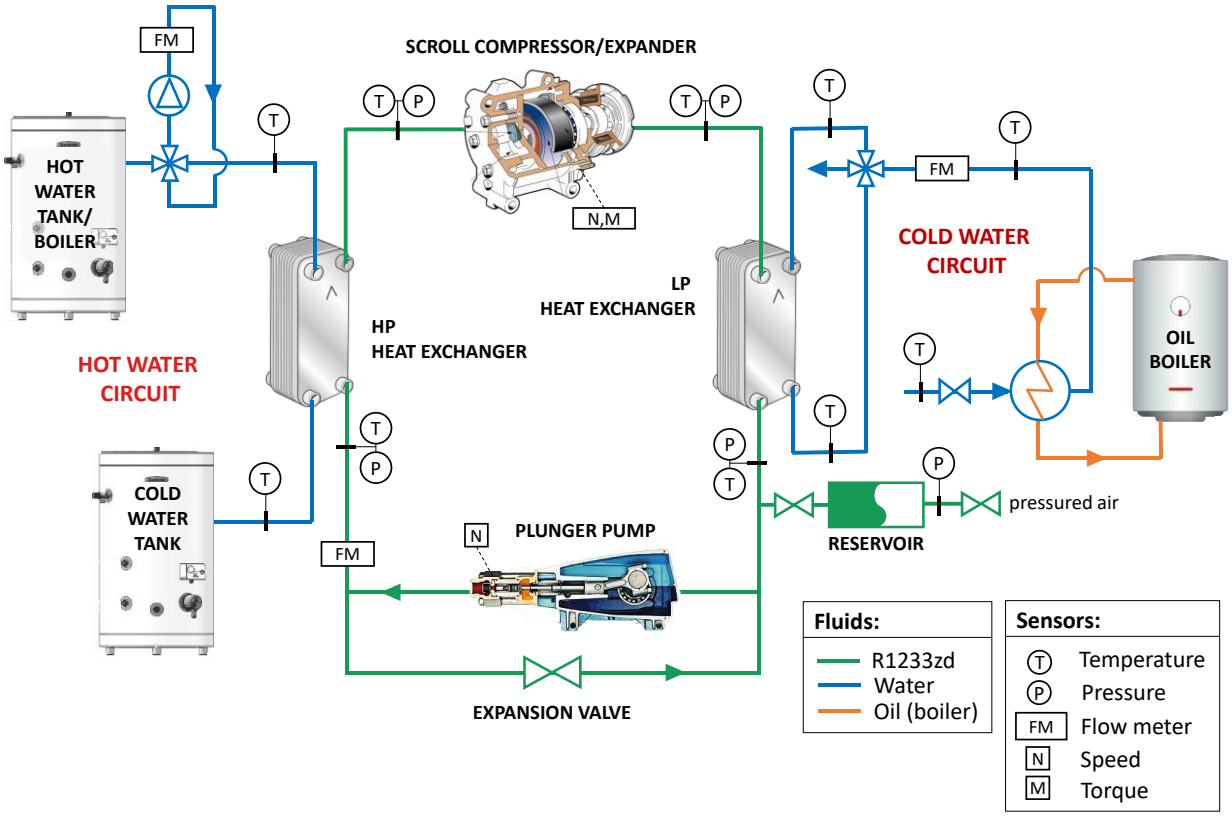

Figure 6-1 - Hydraulic scheme of the prototype of reversible HP/ORC power system [59].

More in detail the components specifications are described in Table 6-1. The volumetric machine is a scroll compressor from the automotive industry, which has been modified to be able to work reversibly as an expander. The ORC pump is a plunger pump chosen for its high volumetric and isentropic efficiency. Regarding the expansion valve, a solenoid valve is used to adjust the compressor suction superheating in heat pump mode. Two 900 liters storages are used to store 10 kWh of energy on the hot water side. The condenser and the evaporator are plate heat exchangers, sized to keep the pinch point below 2 K. Then the test-rig is fully equipped with high accuracy sensors to determine the thermodynamic state of the fluids in each point of the cycle and the involved powers.

Table 6-1 -Test rig components technical data [59].

Component	Parameter	Value
Scroll compressor Sanden TRSA09	Swept volume (cm^3)	85.7
	Shaft speed (rpm)	500-8000
	Volume ratio	2.2
Plunger pump Hyproplunger 2220B-P	Flow rate (l/s)	0.159
	Shaft speed (rpm)	1725
	Maximum pressure (bar)	137
Expansion valve Asco 290	Flow coefficient – K_v (m^3/h)	2.7
	Maximum temperature (°C)	90
	Maximum differential pressure (bar)	6
Auxiliary pump (HP) Grundfos CRE1-4	Maximum flow (l/s)	0.5
	Head (m)	15
	Maximum temperature (°C)	95
Liquid tank	Maximum pressure (bar)	10
	Volume (l)	5
	Maximum temperature (°C)	110
Storage (x2)	Volume (m^3)	0.9 (x2)
Low pressure heat exchanger B85Hx44	Area (m^2)	2.52
	Number of plates (-)	44
High pressure heat exchanger B26Hx060	Area ($m^{2)}$	2.38
	Number of plates (-)	60

The sizing of the prototype and the choice of the working fluid were achieved by assuming target boundary conditions representative of many industrial applications, with the aim of obtaining an electrical production almost equal to the electrical consumption [98]:

- Ambient temperature equal to 15°C and waste heat temperature equal to 75°C;
- Storage capacity around 10 kWh;
- Hot source temperature glide through the HP heat exchanger equal to 10 °C;
- Nominal electrical power of the volumetric machine of about 3 kW.

In the design of the prototype, particular attention was paid to the Reynolds ratio parameter. The latter is defined as the ratio between the highest Reynolds number of the ORC mode and the highest Reynolds number in the HP mode, and should be set to about one in order to obtain similar working conditions and therefore good performance both in HP and ORC mode [98].

Under these assumptions, HFO-1233zd(E), with a critical temperature of 165 °C and a critical pressure of 35.7 bar, is chosen as high performant refrigerant [98]. It is a non-flammable, ultra-low GWP (=1) born as replacement for R-123 for low pressure centrifugal chillers, which are most often used to cool large buildings [99]. Its thermodynamic characteristics are shown in the pressure-enthalpy diagram of Figure 6-2.

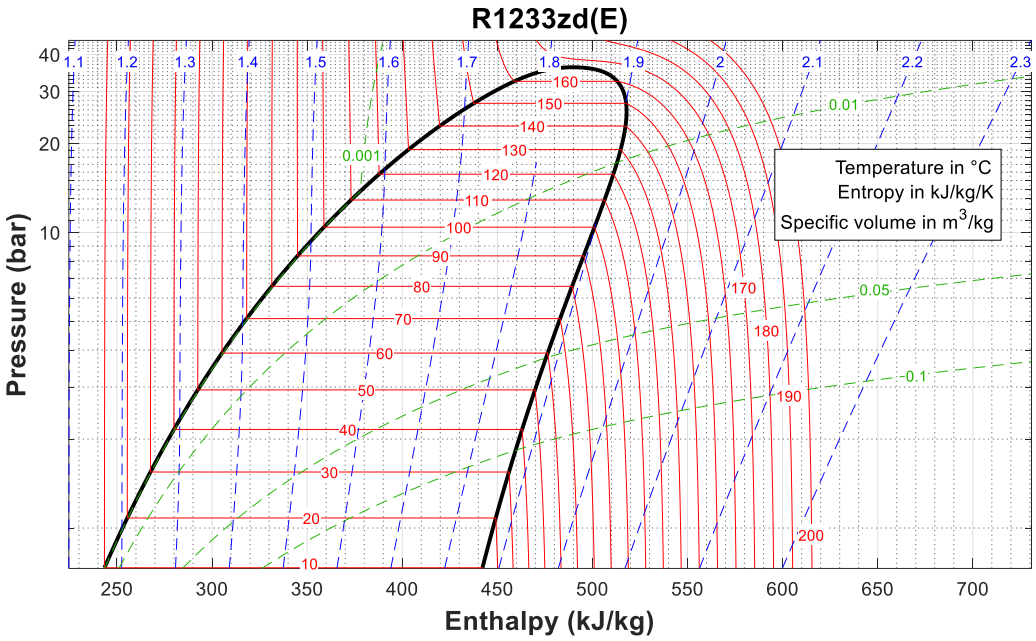

Figure 6-2 - R12333zd(E) thermodynamic diagram §§.

6.2.2 Experimental tests

Experimental data collected on the rig are presented in [59]. The prototype has been tested in both ORC and HP mode for several operating points, characterized by a variable hot and cold source temperature and a variable working fluid flow rate. An overview of the tested conditions is shown in Figure 6-3 and Table 6-2.

The Carnot battery has been tested in ORC mode for a hot source temperature ranging between 70 and 90 °C, where the cold source temperature varied between 10 and 30 °C depending on the ambient conditions. The HP mode, instead has been tested for more variable values of the hot source and cold source temperature, both varying between 15 and 80 °C, with a maximum temperature lift is equal to about 30 °C. The maximum tested working fluid flow rate is around 0.1 kg/s.

§§ Curves obtained using data from the RefProp thermodynamic library [63].

The variation of the aforementioned control variables leads to the variation in the Carnot battery operating conditions in terms of: thermal power transferred into the heat exchangers, evaporating and condensing pressures, subcooling at the condenser outlet and superheating degree at the evaporator outlet. More in specific, thermal power ranging between 1 and 18 kW have been tested. ORC mode evaporating pressure varies between 3.4 and 5.8 bar, whilst the condensing pressure does not overcome 2 bar. In the HP mode the condensing and evaporating pressure tested range is more similar and limited between 0.65 and 7.2 bar.

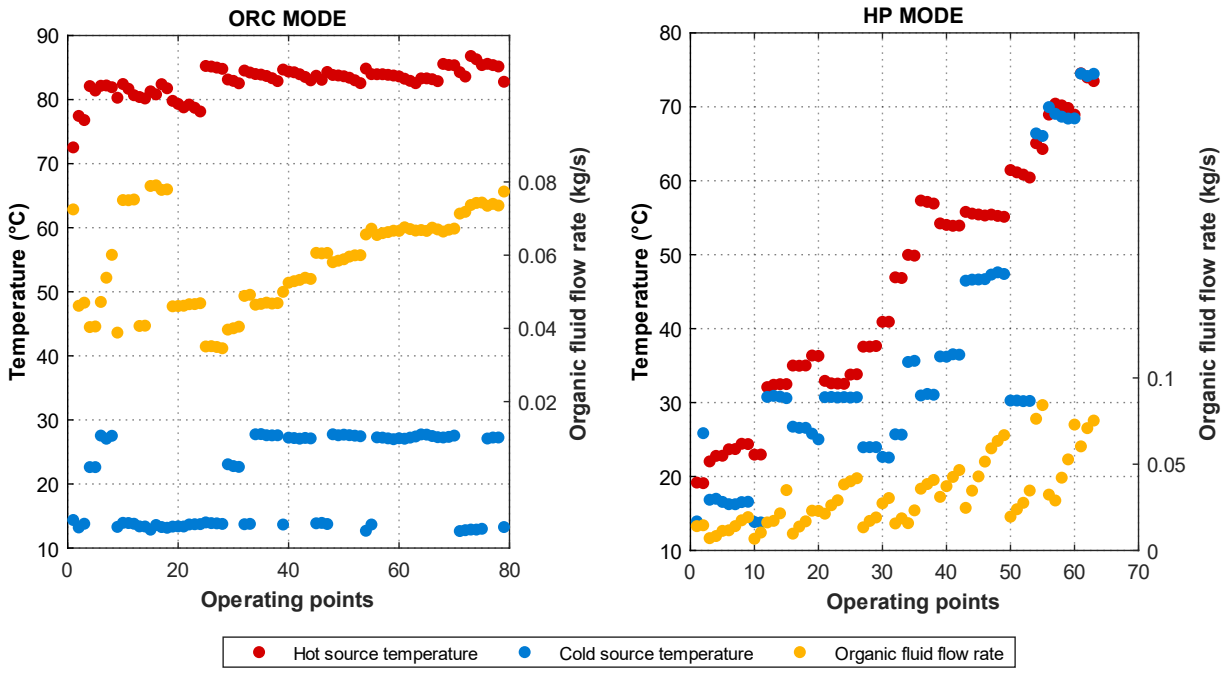

Figure 6-3 - Map of tested operating conditions.

Table 6-2 - Overview of tested operating conditions.

Parameter	ORC	HP
Evaporator thermal power (kW)	8.4-18.2	1.2-13.4
Condenser thermal power (kW)	0.7-16.2	1.3-14.5
Evaporation pressure (bar)	3.4-5.8	0.65-4.9
Condensation pressure (bar)	1.1-1.9	1.6-7.2
Subcooling (°C)	6.2-8.8	4.1-28.9
Superheating (°C)	4.0-25.7	3.3-6.3

6.3 The model and the optimal regulation strategy

6.3.1 Structure

The ORC/HP reversible model is composed by an ORC model to simulate the ORC mode and an HP model to simulated instead the HP mode. The ORC and HP models, as described below, can

predict the performance of the two separated modes under several combinations of boundary conditions and control variables values. However, in a realistic application the two modes must be considered together into a comprehensive Carnot battery model. The Carnot battery system can be assumed to be composed by the reversible ORC/HP plant and a single tank which serves as thermal energy storage. Thus, considering the whole system and its operation in a real application, the two different models are integrated into a global Carnot battery model, involving:

- a strategy to manage the single modes (called "optimal mode regulation strategy");
- a strategy to decide when turn on/off the Carnot battery and switching mode (called instead "Carnot battery regulation strategy").

In this paragraph a sub-paragraph is dedicated to each of these aspects, i.e.: i) the modelling of the ORC and the HP mode, ii) the optimal model regulation strategy and iii) the Carnot battery regulation strategy.

6.3.2 ORC and HP models

Components sub-models

The methodology used to model the ORC and the HP components is based on a semi-empirical approach, as described in chapter 4, for the off-design modelling of micro-ORCs; more in detail:

- The heat exchangers are modelled by means of the moving boundaries method (see paragraph 4.3). A corrected version of the Cooper's (Eq. (6-1)) and the Gnielinski's (Eq. (6-2)) correlations is used to evaluate respectively the evaporating and the condensing convective heat transfer coefficients, as proved to be effective to simulate heat transfer in ORC applications [84]. The correction coefficients are here named as c_1, c_2 and c_3. The one phase regions convective heat transfer coefficient is determined instead by means of the Dittus Boelter correlation.

$$h = c_1 \cdot \left(\frac{\dot{Q}}{A}\right)^{0.67 \cdot c_2} \cdot 55 \cdot {p_r}^{0.12 - 0.2 \cdot log P_r} \cdot -\log\left(p_r\right)^{-0.55 \cdot c_2} \cdot M^{-0.5} \tag{6-1}$$

$$Nu = c_3 \cdot \frac{f/8 \cdot (Re - 1000) \cdot Pr}{1 + 12.7 \cdot (f/8)^{0.5} \cdot Pr^{2/3-1}} \tag{6-2}$$

  p_r indicates the reduced pressure, M, the molecular weight and f the Darcy friction factor.
- The scroll compressor is modelled by means of the lumped parameter approach originally proposed by Lemort [100] for scroll compressors (based on the same equations described in paragraph 4.2.3). Besides of under- and over-expansion/compression losses (due to the fixed built-in volume ratio of the machine), the model can account for pressure drops and heat transfers at the inlet and outlet ports of the machine, internal leakages, mechanical losses and heat losses to the environment. There is not a re-compression loss contribution associated to the scroll expander operation, thus it is not considered, differently from the piston expander case.
- The ORC pump model relies on Eq. (6-3), as proposed in [21]. According to Eq. (6-3) the performance of the pump is influenced by its operating conditions in terms of rotational speed, elaborated volume flow rate and pressure rise. The performance depends also on the pump load and how much it deviates from the nominal point, represented by a nominal engine absorbed

power, $\dot{W}_{eng,nom}$, rotational speed, $N_{pp,nom}$, and efficiency, $\eta_{eng,nom}$. The pump absorbed power is correlated to all these variables through the empirical parameters K_1, K_2, K_3 and K_4.

$$\dot{W}_{pp} = K_1 + K_2 N_{pp} + K_3 \dot{V} \Delta P + \dot{W}_{eng,nom} \left(\frac{1}{\eta_{eng,nom}} - 1 \right) \left(K_4 \frac{(K_2 N_{pp} + K_3 \dot{V} \Delta P)^2}{\dot{W}_{eng,nom}^{\ 2}} + (1 - K_4) \frac{N_{pp}^{\ 2}}{N_{pp,nom}^{\ 2}} \right) \quad (6\text{-}3)$$

- The HP expansion valve is represented by an isenthalpic expansion between the high (condensing) and the low (evaporating) pressure of the cycle.
- The pressure drops are evaluated with Eq. (6-4).

$$\Delta P = k \cdot \dot{m}_{wf}^{\ 2} \quad (6\text{-}4)$$

- The auxiliary pumps consumption is also accounted using Eq. (6-5) and considering a constant efficiency. Where the auxiliary pumps are these pumps moving the secondary fluid into the hot and cold external circuits.

$$\dot{W}_{aux} = \dot{V} \cdot \Delta P \ [Pa] / \eta_{pp,aux} \quad (6\text{-}5)$$

- The storage model is based on the resolution of the energy balance on the storage volume, V_{sto}, in the time variable (see Eq. (6-6)). The output is the storage temperature at the current time step, $T_{sto,i}$, which can increase or decrease if compared to the temperature at the previous time step, $T_{sto,i-1}$, depending on the amount of the external provided thermal power (negative if absorbed), $\dot{Q}_{ext}$, and the heat losses contribution, $UA_{sto} \cdot \left(T_{sto,i-1} - T_{amb} \right)$, both integrated into the timestep, Δt. The storage inertia depends on the mass of fluid contained into the storage, $V_{sto} \cdot \rho$, and on its specific heat capacity, c_p.

$$T_{sto,i} = T_{sto,i-1} + \left(\dot{Q}_{ext} - UA_{sto} \cdot \left(T_{sto,i-1} - T_{amb} \right) \right) \cdot \frac{\Delta t \ [s]}{V_{sto} \cdot \rho \cdot c_p} \quad (6\text{-}6)$$

It must be noticed that the ORC and the HP components sub-models are assumed to be timed-independent, which is a realistic assumption in case that the transient phenomena duration is negligible if compared to the analyzed timestep. In the view of the above, the ORC and the HP models are steady state models, and, in their applications, the ORC/HP system will be considered to work at fixed-point on the timestep interval.

Problem resolution

The components sub-models are connected with each other as schematized in Figure 6-4 and Figure 6-5, respectively for the ORC and the HP model; where the green lines represent the inputs and the outputs of the sub-models, the red lines the iterative variables and the dot lines the iterative cycles.

The inputs of the model represent the boundary conditions and the control variables of the system. The boundary conditions depend on the site and on the involved processes, and they are primarily the hot source and the cold source fluid state and the ambient temperature. The control variables are instead those variables which can be manipulated by an operator, such as the secondary fluid temperature glide through the heat exchangers, the refrigerant flow rate, the

superheating degree at the evaporator and the subcooling degree at the condenser. The latter are decisive parameters to adjust so as to achieve the best possible performance from the Carnot battery system for given boundary conditions.

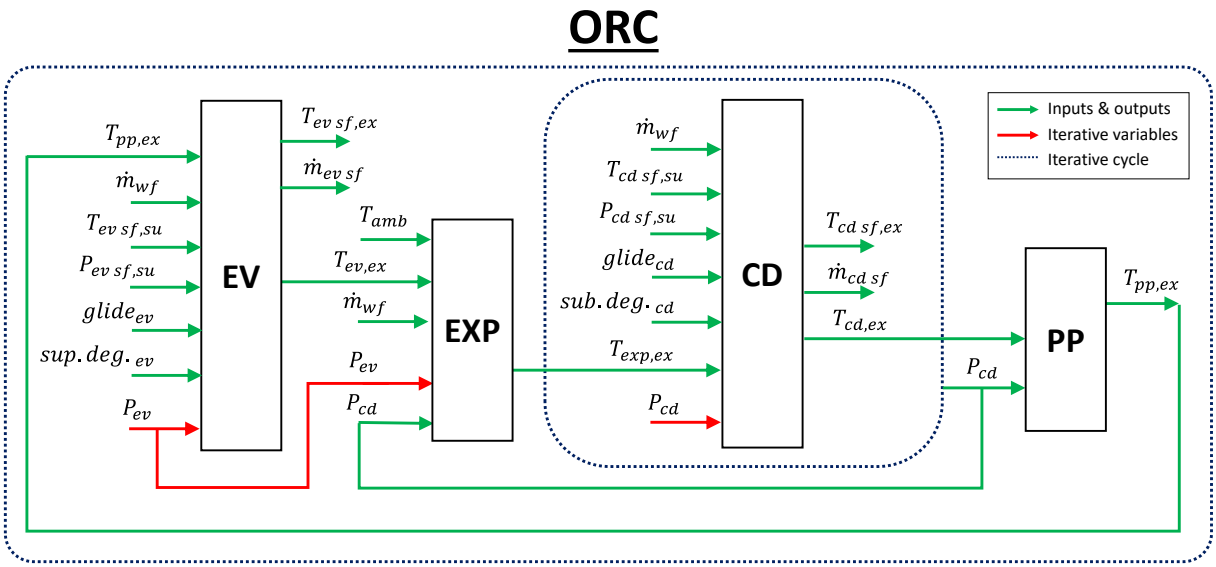

Figure 6-4 - ORC off-design model scheme.

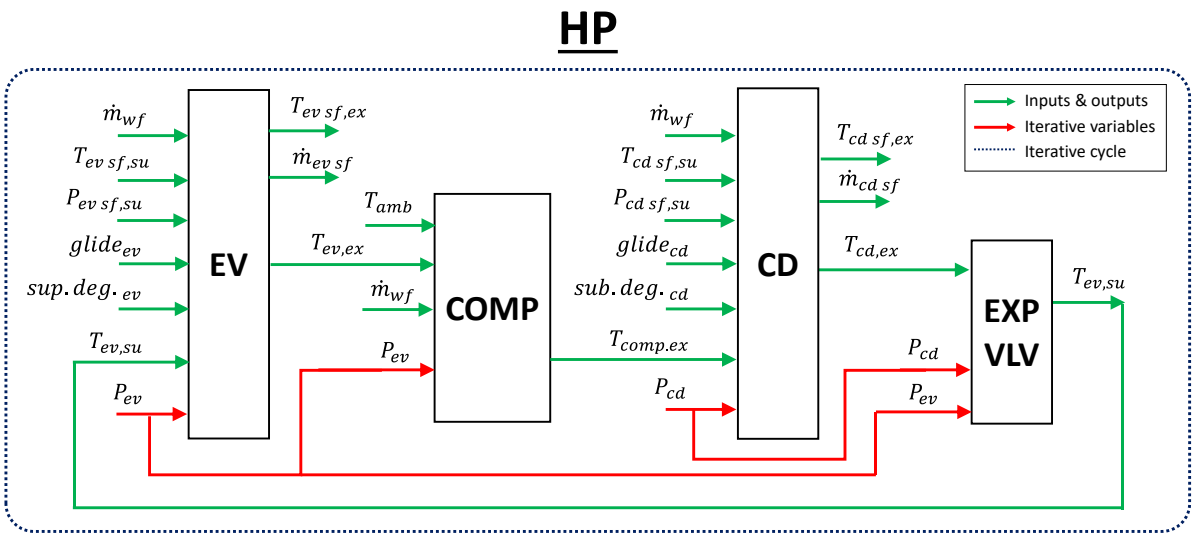

Figure 6-5 - HP off-design model scheme.

Solving the problem via iterations over the cycle pressures, the part load model is able to evaluate as output: the fluid state in each point of the cycle, the thermal power exchanged into the heat exchangers, the secondary fluids flow rate and the power consumed or produced by the machines. Other fundamental performance outputs that identify the Carnot battery performance are derived by means of Eqs. (6-7)-(6-10) and they are: the net power output, the ORC net efficiency, the HP coefficient of performance (*COP*), the Carnot battery load and its charge/discharge time.

$$\dot{W}_{net,ORC} = \dot{W}_{exp} - \dot{W}_{pp} - \dot{W}_{aux} \quad | \quad \dot{W}_{net,HP} = \dot{W}_{comp} + \dot{W}_{aux} \tag{6-7}$$

$$\eta = \dot{W}_{net,ORC}/\dot{Q}_{ev,ORC} \quad | \quad COP = \dot{Q}_{cd,HP}/\dot{W}_{net,HP} \tag{6-8}$$

$$load = \frac{M_{sto} \cdot c_p \cdot (T_{sto} - T_{ORC,min})}{M_{sto} \cdot c_p \cdot (T_{sto,max} - T_{ORC,min})} \tag{6-9}$$

$$t_{disch} = \frac{M_{sto} \cdot c_p \cdot (T_{sto} - T_{ORC,min})}{\dot{Q}_{ev,ORC,av}} \quad | \quad t_{ch} = \frac{M_{sto} \cdot c_p \cdot (T_{sto,max} - T_{sto})}{\dot{Q}_{cd,HP,av}} \tag{6-10}$$

Whilst the first three indexes are widely employed and do not need further explanation, the last two maybe are not, since more specific for the Carnot battery application. The Carnot battery load is here defined as the ratio between the stored and the maximum storable energy into the thermal storage (Eq. (6-9)). The energy magnitude is defined based on a reference minimum ORC acceptable temperature at the evaporator inlet, $T_{ORC,min}$, below which is not convenient or possible running the ORC. $T_{sto,max}$ corresponds instead to the maximum temperature allowed into the storage. Then, the discharge/charge time is the time it takes the Carnot battery to fully discharge/charge, starting from a given storage temperature. Thus, the discharge time, t_{disch}, is computed as the ratio between the stored energy and the average thermal power subtracted by the ORC during the discharge process, $\dot{Q}_{ev,ORC,av}$. At the contrary, the charge time, t_{ch}, is computed as the ratio between the still storable energy and the average thermal power provided by the HP during the charge process, $\dot{Q}_{cd,HP,av}$.

Empirical parameters

The components sub-models since semi-empirical models necessitate of parameters to be calibrated or to be provided by the manufacturer. For the case study, these parameters and their values are listed in

Table 6-3. In this case, parameters such as the components dimensions and the volumetric machines performance were known (and provided in [59]), whilst others, namely the correction constants for the heat transfer correlations, were not and had to be calibrated against experimental data. Experimental data used for the calibration of the remaining parameters come from past preliminary tests conducted on the prototype and presented by Dumont et al. in [59].

The heat transfer correlation coeffecients' calibration process is very similar to the one proposed in paragraph 4.2.4. The procedure is applied to each heat exchangers both in ORC and in HP mode and it consists in two steps: i) the calculation of the two phase convective heat transfer coefficient for each experimental data's operating point, ii) the fitting of the data to obtain the coefficients that minimize the mean square error between the experimental and calculated values. The accuracy of the calibration can be evaluated by testing the calibrated model in the prediction of the main outputs, i.e. the exchanged thermal power, the pressure and the secondary fluid flow rate. The comparison between the calculated and the measured output values is shown by the parity plots of Figure 6-6, which highlights a limimted mean relative error value.

Table 6-3 - Models' parameters.

Component	Parameter	Value
Pump (PP)	K_1 (W)	20
	K_2 (W·s)	0.07
	K_3 (-)	1.17
	K_4 (-)	0.6
Compressor (COMP)	Ambient heat losses (W/(m² K))	5
	Supply heat losses (W/(m² K))	10
	Exhaust heat losses (W/(m² K))	10
	Leakage area (m²)	1e-8
	Mechanical proportional losses (-)	0.15
	Mechanical constant losses (W)	10
	Swept volume(m³)	8.57e-5
	Exhaust pressure drop diameter (m)	0.098
Expander (EXP)	Ambient heat losses (W/(m² K))	1
	Supply heat losses (W/(m² K))	50
	Exhaust heat losses (W/(m² K))	94
	Leakage area (m²)	2.6e-6
	Mechanical proportional losses (-)	0.02
	Mechanical constant losses (W)	8
	Swept volume(m³)	3.8e-5
	Supply pressure drop diameter (m)	0.098
High pressure Heat exchanger (HP-CD/ORC-EV)	Equivalent diameter (m)	0.02
	Surface (m²)	2.52
	Cooper correlation coefficient, c_1 (-)	0.98
	Cooper correlation coefficient, c_2 (-)	1.08
Low pressure Heat exchanger (HP-EV/ORC-CD)	Equivalent diameter (m)	0.02
	Surface (m²)	2.38
	Gnielinski correlation coefficient, c_3 (-)	4.62
Secondary fluid pumps	Efficiency (%)	50

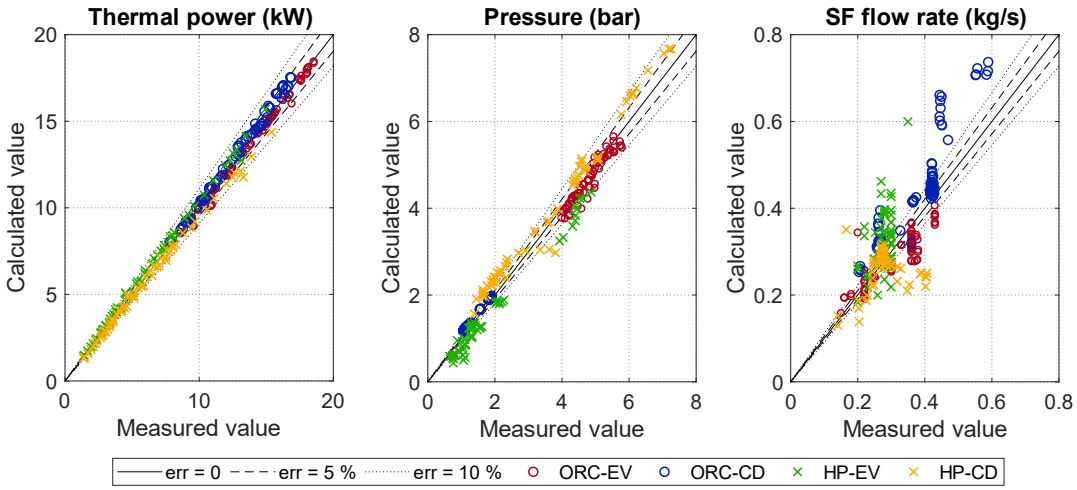

Figure 6-6 - Heat exchangers model validation.

6.3.3 Optimal mode regulation strategy

According to the proposed regulation strategy, the Carnot battery is managed in order to work in each mode (ORC or HP) at maximum net efficiency (or COP, in HP case) under the imposed boundary conditions. To this aim, an "optimal mode regulation strategy" model has been implemented, in order to identify the control variables values that allow to obtain the best performance from the ORC and the HP modes in terms of efficiency. Indeed, for each combination of available hot source temperature (i.e. storage temperature) and available/demanded power (respectively in ORC/HP mode), it exists an optimal value of the secondary fluid temperature glide (or more simply called "glide") and of the working fluid flow rate that maximize the system net efficiency. It must be highlighted that the maximum efficiency point does not always corresponds to the maximum power production, in ORC mode, and to the minimum power consumption, in HP mode [101].

The steps to implement the "optimal mode regulation strategy" model for both the ORC and the HP modes, were the following (as illustrated in Figure 6-7):

3. Two lookup tables are created as the result of a matrix of simulations exploring the entire range of the possible boundary and control variables conditions values. The lookup tables (3D matrixes of Figure 6-7) express the relationship between: i) the net efficiency (or COP in HP mode) and the hot source temperature, the glide and the working fluid flow rate inputs; ii) the demanded/available power, $\dot{W}_{req/ava}$, and the hot source temperature, the glide and the working fluid flow rate inputs.
4. Three new lookup table (2D matrixes in Figure 6-7) are created starting from the first two lookup tables, by extracting for each combination of the hot source temperature and the demanded/available power, the maximum efficiency operating point. The first new lookup table expresses the relationship between the maximum achievable efficiency, the hot source temperature and the demanded/available power. The other two allow to identify the optimal glide and working fluid flow rate values, which allow to work at maximum efficiency as function of the storage temperature and the demanded/available power.

5. The optimal regulation function interpolates the data contained into the optimal regulation lookup tables, to obtain the optimal value of the glide and of the working fluid flow rate that maximize the system net efficiency

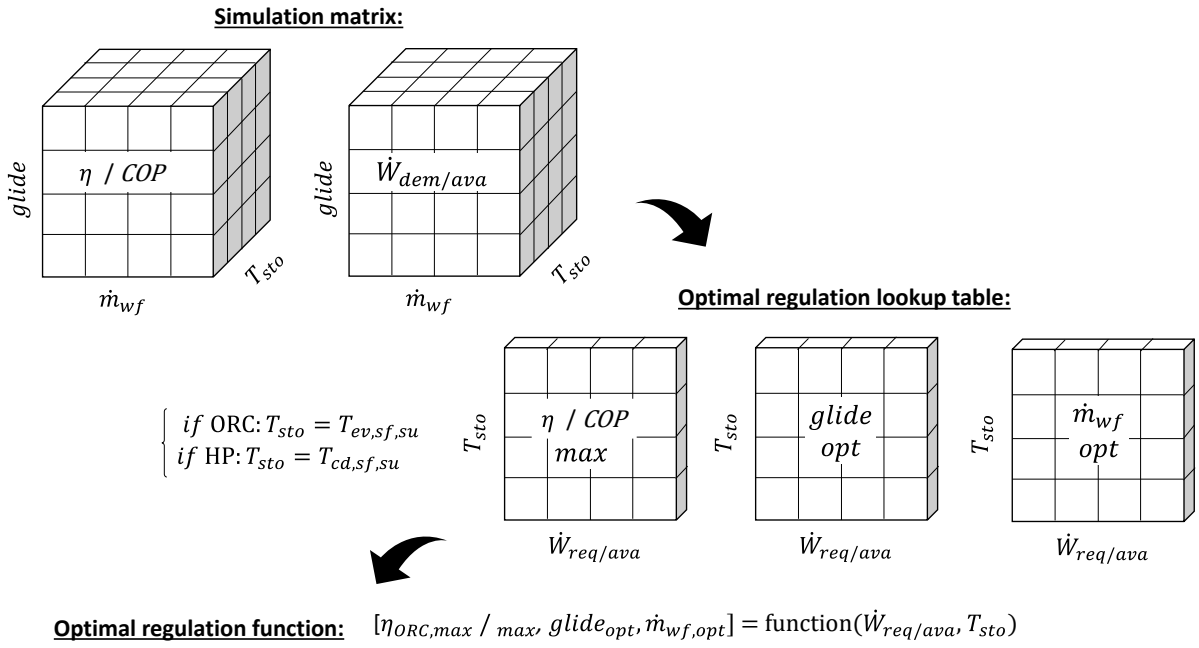

Figure 6-7 - Optimal mode regulation strategy implementation steps.

6.3.4 Carnot battery regulation strategy

A "Carnot battery regulation strategy" is implemented beside the "optimal mode regulation strategy" to decide when turn on/off the Carnot battery and switching mode. This decision is taken every timestep on the basis of the application and the process conditions. A generic application comprising the following elements is considered as case study (see Figure 6-8):

- A power user, which requires to satisfy a certain power demand. However, it can be observed that in many industrial and tertiary applications is not uncommon to find processes including a waste heat release [5]. In these cases, the user can be also considered as a free thermal power source that can help charging the Carnot battery storage to increase the ORC mode power production.
- The electric grid, from which it is possible to purchase the necessary missing amount of power to entirely satisfy the power demand.
- A renewable energy power plant, which can provide part of the entire power demand or the entire power demand or a surplus power production, depending on the availability of the energy source. In case of surplus of power production, the exceeding energy can be sold to the grid or stored into the Carnot battery to be released in a second moment.
- The Carnot battery, which can be charged exploiting the renewable energy power plant production and discharged to cover the user demand when requested.

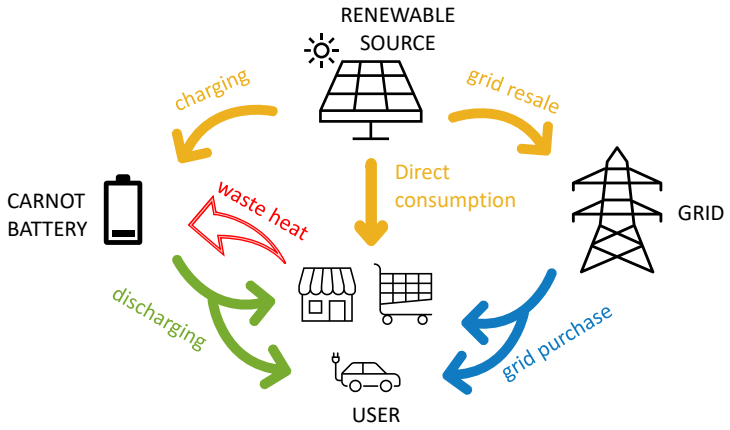

Figure 6-8 - Example of a Carnot battery application.

It can be noticed that the scheme does not include the possibility of charging the Carnot battery with the power from the grid, since, in general, there is no need to store the energy coming from the grid, which is available at every hour of the day. The passage through the Carnot battery would only lead to an energy loss (proportional to the system roundtrip efficiency) with no beneficial neither from the energetic nor from the economic point of view.

According to this scheme, supermarkets are an example of a possible Carnot battery application. In this case the power consumption mainly come from the lightning, the air conditioning, the chillers and occasionally from ovens, which also can act as free thermal power producer; an additional power request can eventually come from electric vehicles charging stations made available by the supermarket's parking. Eventually, a diffused renewable energy power plant that can be easily found in supermarkets is the solar photovoltaic.

Considering a generic case study involving these elements, the "Carnot battery regulation strategy" proposed in the flowchart of Figure 6-9 can be applied. Basically, four different situations may occur (indicated with number into circles in Figure 6-9):

- The demanded power, $\dot{W}_{demanded}$, may be not entirely covered by the renewable energy source power plant production, $\dot{W}_{renewable}$, resulting in a power deficit. In this case, the ORC operating limits may be respected or not [***] :
  1. if yes, the ORC is run according to the optimal mode regulation strategy producing the power $\dot{W}_{ORC}$ by discharging the thermal storage. If the boundary conditions allow it, the ORC is regulated to totally cover the required power, $\dot{W}_{req}$, otherwise, it is regulated to work at the maximum possible power production.
  2. if not the, the ORC is not run and the storage is not discharged. However, the storage temperature decreases due to the heat losses to the ambient.

[***] the ORC operating limits are the minimum secondary fluid temperature at the evaporator inlet, $T_{ORC,min}$, and the ORC technical minimum, $\dot{W}_{ORC,min}$

The amount of power purchased by the grid, $\dot{W}_{grid,purchase}$, is given by the difference between $\dot{W}_{req}$, and $\dot{W}_{ORC}$.

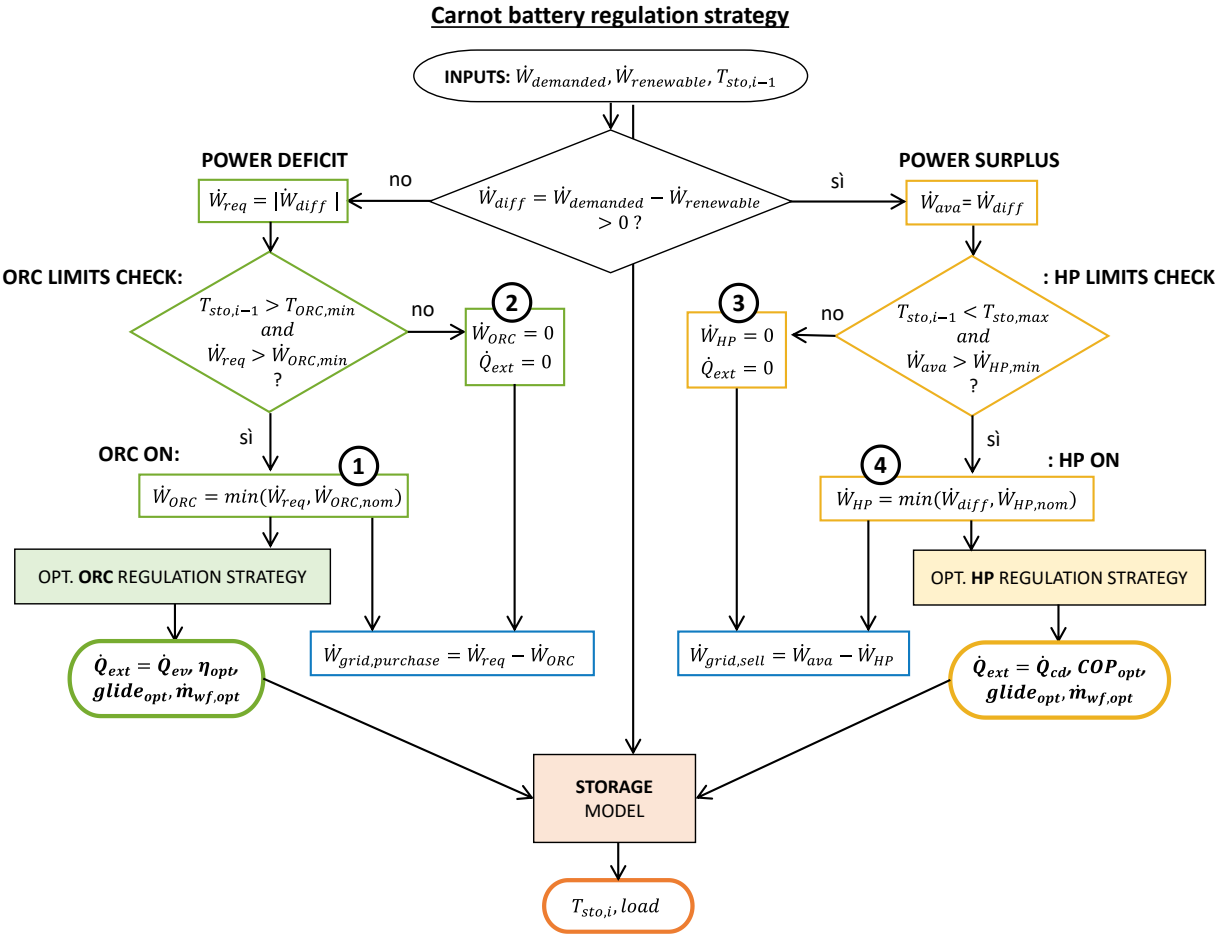

Figure 6-9 - Carnot battery regulation strategy flowchart.

- $\dot{W}_{renewable}$ may overcome $\dot{W}_{demanded}$ resulting in a power surplus. In this case, the HP operating limits may be respected or not †††:
  3. if yes, the HP is run according to the optimal mode regulation strategy absorbing the power $\dot{W}_{HP}$ to charge the storage. If the boundary conditions allow it, the HP is regulated to exploit all the available power, $\dot{W}_{ava}$, otherwise, it is regulated to exploit the maximum possible available power.
  4. if not the, the HP is not run, the storage is not charged and the storage temperature decreases due to the heat losses to the ambient.

††† the HP operating limits are the maximum secondary fluid temperature at the condenser, which must respect the maximum storage temperature limit, and the HP technical minimum, $\dot{W}_{HP,min}$

The amount of power sold to the grid, $\dot{W}_{grid,sell}$, is given by the difference between the available power, $\dot{W}_{ava}$, and $\dot{W}_{HP}$.

At the end of the computational routine, on the basis of the results of the Carnot battery regulation strategy, the storage model updates the storage temperature value.

6.4 Analysis of the system performance under regulation

6.4.1 Performance maps

For the case study, the simulation matrixes (described in paragraph 6.3.3) have been created by assuming for the ORC a value of the superheating and the subcooling degree of 5 °C whilst for the HP a value equal to 10 °C, in line with the reference test bench experimental data [59]. An ambient temperature equal to 20 °C is set as reference and the evaporator and the condenser glides are considered the same. Under these assumptions, a performance map is extracted from the simulation matrixes to show the influence of the glide and the mass flow rate, for given available storage temperature, equal to 85 °C and 25 °C for the ORC and the HP respectively (see Figure 6-10). The empty areas correspond to not physically feasible operating points and represent the operating limits of the system.

For the ORC operating mode, some observations can be made:

- Increasing the mass flow rate leads to an increasing of the expander power output but also of the ORC pump consumption and the requested thermal power input at the same time. Thus, generally, the electrical power output increases with the mass flow rate until reaching its maximum at high mass flow rate, whilst the ORC efficiency follows the opposite trend. This leads to the conclusion that the maximum efficiency point does not always corresponds to the maximum power production, highlighting the necessity of implementing an optimal regulation strategy to ensure to achieve the best efficiency under given boundary conditions and requested power production.
- The glide influences the pressures inside the cycle and, thus, the available cycle pressure ratio. It follows that the expander is not working in optimal conditions for some values of the glide, since under-expansion and over-expansion losses affect the expander efficiency, respectively for low and high values of the glide (see ORC T-s diagrams in Figure 6-10).

Concerning instead the HP, it can be noticed that:

- Generally, the absorbed power increases with the mass flow rate (thus, the compressor shaft speed) and with the glide, while the *COP* follows the opposite trend. It results that, differently from the ORC case, the maximum *COP* operating point is closer to the point of minimum power consumption. The power discharged by the condenser also increases with the working fluid mass flow rate.
- In this mode too, the compressor efficiency is affected by over-compression and under-compression losses, which become important at low and high values of the glide, respectively (see HP T-s diagrams in Figure 6-10).

It must be added that for both the operating modes, lower values of the glide are obtained by increasing the secondary fluid flow rate and thus the auxiliary pump consumption. Consequently, the ORC net power production further decreases and the HP total absorbed power increases on the contrary when the glide decreases. The heat exchangers performances are also influenced by the glide, and in particular, too high values of the glide can lead to an increment of the heat transfer irreversibilities, due to a not optimal coupling between the secondary fluid and the working fluid heat transfer curves.

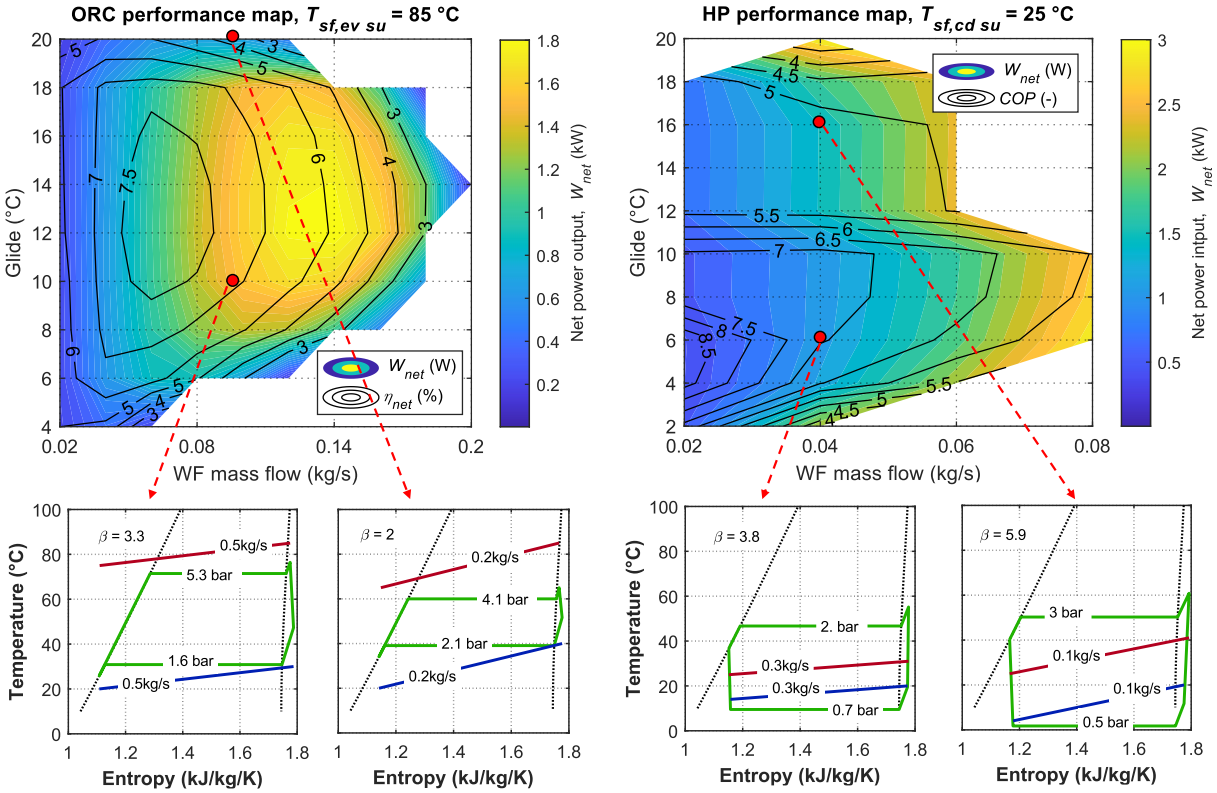

Figure 6-10 - ORC and HP performance map at storage temperature of 85 °C and 25 °C, respectively.

6.4.2 Optimal regulation maps

The results of the optimal regulation strategy model can be summarized into the regulation maps of Figure 6-11 for the ORC and Figure 6-12 for the HP. These maps show the trend of the glide and of the working fluid flow rate optimal values, and the optimal net efficiency/*COP* as function of the demanded/available power and the storage temperature.

For the ORC (see Figure 6-11), a possible operating range of temperature from 70 to 100 °C is considered, resulting in a maximum net power output of about 3 kW. The results show that the optimal ORC net efficiency increases with the temperature and the demanded power output, ranging between 5 and 8.5 %. In order to reach the maximum efficiency for each boundary conditions' combination, the working fluid mass flow rate must be incremented with the demanded power

output. In most of the cases, instead, the glide must be incremented with the available hot source temperature.

Concerning the HP (see Figure 6-12), the hot source temperature lower and upper operating limits are set equal to 20 to 90 °C. The results show that the lower are the storage temperature and the absorbed power, the higher is the achievable total *COP*, which can reach a maximum value of 10. In order to reach the maximum *COP* for each boundary conditions' combination, the working fluid mass flow rate must be incremented with the available power. The glide, instead, must be reduced as the available power and the storage temperature decrease.

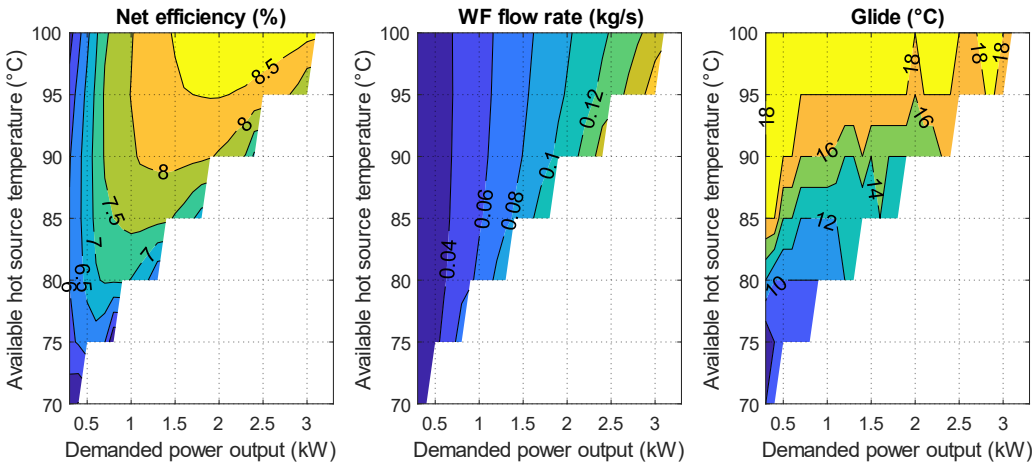

Figure 6-11 - ORC optimized regulation for given boundary conditions.

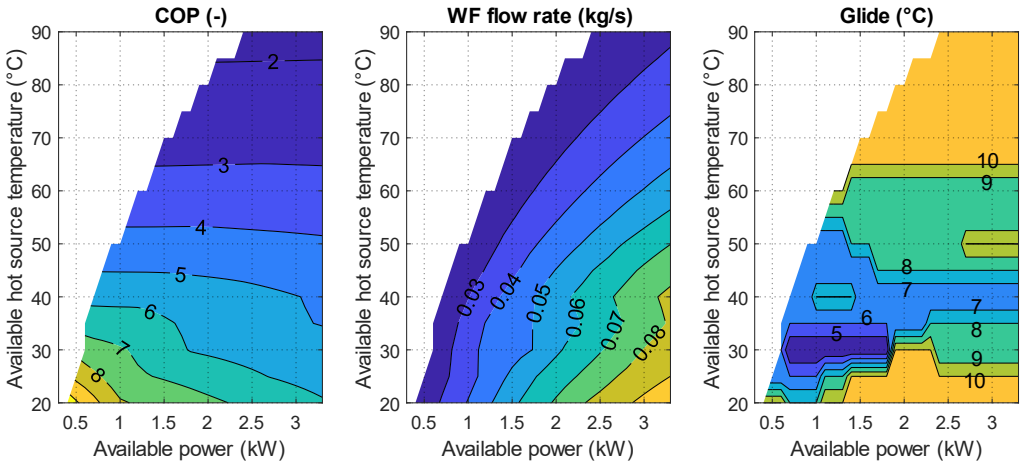

Figure 6-12 - HP optimized regulation for given boundary conditions.

6.5 Analysis of feasibility

6.5.1 Case study

This chapter proposes an analysis of feasibility of the Carnot battery system as function of the magnitude of the process energy demand/availability and of an external heat source. Some considerations about the optimal sizing of the storage, depending on the application, are also made.

As case study, a possible industrial energy profile over 160 hours is considered [102] (see Figure 6-13), involving: i) an electric power consumption by the user, ii) an electric power production generated by a solar photovoltaic power plant (PV), and iii) a given amount of thermal power released from the process. According to the considered profile, an almost constant power demand is required during the entire days, slightly rising during the working hours. The PV production instead starts with the daylight to end at the sunset, with peaks in correspondence of the central hours of the day, which lead to an energy surplus production. The waste heat production is also considered intermittent but constant during the working hours.

Considering the introduction of the Carnot battery, part of the energy surplus, which was previously sold to the grid (E_{HP}), could be otherwise exploited to charge the storage resulting in a loss of profit. On the other hand, part of the energy deficit (E_{ORC}) would be covered by the Carnot battery energy production, in place of the grid, leading to an avoided cost. So that the economic gain (or cost) introduced with the Carnot battery, $CB\ gain$, can be evaluated as the difference between the loss and the avoided cost, as shown in Eq. (6-11).

$$CB\ gain = E_{ORC} \cdot C_{purchase} - E_{HP} \cdot C_{sell} \tag{6-11}$$

Where $C_{purchase}$ is the purchase price, considered equal to 0.2 eur/kWh, and C_{sell} is the sell price, considered equal to 0.07 eur/kWh [102].

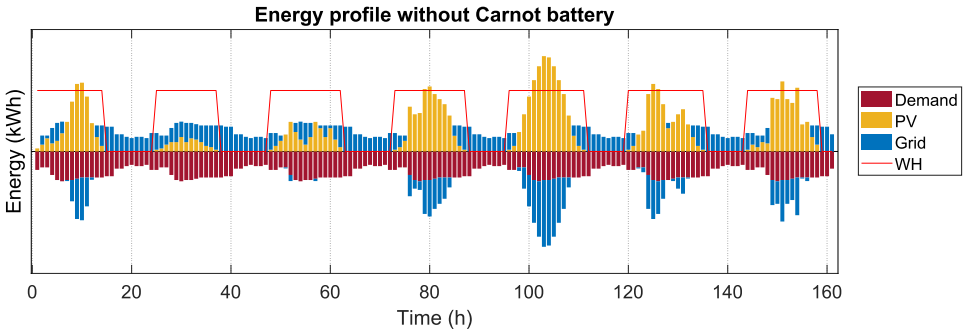

Figure 6-13 - Case study energy profile without Carnot battery.

Another important aspect to consider is the payback period of the investment, which can be simply considered as the ratio between the investment and the $CB\ gain$ calculated over a year. For a comprehensive analysis this index is also taken into account. The $CB\ gain$ over the year is assumed in first instance equal to the $CB\ gain$ over the 160 hours, on which the energy profile is known, scaled on the year basis. The investment on the Carnot battery is calculated as the sum of two cost contributions, one related to the storage and the other related to the reversible ORC/HP system. The

cost of the reversible ORC/HP system is assumed equal to the cost of a simple ORC, estimated by means of the micro-ORC cost correlation introduced in Figure 1-13. According to this correlation the cost of a 3 kW scale micro-ORC can be assumed equal to 14 151 €. The storage cost correlation curve derives instead by the interpolation of commercial insulated buffer tanks prices, proposed by the Bespoke Tank supplier [103]. Data for tank size ranging from 0.5 to 8 m^3 have been included.

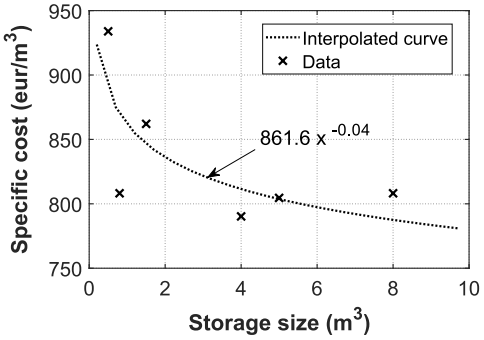

Figure 6-14 - Storage specific cost correlation, derived by manufacturer's data [103].

6.5.2 Cost parametric analysis and storage volume optimum design

The Carnot battery economic convenience is investigated by varying some parameters, namely the WH thermal power value‡‡‡ and the $Scaling\ factor$, here defined as the ratio between the Carnot battery nominal power, $\dot{W}_{nom,CB}$, and the demand power peak, $\dot{W}_{demanded,peak}$ (see Eq. (6-12)); this parameter gives an indication of the size of the industrial process compared to the one of the reversible ORC/HP system.

$$Scaling\ factor = \dot{W}_{nom,CB}/\dot{W}_{demanded,peak} \tag{6-12}$$

For each combination of the scaling factor and the available WH thermal power, the storage size has been optimized to return into the investment in the lowest possible payback period. The results of the optimization are presented in the maps of Figure 6-15. The analyzed parameters are the $CB\ gain$ and the Carnot battery average load, $av.load_{CB}$, (see Figure 6-15a), the payback period, PB, and the optimal storage size, V_{sto} (see Figure 6-15b). Empty spaces represent the areas where there is not gain, in Figure 6-15a, or the payback period is higher than 40 years, in Figure 6-15b. The red dots represent four different scenarios for which the energy profiles are shown in Figure 6-16, to support the comments on the results.

The results show that the payback period strongly decreases with the WH thermal power and slightly increase with the scaling factor. In the best case the payback period can even drop below the 10 years, but to have reasonable values of the payback period (PB < 20 years) a WH thermal power higher than 20 kW is required. The gain also strongly increases with the WH thermal power and slightly increase with the scaling factor, for thermal power until 40 kW. Above this value the maximum gain shifts towards lower values of the scaling factor and it reaches its global maximum

‡‡‡ value during the heat releasing process operative hours.

in correspondence of the maximum WH thermal power (50 kW) and a scaling factor equal to 0.3. This trend is determined by the influence of the Carnot battery average load; indeed:

- low values of the average load indicates that the storage is often empty. That means that the thermal inertia of the storage is only limitedly exploited and the ORC mode depletes the stored energy in a short time. See for example Figure 6-16, scenario 3, which exhibits a high slope of the discharge curve and a low value of Carnot battery operating hours. In this case the Carnot battery is empty for a great number of hours.
- higher values of the average load are instead beneficial since the battery discharge time is more comparable to the demand need; see for example Figure 6-16, scenario 2, where the end of the discharge curve often coincide to the begin of the consecutive charge curve. From the cost maps, an optimal value of the average load, equal to 60 %, can be identified, in correspondence of the maximum gain. Above this value, the battery is almost always full charged given that the ORC production cannot be further exploited (limited by the Carnot battery nominal power); thus, it is more convenient to under size the reversible ORC/HP (system have lower scaling factors) to decrease the investment costs.

The average load increases:

- with the scaling factor since the relative demanded power decreases and the average storage discharge time increases as consequence (see Figure 6-17), despite low demanded power value affects the performance of the ORC mode so that the ORC consumes higher related thermal powers to operate. This second effect however is less significant.
- with the WH thermal power because the higher is the thermal power, the lower is the average storage charge time (see Figure 6-18). The HP performance also improves with the WH thermal power, since the higher is the WH thermal power, the lower is the time the HP has to work at low *COP* operating conditions (i.e. high condensing temperature).

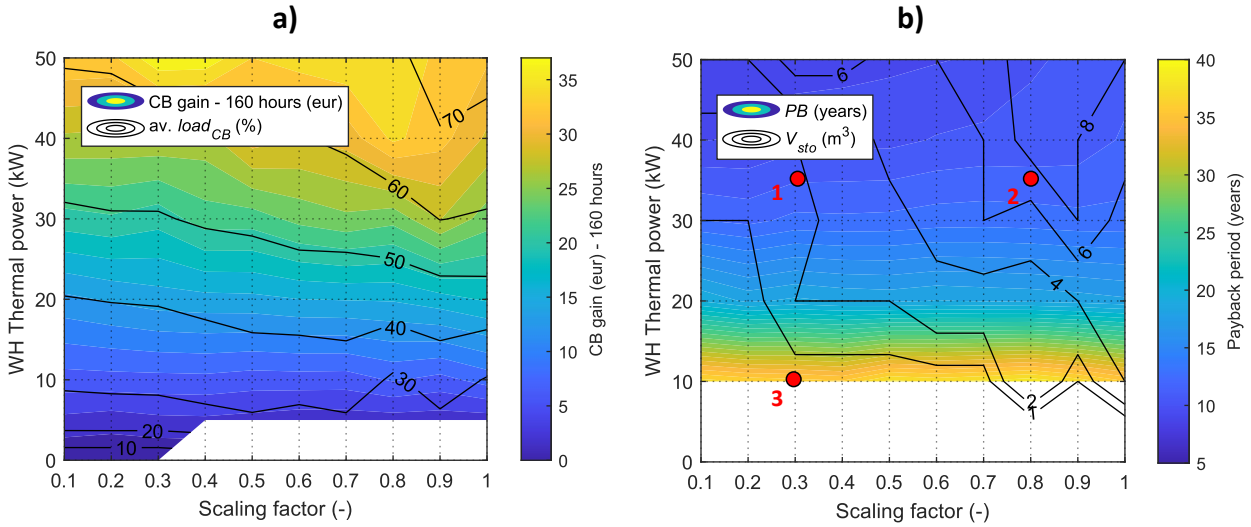

Figure 6-15 - Economic feasibility of the Carnot battery as function of the WH thermal power and the scaling factor, at optimized storage size.

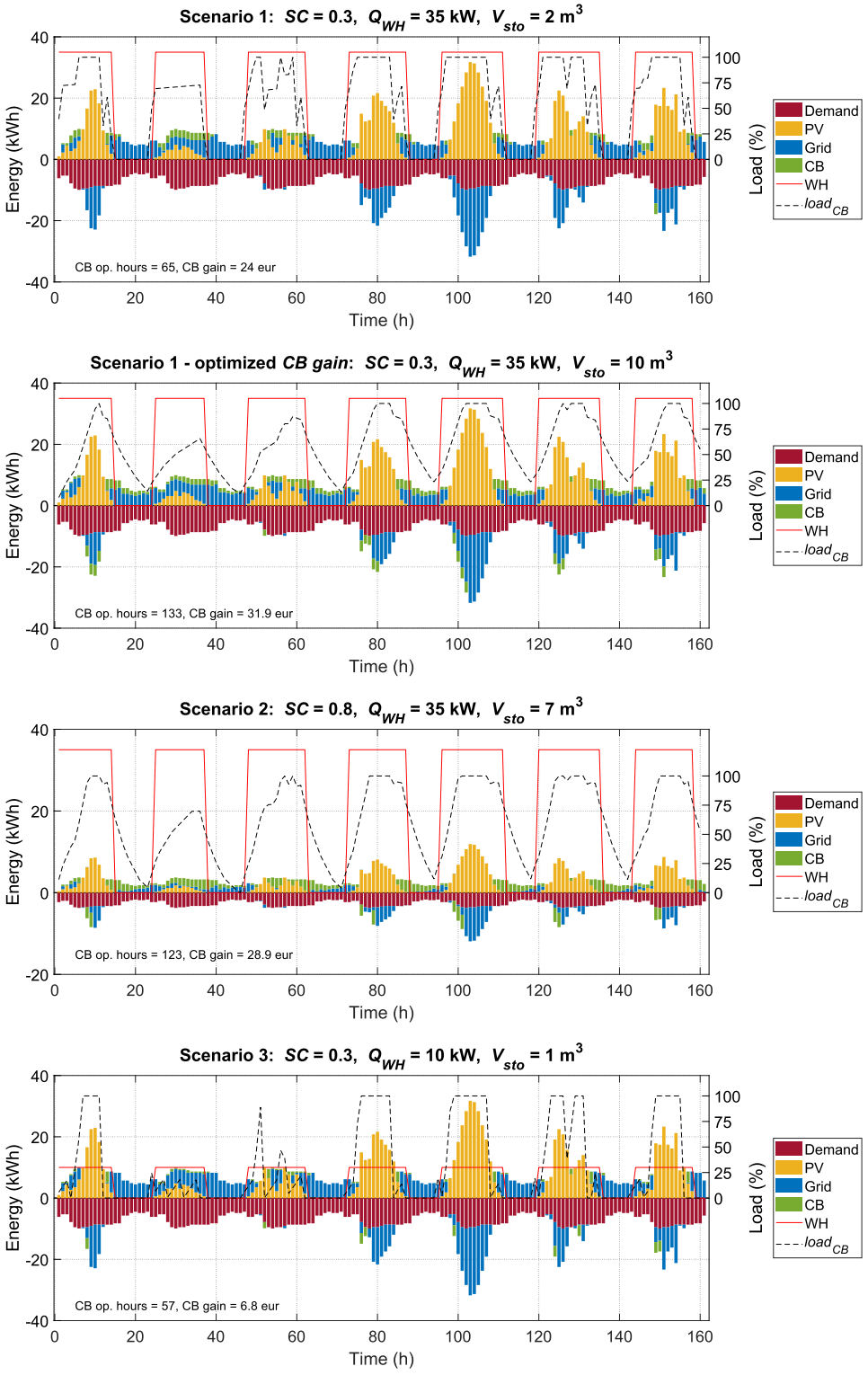

Figure 6-16 - Case study energy profile with the Carnot battery in different scenarios.

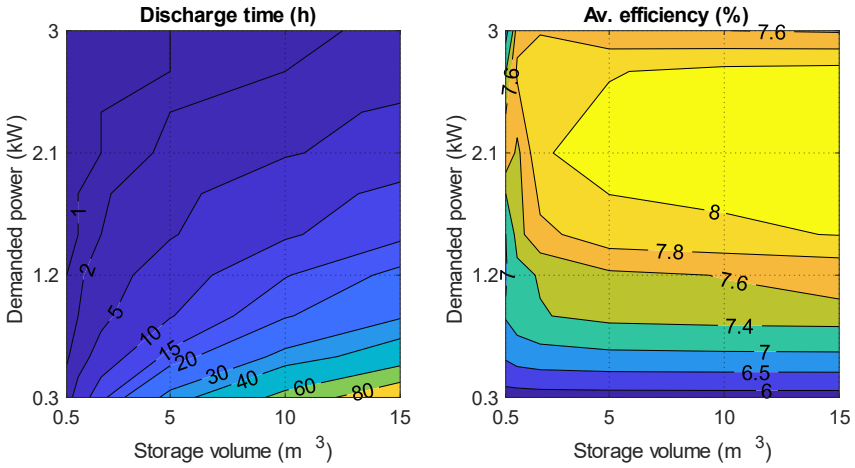

Figure 6-17 - Discharge performance as function of the storage size and the demanded power – hypothesis: WH thermal power = 0 kW.

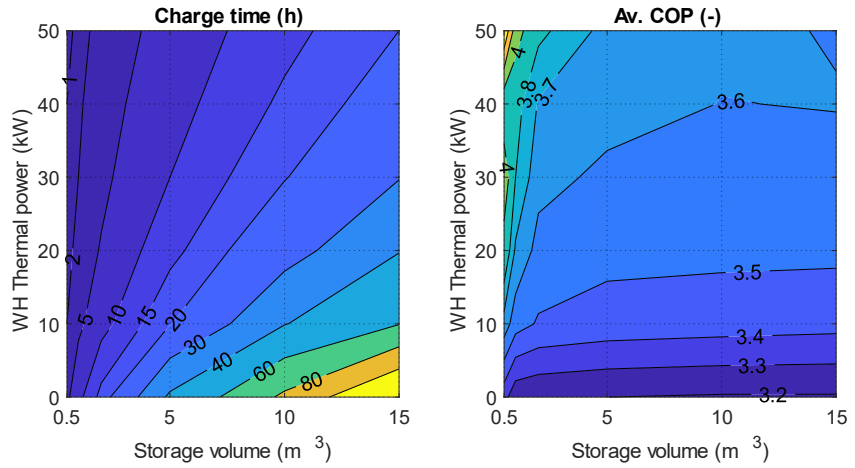

Figure 6-18 - Charge performance as function of the storage size and the WH thermal power– hypothesis: W_{ava} = 3 kW.

The storage size also strongly influences the charge and the discharge time and that's why it is a crucial parameter to optimize. In particular, the more the storage volume is big the more the thermal inertia is higher and so are also the charge and the discharge time.

As expected, the optimal storage size (see Figure 6-15b) follows a trend similar to the one of the average load (see Figure 6-15a), because the higher is the WH thermal power, the higher is the storable energy and the potential economic gain. Nevertheless, the optimal storage size decreases at lower scaling factor because there is less and less convenience on invest on large storage size, since the storage cost increases significantly with the size whilst the increment of the economic gain increases less and less, due to the decrease of the relative Carnot battery production. Consequently, for high WH thermal powers and low scaling factors, it less convenient to use the HP mode and it is rather preferable to under size the storage and sell the surplus of electric energy produced by the renewable source. It can be seen for example comparing, scenario 1 to scenario 1 – *CB gain* optimized (Figure 6-16), where the storage size is optimized to minimize the payback period in the first case

and to maximize the gain in the second one. It can be observed that the optimal storage size increases from 2 to 10 m^3, the number of the HP operating hours pass from to 1 to 20, the gain slightly increases but also the payback period (from 12 to 13 years) due to the higher investment on the storage.

6.6 Conclusion

In conclusions, the results of this analysis can be summarized per points:

- The Carnot battery performance are influenced by the boundary conditions and by the control variables, namely the working fluid flow rate and the secondary fluid glide at the heat exchangers (influenced by the secondary fluid flow rate, for given working fluid flow rate). The glide in particular influence the pressures inside the cycle and, thus, the available cycle pressure ratio. It follows that the expander/compressor is not working in optimal conditions for some values of the glide, since under-expansion/compression and over-expansion/compression losses can occur, affecting the machine efficiency. A proportionality between the produced/absorbed power is observed when the working fluid flow rate increases, respectively for the ORC/HP mode. The thermal power input/output (exchanged at the evaporator/condenser in ORC/HP mode) is also proportional to the mass flow rate. Finally, the performance maps highlight that the maximum efficiency/COP point does not always corresponds to the maximum power production/minimum power production, for the ORC/HP mode respectively.
- According to the proposed regulation strategy, the Carnot battery is managed in order to work in each mode (ORC or HP) at maximum net efficiency (or COP, in HP case) under the imposed boundary conditions. The results of the optimal control strategy application show that in order to reach the maximum ORC efficiency for each boundary conditions' combination, the working fluid mass flow rate must be incremented with the demanded power output. In most of the cases, instead, the glide must be incremented with the available hot source temperature. Concerning the HP, in order to reach the maximum *COP* for each boundary conditions' combination, the working fluid mass flow rate must be incremented with the available power. The glide, instead, must be reduced as the available power and the storage temperature decrease.
- From the economic point of view, the results show that in the best case the payback period can even drop below the 10 years, but to have reasonable values of the payback period (PB < 20 years) a WH thermal power integration higher than 20 kW is required. The Carnot battery average load during operation can be index of the good operation of the Carnot battery. Indeed, low values of the average load indicates that the thermal inertia of the storage is only limitedly exploited and the ORC mode depletes the stored energy in a short time. Higher values of the average load are instead beneficial until the battery discharge time is comparable to the demand need; namely, the end of the discharge curve often coincide to the begin of the consecutive charge curve. In particular, the average load increases: i) with the scaling factor since the demanded power decreases and the average storage discharge time increases as consequence; and ii) with the WH thermal power because the higher is the thermal power, the lower is the average storage charge time.

- The storage size also strongly influences the charge and the discharge time. The storage size that minimizes the payback period follows a trend similar to the one of the average load, because the higher is the WH thermal power, the higher is the storable energy and the potential economic gain. Nevertheless, the optimal storage size decreases at lower scaling factor because there is less and less convenience on invest on large storage size, since the storage cost increases significantly with the size whilst the increment of the economic gain increases less and less, due to the lower relative Carnot battery production. Consequently, for high WH thermal powers and low scaling factors, it is less convenient to use the HP mode and it is rather preferable to under size the storage and sell the surplus of electric energy produced by the renewable source. However, even if these considerations are valid for this size of the Carnot battery (3 kW), they could not be rigidly shifted to greater scales. Considering the case that the Carnot battery size is scaled up, the gain would increase more than the investment costs, thanks to the scale effect. In this situation it would be more convenient to invest on larger storage and obtain even bigger economic benefit, also by exploiting more the HP mode.

PART II

ORC for the medium to large scale industrial WHR

7 Modelling approach

Summary: In this section, a different modelling approach is used to reproduce the behavior of the ORC and the other energy systems in exam. In this case, a software born to simulate complex power plants in both design and off-design condition, i.e. *Thermoflex* [80], is chosen as simulation tool. Differently from small-scale ORC, indeed, systems whose size is in the range of the MW are formed by commercial machines, for which reliable models are already provided also by commercial softwares. Even if these models are already available, nevertheless, it is up to the user to make effective decisions on the model parameters in order to obtain realistic results. Among these parameters are for example some indexes related to the nominal performance of the components and the strategies of control of the plant at part-load operation.

It is the aim of this chapter to describe the modelling approach implemented in *Thermoflex* and explain the choices made to simulate the systems in exam in the most possible realistic way.

7.1 Energy system layout

The energy system analyzed in the following chapter is in its most generic configuration composed by a topper cycle, releasing waste heat, and a bottomer cycle, converting this heat into electric power. The topper/bottomer waste heat recovery configurations taken into account is schematically presented in Figure 7-1. In this study, the topper cycle is a gas turbine (GT) power plant and the bottoming cycle is an ORC, composed by a one through boiler, a centrifugal turbine, a condenser, a centrifugal pump and a recuperator. Depending on the topper/bottomer thermal connection, an intermediate heat transfer fluid (IHTF) circuit may also be placed in between exhaust gases and organic fluid.

The integration of the ORC into natural gas compressor stations is considered as case study in the following paragraphs. Thus, a brief description of the ORC possible integration arrangements for this application is reported. Natural gas compressor stations are installed along the natural gas transmission lines, every 100-140 km, in order to overcome the pressure drops resulting from the frictional gas flow in the pipeline and so move the gas at high pressures over long distances from gas sources or storage sites to distribution centers. The gas compression is usually performed in centrifugal or reciprocating compressors driven by GTs, electric motors or reciprocated engines. The typical installation arrangement consists of multiple driver units with a potential of operating under part-load conditions and redundant installed capacity in order to ensure the necessary reserve power and the safe operation of the compressors (see Figure 7-2a).

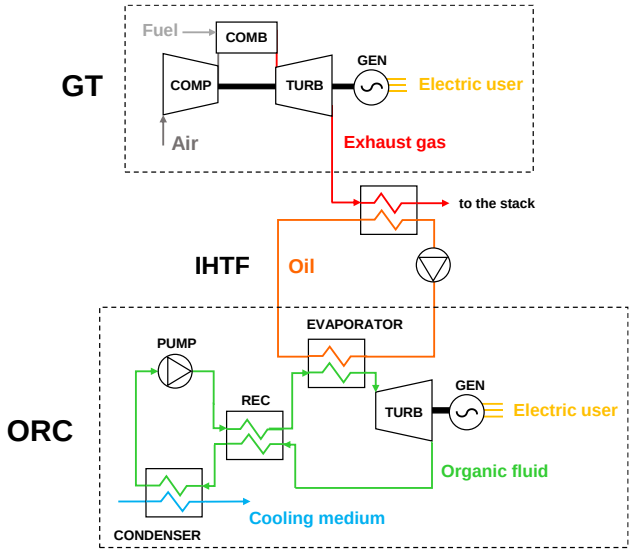

Figure 7-1 - Generic energy system configuration.

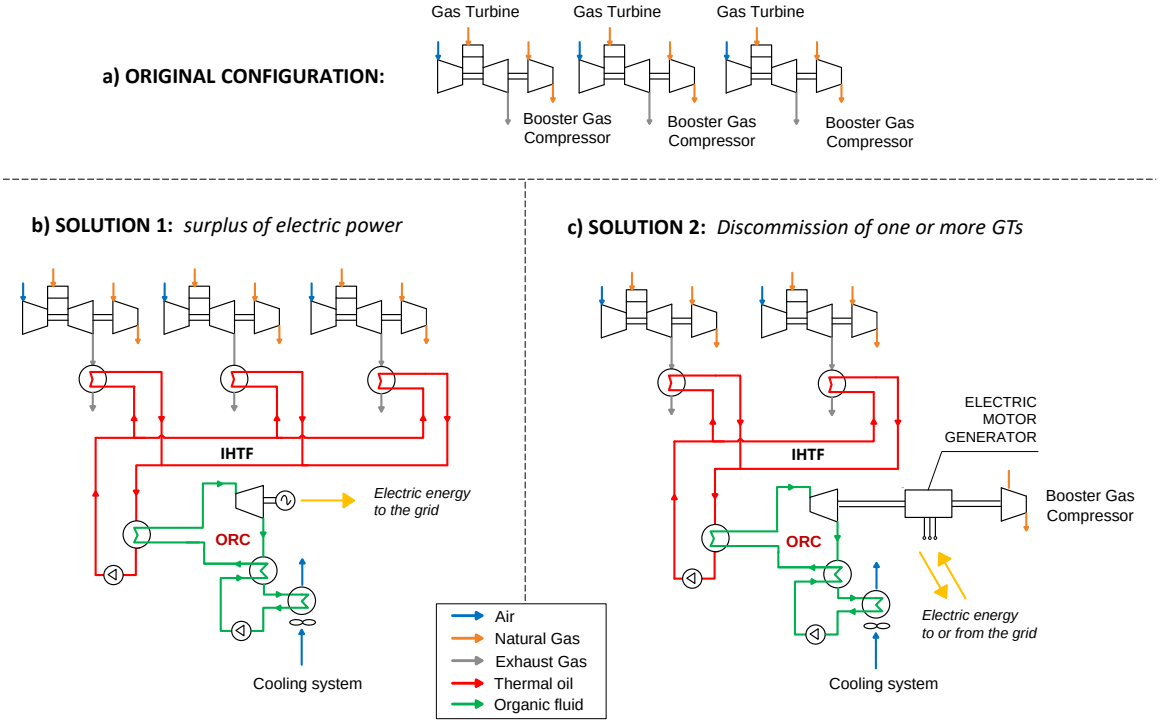

Figure 7-2 - schematic of ORC possible integration arrangements.

The ORC bottomer cycle can be integrated into the original GT drivers' arrangement with two different purposes:

- Solution 1: the generation of electricity, through waste heat recovery, keeping the actual GT drivers' arrangement. Realizing this solution, the ORC generator produces a surplus of electrical power output that will be fed into the grid (Figure 7-2b).

- Solution 2: the generation of mechanical power to drag a compressor, compensating the decommissioning of one or more GT units. Thus, this solution involves a change in the original drivers' arrangement (Figure 7-2c) that could be beneficial in terms of primary energy and, consequently, CO_2 reduction. This alternative not yet investigated in literature, can be preferred for remote applications when the electric energy sale to the grid can be discouraged.

The arrangement (b) is the simplest and most diffused topper-bottomer solution where the surplus of energy, generated with the ORC, is sent to the grid in the form of electricity. The alternative (c), as more innovative and environmental-friendly solution, implies a reduction of the original GT number and the addition of an electric motor generator (EMG). Indeed, ORC turbines available on the market are conceived for electric power production purpose, thus they are designed to rotate at the shaft speed imposed by the electric grid, i.e. 3000 or 3600 rpm, depending on the grid frequency. Centrifugal compressors, instead, run at very higher speeds, which range between 10000 and 30000 rpm, depending on size [104]. In order to connect these two components, a simple solution is conceived by connecting the ORC to the compressor through a variable speed electric motor driven-unit (the EMG) which converts the ORC generator electric power output into mechanical power to drive the compressor. In this way, the ORC expander and the natural gas compressor are not bounded to rotate at the same shaft speed. Thus, the ORC unit and the EMG, will provide the mechanical power necessary to drag the compressor in place of the decommissioned GT. The EMG unit can behave as a motor if the ORC cannot provide the entire mechanical power required by the compressor, or as a generator if the ORC produces a surplus of mechanical power; consequently, the electric energy can be withdrawn or supplied to the electric grid, respectively.

7.2 The Thermoflex model

7.2.1 Modelling steps

The *Thermoflex* software [6] allows for the thermodynamic modelling of power plants, starting from built-in library single components assembly, by means of a lumped parameters approach. Organic fluid properties are evaluated according to Refprop thermodynamic database [63].

More in detail, the topper cycle of the integrated system has been simulated as a single component according to Thermoflex large database of existing gas turbine models; indeed, more than hundred models of industrial gas turbines are featured in the library, provided with the design and off-design characteristics as communicated by the producers. Thus, the model consists in a black box, which only requires to select the gas turbine model the user wants to simulate. The bottomer cycle instead is modelled by connecting the single components that constitutes it: i.e., the heat exchangers, the turbine, the condenser and the operating machine. In this case, other inputs defining the components performance must be imposed by the user, as described in paragraph 7.2.3.

Once the system layout and the inputs are set, the software allows for the simulation of the energy systems performance both in design and off-design operation, by following three consecutive steps, namely "Thermodynamic design", "Engineering design" and "Off-design":

1. In the "Thermodynamic design" step the scheme of the system and the boundary conditions are given, as fixed inputs, on the basis of which the program computes preliminary heat and mass balances.
2. In the second step, the "Engineering design", the size and the geometry details of each component is established, on the basis of the imposed design boundary conditions and components specifics.
3. Finally, in the "Off-design" step, being defined the design characteristics and fixed the geometry of the components, depending on selected control logics, it is possible to predict both components and overall system behavior under different operating conditions, thus obtaining off-design performance.

7.2.2 Part-load models

In particular the approach followed to model the single components of the plant at part-load conditions is described below:

Gas turbines

The off-design performances of GT units (i.e. performance at part-load conditions and/or ambient derating) are obtained by means of the black box model based on the manufacturers guaranteed data.

Heat exchangers

The heat exchangers off-design behavior is described by the so called "thermal resistance scaling" method. Following this method, the design point convective heat transfer coefficients (UA_{des}) of the generic fluid involved in the heat exchange, is scaled as function of the ratio between the actual mass flow rate, $\dot{m}$, and the one calculated in the design point, $\dot{m}_{des}$. A scaling exponent equal to 0.8 (which recalls the exponent for the Reynolds number in the Dittus Boelter correlation) is applied to the mass flow rate ratio. This approach is valid since the thermal-hydraulic properties of the fluids do not change much over the range of considered conditions, and the fluid velocity remains the main parameter affecting the heat transfer coefficients.

$$UA = UA_{des} \cdot \left(\frac{\dot{m}}{\dot{m}_{des}}\right)^{0.8} \tag{7-1}$$

It can be pointed out, that in conditions of fluid phase change or in proximity of the critical pressure, the program implements a discretization of the heat exchanger for the determination of the heat exchanger's UA, automatically assigning distinct zones for each phase of the fluid, or if the pressure is near the critical pressure, 13 equally weighted zones are assumed.

Normalized heat loss in the heat exchangers is computed as a percentage, relative to the heat transferred out of the higher temperature fluid. Flow resistance coefficients, initialized at the design-point stage, are used to model the pressure drops, Δp, across each side of the heat exchanger in off-design operation. Eq. (7-2) expresses the relationship between the flow resistance coefficient, ε, (initialized in the design-point), the pressure drops, the mass flow rate, $\dot{m}$, a dimensional constant, C, and the average specific volume, v (mean between the specific volumes at the inlet and at the outlet).

$$\varepsilon = \frac{\Delta p}{v \cdot \dot{m}^2 \cdot C} \tag{7-2}$$

Bottoming cycle turbine

The turbine inlet conditions, in terms of temperature and flow rate, vary at part-load operation depending on the exhaust gas temperature and flow rate values. The turbine inlet temperature, T, is kept equal to its maximum possible value, respecting the constraints related to the evaporator performance and the fluid thermal stability limit. The off-design inlet pressure, p, is determined consequently by assuming the "sliding pressure" part-load control. Following this regulation strategy, the pressure at the turbine nozzle inlet vary proportionally to the mass flow rate, $\dot{m}$, in order to keep constant the flow function parameter value, ff, assuming chocking conditions.

$$ff = \frac{\dot{m} \cdot \sqrt{T}}{p} = \text{const} \tag{7-3}$$

However, there are situations in which it is not possible to maintain constant the flow function parameter, as happens for example when the fluid temperature at the expander inlet changes significantly. In this case the turbine isentropic efficiency, η_{is}, is reduced with respect to its full load value, $\eta_{is,des}$, based on the flow function, as follow:

$$\eta_{is} = \eta_{is,des} - \frac{\left(\dot{m} \cdot \sqrt{v/p}\right)_{des}}{\dot{m} \cdot \sqrt{v/p}} \tag{7-4}$$

7.2.3 Choice of the system specifics

Differently from small-scale ORC, systems whose size is in the range of the MW, as it is the case, are formed by commercial machines, whose performance are already assessed in several applications. For this reason, ORC design data to provide to the model are selected based on existing large-scale state of the art products and in particular in line with Turboden typical operating parameters [23] (see Table 7-1). In particular:

- The cyclopentane and the Hexamethyldisiloxane (MM) (respectively belonging to the hydrocarbons and the siloxanes families) are the selected fluids being typical organic fluids in industrial medium waste heat recovery application state of the art [19]. Fluids belonging to the hydrocarbons and the siloxanes families are demonstrated to be the most suitable fluids for the medium temperature applications, thanks to their quite high critical temperature. Indeed, a value of the critical temperature quite similar or slightly higher than the target evaporation temperature is suggested, to achieve at the same time a good thermal matching between fluids and exhaust gas and avoid excessively low vapor densities, which lead to increasing system cost. Cyclopentane and MM feature similar critical temperature, around 240 °C (see Figure 7-3), and thermal stability limits, while they appreciably differ in terms of critical pressure and molecular weight. In particular MM presents a higher molecular weight (162 kg/kmol against 70 kg/kmol of the cyclopentane) which leads to lower speed of sound during the expansion, allowing to design the turbine with a lower number of stages (even only a single stage). This is the main reason why MM is the ideal candidate for small size applications (ORC size < 3 MW), even if due

to its high molecular weight MM presents also smaller enthalpy drop and expansion specific works if compared to cyclopentane.

- the expander inlet state is set to superheated vapour at a temperature determined by the gas exhaust heat exchanger performance and by the cycle maximum pressure. Temperature is conservatively limited to 280 °C, in order to not overcome thermal stability limit corresponding to 300 °C. The cycle maximum pressure (corresponding to the evaporating pressure) is limited to the 90 % of the fluid critical pressure value, equal to 45.1 bar for the cyclopentane and 19.4 bar for the MM (see Figure 7-3).
- the condensing pressure first guess value can be imposed equal to the fluid saturation pressure value at the cooling medium temperature, according to data in Figure 7-3. The program then, during the computation will adjust this value to match the minimum condensing pressure which respect the minimum pinch point allowed by the heat exchanger. The minimum allowed pressure value is set equal to 0.3 to limit the investment costs.
- the turbine and the pump isentropic efficiencies values are considered different for ORC power plant size lower or higher than 3 MW, to account for the machine size-effect over the performance.

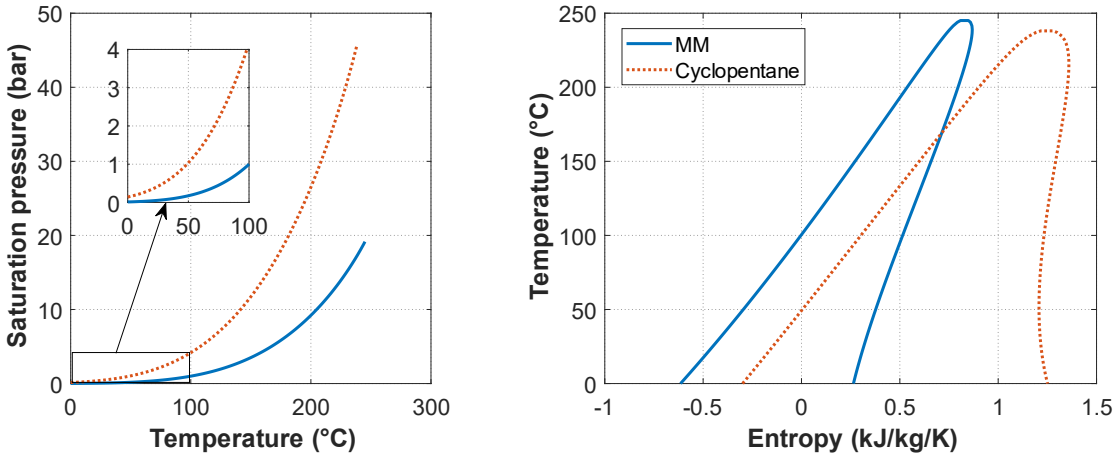

Figure 7-3 - Saturation thermodynamic properties of MM and Cyclopentane §§§.

Other general parameters to impose concern the ambient condition and the heat recovery circuit. In particular, in the next paragraphs, unless otherwise noted, the site conditions are considered ISO and the ORC cooling medium is air. The minimum GT stack temperature is bounded below at 125 °C to avoid the cold-end corrosion issues in the exhaust stack. Then, when the intermediate heat transfer loop is present, Therminol 66 is chosen as intermediate fluid and a temperature limit is set, in order to not overcome its thermal stability limit.

§§§ Curves obtained by means of the RefProp thermodynamic library [63].

Table 7-1 - GT-ORC design assumptions.

General	**Site ambient conditions**	ISO
	Miscellaneous GT aux. load (% of GTs power)	0.7
	Inlet/outlet duct pressure losses (mbar)	10
	Minimum GT stack temperature (°C)	125
IHTF	**Intermediate heat transfer fluid**	Therminol 66
	IHTF maximum temperature (°C)	315
	IHTF loop max. pressure (bar)	15
	Pressure drop in IHTF loop (bar)	2
	HX pressure drop, IHTF/ gas side (bar)	1.5/0.015
ORC	**Organic fluid (small size ORC ≤ 3 MW)**	MM
	Organic fluid (large size ORC > 3 MW)	Cyclopentane
	ORC expander isentropic efficiency (large/small size expander) (-)	0.85/0.80
	ORC evaporative pressure-critical pressure ratio (-)	0.76
	Boiler pressure drop, organic fluid/ IHTF/gas side (bar)	2/1/0.015
	REC effectiveness (%)	85
	REC pressure drop ORC liquid/vapour side (bar)	1/0.55
	Subcooling ORC outlet condenser (°C)	5
	Condensing pressure Cyclopentane/MM (bar)	0.6/0.3
	Condenser pressure drop, organic fluid side (bar)	0.1
	Cooling medium	air
	Heat exchangers thermal loss (%)	1
	Pumps mechanical efficiency (%)	80
	Pumps nominal isentropic efficiency (%)	60

7.3 Assessment indexes

Different kind of indexes, of energetic, economic and environmental nature, are evaluated to support the analysis of the power plants in exam.

7.3.1 Power plant performance

The most relevant performance indexes analyzed in the following chapters are (as defined in Table 7-2): i) machine available isentropic power (Eq. (7-5)), ii) the bottomer power production (Eq.(7-6)), iii) the net total power production (Eq. (7-7)), iv) the plant electric efficiency (Eq. (7-8)), and in the cogenerative cases also v) the thermal efficiency (Eq. (7-9)) and vi) the *PES* index (Eq. (7-10)).

Table 7-2 - Performance indexes for design performance evaluation.

Index	Equation
Machine available isentropic power	$\dot{W}_{is} = \dot{m} \cdot (h_{in} - h_{out,is}(s_{in}, p_{out}))$ (7-5)
Bottomer expander power	$\dot{W}_{exp}$, with $\dot{W}_{net,bott} = \dot{W}_{exp} - \dot{W}_{op.machine}$ (7-6)
Net electric power	$\dot{W}_{net,tot} = \dot{W}_{GT} + \dot{W}_{net,bott} - \dot{W}_{misc}$ (7-7)
Electric efficiency	$\eta = \frac{\dot{W}_{net,tot}}{F}$ (7-8)
Thermal efficiency	$\tau = \frac{\dot{Q}_{cog}}{F}$ (7-9)
Primary energy saving for cogenerative power plants	$PES = 1 - \frac{1}{\frac{\eta}{\eta_{ref}} + \frac{\tau}{\tau_{ref}}}$ (7-10) with η_{ref} =52.5 % and τ_{ref} = 90 % (source [105])

- The expander/operating machine available isentropic power ($\dot{W}_{is}$) is given by the difference between the machine inlet enthalpy, h_{in}, and the value the enthalpy would have at the machine outlet if the process were isentropic, $h_{out,is}$, multiplied to the fluid mass flow rate, $\dot{m}$. The isentropic outlet condition is evaluated at the machine outlet pressure, p_{out}, and machine inlet entropy, s_{in}. Isentropic power is a useful thermodynamic index to evaluate theoretical power available for the expansion process or absorbed by the operating machine.
- The net electric power ($\dot{W}_{net,tot}$) is given by the sum of the net electric power generated by the gas turbine, $\dot{W}_{GT}$, and the net electric power generated by bottomer cycle, $\dot{W}_{net,bott}$, minus the plant miscellaneous absorbed power, $\dot{W}_{misc}$.
- The Net electric efficiency (η) is given by the ratio between the net electric power and the GT fuel input power with reference to the lower heating value, F.
- Recovered thermal power for cogenerative purpose ($\dot{Q}_{cog}$) is calculated as the product of cooling medium mass flow rate and the enthalpy difference through the cogenerative heat exchangers.
- Thermal efficiency (τ) is given by the ratio between the recovered thermal power and the GT fuel inlet power, F.
- Primary energy saving (*PES*) is a quite common performance indicator for cogenerative energy systems and accounts for both the electric and the thermal production. In particular, the *PES* represents the energy savings of the considered combined heat and power plant with respect to a reference scenario of separate electric and thermal production. The reference electricity is supposed to be generated with a conventional pure electric system having an electric efficiency η_{ref} and the reference thermal production is generated with a standalone heat generator with thermal efficiency equal to τ_{ref}. The reference values selected for electric efficiency and thermal efficiency are 52.5 % and 90 %, respectively based on the European directive [105].

7.3.2 Component's size

Besides performance considerations, it may be also important to take into account some design aspects related to the investment cost and the space requirements. For this purpose, the size of key components (heat exchangers and expander) can be preliminary evaluated by means of the presented indexes. The following parameters are computed in a second step, as function of the performance results obtained by means the Thermoflex software:

- The heat exchanger size parameter (A) is defined as the heat exchanger surface area, as function of the global heat transfer coefficient, U, the exchanged thermal power, Q, and the heat exchanger mean logarithmic temperature difference, ΔT_{ml}, for a given heat exchanger:

$$A = \frac{Q}{U \cdot \Delta T_{ml}} \tag{7-11}$$

  The global heat transfer coefficient is computed as function of the convective coefficients of the two fluids involved into the heat exchange process, neglecting the conductive contribution at the wall:

$$U = \left(\frac{1}{\alpha_1} + \frac{1}{\alpha_2}\right)^{-1} \tag{7-12}$$

  Assuming fully developed turbulent flow in forced convective regime, Dittus-Boelter correlations is used to estimate the convective heat transfer coefficients, α_1 and α_2.
- The expander size parameter (SP) is proposed to evaluate expander size as function of the fluid operating condition inside the machine. This nondimensional index is defined as the ratio between the fluid volume flow rate evaluated at the expander outlet pressure, and the isentropic enthalpy drop trough the expander, Δh_{is} [8]. The volume flow rate is given by the ratio between the fluid mass flow rate, $\dot{m}$, and its density, $\rho_{out,is}$.

$$SP = \frac{(\dot{m}/\rho_{out,is})^{0.5}}{\Delta h_{is}{}^{0.25}} \tag{7-13}$$

7.3.3 Environmental and economic benefit

The environmental and economic benefit introduced with the ORC are evaluated by comparing the ORC solution with a reference scenario, to compute the differential emissions and costs. In this study, depending on the ORC arrangement, the environmental and economic benefit will be assessed using different assumptions, as described below.

Possible arrangements

The feasibility of the GT-ORC integration is evaluated comparing an original layout without ORC with different possible modified arrangements. Figure 7-4 schematically illustrates both proposed arrangement solutions, highlighting the energy flows between the main components.

The original topper layout consists in a GT or a GT train installation with multiple identical machines in a parallel set-up. Choosing as example a natural gas compressor station application, GT

is supposed to drive a compressor unit. The ORC bottomer cycle can be integrated into the original GT drivers' arrangement with two different purposes (as anticipated in paragraph 7.1, Figure 7-2):

- Case a: the generation of electricity, through waste heat recovery, keeping the actual GT drivers' arrangement. Realizing this solution, the ORC generator produces a surplus of electrical power output that will be fed into the grid (Figure 7-2a).

Case b: the generation of mechanical power to drag a compressor, compensating the decommissioning of one or more GT units (Figure 7-2b). In the scenarios in which the electric motor generator is necessary for an energy integration, it will be simulated according to the conversion efficiency curve presented in Figure 7-5.

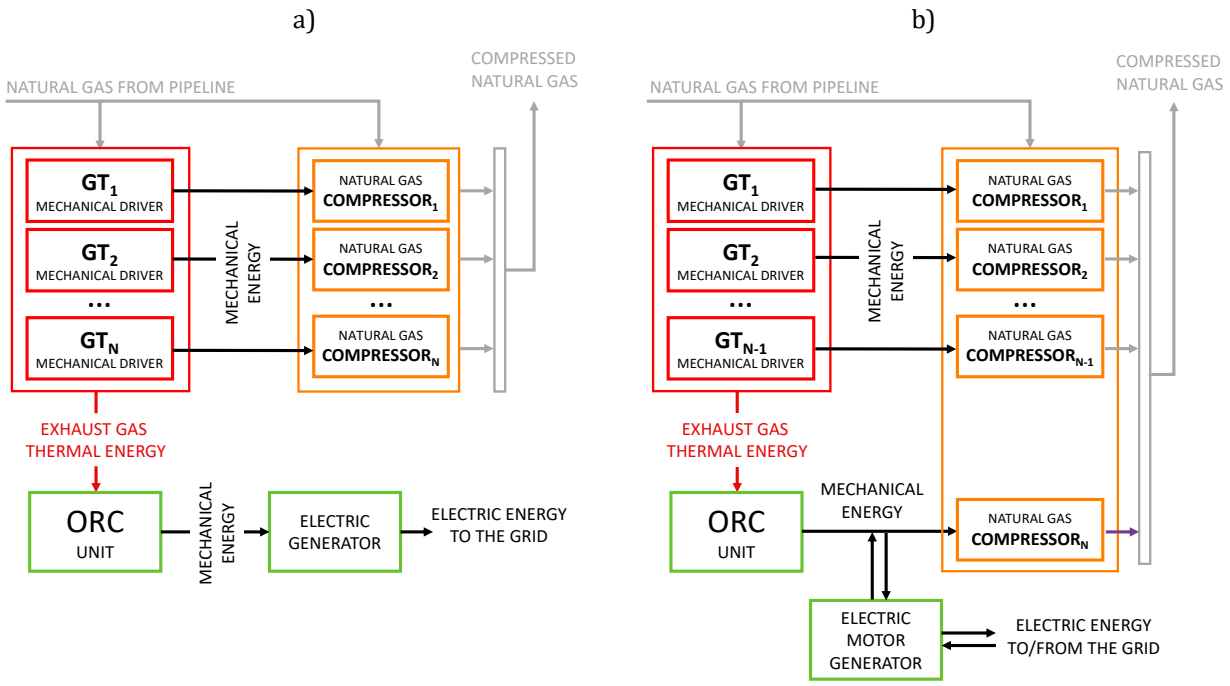

Figure 7-4 - Schematic of the ORC possible management strategies: a) surplus of electric energy generation; b) natural gas compressor drive.

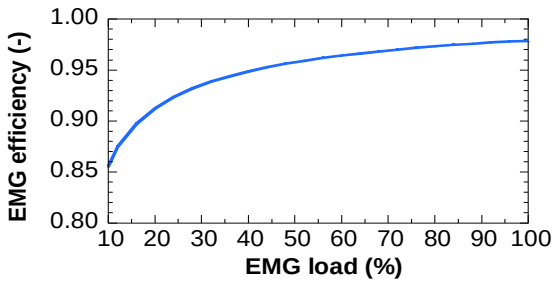

Figure 7-5 - EMG efficiency at part-load operation (data source [26]).

Its performance thus depends on its load: the efficiency reaches is maximum value of 98 % at nominal condition and slightly decrease with the load. In order to account for the additional cost

of the EMG, the ORC investment curve, inclusive of the cost of the electric generator, is increased by a correction factor proportional to the required mechanical power to be integrated [26].

The comparative indexes

The benefit due to the introduction of the ORC is related to the saving of primary energy, which leads to a gain from both economic and environmental perspective. The benefit is evaluated differently depending on the adopted ORC integration arrangement, using equations reported in Table 7-3:

Table 7-3 - Comparative indexes.

Index	Equation depending on the ORC arrangement		
	Surplus of electric energy	**Natural gas compressor drive**	
Primary energy saving	$E_{PES} = \frac{E_{net,bott}}{\eta_{ref}} + \frac{E_{cog}}{\tau_{ref}}$	$E_{PES} = \frac{E_{ORC} + E_{grid}}{\eta_{GT}}$	(7-14)
Consumed mass of fuel	$\Delta m_{FUEL} = \frac{E_{PES}}{LHV}$		(7-15)
Avoided emissions	$\Delta m_{CO_2} = \frac{44}{12} \cdot x_C \cdot \Delta m_{FUEL}$	$\Delta m_{CO_2} = \frac{44}{12} \cdot x_C \cdot \Delta m_{FUEL} - \beta_{CO_2,grid} \cdot \frac{E_{grid}}{\eta_{EMG}}$	(7-16)
Revenue	$R = \Delta m_{FUEL} \cdot C_{FUEL} + \Delta m_{CO_2} \cdot C_{CO_2}$		(7-17)
Cost	$C = 0$	$C = E_{grid} \cdot C_{EL}$	(7-18)

- Case a: the original arrangement is not modified. The evaluated gain is a fictious gain, evaluated on a global scale, considering that the energy produced from the ORC for free, will not be produced by the national energy mix, likely consuming fossil fuel.

  The return on the investment is estimated by assuming that introducing the bottoming cycle produces a fuel saving as it would cover the energy demand that otherwise should be provided by another reference energetic system. This primary energy saving, E_{PES}, is computed by means of Eq. (7-14), if considering both an electric, $E_{net,bott}$, and a thermal energy production, E_{cog}, in cogenerative configuration; where the reference efficiencies values are assumed equal to the ones used for the *PES* calculation [105].
- Case b: the ORC drives a natural gas compressor in place of a gas turbine. The gain is evaluated on the compressor station scale and it corresponds to a tangible gain for the industry, coming from a lower fuel consumption. In this case, the reference efficiency for the electric power production, is the one of the GT, η_{GT}. The amount of energy no more produced by means of the GT is given by the sum between the ORC energy production, E_{ORC}, and the energy purchased by the grid, E_{grid}, if necessary.

The differential consumed mass of fuel, Δm_{FUEL}, is quantified by means of Eq. (7-15), as the ratio between E_{PES} and the fuel lower heating value, LHV. Where the lower heating value is the one of the natural gas, assumed equal to 47 MJ/kg [106].

It is assumed that the avoided CO_2 emission, Δm_{CO_2}, is equal the CO_2 mass that would be produced by the stoichiometric combustion of the fuel saved (the fraction of carbon, x_C, is likely considered equal to 0.75 for the natural gas) (see Eq. (7-16)). In case 2, when the EMG is called to intervene, another term is added to the equation, related to the EMG operation in place of the GT. Where η_{EMG}, is the EMG conversion efficiency and $\beta_{CO_2,grid}$ is the CO_2 emission factor associated to the energy mix producing the energy purchased by the gird, E_{grid}.

The economic feasibility is determined by evaluating the differential net present value, ΔNPV, at the end of ORC assumed operating life. The ΔNPV is defined as:

$$\Delta NPV = \sum_{i=1}^{n} \frac{R_i - C_{,i}}{(i+q)^i} - I_{TOT} \tag{7-19}$$

The cash flow at the i-th year is computed as the difference between the yearly earnings, R_i, and the yearly costs, C_i. q is the discount rate assumed equal to 6 %, and I_{TOT} is the initial investment. Where the earnings comprehend the costs avoided thanks to the primary energy saving, in terms of fuel consumption and CO_2 emissions (if any carbon tax is present), see Eq. (7-17). In case a), no differential cost is present, whilst in case b) the costs include the potential cost of electricity which could be purchased from the grid, C_{EL}, in case the user demand is not covered by the GT and the ORC production, see Eq. (7-18).

The ORC specific investment cost trend assumed in this analysis is shown in Figure 7-6, consistent with Turboden products [23]. It can be observed that a slight increase of the cost is expected when the intermediate heat transfer circuit is required with respect to the direct heat transfer configuration (DHT), for large ORC sizes.

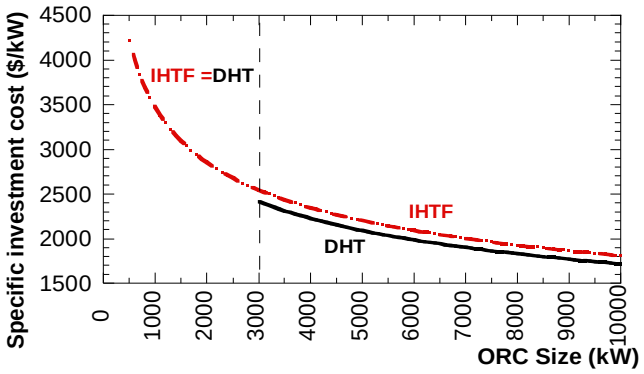

Figure 7-6 - ORC specific investment cost as function of the ORC plant size (data source [26]).

8 Factors of influence on the design of ORC as WHR solution in natural gas compressor stations

Summary: This chapter investigates the optimum size and potential economic, energetic and environmental benefits of ORC applications, as bottomer section in natural gas compressor stations. Since typical installations consist of multiple gas turbine units in mechanical drive arrangement, operated most of the time under part-load conditions, the economic feasibility of the ORC can become questionable even though the energetic advantage is indisputable. Depending on mechanical drivers' profile during the year the optimum size of the bottomer section must be carefully selected in order not to overestimate its design power output. To achieve this goal a numerical optimization procedure has been implemented, based on the integration of a in house-developed code with the commercial software for the thermodynamic design and off-design analysis of complex energy systems, *Thermoflex*. Thus, the optimal ORC design power size is identified in the most generic scenario, in terms of compressors load profile, installation site conditions (i.e. ambient conditions and carbon tax value) and gas turbine models used as drivers.

8.1 Contribution

In this study a methodology aimed at evaluating the feasibility and optimal design of an ORC system as the bottomer cycle of a natural gas compressor station group is presented. As main novelty, with respect to the state-of-the art literature on this topic, a code able to predict ORC performance in the most possible generic scenario, in terms of compressor station load profile, installation site conditions and gas turbine model has been developed. In order to determine the actual performance of the GT-ORC integrated system into a compressor facility, it is fundamental to investigate its operation in off-design conditions. To this end the integrated system has been modeled in the Thermoflex environment (see chapter 7 for more details) to account for GT and ORC part-load behavior and ambient temperature performance derating. Results of the thermodynamic modelling have been incorporated into a *Matlab* calculation routine for the optimization of the ORC design for each analyzed scenario. The solution based on the reduction of the original GT number and the addition of the ORC with an electric motor generator is analyzed as case study (a complete description of this solution is reported in paragraph 7.3.3)

8.2 Factors of influence on the ORC feasibility

In this paragraph, the main factors of influence on the feasibility of the ORC as WHR in natural gas compressor stations are listed and described. Different combinations of this factors lead to different possible scenarios in which the ORC could be inserted. These factors are the following and their influence will be discussed in paragraph 8.4 as a result of this study:

- the yearly mechanical drivers load profile.
- the compressor station installation site.
- the gas turbines model.
- the heat recovery configuration.

8.2.1 The yearly mechanical drivers load profile

According to the mechanical power request by the compressors, the load profile of GTs used as drivers varies during the year. Indeed, depending on compressor station purpose, the drivers' cumulative profiles can differ substantially. As example, Figure 8-1 shows three different gas turbines yearly load duration curves of operative natural gas compressor stations (as provided by Turboden): the load profile A is representative of a compressor station working continuously during the entire year to pump gas along the pipelines; the load profile B is typical of a compressor station with inactivity periods; finally, the load profile C is related to a facility committed to gas storage only for a limited amount of time during the year.

Clearly, the GTs part-load operation influences the heat discharged with the exhaust and, consequently, the performance of the ORC system to be installed; therefore, the knowledge of topper load profile during the year is of fundamental importance. Inactivity periods due to the lack of energy demand or for unit maintenance outage are also included in the analysis.

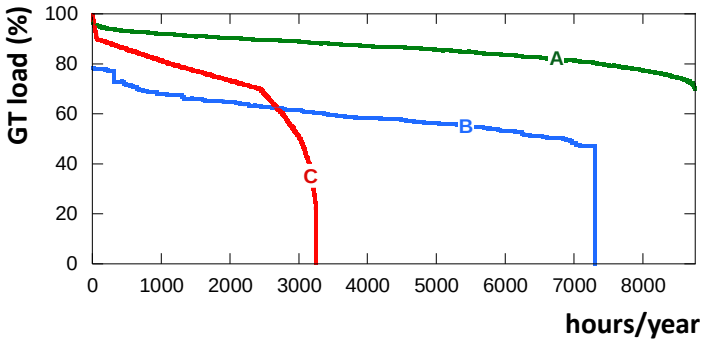

Figure 8-1 - Gas turbines load duration curves for three different compressor station working purposes.

8.2.2 Gas turbines model

The gas turbine model strongly influences the performance of the ORC bottoming cycle and thus its optimal design. In particular different gas turbine models are characterized by different sizes, different efficiencies and different regulation strategies. In general, the bigger is the gas turbine and the lower is its efficiency, the higher is the heat released with the exhaust gas, and thus, the ORC

input thermal power. For what concerns the GT control strategy, this aspect determines the trend of the temperature and the available thermal power during the plant regulation at part-load conditions, which both are crucial parameters for waste heat recovery applications.

In particular, the gas turbine regulation can be performed by means of:

- fuel flow management whereby a variable amount of fuel is injected into a constant air mass flow rate in the combustor (hence making the fuel-air mixture become leaner or richer and so reducing or increasing turbine inlet temperature respectively) (GT with VTIT in Figure 8-2).
- variable compressor geometry for variable air mass flow (GT with VIGV in Figure 8-2).
- variable shaft speed at the gas generator (high pressure shaft) in multi-shaft engines (GT with VSS in Figure 8-2).

Some machines can also feature a combination of the control load strategies just listed above.

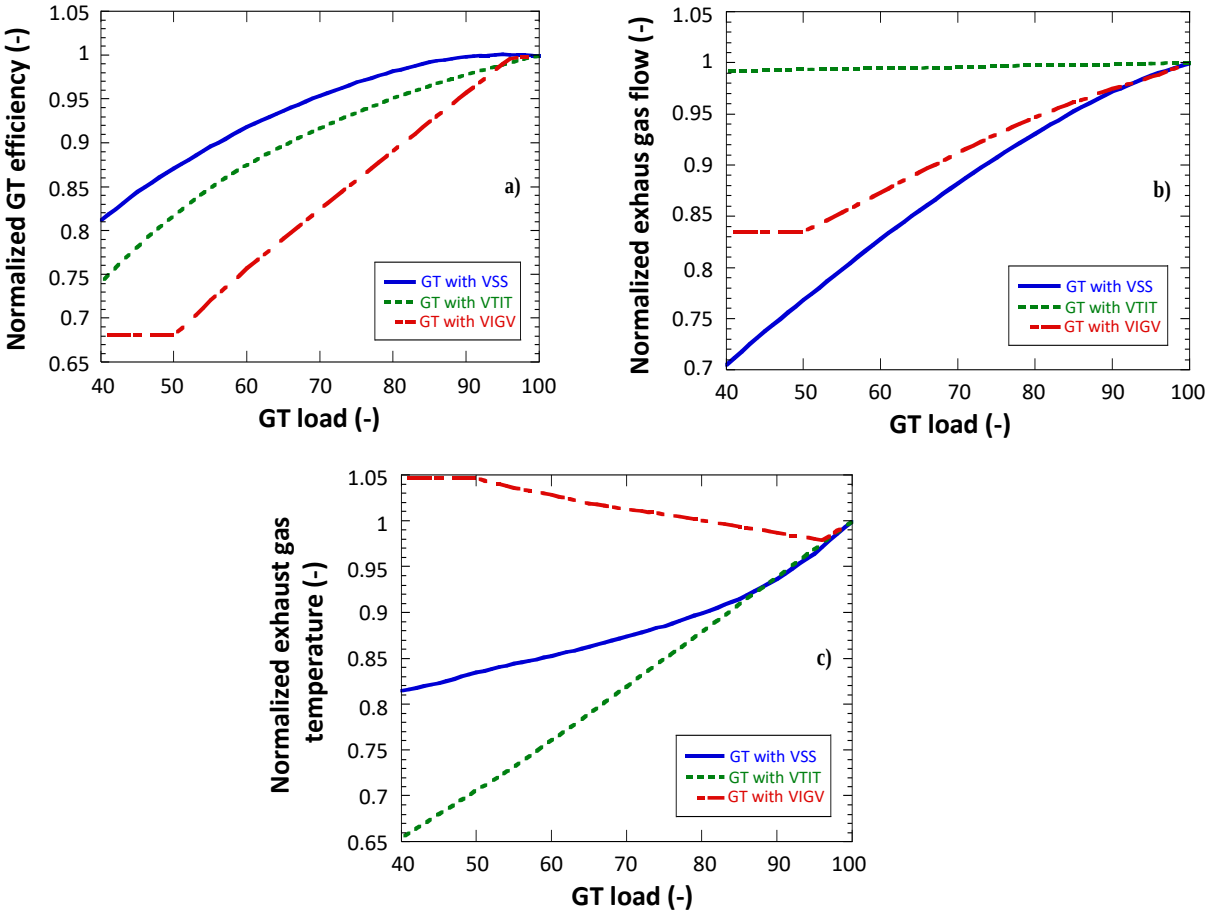

Figure 8-2 - GT shaft efficiency (a), exhaust mass flow (b) and temperature (c) normalized values as function of the GT control strategy and load [****].

[****] Curves obtained by means of simulation with the Thermoflex software [6].

In Figure 8-2 the trends of the normalized GT shaft efficiency (Figure 8-2a), the exhaust gas flow (Figure 8-2b), and temperature (Figure 8-2c), are plotted as function of the GT load, for three GT models representative of the control load strategies above described. General Electric PGT 25 GT model has been chosen to show the typical performance of GTs regulated with VSS control load strategy, Siemens SGT-100 as representative of GTs with VTIT and Solar Mars 100 T16000S of GTs with VIGV. In case of variable compressor geometry (VIGV in Figure 8-2), when the GT load is reduced from the design conditions, the exhaust gas flow and the shaft efficiency decrease, while the exhaust gas temperature increases. As opposite, in case of GT with VTIT control the exhaust gas flow rate is kept constant, decreasing its temperature at part-load operation. Variable shaft speed control strategy (VSS in Figure 8-2) allows for a more limited reduction in shaft efficiency compared to other strategies.

Figure 8-3 shows the trend of the ORC generated power at part-load operation considering different GT regulation strategies, as a result of the simulations performed with the model presented in chapter 7. As highlighted in Figure 8-7, the ORC performance derating is strictly influenced by the GT model assumed in the topper cycle (i.e. part-load regulation strategy applied). Highest ORC performance reduction is observed in case of GT with VTIT. Indeed, as shown in Figure 8-2c, at reduced GT load the VTIT regulation causes a significant decrease in the exhaust gas temperature compared to full-load operation, thus reducing the ORC thermal input. Conversely, VIGV control does not significantly penalizes the bottomer performance keeping normalized power output close to the value related to full-load operation.

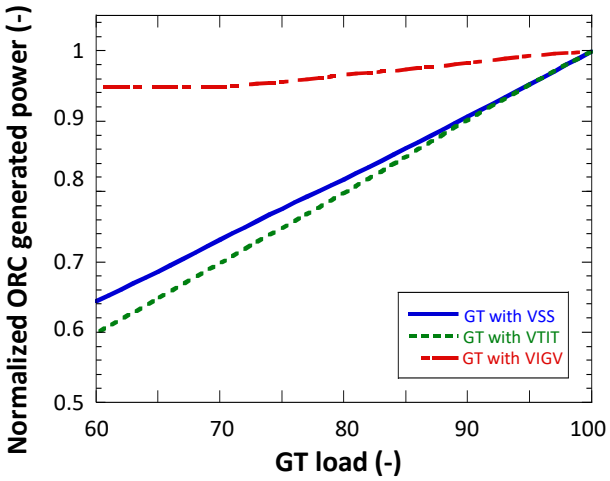

Figure 8-3 - Normalized ORC generated power at part-load operation considering different GT regulation strategies.

8.2.3 Heat recovery configuration

The topper-bottomer thermal connection can be realized by means of two different heat recovery configurations: a direct heat transfer (DHT) and an intermediate heat transfer fluid (IHTF) loop configuration (see Figure 8-4). Depending on the application, an intermediate heat transfer fluid circuit can be placed in between exhaust gases and organic fluid, with the aim of maintaining a higher degree of control on the maximum organic fluid temperature inside the ORC circuit. Otherwise, the

direct heat transfer configuration can be adopted, in those cases where there is not risk of overcoming the thermal stability limits. Turboden for example has already successfully employed DHT realizations for GTs or internal combustion engines WHR applications [107]. The advantage of this second configuration is in the lower investment cost and in the higher heat transfer performance.

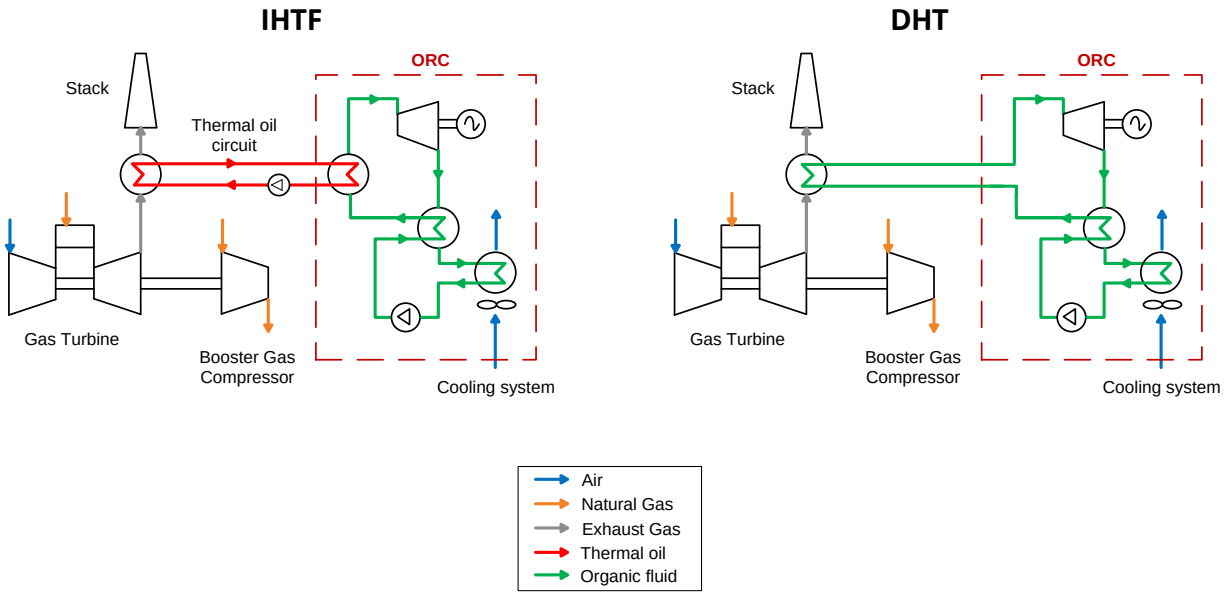

Figure 8-4 - Possible heat recovery configurations.

8.2.4 Compressor station installation site

The compressor facility installation site could have directly impact on the energy system performance but also on some cost parameters that influence the economic evaluation. The aspects affected by the location of the site are: the carbon tax value (if applied), the local reference carbon dioxide emission factor, the specific cost of the natural gas, the price of electricity and finally the performance derating of the integrated system due to ambient conditions, if significantly different from the ISO values.

Costs and emission factors

The values of the carbon tax applied worldwide (see Figure 8-5), as provided by the 2017 edition of "State and Trend of Carbon Price" report [108], have been considered. Currently, only few governments impose a carbon tax and prices are extremely variable from country to country, ranging from few \$/tonCO_2 up to 140 \$/tonCO_2 of Sweden. Since the installation of an ORC could allow for primary energy saving and CO_2 reduction, the correct evaluation of avoided local taxes and gas price is of fundamental importance.

The reference local values of the CO_2 output based emission factor, the price of natural gas and electricity are listed in Table *8-1*, as provided by the International Energy Agency (IEA) [109], [110], for the main geographic areas of interest considered in this study. Looking at the European situation, if Scandinavian countries enjoy the lowest electricity prices, Italy deals with the highest electricity prices worldwide, (mainly due to the high charged tax and the lack of nuclear power plants) leading,

instead, to high average value of electricity price in OECD Europe. The energy generation mix also influences the carbon dioxide output-based emission factor: fossil-fuel based country (such as USA and Middle East countries) features the highest values of $kgCO_2/MWh_{el.}$

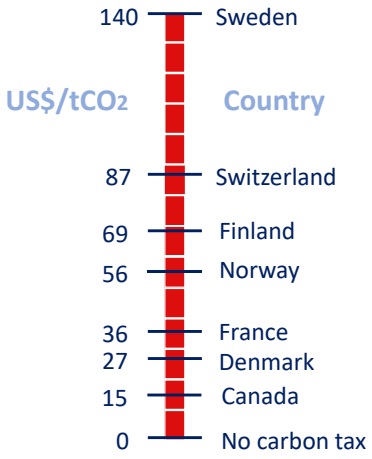

Figure 8-5 - values of the carbon tax, provided by the "State and Trend of Carbon Price" report [26]††††.

Table 8-1 - Factors depending on the geographic area: emissions [109] and costs [110] ‡‡‡‡.

	CO_2 emissions ($kgCO_2$/MWhel)	**NG prices (US$/MWh)**	**electricity prices (US$/MWh)**
Average over OECD Countries	408	20.2	92.3
Average over OECD Europe	300	28.9	108.5
Average over Scandinavia	103	43.5	60.3
USA	479	13.7	69.1
Canada	146	13.8	83.8
Average over Middle east	678	22	87.5

Ambient temperature

Different geographic areas have been identified based on the "Mean seasonal and spatial variability in global surface air temperature" report [111], as shown in Figure 8-7Figure 8-6. Thus, annual average ambient temperature values have been associated to each identified climatic zone.

The influence of ambient derating on GT and ORC performance has been also evaluated by means of the model presented in chapter 7. Figure 9 shows the results in term of ORC mechanical power output as function of the ambient temperature. In general, low ambient temperatures have a positive effect on the ORC condensation pressure value, and the lower is the condensing pressure the higher

†††† Data referred to 2017.

‡‡‡‡ Data referred to 2017.

is the enthalpy drop that can be exploited by the ORC turbine. However, it can be noticed that the ORC power output shows a parabolic trend, not significantly influenced by the GT control load strategy. Indeed, decreasing the ambient temperature values also affect the ambient air properties at the GT compressor inlet, causing an increase in the GT exhaust gas mass flow rate but, at the same time, a decrease in the exhaust temperature value. Depending on which of these two effects prevails, the amount of the GT discharged can increase or decrease compared to ISO condition varying the performance of the bottoming cycle.

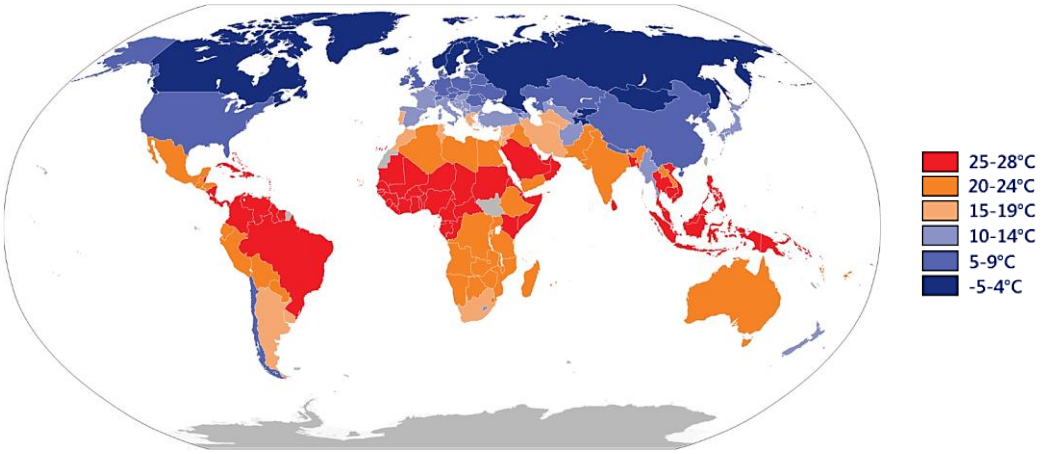

Figure 8-6 - Global map of the annual average ambient temperature in Celsius degrees [111].

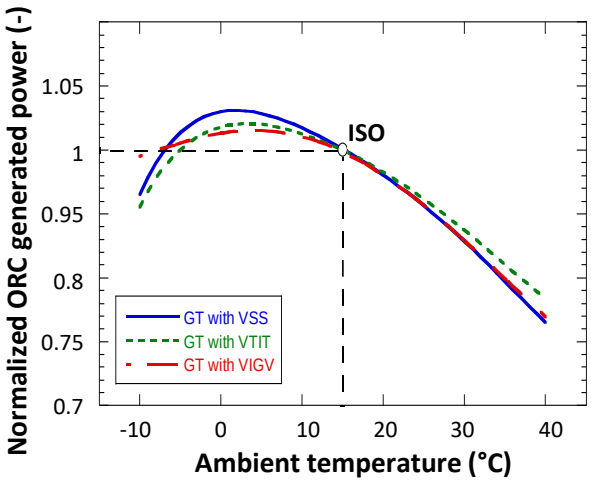

Figure 8-7 - Influence of the ambient temperature on the ORC normalized power output.

8.3 Optimization problem

An optimization routine has been implemented with the aim of identifying the optimum size of an ORC system, as bottomer section in natural gas compressor stations in different possible scenarios by varying the factors described in the paragraph above (paragraph 8.2). The numerical optimization procedure is based on the integration of a in house-developed code, implemented in the *Matlab* environment, with the energy system model developed in *Thermoflex* (see chapter 7).

A schematic flowchart of the calculation code routine is shown in Figure 8-8. Three different stages can be highlighted in the code structure, namely:

1. "Inputs and parameters", which requires the definition of the installation site operating conditions and specifics, and information about the economical context.
2. "Performance simulation", which solves the GT-ORC integrated system model based on the inputs provided in step 1). The purpose of this step is to obtain the curve of the normalized ORC power production, γ, as function of the GT load. This data allows to express the dependence of the economic indexes from the ORC size inside the objective function, as better detailed below.
3. "Optimization problem", which actually determines the ORC optimal size based on the optimization of the selected objective function.

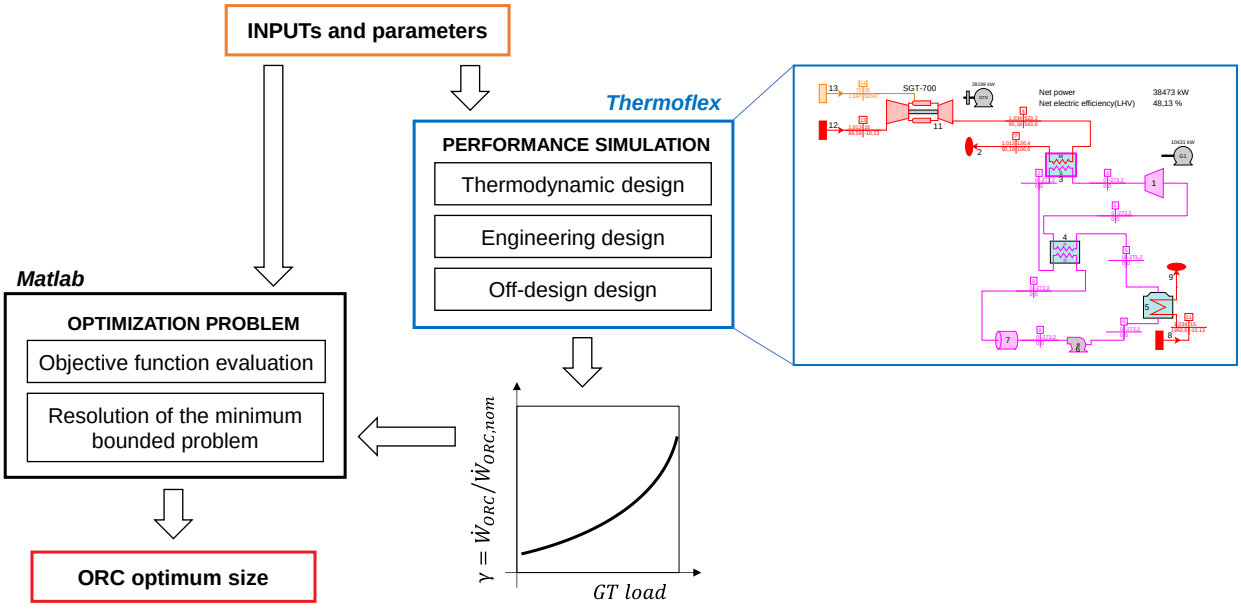

Figure 8-8 - Flowchart of the procedure to identify the ORC optimal design size.

In this case the objective is to maximize the economic profit resulting from the introduction of the ORC, thus the objective function corresponds to the expression defining the differential net present value (see Eq. (7-19)). The variable of the objective functions is the ORC design power and the problem is a find-minimum-problem of a single-variable function on a fixed interval. The ORC design power upper constraint is related to the maximum verifiable GT load during the operative hours, whilst its lower constraint is bounded to the minimum verifiable GT load (normally close to 40 % of GT nominal power). Being a non-linear problem, the optimization is performed into the

Matlab environment taking advantage of the *fminbnd* function tool, based on the golden section search and parabolic interpolation algorithm [86].

The problem is built by expressing the E_{ORC} and the E_{grid} terms of Eq. (7-19) as function of the ORC design power, $\dot{W}_{ORC,nom}$. In particular:

- the normalized ORC power production yearly profile, $\bar{\gamma}$, is computed as function of the GT load profile, $\overline{load}_{GT}$, input of the optimization routine (see paragraph 8.2.4), using the curve obtained through the "Performance simulation" step. The absolute ORC generated power profile, $\bar{W}_{ORC}$, is given thus by the product between $\bar{\gamma}$ and $\dot{W}_{ORC,nom}$. E_{ORC} is the sum over the year of the hourly ORC generated power, $\bar{W}_{ORC}$.

$$E_{ORC} = \text{sum}\,(\bar{W}_{ORC}) \quad , \quad \bar{P}_{ORC} = \bar{\gamma}\,(\overline{load}_{GT}) \cdot \dot{W}_{ORC,nom} \tag{8-1}$$

- E_{grid} is given instead by the difference between the yearly demanded energy and E_{ORC}. The yearly demanded energy is equal to the sum over the year of the hourly demanded power, $\bar{W}_{demanded}$. Where $\bar{W}_{demanded}$ is equal to the product between $\overline{load}_{GT}$ and the GT nominal power of the original arrangement, $\dot{W}_{GT,nom,original\ arrangement}$.

$$E_{grid} = \text{sum}\,(\bar{W}_{demanded}) - E_{ORC} \quad , \quad \bar{W}_{demanded} = \left(\overline{load}_{GT}\right) \cdot \dot{W}_{GT,nom,original\ arrangement} \tag{8-2}$$

8.4 Parametric analysis

In this paragraph, three significant case studies are presented and compared. Table 8-2 collects main inputs and outputs of the analyzed cases. In all the considered case studies we assume to modify the original compressor station arrangement (see Figure 7-2a), shutting down one or more GT units (see Figure 7-2c) compensating with the ORC and the electric motor (if needed) the lack of mechanical power. The GT models selected as compressor drivers for the cases study belong to the group of the most employed machines models [112].

The Case #1, assumed as reference case for the comparison, represents a compressor station located in an OECD country where no carbon tax is applied, and it is characterized by a load profile of B type (see Figure 8-1), using GTs with VIGV strategy. Cases #2 to #4 are compared to the reference case in order to account for the impact of the inputs' variation on the ORC optimum size and on techno-economic feasibility.

Comparison of case studies in details:

- Cases #1 Vs. #2 shows the effect of two different compressor station load profiles.
- Cases #1 Vs. Cases #3 compares the effect of GT control load strategies.
- Cases #1 Vs. Cases #4 highlights the effect of the compressor station location.

The main energetic, environmental and economic results evaluated in this paragraph include ORC optimal design power output, Max/Min/average ORC power output during operating hours, equivalent operating hours, mechanical energy generated with ORC and EMG operation, differential Net Present Value at 20th year, Payback period and total amount of CO_2 avoided.

Table 8-2 -Parametric analysis results.

Case characteristics / Case number	#1 (ref. case)	#2	#3	#4
NG CS load profile	B	**C**	B	B
GT control load strategy *	VIGV	VIGV	**VSS**	VIGV
heat recovery configuration	DHE	DHE	DHE	DHE
NG CS location	OECD	OECD	OECD	**Sweden**
carbon tax ($/tonCO2)	no	no	no	**140**
GT shaft efficiency (%)	33.3	33.3	37.1	33.3
Number of GT drivers original arrangement (-)	6	6	**3**	6
GT installed total power original arrangement (kW)	68184	68184	71052	68184
Number of GT drivers new arrangement (-)	4	4	**2**	4
GT installed total power new arrangement (kW)	45456	45456	47368	45456
Results				
ORC optimal design power size (kW)	**13837**	**17635**	**11126**	**13837**
ORC design power/ GTs power new arrangement (-)	0.304	0.388	0.235	0.304
Minimum ORC power during operative hours (kW)	12761	15852	5453	13021
Average ORC power during operative hours (kW)	13014	17033	6863	13348
Yearly ORC generated mechanical energy (GWh/year)	94.64	55.34	44.49	97.06
ORC equivalent operative hours (h/year)	6840	3138	4485	7015
CO_2 saving (kton/year)	53.49	26.7	27.87	57.8
Payback period (years)	6	no	no	2
ΔNPV_{20} (M$)	29.7	-7.13	-52.57	207.58
Yearly EMG generated mechanical energy (GWh/year)	13.31	18.54	64.82	12.4

*VIGV = SOLAR MARS 100; VSS = GENERAL ELECTRIC PGT25

8.4.1 Cases #1 Vs. #2 - influence of the yearly mechanical drivers' profile

The load profile B is characterized by a higher number of operative hours, if compared with the load profile C, however part-load operation occurs always in the load profile B while a limited number of operating hours at full load capacity is observed in profile C. For this reason, the ORC design power, as result of the optimization, is slightly higher for the Case #2 compared to Case #1 (equal to 17635 kW and 13837 kW, respectively). Indeed, in Case #2, ORC optimal design equals maximum value at GTs full-load operation. Conversely, ORC generated yearly mechanical energy, equivalent operating hours, CO_2 avoided emissions and economic results differ significantly. In agreement with the assumed load profiles the ORC equivalent operative hours are greater for the Case #1: the ORC generates about twice the annual mechanical energy of the Case #2, the CO_2 saving is doubled and the investment cost is recovered in the plant lifespan only in Case#1 where payback period is equal to 6. Since new assumed arrangement, in both cases, is characterized by a lower number of GT driver units (2 GTs have been decommissioned) loosing 22.7 MW of mechanical power, an electric motor is needed to compensate, together with the ORC, the lack of the driving power. The electric motor mechanical energy generated during the year is close to 13.3 and 18.5 GWh/year, respectively for Case #1 and Case #2.

8.4.2 Cases #1 Vs. #3 - influence of GT control load strategies

Comparing Case#1 and Case#3, two different GT models have been selected in order to show the influence of topper part-load control strategies in the ORC optimal design. The GT models and number are chosen to obtain similar compressor stations installed power both in the original and in the new arrangement, to perform a fair comparison between the two cases. Thus, in Case #3 the number of installed GTs is decreased by half compared to Case #1.

The results show that the ORC performance and design power obtained in Case #3 are remarkably lower compared to Case #1 results. Indeed, part load operation of the topper cycle with VSS control load strategy (Case #3) entails a remarkably decrease in exhaust mass flow and temperature (see Fig. 6 b, c) compared to VIGV regulation (Case#1) thus largely reducing the amount of heat input to the ORC cycle. The ORC generated mechanical energy is reduced by half (95 GWh/year vs. 45 GWh/year), the equivalent operating hours are reduced down to 4500 h/year and CO_2 savings are reduced of about 26 10^3 ton/year. From the economic point of view, the application of ORC in Case #3 is not feasible, since no return of investment is expected within the ORC assumed operating life (20 years).

8.4.3 Cases #1 Vs. #4 - influence of the natural gas compressor station location

For the comparison, two different compressor station locations, in terms of annual average ambient conditions, CO_2 output-based emissions reference value and carbon tax applied, are selected: OECD country without carbon tax for the Case #1 and Sweden for the Case #4. Sweden is characterized by an average annual temperature of 5 °C, a low CO_2 emission factor and the highest value of carbon tax (140 \$/tonCO_2); whilst OECD countries present an annual average temperature of about 15 °C, a medium CO_2 emission factor and no carbon tax. The results show that, as expected, ORC optimal design power is equal in both analyzed cases. The annual ORC generated mechanical energy and equivalent operating hours are quite the same, but slightly higher for Case #4 due to the lower ambient temperature positive influence on the performance. The annual CO_2 savings are slightly higher for the Case #4 compared to Case #1, mainly thanks to the lower emissions associated to the EMG operations. The carbon tax value strongly affects the economic gain: the ΔNPV at 20 years since the investment increases considerably, from 30 M\$ to 208 M\$ thus, the payback period is reduced from 6 down to 2 years.

8.5 Conclusions

The feasibility and optimal design of an ORC system as the bottomer cycle of a natural gas compressor station is studied as function of different factors depending on the facility demand profile, the gas turbines model and the site location. The influence of these parameters is briefly commented per points below:

- Results show that load profiles characterized by a higher number of operative hours (typical of natural gas compressor station), even if more distributed towards part-loads, are more beneficial for the investment on an ORC than load profiles characterized by a lower number of operative hours but more distributed towards the full load (typical of facilities dedicated only to

the storage); the ORC energy production and the CO_2 avoided emissions can even double. The optimal ORC design power, as result of the optimization, is slightly higher when considering load profiles more distributed towards higher loads.

- Different GT models can be based on different part-load control strategies, influencing the ORC optimal design. The results show that the ORC performance and design power can be remarkably lower if comparing VSS or VTIT control load strategy to VIGV regulation. The VSS and the VTIT regulation strategy indeed entails a remarkably decrease in exhaust mass flow and temperature at part load thus largely reducing the amount of heat input to the ORC cycle. At the contrary the VIGV control does not significantly penalizes the bottomer performance keeping normalized power output close to the value related to full-load operation. From the economic point of view, the topper cycle regulation strategy can determine the feasibility or not of the ORC. Indeed, the application of ORC in the analyzed case, using GTs regulated by means of the VSS strategy, is not feasible, since no return of investment is expected within the ORC assumed operating life (20 years). Conversely, it is when considering the GTs regulated by means of VIGV.
- The natural gas compressor station location ca also be a crucial factor of influence on the return of the investment, maybe the more important. Indeed, the factor that more affects the return on the investment is the carbon tax value strongly influencing the economic gain. Thus, this analysis highlights the strict correlation between the magnitude of the green incentives and the effective possibility of reduction of the greenhouse gas emissions. For what concerns the system design, instead, the results show that, being equal the facility, changing only the location, the ORC optimal design power does not change. Thus, the ORC production and equivalent operating hours are quite the same, but slightly higher when it operates at lower ambient temperature, which positively influence the performance of both the GT and the ORC systems. The annual CO_2 savings can also slightly differ due to different emissions associated to the EMG operations, determined by the emission factor of the energy mix of the considered country.

9 Optimal load Allocation between topper and bottomer system

Summary:This chapter analyzes the feasibility of adding additional compressor capacity inside the station, with the help of an ORC, as waste heat recovery technology. In particular, a procedure to identify the bottomer cycle optimal size and to re-define the optimal distribution of driver's loads inside the station is proposed. The strategy consists in the resolution of a minimum constrained problem, for which the loads are re-allocated between GTs and ORC, in order to minimize the fuel consumption of the natural gas compressor station. Constraints of the problem are the load balance of the system and the regulation limits of each component. The optimal load allocation routine has been implemented in Matlab™ environment; it includes the simulation of the gas turbines units, the centrifugal compressors and the ORC bottomer cycle. Two shaft gas turbine units and centrifugal gas compressors are modeled and matched, both in design and in off-design, using the machines' performance maps and matching equations. A typical interstate gas compressor station, with about 24 MW of mechanical drivers installed is taken as case study.

9.1 Contribution

This chapter explores more in detail the innovative natural gas compressor station configuration relying on the replacement of a compressor prime mover with an ORC. This solution, indeed, can be interesting for some remote applications in which the energy sell can be discouraged, due to lack of grid connections. In this context, demonstrating the feasibility of this configurations could incentive the investment on the ORC technology for such applications, not yet deeply examined in literature.

Considering the implementation of this solution, a re-allocation of the station load between the prime movers and the ORC is required and can be performed by means of the procedure proposed here. With the aim of enriching the current literature on the topic, this chapter discusses the development of an optimal topper system–ORC load allocation strategy, accounting for the part-load operation of the industrial process in which the ORC is inserted. The strategy is finally applied to a case study of a natural gas compressor station run by Solar models' gas turbines.

9.2 Case study

In this study, a typical natural gas compressor station arrangement is taken as reference**.** The compressor station original set-up is made of three GT prime movers, each one driving a centrifugal compressor in a parallel configuration. For instance, Solar *Taurus*™ 70 has been chosen as GT model to be coupled with Solar's C45 family gas compressor, specifically designed for applications with *Taurus*™ 70 [113]. Indeed, a two-shaft GT model with variable inlet guide vanes, has been chosen, since it represents the most advantageous solution when working with variable speed loads, as in case of gas compressors [114]. Selected units' nominal performance are resumed in Table 9-1.

The facility is conceived to elaborate a variable natural gas mass flow rate during the year between 40 % and 100 % of the compressor station nominal capacity. As a consequence, the GTs load profile varies concurrently according to compressors power consumption. In this study, a typical yearly flow request trend [114], as representative of actual operation inside an interstate compressor station, is considered. Figure 9-1 shows the considered profile in term of relative number of operating hours at which the station elaborates a given value of relative flow. It is shown that the flow demand is equal to its nominal value for about half of the operating hours, whilst for the rest of the time, the flow demand is almost equally distributed between the 50 % and the 90 % of its nominal value.

Table 9-1 - Gas turbine and natural gas compressor nominal performance.

GT TAURUS 70	
Net output power (kW)	8050
Heat rate (kJ/kWh)	10324
Thermal efficiency (%)	35
Inlet air flow (kg/s)	26.3
Power turbine exhaust flow (kg/s)	26.8
Power turbine temperature (°C)	504
Power turbine optimum speed (rpm)	11531

COMPRESSOR C45-2	
Suction pressure (bar)	71
Discharge pressure (bar)	100
Mass flow (kg/s)	153
Power (kW)	7766
Nominal speed (rpm)	9364
Isentropic efficiency (%)	87

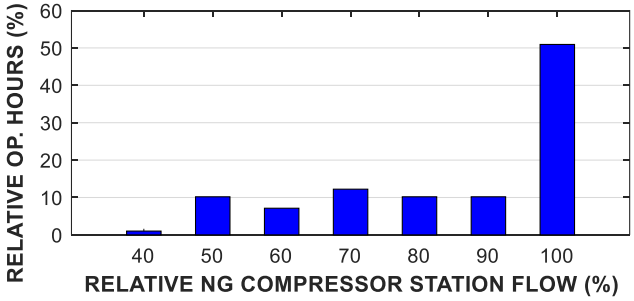

Figure 9-1 - Yearly natural gas flow request profile.

In the new proposed set-up, an ORC is added, as bottomer cycle of the topper driving units. In particular, the GTs exhaust gases are mixed into a collector and used to heat an intermediated heat transfer fluid circuit interposed between the topper units and the ORC (see Figure 9-2). The IHTF

configuration is chosen in order to avoid the fluctuation of organic fluid local temperature and the risk of ORC fluid chemical degradation.

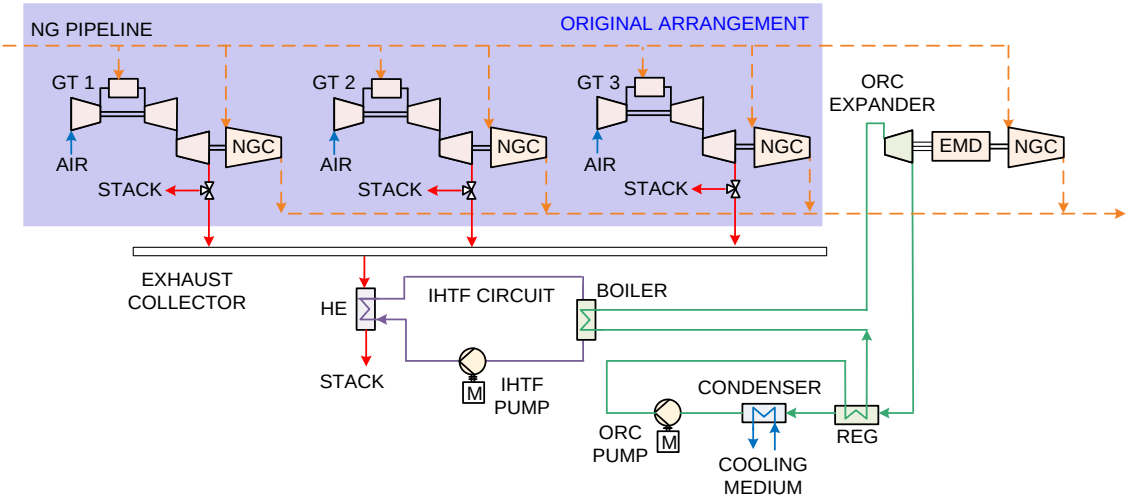

Figure 9-2 - Schematic of the natural gas compressor station of the case study.

9.3 Gas turbine units' simulation

Gas turbine driven compressor units are modelled and matched starting from their characteristic maps, following the approach presented in the paragraphs below, in order to calculate the actual operating point and their waste heat potential, to feed the ORC bottoming cycle.

This approach is used in this case instead of the *Thermoflex* GT unit black box, in order to account for the natural gas compressor part load performance (provided by the manufacturer) and regulation strategy and how it influences the GT performance.

9.3.1 Natural gas compressor

Centrifugal compressors are usually regulated by varying their rotational speed with the aim of controlling a process parameter, such as the suction pressure, the discharge pressure or the flow [104]. In this work, constant suction and discharge pressure values are assumed, so that the amount of compressor power required changes only with the pipeline flow request. This assumption is valid in case of weak head flow relationship: the process dictates a constant suction pressure, while the discharge gas is fed via a short pipe into a larger flowing pipeline and thus the compressor discharge pressure is more or less dictated by the pressure in the large pipeline [115].

Once the suction pressure is set, part-load performance of centrifugal compressor can be displayed in a map that defines the relationship between the discharge pressure (or required pressure) and the actual inlet flow, with the compressor speed and power as parameters (Figure 9-3). The map shows that, starting from the design point operation "DES", any deviation from the design flow leads to an adjustment of the absorbed power, which results in a change in the compressor speed ("OD" in Figure 9-3). In particular, power and speed can decrease with the elaborated flow until reaching the surge limit.

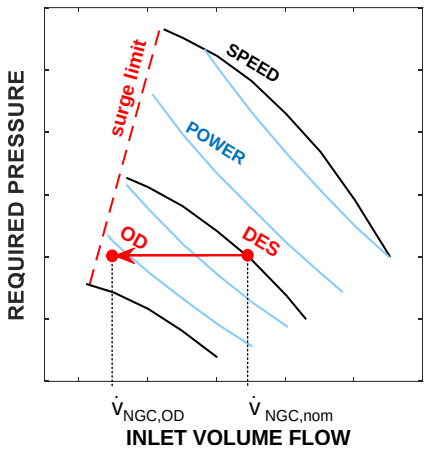

Figure 9-3 - Natural gas compressor map and part-load operation.

In this study, the natural gas compressor (NGC) model is developed in accordance to the method discussed in [104]. More in detail, the characteristic map of Solar C45 gas compressor, provided by the manufacturer, is used to create a lookup table, by interpolating the points on the speed and power lines with 2nd order polynomials. Thus, depending on gas flow request, the corresponding values of speed and power at which the compressor works, are determined.

9.3.2 Natural gas compressor and gas turbine matching

Each NGC is directly coupled with the power turbine of a two-shaft gas turbine, so that, the power turbine (PT) rotates at the speed imposed by the NGC shaft. In part load operation, the GT model of the case study, is regulated by means of a combination of two control load strategies: (i) variable GT compressor geometry, i.e. via variable inlet guide vanes (VIGV) for variable air mass flow, and (ii) variable shaft speed (VSS) at the gas generator turbine, controlled by a variation of the fuel flow. On the basis of the power absorbed and speed required at the NGC, the gas generator is regulated in this way: changing the NGC speed causes the control system to modify the fuel flow into the engine, and thus a change in the gas generator speed (where a reduction in the fuel flow leads to a reduction in speed and vice versa). Increasing/decreasing the fuel flow at the gas generator provides the PT with gas at higher/lower energy, which allows the PT to produce more/less power.

The gas generator matching with the PT is obtained by means of an iterative procedure, by imposing the flow continuity between the two components, and, at the same time, considering that the pressure ratio available to the PT is set by the gas generator pressure ratio (consult [104] and [116] for more detailed information on the components interaction). This procedure allows to determine the equilibrium running line between the components and thus the GT performance map for part-load operation.

9.3.3 Gas turbine part-load power and waste heat

For a given value of gas generator speed (i.e. fuel flow), the PT power (i.e., the GT output power) can be presented as function of its speed, as provided in the typical experimental plot in Figure 9-4a

[116]. The figure shows that there is an optimum PT speed at which the power turbine operates at its highest power and efficiency. The optimal PT speed depends in its turn on the gas generator speed and on the load; in particular, the optimal PT speed decreases with the load decrease, as shown in Figure 9-4b, reporting the experimental trend of the considered machine.

Thus, PT power output is a function of both gas generator speed and power turbine speed. The gas generator load and speed, instead, are determined only by the fuel flow. Thus, it is possible to trace the trend of the fuel flow consumed as function of the GT load, also reported in Figure 9-4b. The combination of the trends presented in Figure 9-4a and b completely define the behavior of the GT unit.

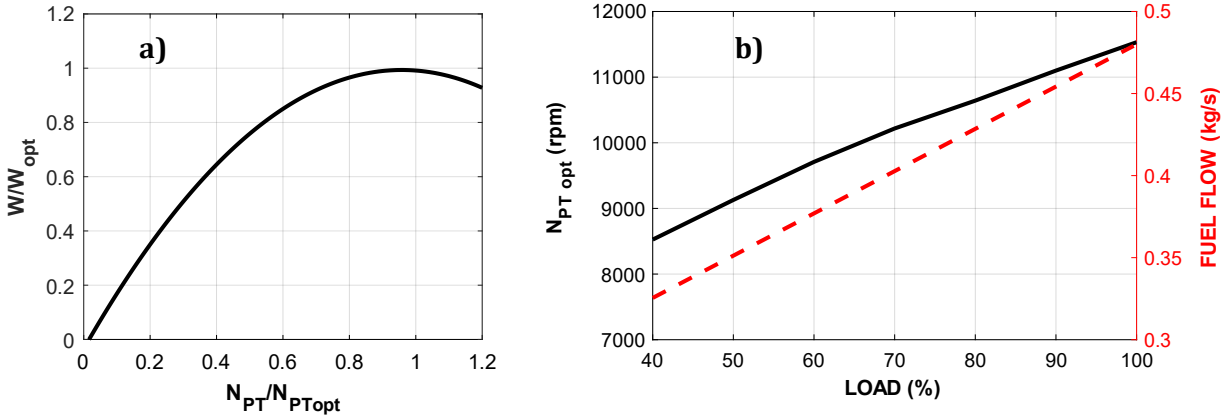

Figure 9-4 - GT regulation maps: a) optimal power turbine speed vs GT load, b) output power vs power turbine speed.

Curves of Figure 9-4 are the starting point to model flow and temperature of exhausted gas as function of the load. Indeed, the GTs part-load operation influences the heat discharged with the exhaust and thus the ORC performance. For the specific GT model, the exhaust temperature and mass flow, exhibit the trends reported in Figure 9-5. The combination of the VIGV and VSS control load strategies allow to work proximate to the maximum turbine inlet temperature, for any operating condition, while maintaining a constant fuel-air ratio. For this reason, exhaust temperature trend is practically flat, whilst the exhaust flow and the fuel flow decrease almost linearly with the GT load.

9.3.4 Bottomer cycle modelling

ORC performance derating is strictly influenced by the GT model assumed in the topper cycle (i.e. part-load regulation strategy applied). In particular, the VIGV control strategy enables to keep the ORC temperature input almost close to the value related to full-load operation (see Figure 9-5). As a consequence, we expect that the GT performance at part-load operation would not significantly penalize the bottomer performance.

Actually, as mentioned before, the exhaust gas feeding the IHTF circuit results from a mix of the exhaust gases coming from each GT units. Then, the mixed flow is given by the sum of the single GT exhaust flows and the mixed temperature is computed as the weighted average of the single GT exhaust temperatures over the exhaust flows.

Using this input, the ORC system is simulated by means of the *Thermoflex* model presented in chapter 7. The EMG mechanical power output is used to run the additional NGC connected to the ORC expander. The latter will be sized on the basis of the ORC optimal size, resulting from the optimal load allocation procedure. Then, using the compressor map (see Figure 9-3), it will be possible to determine the volume flow which can be elaborated by the additional compressor, when providing a certain mechanical power.

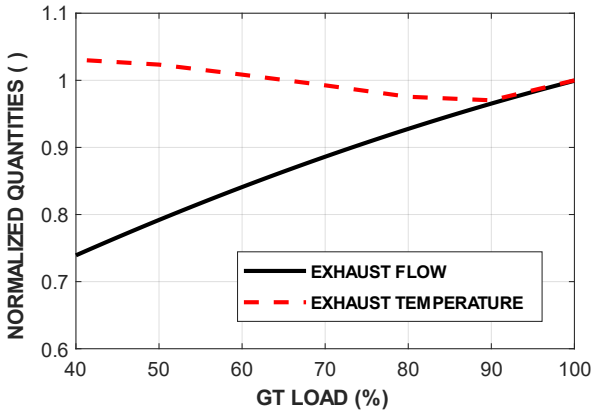

Figure 9-5 - GT fuel flow, exhaust mass flow and temperature normalized values at GT load.

9.4 Optimal load allocation strategy

The objective of this study is to define a procedure to re-distribute the loads of a compressor station, when introducing additional compressor capacity with an ORC. With this purpose, an optimum load allocation strategy is discussed in this section. The optimum load allocation strategy consists in two main steps:

1. the optimal distribution of the loads is re-defined in nominal conditions. In this step the optimal sizes for the ORC and the electric motor driven compressor to be installed, are identified.
2. Once the size is set, off-design performance of the power plant can be explored. Thus, the optimal distribution of the loads can be assessed also in off-design conditions (i.e. gas flow demand different from nominal value).

For the sake of clarity, the implemented method is illustrated in the flow chart of Figure 9-6 and described more in detail in the following paragraphs. First, the minimum problem concept is presented and then its implementation is described.

9.4.1 The minimum problem

The optimum load allocation strategy can be described by the system of equations (9-1). The procedure consists in the resolution of a minimum constrained problem. The loads are re-allocated between GTs and ORC, so as to:

- cover the overall gas flow demand, $\dot{V}_{NG\ CS}$, with the sum of the natural gas flow elaborated by the GT-driven compressors, $\dot{V}_{NGC-GT}$, and the natural gas flow elaborated by the ORC-EMG compressor, $\dot{V}_{NGC-EMG}$.
- while minimizing the fuel consumption of driving units.
- while satisfying the regulation constraints of each component.

For any possible value of the natural gas flow demand, an optimal solution of the problem can be found in terms of minimum fuel consumption and optimal allocation of the load between GT units ($load_{GT1}, load_{GT2}, load_{GT3}$) and ORC ($load_{ORC}$). The optimal design size of ORC, EMG and ORC driven NGC are also output of the problem. The problem has to be solved by means of an iterative procedure, given that $\dot{V}_{NGC-EMG}$ depends on the ORC power output, which depends in its turn on the GTs loads (i.e. the heat discharged by the GT units), not known a priori.

$$\begin{cases} \min_{\bar{x}}\ m_{FUEL}(\bar{x}), \qquad \text{with } \bar{x} = load_{GT1}, load_{GT2}, load_{GT3} \\ \text{such that:} \\ \dot{V}_{NG\ CS} = \sum_{i=1}^{3} \dot{V}_{NGC-GTi}(x_i) + \dot{V}_{NGC-EMD}\left(load_{ORC}(\bar{x})\right) \\ 40\ \% < load_{GTi} < 100\ \% \\ surge\ limit\ load < load_{NGCi} < 100\ \% \\ 30\ \% < load_{ORC}(\bar{x}) < 100\ \% \end{cases} \tag{9-1}$$

9.4.2 The iterative procedure

The input of the calculation routine is the volume flow demand $\dot{V}_{NG\ CS}$. Based on the input, an attempt solution of flow elaborated by the GT-driven compressors, $\dot{V}_{NGC-GT}$, is chosen to start the iterative procedure. $\dot{V}_{NGC-GT}$ is distributed between the GT-drivers such that the GT units are loaded evenly and by running the least number of units necessary. Indeed, if the units involved are equal in size, this is the strategy that guarantees the minimum fuel consumption, as dictated by the equal incremental principle [117].

Once the GTs loads are known, it is possible to use the GT map of Figure 9-5 to determine the exhaust gas temperature and flow of the single GT units, then the mixed exhaust temperature, $T_{ex\ MIX}$, and flow, $\dot{m}_{ex\ MIX}$, as explained in paragraph 9.3.4. Performance of the ORC power plant, in terms of electric power output, as function of the mixed exhaust gas temperature and flow, are obtained through *Thermoflex*™ simulation. The mechanical power available at the ORC driven NGC is obtained by means of the EMG map (Figure 7-5). The resulting value of mechanical power is the input for the ORC driven NGC map (Figure 9-3). This map, finally, allows to compute natural gas flow portion elaborated thanks to the ORC power contribute.

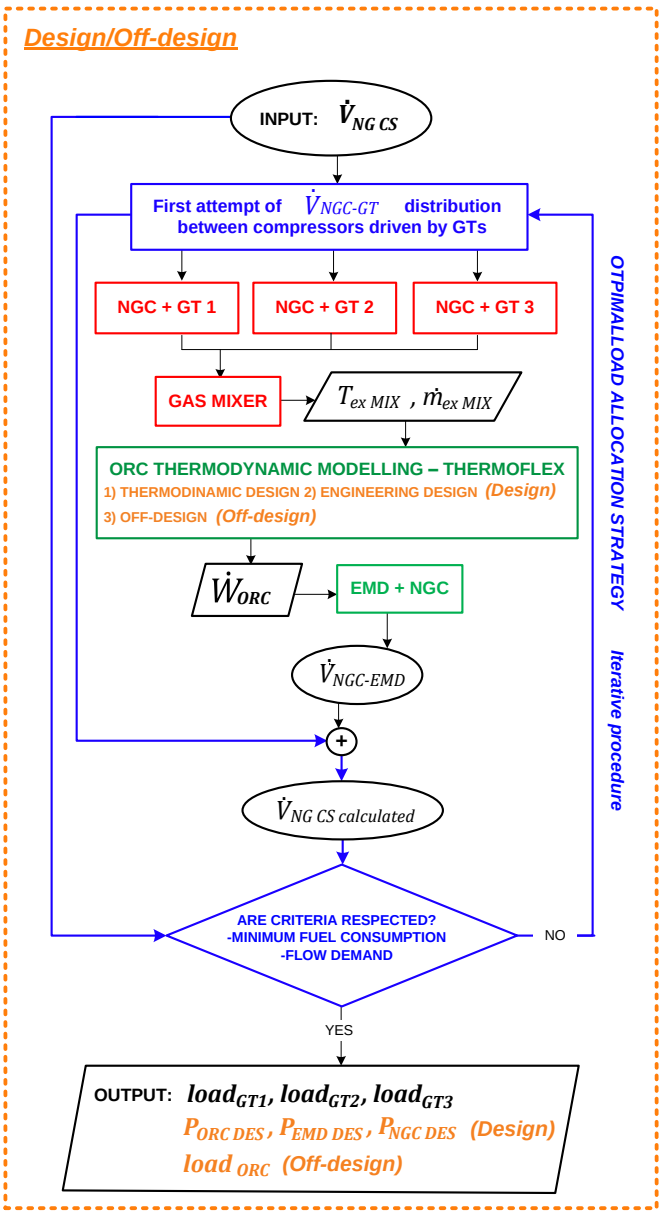

Figure 9-6 - Optimal load allocation routine.

At this point, the flow elaborated by NGC-GTs and the one elaborated by NGC-EMG are summed to be compared with the original compressor station input flow value. If the flow demand is covered, the constraints of the minimum problem and the convergence criteria are respected, and the optimal solution is determined. Otherwise, the attempt solution of flow distribution has to be corrected and the optimal load allocation calculation has to be repeated until the solution is found.

The procedure consists in two stages, indicated in Figure 9-6, as i) Design, ii) Off-design. The first step of the optimal load allocation strategy is finalized at finding the optimal ORC, EMG and EMG-driven NGC sizes. Thus, in order to determine the ORC design, the optimal load allocation is performed for the first time for the nominal value of the natural gas flow, so that, the ORC is sized on

the basis of the nominal operation of the compressor station (which occurs half time during the year (see Figure 9-1)). As far as the ORC design is set, it is possible to simulate its part-load operation with *Thermoflex*™ off-design analysis. At this point, the load allocation routine can be run to find the optimal load allocation solution for natural gas flow values different from the nominal one.

9.5 Results

In this section, the obtained results of the optimal load allocation strategy applied to the case study are presented: (i) the original compressor station arrangement (without ORC) optimal load allocation; (ii) the ORC design; (iii) the new compressor station arrangement (with ORC) optimal load allocation; (iv) energy, environmental and economic assessment on yearly basis.

9.5.1 Original arrangement optimal load allocation

In the original arrangement, the compressor station flow demand is covered only by the GT units. The total required gas flow, and thus the corresponding required power, is allocated between the three GTs. Results in terms of GTs load allocation are shown in Figure 9-7 for each value of the compressor station flow, ranging between the 40 % and the 100 % of the nominal capacity.

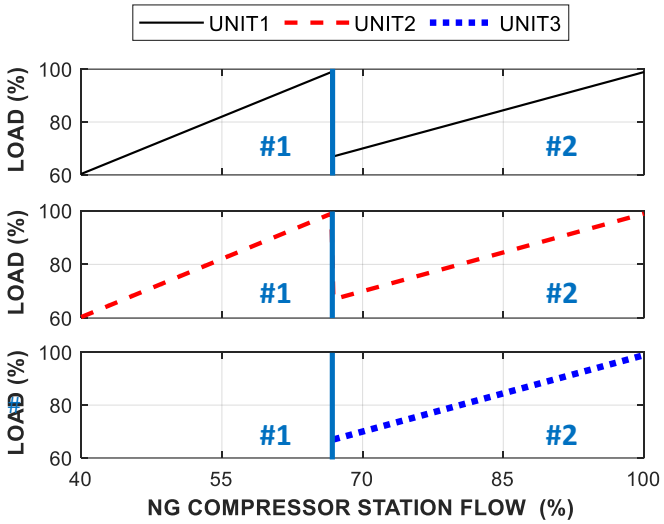

Figure 9-7 - Original compressor station arrangement optimal load allocation.

Two operating zones (namely zone #1 and zone #2 in Figure 9-7) can be identified: it can be observed that in the lower load zone #1 (from the 40 % to about the 67 % of the gas station flow), two GT units are enough to cover the flow demand, whilst starting from about 67 % of the station flow (load zone #2), it is necessary to turn on the third unit. Within each zone, the load is evenly distributed between the running units.

9.5.2 ORC design

Once the load allocation strategy between the GT units is defined (see Figure 9-7), the GTs loads univocally define the ORC boundary conditions, in terms of mixed exhaust gas temperature and flow feeding the IHTF circuit. The exhaust gas conditions profile, represent the starting point for the ORC simulation. The current "total GT load" is defined according to equation (9-2) as the ratio between the actual power produced by the GTs (including only the power output contribution by each active unit, P_{GTi}) and the GTs nominal capacity of the whole compressor station, sum of the rated power of the single units, $P_{GT,nom\ i}$:

$$total\ GT\ load = \frac{\sum_{i=1}^{3} P_{GTi}}{\sum_{i=1}^{3} P_{GT,nom\ i}} \tag{9-2}$$

The trend of the mixed exhaust gas temperature and flow as function of the total GT load, are shown in Figure 9-8. In the two zones the positive slope of the exhaust flow versus load is equal, but a sudden rise in mass flow values occurs when the third unit is activated. Instead, the exhaust temperature profile versus load is similar in the two zones, showing same fluctuation of values and extreme min/max temperature values. It follows that, during its operation, the ORC could work with exhaust gas with a temperature ranging between 490 and 510 °C, and a mass flow varying between 45 and 80 kg/s.

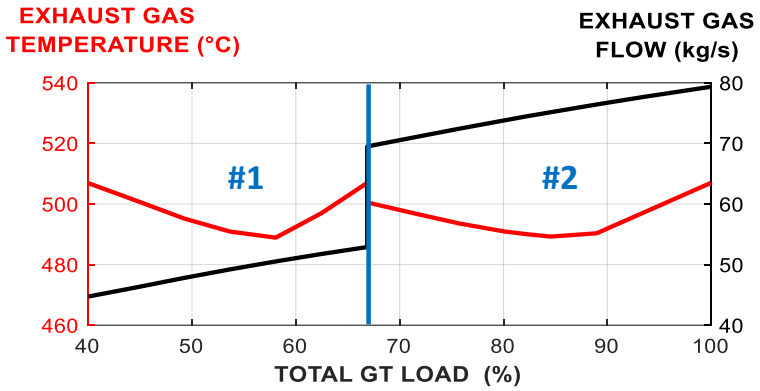

Figure 9-8 - Mixed exhaust gas temperature and flow vs total GT load.

Figure 9-9 reports results in terms of ORC electric power output as function of the total GT load, and ORC optimal size, obtained by solving the optimal load allocation problem. As expected, the ORC output power profile at part-load conditions shows a steep rise versus the total GT load, when the third GT is switched on (at a total GT load close to 67 %).

Results show that, in order to minimize the fuel consumption of the station, the ORC should be sized on the 80 % of the GT station load. It means that in the design operating point, the 80 % of the compressor station absorbed power is covered by the GT units, whilst the remaining 20 % is provided by the ORC. The ORC optimal size turns out to be approximately 5285 kW, obtained by designing the ORC on the basis of an exhaust gas temperature of about 490 °C and an exhaust gas flow of 74 kg/s.

The operating load of the ORC can range between the 30 % and the 100 %. According to typical specification by the manufacturer [23], the ORC can be operated over the full load condition, up to 110 % of the rated power, only for a limited amount of hour per year. It means that, in case the compressor station flow demand exceeds the nominal flow demand, the total GT load can be increased until the 96 %, condition in which the ORC can reach the 110 % of its load.

The EMG has been sized on the basis of the ORC nominal electrical power output, whilst, the additional compressor, on the account of the EMG mechanical power output. On the basis of the powers involved, an EMG with a nominal efficiency of 92 % is considered, which results in a maximum power output of 4863 kW that can be provided to the ORC driven NGC. The powers involved, have led to choose a compressor belonging to Solar's C40 family gas compressors. Whilst the original set-up capacity was equal to 24150 kW, the new arrangement total mechanical installed power is equal to 29330 kW, representing an increase of 21 %.

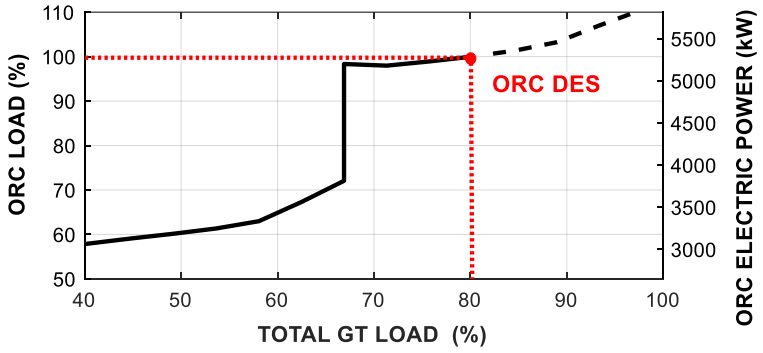

Figure 9-9 - ORC electric power output vs total GT load.

9.5.3 New arrangement optimal load allocation

In the new arrangement the compressor station total absorbed power is covered by the GT units with the ORC boost. The optimal loads allocation is shown in Figure 9-10, as function of the compressor station flow. In this case, four different load zones can be recognized:

- *Zone #1:* Two GT units are enough to cover the gas flow demand, thus the GT load of unit 1 and unit 2 increases linearly from the 60 % until reaching the 80 %. the demand is still relatively low and the ORC is not yet called to operate.
- *Zone #2:* the natural gas flow demand is higher and it opens up the possibility to exploit the ORC to cover part of the demand. The load of GT units 1 and 2 goes back to 60 % and the ORC is turned on at 60 % of its capacity. Starting from there, the operating GTs increase their load until reaching full capacity, in correspondence of the 70 % of the ORC load. Beyond this point, two GT units are not enough to cover the whole demand and the third unit must be powered on.
- *Zone #3:* the ORC would not be called to operate, since turning on the ORC would cause a surplus of unused electrical power production and the constraint of the optimum problem would not be respected. Indeed, the start-up of the third turbine would imply an ORC output power step, from the 72 % to the 98 % of the ORC nominal power. According to the setting of the problem, the results of the optimal load allocation strategy suggest operating all the three GTs increasing their

load, from the 80 % to about the 90 %. However, in real operation, two strategies could be implemented to avoid over-generation, still running the ORC unit: i) the use of diverter valves to regulate the bottomer cycle thermal input such that a fraction of the GTs exhausted is directly send to the chimney, thus by-passing the IHTF exchanger; ii) the partial by-pass of the vapour at the ORC expander inlet. This second option allows limiting the ORC electrical output regulating the amount of expanded vapour. Indeed, a vapour fraction is directed to the condenser section, after an isenthalpic lamination process, to be mixed with the fraction coming out from the expander.

- *Zone #4:* The demand is greater than in the zone #3, and the ORC becomes helpful again to cover part of the demand. In this zone the ORC works close to its maximum load, while GTs loads are reduced compared to zone #3.

The results obtained for zone #3 bring to light an interesting consideration about what a brand-new design of a natural gas compressor station should account for, when considering the introduction of an ORC as WHR system. The ORC operation gap (zone #3) can be filled through a different design of the original plant, employing GT runners of different capacities, allowing a wider margin of regulation. Other studies related with multiple unit energy systems for different applications demonstrate the effectiveness of this solution (see for example [118]).

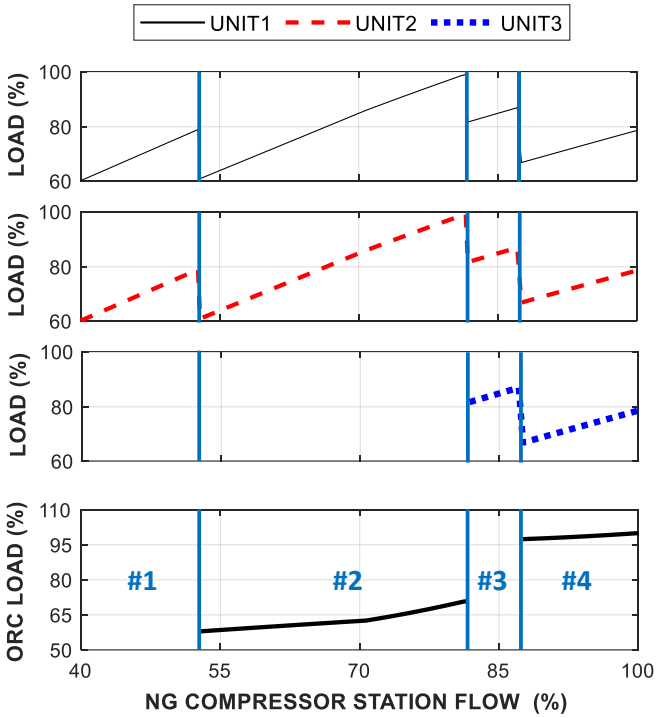

Figure 9-10 - New compressor station arrangement optimal load allocation.

9.5.4 Energy, environmental and economic assessment

The original and the new arrangement are compared in terms of energy, environmental and economic aspects following the approach described in paragraph 7.3.

The power required during the year is covered, as shown in Figure 9-11a, following the optimal power allocation profile obtained. Consequently, the optimal mechanical energy allocation profile, between GT units and ORC, is obtained as reported in Figure 9-11b. In Table 9-2 the main energy and environmental outcomes are summarized.

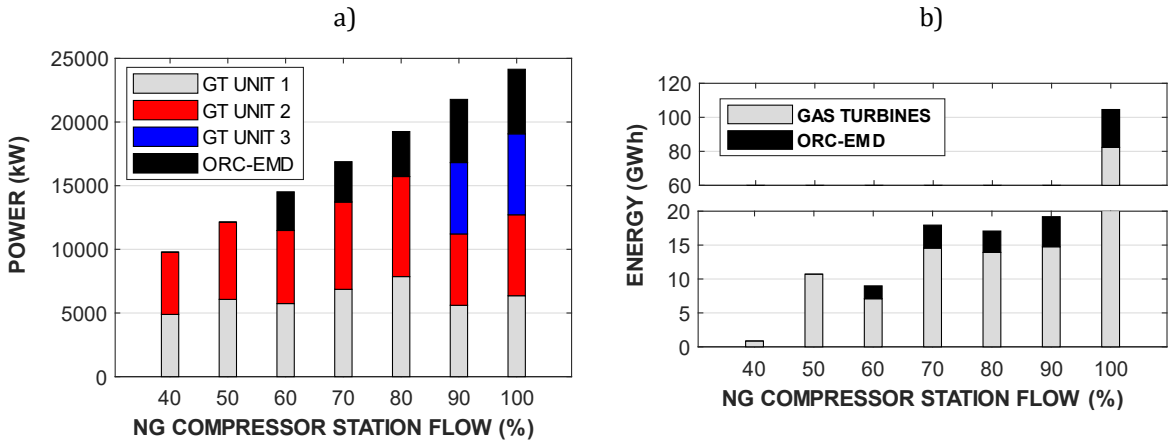

Figure 9-11 - Optimal a) power and b) annual energy allocation profile.

Table 9-2 - Main output of the optimization procedure.

ORC optimal design power (kW)	5285
ORC-EMG max. power output during operating hours (kW)	4863
ORC-EMG min. power output during operating hours (kW)	2910
ORC-EMG average power output during operating hours (kW)	4287
Yearly GT generated energy (GWh)	148
Yearly ORC-EMG generated energy (GWh)	33
ORC equivalent operating hours (h)	6874
ORC operating hours (h)	7796
Yearly CO_2 avoided (kton)	23.5

As main results of this analysis:

- The optimal ORC size is about 5285 kW, which results in a maximum power output of 4863 kW that can be provided to the EMG driven NGC. The resulting ORC design allows to run the ORC for 7796 hours per year, producing with the ORC – EMG, 33 GWh per year of clean mechanical energy, equal to the 18 % of the total yearly compressor station mechanical energy demand.
- The ORC introduction causes fuel saving, as it covers part of the required power in place of the GT units. The reduction of fuel consumption is reflected in reduced greenhouse gas emissions

and in reduced plant operation costs. The estimated amount of CO_2 avoided is equal to 23.5 kton per year; thus, a reduction of 22 % compared to the original arrangement is achieved.

Finally, an economic analysis is proposed, evaluating the investment on the EMG-NGC unit. Being an innovative solution, the price of this component is not yet defined. Thus, the economic feasibility of the ORC solution is assessed by considering the cost of the EMG-NGC unit as a variable. At this scope, the ΔNPV equation, Eq. (7-19), has been manipulated to obtain the EMG-NGC investment as an output:

$$I_{EMG-NGC} = \sum_{i=1}^{PB} \frac{C_i}{(1+q)^i} - I_{ORC} \tag{9-3}$$

This equation allows to evaluate the EMG-NGC maximum admissible cost, $I_{EMG-NGC}$, to return on the investment in a given payback period.

The gas price and the carbon tax are also considered as parameters of this analysis, since their values can strongly vary around the world: ranging between 10 to 45 $/MWh for the natural gas price, and between 0 to 140 $/ton as regards the carbon tax (see paragraph 8.2.4).

Figure 9-12 displays the results of the economic assessment, where 3 possible scenarios are highlighted: i) low fuel price (10 $/MWh) and no carbon tax; ii) intermediate fuel price (20 $/MWh) and carbon tax (70 $/ton); iii) high fuel price (30 $/MWh) and carbon tax (140 $/ton). The bands represent all the other intermediate scenarios of combination of fuel and CO_2 prices. Considering a reasonable value of the EMG-NGC investment cost, equal to 10 M$ [119], the payback period, for the intermediate prices scenario and for the high prices scenario, is respectively of 7 years and less than 4 years. Instead, for the low prices' scenario, there is no return on the investment in less than 20 years. As expected, higher prices lead to higher avoided costs, thus to higher saving and lower payback periods.

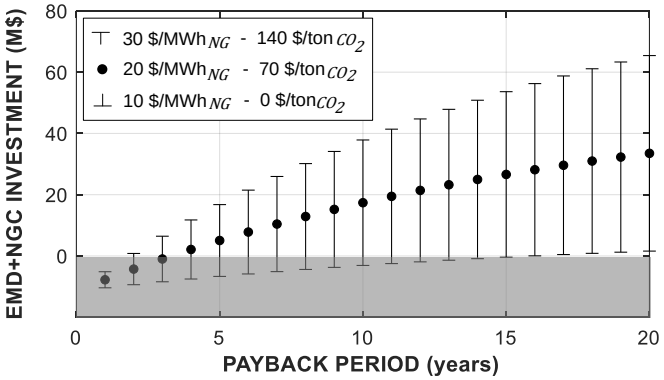

Figure 9-12 - EMG+NGC investment cost vs payback period.

9.6 Conclusions

This chapter discusses the implementation of an optimal load allocation procedure to re-distribute the loads into a gas compressor station, when an ORC type system is added to the

traditional turbo-compressor configuration, as bottomer of the driving units. The strategy consists in the resolution of a minimum constrained problem, for which the loads are re-allocated between GTs and ORC, in order to minimize the fuel consumption of the facility. Constraints of the problem are the load balance of the system and the regulation limits of each component. The load allocation strategy allows to: i) find the optimal size of the ORC and an electric motor driven compressor fed by the ORC electrical power output; ii) define the load allocation that guarantees the minimum fuel consumption.

The procedure has been applied to a case study: a typical interstate gas compressor station, with about 24 MW of mechanical driving capacity installed. The results of the simulation, in terms of optimal load allocation, are presented for the original set-up and for the new one including the ORC, to be compared. The results bring to light an interesting consideration about what a brand-new design of a natural gas compressor station should account for, when considering the introduction of an ORC as WHR system. Namely, a different design of the original plant, employing GT runners of different capacities, can allow a wider margin of regulation and exploitation of the ORC system. This aspect is worth to be further investigated in future studies, dedicated to the design ex novo of new natural gas compressor stations including an ORC.

For the case study, the energetic, environmental and economic assessments are also discussed. The optimal ORC size turns out to be 5285 kW, which results in a maximum power output of 4863 kW that can be provided to the ORC driven NGC. The resulting ORC design allows to produce with the ORC – EMD the 18 % of the yearly station mechanical energy demand. A reduction of 22 % of CO_2 emissions, compared to the original arrangement is achieved. Considering a reasonable value of the EMD-NGC investment, equal to 10 M$, the payback period, ranges between 4 and more than 20 years, depending on the natural gas cost and on the carbon tax, if applied. As expected, higher prices lead to higher avoided costs, thus to higher saving and lower payback periods.

10 A comparison between ORC and supercritical CO_2 cycles

Summary:The present chapter aims at systematically evaluating thermodynamic performance of ORC and supercritical CO_2 energy systems as bottomer cycles of different small/medium size industrial gas turbine models, with different power rating. For this purpose, the Thermoflex commercial software, providing the GT PRO gas turbine library, has been used for the simulations. The ORC and s-CO_2 systems specifics have been chosen in line with industrial products and state-of-the-art research experience, as described below. A systematic analysis has been performed, considering pure electric and combined heat and power plant configurations, discussing energetic results in terms of electric and thermal power production, efficiency, primary energy savings, components dimensions and costs.

A deepen analysis of a cogenerative case study is proposed, since proved to be interesting for the s-CO_2 system application. For this study, also the part-load performance of the two bottoming cycles is analyzed and compared, and the return on the investment is evaluated.

10.1 Contribution

This chapter proposes a systematic investigation on ORC and s-CO_2 potential as energy harvesting technologies inside an industrial facility, employing GTs at both full and part-load operation is proposed. Therefore, except for a few works, literature lacks studies regarding industrial applications of CO_2 based waste heat recovery and specific comparison with ORC, in particular in realistic operating conditions (see paragraph 1.6.1). The performance of ORC and s-CO_2 systems are evaluated, as bottoming of selected industrial GT models, in both pure electric production and CHP configurations. The modelling approach deeply discussed in chapter 7 is adopted.

It is the aim of the present work to offer an original contribution, with respect to the current literature, in the following aspects:

- The s-CO_2 supercritical cycle is systematically evaluated as bottomer of different GT models for industrial applications, considering realistic operating conditions.
- A comparison between ORC and s-CO_2 power systems performance as industrial WHR solutions is performed. The analysis accounts not only for the thermodynamic cycle but also for the systems specific and technological limits determined by the state of the art of the technologies.

- An investment cost assessment is proposed for a comprehensive comparison between ORC and s-CO_2 power systems. The influence of the design aspects affecting the investment cost are discussed in detail, highlighting the difference between the compared systems.
- The performance of the whole power plant is evaluated both in design and in part-load operating conditions, to account for a realistic load profile, for a cogenerative case study.

10.2 Heat recovery configurations

As schematized in Figure 10-1, the examined power plant configurations comprise a topper gas turbine unit and a bottomer cycle, generating electricity to sustain the electric user. In the considered configuration, the gas turbine exhaust gas is directly conveyed into the heat recovery heat exchanger, here named "GAS HX". Four different heat recovery arrangements are analyzed in this study (see Figure 10-1): a) a s-CO_2 base configuration, b) an ORC base configuration, c) a s-CO_2 cogenerative (COG) configuration and c) an ORC cogenerative configuration. Thus, for both the ORC and the s-CO_2 solutions, two different scenarios are considered, assuming different boundary conditions:

- a "BASE" scenario, considering the pure electric energy production. In this configuration, the bottoming cycle provides only electric energy to the user (see Figure 10-1a and b). The chosen cooling medium is ambient air, as more suitable for water-scarce environments, such as remote installations.
- a cogenerative scenario ("COG") involving both the electric and the thermal energy production. This configuration requires an electric consumer as well as a thermal user (see Figure 10-1c and d). The layout difference between COG and BASE option is in the use of water in a closed-loop configuration, in place of ambient air, as cooling medium. In this case, the presence of water is justified by its use into a hot water circuit providing heat to the thermal user.

10.2.1 S-CO_2 configuration

More in specific, the considered s-CO_2 bottoming cycle is a thermodynamic variant of the Brayton closed cycle arrangement (see Figure 10-1a). In this cycle, the CO_2 circulates through the plant being heated into the heat recovery heat exchanger ("GAS HX"), expanded into the turbine, cooled (into the "COOL HX"), and pressurized by means of a compressor. A simple recuperated cycle is considered, as basic compact and flexible setup [120]. Thus, the efficiency of the s-CO_2 is enhanced using an internal heat recuperator ("REC HX"). A generator (GEN) converts the shaft mechanical power into electric power to supply to the electric user. In the cogenerative configuration, instead, two heat exchangers employed for cogenerative purpose are present into the plant, named "COOL HX1" and "COOL HX2", recovering heat respectively from the s-CO_2 cooling heat exchanger and from the exhaust gas, downstream of the GAS HX, to supply thermal power to the thermal user hot water circuit (see Figure 10-1c).

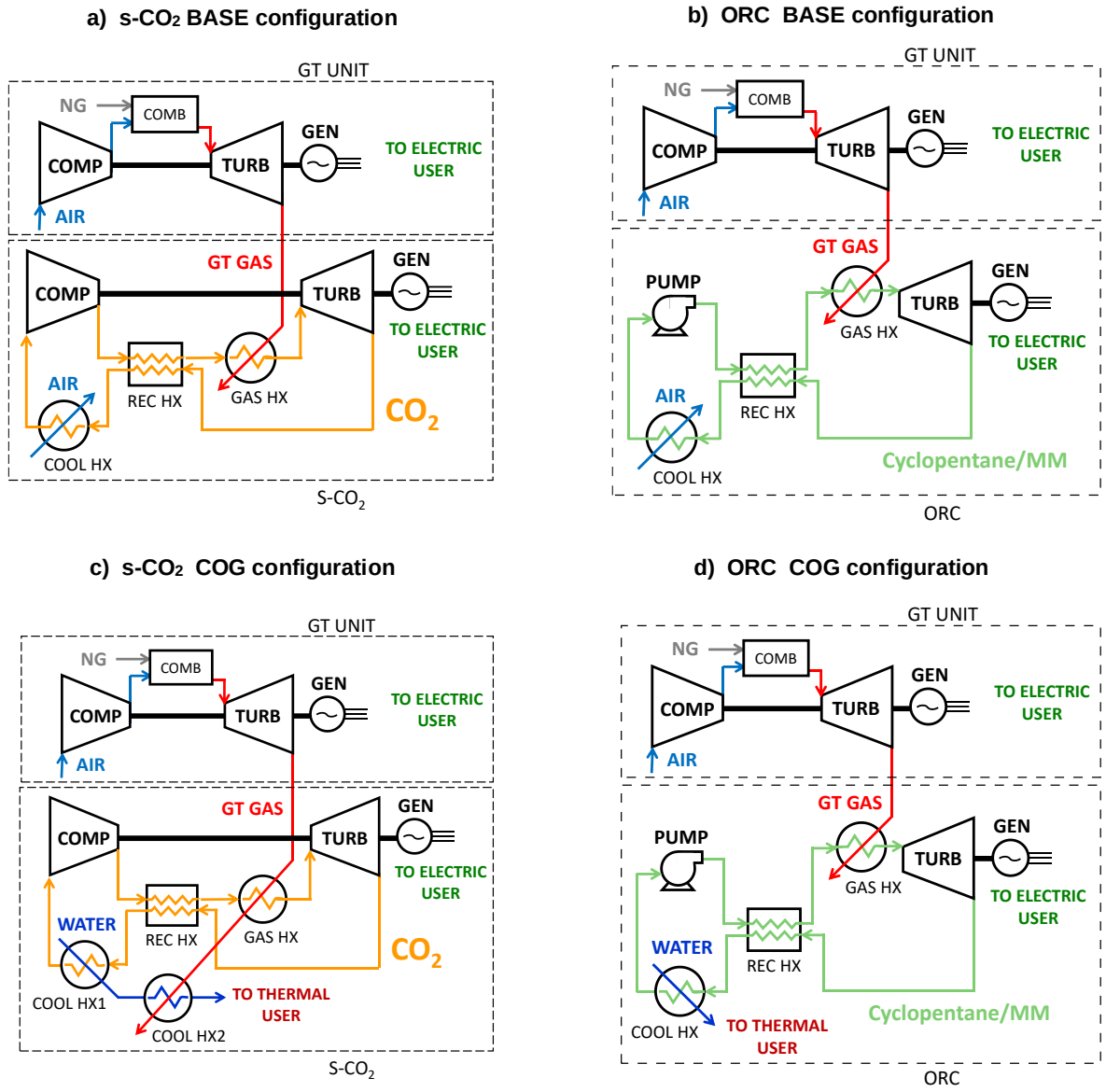

Figure 10-1 - Analyzed configurations layouts:
a) s-CO_2 base, b) ORC base, c) s-CO_2 cogenerative, d) ORC cogenerative.

10.2.2 ORC configuration

The ORC subcritical recuperated architecture is chosen as comparative bottoming system, according to the current state of the art of waste heat recovery applications [5] (see Figure 10-1b). Direct heat recovery solution, without intermediate heat transfer fluid between the GT exhaust and the organic fluid, is considered. In this cycle, an organic fluid circulates through the plant being evaporated and superheated into the heat recovery heat exchanger ("GAS HX"), expanded into the turbine, condensed (into the "COOL HX"), and pressurized by means of a pump. An internal heat recuperator ("REC HX") is used also in this case to improve the cycle efficiency, without over complicating the plant. A generator (GEN) converts the shaft mechanical power into electric power

to supply to the electric user. In cogenerative application, the condenser of the ORC serves as heat exchanger for cogenerative purpose, to supply thermal power to the thermal user hot water circuit (see Figure 10-1d).

10.2.3 Boundary conditions

Before discussing the single systems specifics, some boundary operating conditions concerning the whole power plant operation, are here introduced, see Table 10-1. These conditions regard: i) the hot water temperature requested by the thermal user and its return temperature, assumed equal to 90 °C and 25 °C, respectively; ii) the minimum temperature of the gas turbine exhaust gases at the exhaust stack, limited at 125 °C to avoid the cold-end corrosion issues in the exhaust stack.

Related to these assumptions is the choice of considering two gas heat exchangers for the s-CO_2 configuration, instead of one (see heat exchangers GAS HX and COOL HX2, in (see Figure 10-1c). COOL HX2, placed downstream GAS HX, allows to maximize the gas residual heat recovery, by further cooling down the gas until the minimum stack temperature and provide additional thermal power to the cogenerative thermal user. Indeed, in the s-CO_2 case, it has been observed that a single heat exchanger would not allow to discharge the gas below 250 °C, causing just a partial heat recovery. On the contrary, the GAS HX of the ORC solution has proved to be more performant, as discussed more in detail in the results paragraph.

Table 10-1 - General boundary conditions.

General specifics	
Inlet air properties	**ISO conditions**
Minimum GT stack temperature	125 °C
Hot water temperature to thermal user (COG configuration)	90 °C
Hot water temperature return from thermal user (COG configuration)	25 °C

10.3 Gas turbines selection

A variety of gas turbine models with different size are employed in industrial applications. Small and mid-size machines (MW size range) are used in flexible multiple arrangements, installed on board of small production facilities, usually operating at part-load conditions, e.g. in off-shore plants. Larger power rating units (ranging up to tens of MW), both heavy-duty and aeroderivative machines, are preferred instead on larger facilities requiring higher power needs and working under more stable conditions. Thus, to perform a systematic analysis, four different types of commercial gas turbines, in terms of size and regulation strategy are investigated; in particular gas turbine models often used in the oil and gas sector are considered [23], [121]. The selected gas turbines having different characteristics (as highlighted in Figure 10-2) can represent different possible scenarios of the energy landscape.

The selected GT units design data are summarized in Table 10-2.

Table 10-2- Gas turbines nominal data.

	Kawasaki GPB15 -GT1-	GE5 -GT2-	Solar Titan 130 -GT3-	Siemens GT 700 -GT4-
Output power (MW)	1.5	5.5	15	30
Turbine inlet temperature (°C)	991	1232	1093	1260
Pressure ratio (-)	9.4	14.8	15.7	17.6
Efficiency (%)	24.2	30.6	33.3	36
Exhaust flow rate (kg/s)	8	19	49	89
Exhaust temperature (°C)	520	574	474	518
Regulation strategy	VTIT	VIGV	VTIT	VSS

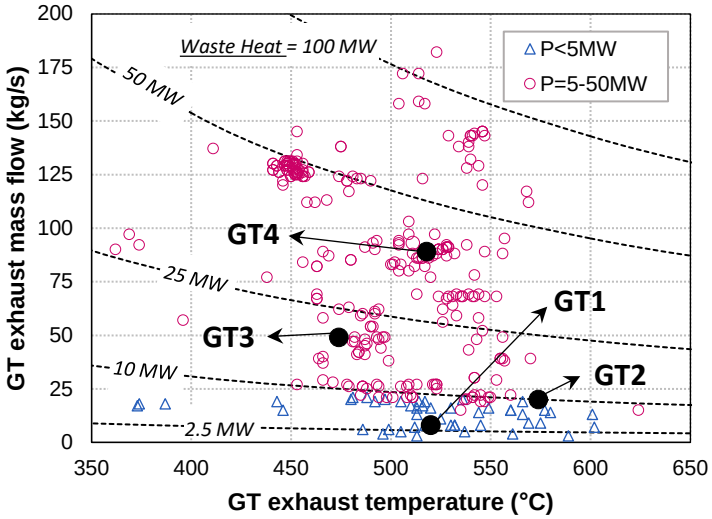

Figure 10-2 - Industrial gas turbines overview §§§§ (black dots highlighted the characteristics of the GTs considered in this analysis).

These gas turbine models are characterized by sizes ranging between 1 MW to 30 MW, with efficiency values increasing with the size, from 24 % for Kawasaki GPB15 up to 36 % for Siemens GT 700 machine. Important variables to consider are also the temperature and the flow rate of the exhaust gases, which affect the amount of energy that can be recovered by the bottomer power cycle. In particular, exhaust gas mass flow rate raises with the gas turbine size and it ranges between 8 and 89 kg/s for the selected gas turbines. Exhaust gas temperature is centred around 500-550 °C, varying between 474 °C and 574 °C. It can be noticed that different models with different regulation strategies have been selected. This aspect will affect the part-load performance of the bottoming cycle, as discussed for the case study presented later in paragraph 10.6.

§§§§ Data from *Thermoflex* industrial gas turbines database [6], obtained considering full load conditions and assuming to cool down to 80°C the exhaust gas.

10.4 Supercritical CO_2 cycle and ORC specifics

10.4.1 Components

The choice of the s-CO_2 components specifics and boundaries' operating conditions, as resumed in Table 10-3, derives from a literature survey based on different studies and experimental data ([50], [56], [120] and [122]). The compressor minimum inlet temperature and pressure are imposed respectively equal to 35 °C and 75 bar. This choice grants to maintain supercritical conditions all along the cycle, given CO_2 temperature equal to 31 °C and critical pressure equal to 74 bar. In line with the current research data, the cycle maximum pressure is limited to 300 bar because of technological limits. The turbine and the compressor isentropic efficiencies values are considered different for s-CO_2 power plant size lower or higher than 3 MW, to account for the machine size-effect over the performance. The recuperator thermal effectiveness minimum pinch point assumed for the heat exchangers, pressure drops and heat loss values are also reported in Table 10-3, and are chosen equal for the ORC and the s-CO_2 systems for a fair comparison between the two systems.

The ORC system specifics selection procedure, instead, is the same deeply described in chapter 7, to which the lecturer is sent back for further details. However, it must be pointed out that in cogenerative configuration some specifics are modified, compared to Table 7-1. Namely, the condensing pressure values, which depend on the cooling medium temperature (see "Low pressure" in Table 10-3), increases for the COG case, following the parabolic trend of the saturation pressure with the temperature (reported in Figure 10-3a).

Table 10-3 - Bottomer cycles design specifics.

	s-CO_2		**ORC**	
Size	**< 3 MW**	**> 3 MW**	**< 3 MW**	**> 3 MW**
Fluid	Carbon Dioxide		MM	Cyclopentane
Low pressure (*BASE/COG case)	75 bar		0.3/0.9* bar	0.6/3.7* bar
High pressure upper limit	300 bar		17 bar	40 bar
Turbine isentropic efficiency	85 %	90 %	80 %	85 %
Op. machine isentropic efficiency	70 %	80 %	60 %	
Recuperator thermal effectiveness	80 %			
Pressure drop across heat exchangers	1 %			
Heat exchangers normalized heat loss	1 %			
Heat exchangers minimum pinch point	5 °C			
Other limits	Min. temperature = 35 °C (supercritical threshold)		Max. temperature = 280 °C (stability limit)	

Different fluids are employed for different solutions, i.e., carbon dioxide for the s-CO_2, and MM and cyclopentane for the ORC depending on the system size. The properties of the fluids will affect not only the system performance but also the size and so the investment considerations. To support

the results discussion, thermodynamic properties useful for the analysis are reported in Figure 10-3; where the saturation pressure and density are plotted against temperature for the different fluids.

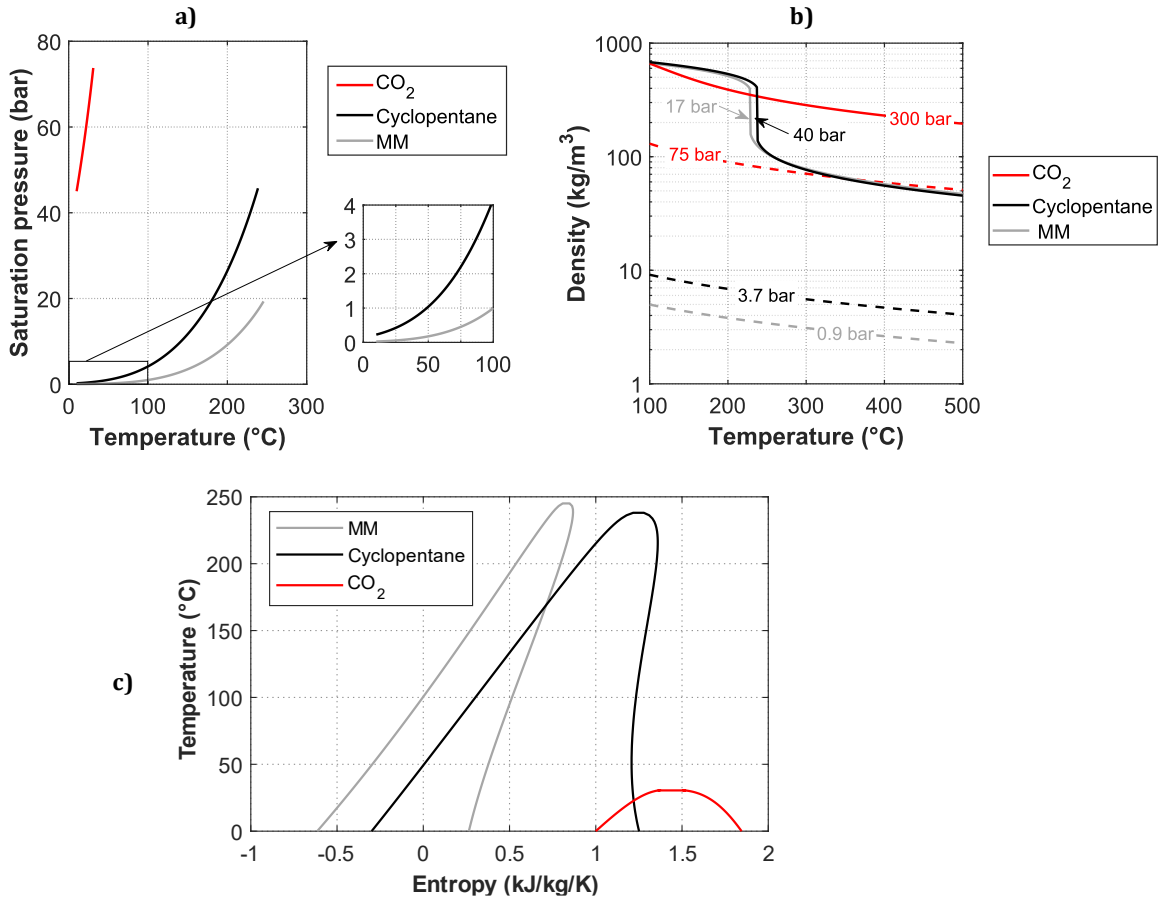

Figure 10-3 - Fluids thermodynamic properties: a) saturation pressure, b) density, c) saturation curves on the temperature-entropy diagram *****.

10.4.2 Cost correlations

In order to compare the investment cost of the two systems, resulting from the simulated operating conditions, the cost of each component is evaluated as described below. The generic formula to evaluate the i-th component investment cost, C_i, is based on re-scaling a reference cost value, C_{ref}, by the ratio between the actual component size, $size_i$, and its reference size value, $size_{\mathrm{ref}}$ [123]. An exponent, n, is usually applied to the scaling factor and the effect of some operating conditions can be accounted by applying some correction factors, *corr* (see Eq. (10-1)). In this analysis, the correlation parameters (as reported in Table 10-4) comes from literature works providing data from s-CO_2 and ORC and specific components vendors (respectively [124] and [125]).

***** Curves obtained by measn of the RefProp thermodynamic library [63].

$$C_i = C_{ref}\left(\frac{size_i}{size_{ref}}\right)^n \cdot corr \qquad (10\text{-}1)$$

Table 10-4 - Cost correlations.

	Component	C_{ref} value	*size* parameter	$size_{ref}$ value	n	$corr$
s-CO_2 ref. [124]	Turbine	149 732 EUR *	P_{exp}	1 MW	0.5561	/
	Compressor	1 008 600 EUR *	$P_{op.machine}$	1 MW	0.3992	/
	GAS HX	40.55 EUR *	$UA_{GAS\ HX}$	1 W/K	0.7544	/
	REC HX	40.55 EUR *	$UA_{REC\ HX}$	1 W/K	0.7544	/
	COOL HX1,2	26.96 EUR *	$UA_{COOL\ HX}$	1 W/K	0.75	/
ORC Ref. [125]	Turbine	1 230 000 EUR	SP	0.18 m	1.1	/
	Pump	14 000 EUR	$P_{op.machine}$	200 kW	0.67	/
	GAS HX	1 500 000 EUR	$UA_{GAS\ HX}$	4000 kW/K	0.9	$f(p_{max})$
	REC HX	260 000 EUR	$UA_{REC\ HX}$	650 kW/K	0.9	$f(p_{max})$
	COOL HX	530 000 EUR	$A_{COOL\ HX}$	3563 m²	0.9	/

* values converted from original values in US dollar

10.5 Results and discussion

This paragraph presents and discusses the results of the comparative analysis, considering design plant performance, bottoming cycle components size and capital costs. Compared configurations (as detailed in the previous paragraphs) include:

- different gas turbine models (see Table 10-2).
- different bottoming solutions: supercritical CO_2 cycle and organic Rankine cycle.
- different heat recovery configurations: involving electric power production only and combined heat power plant (see schemes in Figure 10-1).

10.5.1 Base configuration performance

First of all, results are presented for the pure electric (BASE) case. The bottomer inlet/discharged HX thermal power values and the expansion/compression isentropic power values results are reported respectively in Figure 10-4; these are key components results influencing the net electric efficiency performance of the ORC and s-CO_2 configurations, as reported in Figure 10-5.

In particular, Figure 10-4a shows that the amount of thermal power that can be recovered from the bottoming cycles range between 2 and 40 MW (GAS HX), for the analyzed GTs topper systems. The amount of exchanged heat increases with the topper gas turbine size, mainly due to the increasing of the gas turbine exhaust gas flow with the size. It must be noticed that higher involved

thermal power values are observed for the ORC solution, mainly because of the higher convective heat transfer coefficient of cyclopentane and MM into the evaporator and the condenser, also due to the fluid phase change. This aspect, in particular, will affect the size of the heat exchangers and associated costs.

Figure 10-4b shows the isentropic power values for both the expander and the operating machine, for the different bottoming solutions, combined with the different examined GTs. Results show that despite the ORC exhibit higher recovered thermal power values, the CO_2 solution presents higher isentropic power values available at the expander, due to high pressure ratios. However, the net power production depends not only by the expander output power but also on the operating machine power absorption, and s-CO_2 configurations exhibit also higher power required by the operating machine. It can be observed that the operating machine isentropic power is equal to the 30 % and 3 % of the expander isentropic power, for the s-CO_2 and ORC configuration respectively. Thus, in terms of the net isentropic available power (and of the resulting bottoming cycle net specific work per unit of GT exhaust), the ORC is the most performant solution in all the examined cases.

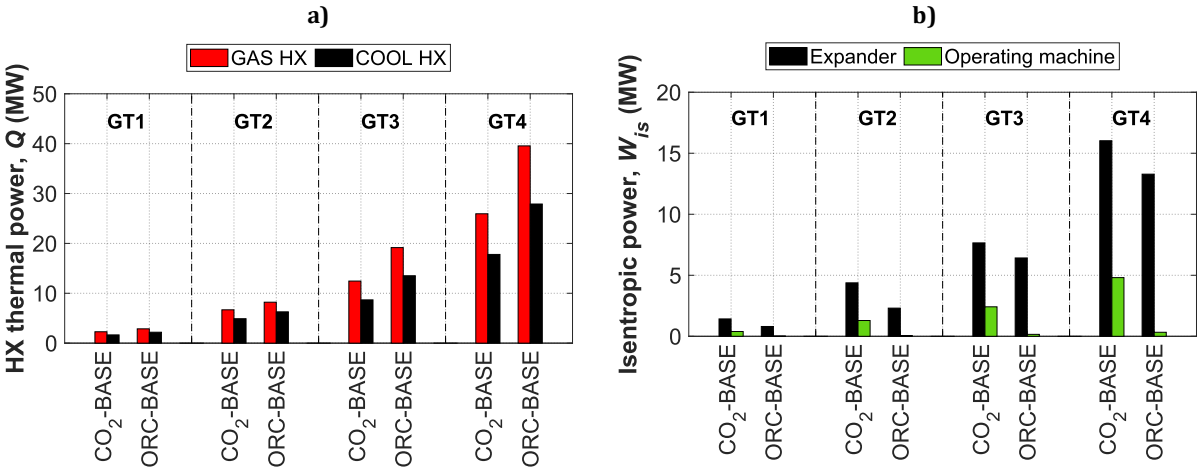

Figure 10-4 - Base case performance comparison: a) HX heat transfer; b) machines isentropic power.

These results on output power obviously affect also the net electric efficiency of the plant, as in Figure 10-5. Indeed, the ORC is the configuration showing the highest plant net electric efficiencies. However, it must be noticed that both the analyzed cycle configurations lead to a remarkable increment in the overall net electric efficiency of the power plant, if compared to the GT simple cycle (green line in Figure 10-5). The achieved average increment in efficiency ranges from 7 to 11 percentage points, respectively if considering s-CO_2 or ORC as bottoming solution. In terms of absolute values, it is observed that net electric efficiency value of the integrated systems increases with the topper gas turbine size. This is mainly due to the increase of the simple cycle GT efficiency with size. In particular, the net electric efficiency value of the combined GT/ORC cycle in pure electric configuration reaches its maximum at 48 %, by combining the ORC optimal design with Siemens GT 700 (GT4) model. The GT/s-CO_2 integrated system in pure electric case achieves efficiency values almost close to 44 % with GT4.

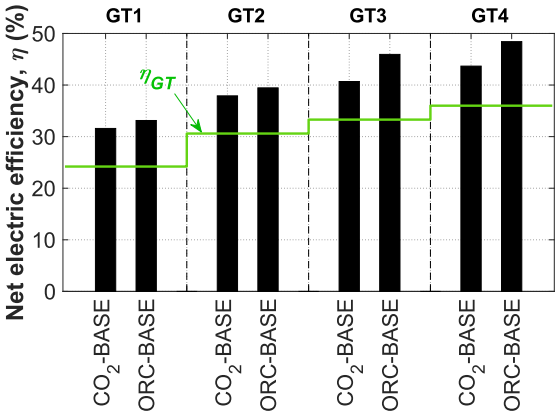

Figure 10-5 - Net electric efficiency of the system (BASE CASE).

10.5.2 Cogenerative configuration performance

The calculated performance results of the COG case are shown in Figure 10-6; the electrical efficiency and thermal efficiency points of the analyzed configurations are shown, and constant *PES* lines are also traced in green in the same graph. The electrical efficiency increases with the GT size; the thermal efficiency generally decreases by increasing the GT size, due to the consequent decreasing discharged heat. The calculated values of thermal efficiency range between 35 % and 45 %. The corresponding *PES* values are increasing with the GT size and largely positive in many cases (up to 22 % for GT4 with s-CO_2 cycle). The achievable primary energy savings are attractive in most of the cases. Only in case of GT1 and with ORC as bottomer the COG configuration becomes less attractive, showing *PES* close to 0. It can be observed that the s-CO_2 COG systems exhibit both higher electric efficiency and higher thermal efficiency, if compared to ORC systems, for all the examined topper GT models. This leads to larger *PES* values in case of the combined GT/s-CO_2 cycles that in case of the GT/ORC systems.

Thermodynamic diagrams of the s-CO_2 and ORC systems as bottomer of GT4 are shown for example in Figure 10-7, to help explaining the main factors influencing the performance of the two systems in COG configuration. More in detail, some considerations can be made about the bottoming cycles performance in combined heat and power application and the influence of the thermal user requested temperature. Indeed, it is observed that the ORC expander enthalpy drop (thus, the specific work) can be considerably affected by the condensing temperature, which determine the condensing pressure and the expander pressure ratio, consequently. This is not valid instead for the s-CO_2 pressure ratio, which does not depend on the thermal user requested temperature, since the s-CO_2 does not present a condensing phase. This explains the derating of the ORC electric production performance in COG case.

The CO_2 COG higher thermal efficiency instead is a consequence of the additional contribution due the second heat exchanger recovering heat from the exhaust GT gas (COOL HX2). The corresponding heat exchange diagram shown in Figure 10-7 reveals indeed that up to 12 MW

additional thermal power can be recovered, combining the s-CO_2 cycle with GT4. It is to remember that the comparison is made being equal the thermal power discharged by the gas turbine. Indeed, in both the cases the exhaust gas is cooled down until about the minimum stack temperature set equal to 125 °C.

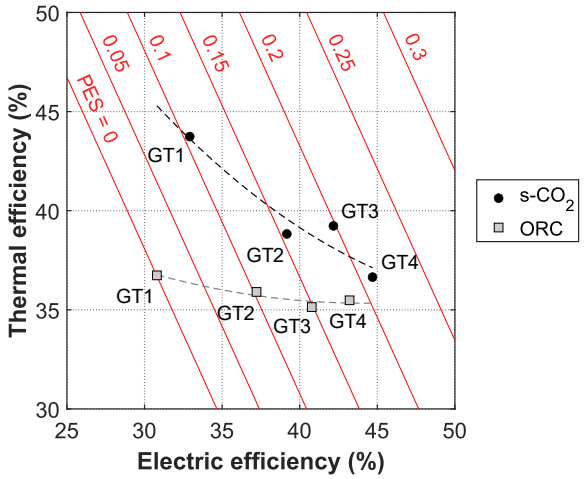

Figure 10-6 - Thermal efficiency vs electric efficiency (COG CASE).

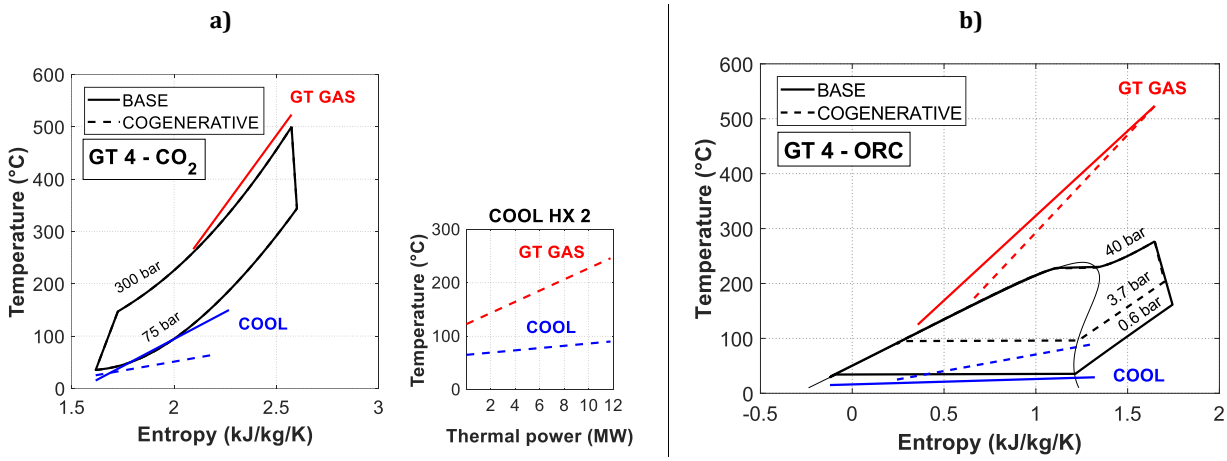

Figure 10-7 - Thermodynamic diagram for the BASE and the COG configurations - GT4 CASE: a) s-CO_2 with COOL HX2 heat transfer diagram and b) ORC.

10.5.3 Power production and bottoming cycle design size

For sake of completeness, electric power in both BASE and COG cases and thermal power production data for COG configurations are presented in Figure 10-8. The green line indicates the GT electric power output as standalone unit, for comparison purpose.

Results show that combining the bottomer cycle with the GT unit allows to produce additional electric power ranging between about 0.5 MW to 10 MW with the best configuration for electric power production (ORC BASE). Instead, the best configuration for cogenerative purpose, namely s-CO_2 COG, allows to produce at the same time, from 0.6 to 7.7 MW of additional electric power and from 2.8 to 30.9 MW of thermal power, depending on the GT size.

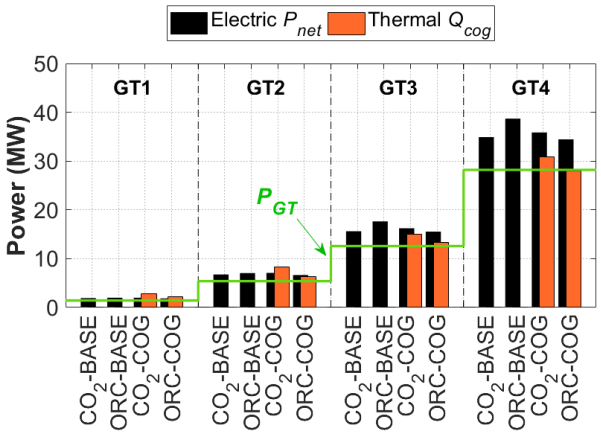

Figure 10-8 - Net electric and thermal power production for the different configurations.

Table 10-5 - Bottomer cycle power size.

Bottomer cycle design size (kW)					
Configuration		**GT1**	**GT2**	**GT3**	**GT4**
CO_2	**BASE**	482	1376	3047	6710
	COG	565	1698	3655	7667
ORC	**BASE**	576	1653	5066	10502
	COG	434	1256	2970	6256

10.5.4 Size and investment considerations

Size parameters

The computed values of the heat exchangers global heat transfer coefficients and the turbine size parameter are reported in Figure 10-9.

Figure 10-9a shows the total heat exchanger size and its distribution between the different heat exchange sections, “GAS, HX”, “REC, HX” and “COOL, HX”, where the size of the GT unit and the exhaust gases temperature levels have a direct influence on the heat exchanger surface area. It can be noticed that the total heat exchanger size is similarly divided among the various heat exchange sections, varying the examined gas turbine, for given bottoming cycle solution. Whilst the $A_{rec,HX}$ value is similar between the s-CO_2 and the ORC solutions, suggesting similar internal heat recovery conditions, $A_{gas,HX}$ and $A_{cool,HX}$ can greatly differ. s-CO_2 $A_{gas,HX}$ is on average 4 times the ORC $A_{gas,HX}$, mainly because of the higher convective heat transfer coefficient of cyclopentane/MM into the evaporator, also due to the fluid phase change, which guarantees a more performant heat

exchange. Concerning instead "COOL HX" (comprehending both "COOL HX1" and "COOL HX2" for the s-CO_2), $A_{cool,HX}$ values are more similar between the different configurations. However, a slight increase of the size parameter is observed when using the ORC rather than the s-CO_2 solution, indicating a worse matching between the working fluid heat exchange profile and the cold source's one. This analysis suggests that higher heat exchangers investment costs can be expected if installing s-CO_2 bottoming cycle rather than ORC, given the higher total heat exchanger size, which can be more than twice the ORC configuration's one.

Opposite conclusions can be drawn from the turbine size parameter analysis. Focusing on Figure 10-9b, it can be noticed that comparing the different bottoming cycle options, the s-CO_2 exhibits lower turbine size parameter values, mainly due to the higher density of the fluid passing through the expander. Indeed, the s-CO_2 cycle works at high pressures, comprised between 300 and 75 bar, corresponding to relatively high CO_2 density values that ranges between 700 e 60 kg/m^3. Cyclopentane and MM, instead, both expand in ORC at lower pressure and lower density (below 10 kg/m^3), leading to less compact expander machines (see Figure 10-3b). It can be noticed that the density of cyclopentane and MM drops markedly in correspondence of the critical temperature value (of about 240°C), because of the fluid phase change.

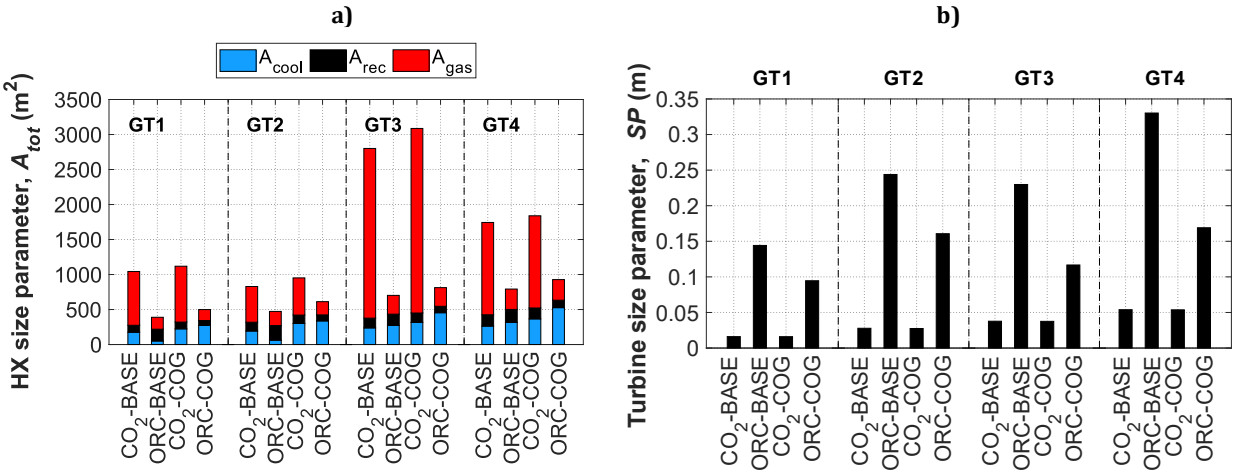

Figure 10-9 - Size indexes: a) heat exchangers size parameters. b) turbine size parameter.

Investment cost

The investment cost results reflect the considerations made about the components size. Figure 10-10 shows that the s-CO_2 requires very higher heat exchangers costs, because of the large size of the GAS HX but also to the high investment cost still associated to this component, due to the current challenges related to the structure design and the selection of materials compatible with the high cycle pressures and the strong corrosive behavior that CO_2 shows at high temperatures [49]. The s-CO_2 also requires larger size (see Figure 10-4b) and more expensive operating machines. On the other hand, the ORC operates with larger turbines, which entail higher expander investment costs. In the view of the above, the total investment cost, given by the sum of the single components costs, result to be pretty higher for the s-CO_2 rather than for the ORC. According to this study, the ORC

configuration, instead, could introduce an economical saving of about the 40 %, with respect to the CO_2 base configuration.

Results of this work can be good guidelines for a preliminary economic comparison, but they cannot allow to establish a priori the optimal heat recovery configuration from the economic point of view. Further investigation should regard the determination of the economic optimum for more specific applications, accounting for the influence of the yearly demand profile (i.e. gas turbines working profile) on the energetic production, the economic gain, and the final return on the investment.

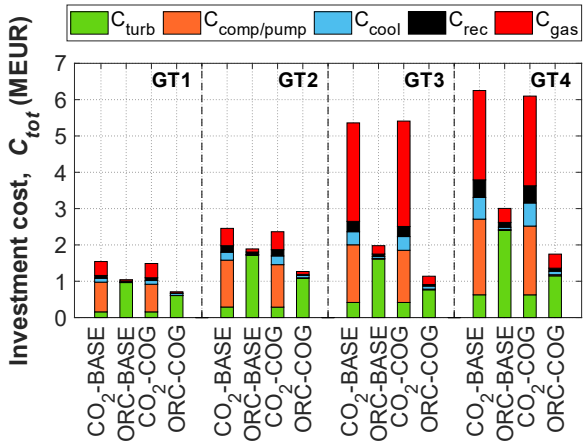

Figure 10-10 - Capital costs.

10.6 Cogenerative application – a case study

10.6.1 The case study

This last paragraph is dedicated to a more detailed comparison between the ORC and the s-CO_2 cogenerative solution; where the cogenerative case is chosen since proven to be an interesting application for the s-CO_2 compared to the ORC, worthy of deeper analysis. Based on a case study, the yearly energetic production of the proposed bottoming cycles is evaluated together with their feasibility. On this occasion, part-load performance of the bottoming cycles is also discussed.

The investigated case study refers to the gas turbine load profile of a natural gas compressor station, presented in Figure 10-11. It is shown that the gas turbine works at full load for about half of the operating hours, whilst for the rest of the time, the GT load is almost equally distributed between the 50 % and the 90 %.

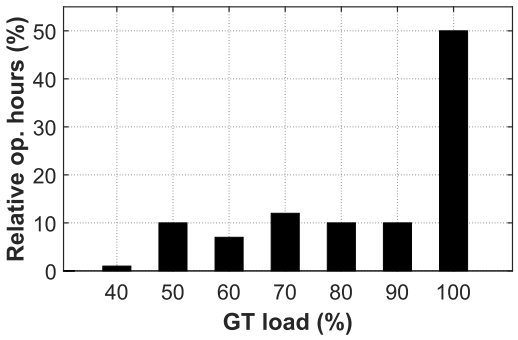

Figure 10-11 - Reference yearly demand profile of a natural gas compressor station.

10.6.2 Part load performance

In this paragraph are analyzed the part-load performance of the bottoming cycles as function of the GT load, varying between its technical minimum, assumed equal to 40 %, and full load.

Figure 10-13a and b reports manufacturer data provided by the GT PRO gas turbine *Thermoflex* library [6], showing how the exhaust flow rates and temperatures values vary with the gas turbine load for the different models. These values can significantly vary at part-load conditions, strongly influencing the bottoming cycle performance. The trends of the bottoming cycle produced electric and thermal power, normalized on their design values, are reported in Figure 10-13; where the normalized values are useful to immediately compare the effect of the gas turbines regulation strategy on the bottoming cycles part-load performance.

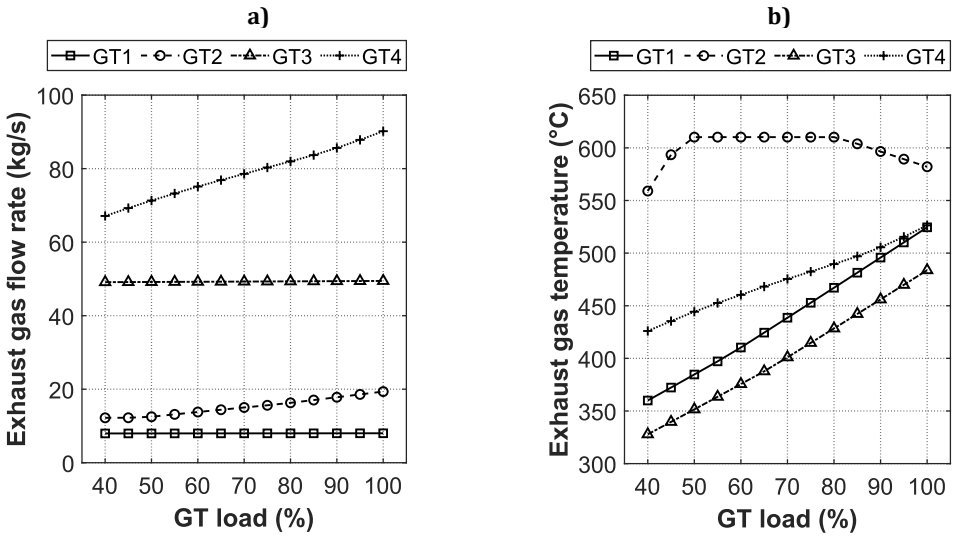

Figure 10-12 - Part load operation: a) exhaust GT gas flow rate, b) exhaust GT gas temperature.

It can be observed that different gas turbine regulation strategies determine different trends, as already discussed in paragraph 8.2.2.. Some considerations made for the ORC can be repeated for the s-CO_2 with different results. Focusing on the electric production (see Figure 10-13a), it can be

noticed that the s-CO_2 system maintains higher part-load performance when working with GT1 and GT3, turbines regulated by means of the VTIT strategy; thus, working with almost constant exhaust flow rate (see Figure 10-13a). On the contrary, the ORC power plant results to be more performant when working with GT2 (VIGV), and following GT4 (VSS), GT1 and GT3; thus, benefitting from working with exhausts temperatures that do not change significantly with respect to the design values (see Figure 10-13b).

The same considerations apply to the thermal power production at part-load conditions (see Figure 10-13b). It can be also observed that a higher performance derating occurs for the ORC configuration with respect to the s-CO_2, except for the GT2 case, which is instead in line with the s-CO_2 curves.

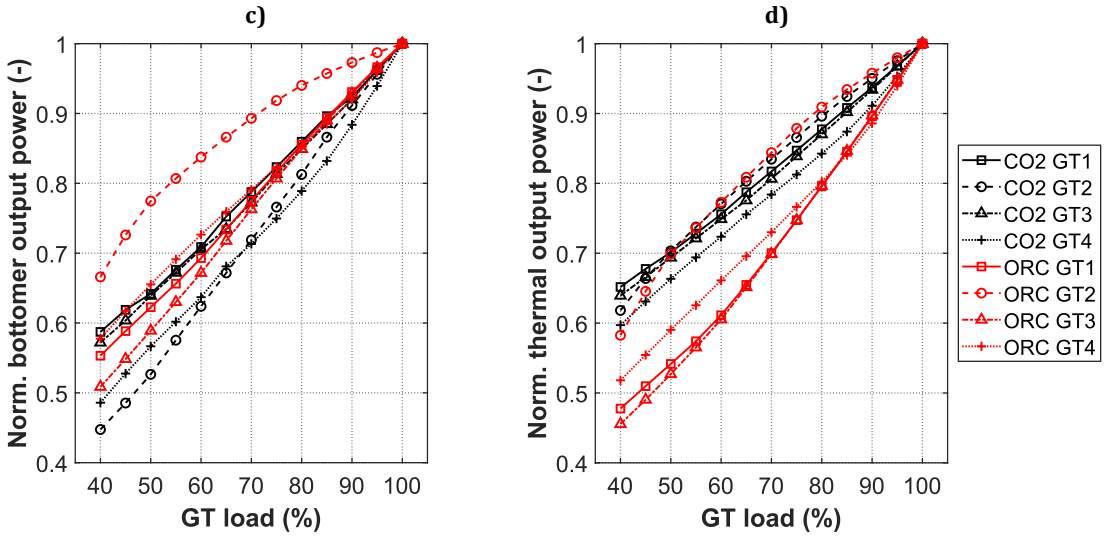

Figure 10-13 - Part load operation: a) normalized electric power output, b) normalized thermal power output on the design condition.

10.6.3 Analysis of feasibility

The return on the investment is estimated by assuming that introducing the bottoming cycle produces a fuel saving as it would cover the energy demand that otherwise should be provided by another external energetic system, following the procedure described in paragraph 7.3.3. The reduction of the fuel consumption is reflected in reduced greenhouse gas emissions and in reduced plant operation costs. The fuel cost is chosen equal to the average natural gas price in Europe in 2019, 26.7 eur/MWh, [126] and a reference carbon tax value is selected equal to 40 eur/ton, as in line with its average value in some European countries [127].

Reference case results

A résumé of the design performance results, the yearly energy production and savings is reported in tabular form (see Table 10-6). As discussed in the previous paragraphs the s-CO_2 cogenerative configurations exhibit better performance than the ORC, in design operation, both concerning the electric and the thermal production. The yearly energetic results demonstrate that this applies also on the yearly based performance; indeed, the s-CO_2 allows to save on average the 16 % of fuel more

than the ORC solution and consequently also the 16 % more of CO_2 emissions. The same increase is observed for the yearly economic gain.

Yet, in spite of the significant economic gain expected from the s-CO_2 operation, the net present value of the investment seems not to be always favorable on this system, as shown in Figure 10-14 (see "s-CO_2 ref" and "ORC ref" data). This is mainly due to the still high investment costs associated to this fledgling technology, in particular for what concerns the recovery heat exchangers. However, given the considerable economic gain, it is not excluded that once the technology will be established, the s-CO_2 may become a very competitive solution for industrial gas turbines heat recovery. On the other hand, the current lower investment costs required to install an ORC system, make this solution yet practical and often profitable.

Table 10-6 - Results résumé.

	GT1		GT2		GT3		GT4	
	s-CO_2	**ORC**	**s-CO_2**	**ORC**	**s-CO_2**	**ORC**	**s-CO_2**	**ORC**
Electric power output (MW)	2	1.87	7.02	6.65	16.25	15.66	35.73	34.54
Thermal power (MW)	2.65	2.23	6.94	6.42	15.07	13.49	29.30	28.36
Electric energy (GWh/year)	15.3	14.4	54.4	52.0	124.8	120.7	274.4	266.9
Thermal energy (GWh/year)	21.5	17.1	56.6	52.5	121.5	103.6	233.2	220.3
Fuel saving (GWh/year)	32.2	25.6	87.6	78.5	189.6	161.8	371.2	342.4
Avoided emissions (ktonCO_2)	1.88	1.50	5.13	4.59	11.09	9.46	21.72	20.03
Economic gain (kEUR/year) *	75.3	60.0	205.1	183.6	443.80	378.6	868.7	801.3

* Reference case results (considering Figure 10-11 demand profile and C_{CO2} = 40 EUR/ton)

Costs parametric analysis

Factors that can influence the bottoming cycles feasibility and which can considerably vary from application to application, are the user profile demand and the carbon tax value. The profile demand can be more or less shifted to the high or low loads; whilst the carbon tax value is variable from country to country, and it can be null or even equal to 140 eur/ton, as it is the case of Sweden. Thus, to complete the economic analysis, the investment is evaluated by considering also more favorable economic conditions, i.e. a full load yearly demand profile (see Figure 10-14a) and an higher carbon tax value, equal to 140 eur/ton (see Figure 10-14b).

These results reveal that among the two analyzed factors, the most decisive one on the return of the investment is surely the carbon tax value. It is observed, indeed, that higher values of the carbon tax reduce the gap between the gain obtained with the ORC and the one obtained with the s-CO_2 (see Figure 10-14b). This is due to the higher valorization of the avoid emissions, which are the 15 % higher for the s-CO_2 than for the ORC (see Table 10-6). Generally, with higher values of the carbon tax the s-CO_2 system may become convenient as bottomer of all the analyzed gas turbines, as well as the ORC, with a net present value more than twice of its reference value. The return on the investment is instead less sensitive to the variation of the profile demand (see Figure 10-14a). Working at full load, during all the year, does not grant such a significant gain equal to the one obtainable by introducing a high carbon tax. Comparing the case at the reference load profile and

the full load profile, the net present value increase of the 17 %. However, in some cases, the yearly demand profile can be decisive to have a return on the investment, for example when the investment is uncertain and the net present value is near to zero. This is the case of the GT1-ORC and the GT3 s-CO_2 configurations, which are not convenient if operating at part-load conditions but they can become if working at full load during all along the year.

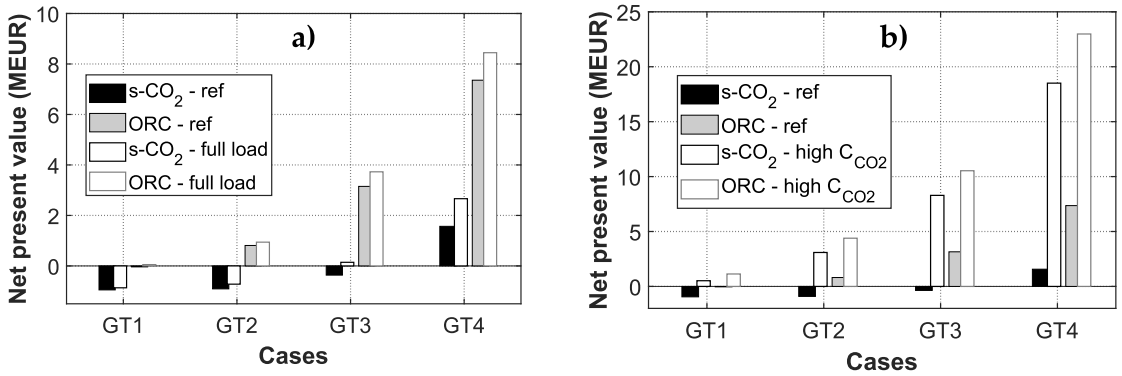

Figure 10-14 - Net present value comparison between the reference case study and: a) a full load yearly operation and b) the application of a higher carbon tax.

10.7 Conclusion

This study presents a detailed investigation and comparison of ORC and s-CO_2 potential as bottoming recovery cycles in combined heat and power plant configuration inside industrial facility, comparing several gas turbine models at part-load operation. Findings of this work can be resumed as follow:

- Higher recovered thermal powers are observed for the ORC solution, mainly because of the higher convective heat transfer coefficient of cyclopentane and MM into the evaporator and the condenser, also due to the fluid phase change. Despite the ORC exhibit higher recovered thermal power values, the CO_2 solution presents higher isentropic powers available at the expander to produce work, thanks to the higher pressure difference. However, supercritical CO_2 configurations exhibit also higher operating machine consumption, which corresponds to the 30 % over the expander isentropic power (against the 3 % of the ORC configuration).
- Results of the energy analysis considering only the pure electric production, highlight that both the configurations lead to a good increment in the overall net electric efficiency of the power plant, if compared to GT in simple cycle; the average increment is of 7 and 11 percentage points, respectively if considering s-CO_2 or ORC as bottoming solution.
- Concerning the cogenerative performance, the s-CO_2 system exhibits at the same time higher electric efficiency and thermal efficiency, if compared to ORC system, being equal the installed topper gas turbine model. The PES values for s-CO_2 cycle range between 10 % and 22 %. The ORC lower performance is due to the high condensing pressure value, imposed by the temperature required by the thermal user. This does not affect instead the s-CO_2 operating pressures, since the s-CO_2 does not present a condensing phase.

- From the economic point of view, this analysis suggests then that higher operating machine and heat exchangers investment costs can be expected if installing s-CO_2 bottoming cycle rather than ORC. Opposite considerations derive instead from the turbine size parameter evaluation. Indeed, the ORC working fluid expands into the ORC turbine in lower pressure and lower density ranges, if compared to carbon dioxide into the supercritical cycle, leading to less compact expander machines.
- To determine the most convenient configuration, both these aspects (i.e. performance and investment cost) must be taken into account. For this reason, a capital cost parameter is considered, calculated as the sum of the expander and the heat exchangers capital costs. Results show that the highest capital cost parameter is associated to the CO_2. According to this study, the ORC configuration, instead, could introduce an economical saving of about the 40 %, with respect to the ORC base configuration.

Results of this work can be good guidelines for a preliminary economic comparison, but they cannot allow to establish a priori the optimal heat recovery configuration from the economic point of view. Thus, further investigation regarded the investigation of the economic optimum for a cogenerative case study, accounting for the influence of the yearly demand profile (i.e. gas turbines working profile) on the energetic production, the economic gain, and the final return on the investment:

- At part load operation, it can be noticed an influence of the gas turbine regulation strategy, over the bottoming cycles performance. In particular, the s-CO_2 system maintains higher part-load performance when working with turbines regulated by means of the VTIT strategy; thus, working with almost constant exhaust flow rate. On the contrary, the ORC power plant benefits from working with exhausts temperatures that do not change significantly with respect to the design values.
- Considering the analyzed scenarios, the high investment costs still associated to the s-CO_2 technology make it not already practical for industrial gas turbines heat recovery applications (no return on the investment), except in the case a high value carbon tax value is applied. On the contrary the current lower ORC investment costs make this solution yet profitable, granting a return on the investment in most of the cases. However, given the considerable economic gain, it is not excluded that once the technology will be established, the s-CO_2 may become very competitive in this sector. Nowadays, a crucial parameter determining the feasibility of the investment is surely the carbon tax value. The influence of the user profile demand is instead less strong, even if it can be decisive when the investment is uncertain and the net present value close to zero.

Final conclusions

The intention of this thesis was to address some of the topical themes in the ORC field, paying particular attention in the development of reliable models based on realistic data and accounting for the off-design performance of the ORC system and of each of its components. The project was split into two main parts, part I "ORC for micro-generation" and part II "ORC for the medium to large scale industrial WHR". Different methodologies have been employed for the different applications and the obtained results can be merged for topics, as listed below:

Part I: ORC for micro-generation

- Implementation of a part load model with focus on the expander modelling approach
- Influence of the working fluid over the performance and the environmental impact
- Optimal management of the power to heat to power reversible ORC configuration

Part II – ORC for the medium to large scale industrial WHR

- Optimal ORC sizing in natural gas compressor stations, analysis of the factors of influence and the regulation strategies
- Comparison between ORC and supercritical CO_2 power cycle as bottomer of industrial gas turbines

Final conclusions of this work are commented following this scheme.

Part I: ORC for micro-generation

Implementation of the part load model with focus on the expander modelling approach

In this work of thesis an off-design model to simulate micro-ORCs was implemented, calibrated and validated versus experimental data collected for the prototype of the University of Bologna, using a reciprocating piston expander as expansion machine. The methodology used to elaborate measures from experiments on the test bench was described, being this step fundamental to obtain reliable data. A semi-empirical lumped parameters approach was used, conceived to describe the part-load behavior of such a system and the performance at component level. A new methodology to account for the change of the working fluid was introduced to determine its influence over the components' performance. A focus on the comparison between different literature models for the reciprocating piston expander was proposed. This analysis shows the importance of implementing models more based on physical equations (such as semi-empirical lumped parameters models) rather than only on efficiencies polynomial functions. Looking at the results, even if both these approaches exhibit a good accuracy in a range of operating conditions close to the training set of data, the polynomial model cannot capture the influence of some phenomena which become important at lower- and higher-pressure ratio values, at the contrary of a lumped parameters

approach. It was concluded that a polynomial functions model can be suitable to be applied into the range of the training data set, with a low effort for its implementation. But, when the aim of the model is to simulate the behavior of the expander under unexplored operating conditions, the best choice is the lumped parameters approach, given its best physical sound in extrapolated conditions. Downstream this analysis, for the purpose of this work, the lumped parameter approach was adopted for the following considerations. Considering then the whole system model, the validation process confirmed the effectiveness of semi-empirical models in predicting part-load behaviour of micro-ORCs, since comparing main output calculated values (of evaporator thermal power, expander produced electrical power and pump absorbed electrical power) with measured ones, most of the points come within a 10 % error band.

Influence of the working fluid over the performance and the environmental impact

The model was used to investigate how the performance of volumetric machines, both the pump and the expander, would change when using the R134a low global warming potential alternatives as working fluids for low temperature applications. Relative importance of the different losses affecting the expander performance, was discussed in detail. This study highlighted the main factors that could affect the performance of a volumetric expander, which are: (i) the fluid saturation pressure (influencing the enthalpy drop available through the expander), (ii) the viscosity (mainly affecting the leakage losses at the pump meatus and thus the elaborated mass flow rate), (iii) the heat transfer coefficients values (influencing the ambient heat loss), (iv) the vapor density (affecting the leakage losses during the expansion process). The lower pressure ratio and the lower viscosity of the HydroFluoroOlefines, in particular, lead to smaller enthalpy drop at the expander and higher leakage losses at the pump meatus, which penalize the performance of such machines if compared to R134a. As final step, a quite simple methodology to identify the optimal expander intake stroke ratio value is proposed. It arises that the optimization of the built-in volume ratio could lead to a substantial increase of the expander performance. For the case study of the prototype of the University of Bologna, it was estimated a potential electric power output gain around 42 %.

In a second step, a method to comprehensively analyze GHG annual impact of an ORC system is discussed and applied to a case study, to establish the real potential of low GWP fluids and their blends with R134a, in reducing the GHG release compared to conventional HFCs. The intention was to propose a new point of view, considering not only direct emissions due to refrigerant leakage but also indirect emissions. The proposed analysis reveals that HFO fluids cannot always guarantee the same performance of commonly used fluid R134a, even if they exhibit very lower GWP. Thus, HFOs and their mixtures introduce an energy production gap, which can be compensated with energy sources outside the ORC system, likely employing fossil fuels. If considering a leak rate equal to 2%, indirect emissions caused using HFOs determine total equivalent emissions of CO_2 greater than the ones related to R134a use, up to + 181 % by employing R1234ze(E). More performant and environmental fluids can be identified among the hydrofluorocarbons and their mixtures, such as the R430A, even if their higher flammability risk make not practical to employ them into a residential ORC system. This study turns the attention on how combined actions are requested in order to effectively reduce emissions related to systems using refrigerants as working fluids, such as micro-ORC. The decrease of working fluids GWP, to limit direct emissions must be accompanied by also a

not negligible reduction of the energy mix emission factor, in order to contain possible indirect emissions.

Optimal management of the power to heat to power reversible ORC configuration

The ORC model was coupled with a semi-empirical lumped parameters model of a heat pump, based on a similar approach, in order to explore the potential and the optimal management strategy of a power to heat to power reversible ORC configuration. The reversible HP/ORC prototype installed at the University of Liège was considered as reference, and experimental data provided by the university are used for the model calibration and validation. The performance of the integrated system was simulated as function of the most influencing factors. From the performance analysis resulted that for each value of the hot source temperature, and the available/demanded power to the HP/ORC it exists a combination of the glide and the mass flow rate value that allows to maximize the system efficiency. Thus, a regulation strategy was proposed to manage the Carnot battery in order to work in each mode (ORC or HP) at maximum net efficiency (or COP, in HP case) under imposed boundary conditions. The results of the optimal control strategy application show that in order to reach the maximum ORC efficiency for each boundary conditions' combination, the working fluid mass flow rate must be incremented with the demanded power output. In most of the cases, instead, the glide must be incremented with the available hot source temperature. Concerning the HP, in order to reach the maximum COP for each boundary conditions' combination, the working fluid mass flow rate must be incremented with the available power. The glide, instead, must be reduced as the available power and the storage temperature decrease.

In conclusion, a preliminary analysis on the system feasibility and the optimal storage size was proposed, evaluating the influence of two parameters: the integrated WH thermal power and the Carnot battery size with respect to the scale of the process demand. From the economic point of view, the results show that to have reasonable values of the payback period (PB < 20 years) a WH thermal power integration higher than 20 kW is required. Concerning the optimal storage size (which minimizes the payback period), the higher is the WH thermal power the higher is the optimum storage size, since the storable energy increases and also the potential economic gain. Nevertheless, the optimal storage size decreases at lower scaling factor because there is less and less convenience on invest on large storage size, since the storage cost increases significantly with the size whilst the increment of the economic gain increases less and less, due to the lower relative Carnot battery production. Consequently, for high WH thermal powers and low scaling factors, it less convenient to use the HP mode and it is rather preferable to under size the storage and sell the surplus of electric energy produced by the renewable source.

Part II – ORC for the medium to large scale industrial WHR

Optimal ORC sizing in natural gas compressor stations, analysis of the factors of influence and the regulation strategies

For the modelling of medium to large scale ORC as bottomer of industrial gas turbines, a software born to simulate complex power plants in both design and off-design condition, i.e. *Thermoflex*, was chosen as simulation tool. A particular attention was paid in the selection of the model parameters,

which involve the nominal performance of the components and the strategies of control of the plant at part-load operation. These parameters were chosen in line with the current state of the art of the technologies with the support of data provided by manufacturers such as Turboden and Solar Turbines.

The feasibility and optimal design of the ORC system was studied as function of different factors depending on the facility demand profile, the gas turbines model and the site location. Results, in brief, showed that load profiles characterized by a higher number of operative hours (typical of natural gas compressor station), even if more distributed towards part-loads, are more beneficial for the investment on an ORC than load profiles characterized by a lower number of operative hours but more distributed towards the full load (typical of facilities dedicated only to the storage). Then, different GT models can be based on different part-load control strategies, influencing the ORC optimal design. The results showed that the ORC performance and design power can be remarkably lower if comparing VSS or VTIT control load strategy to VIGV regulation. Indeed, the VSS and the VTIT regulation strategy entails a remarkably decrease in exhaust mass flow and temperature at part load thus largely reducing the amount of heat input to the ORC cycle, at the contrary of the VIGV control. From the economic point of view, the topper cycle regulation strategy can determine the feasibility or not of the ORC. The natural gas compressor station location ca also be a crucial factor of influence on the return of the investment, maybe the more important. Indeed, the factor that more affects the return on the investment is the carbon tax value strongly influencing the economic gain. Thus, this analysis highlighted the strict correlation between the magnitude of the green incentives and the effective possibility of reduction of the greenhouse gas emissions.

A following analysis concerned the implementation of an optimal load allocation procedure to re-distribute the loads into a gas compressor station, when an ORC type system is added to the traditional turbo-compressor configuration to replace a natural gas compressor prime mover. The strategy consists in the resolution of a minimum constrained problem, for which the loads are re-allocated between GTs and ORC, in order to minimize the fuel consumption of the facility, respecting the machines operating constraints. The procedure was applied to a case study: a typical interstate gas compressor station, with about 24 MW of mechanical driving capacity installed. The results brought to light an interesting consideration about what a brand-new design of a natural gas compressor station should account for, when considering the introduction of an ORC as WHR system. Namely, a different design of the original plant, employing GT runners of different capacities, can allow a wider margin of regulation and exploitation of the ORC system on site. For the case study, the optimal ORC size turned out to be 5285 kW; size which allows to produce with the ORC – EMD the 18 % of the yearly station mechanical energy demand, with a reduction of 22 % of the CO_2 emissions, compared to the original arrangement. The investment resulted to be profitable in particular in higher natural gas prices and carbon tax scenarios.

Comparison between ORC and supercritical CO_2 power cycle as bottomer of industrial gas turbines

This study presented a detailed investigation and comparison of ORC and s-CO_2 potential as bottoming recovery cycles in combined heat and power plant configuration inside industrial facility, comparing several gas turbine models at part-load operation. Results of the energy analysis considering only the pure electric production, highlighted that the ORC exhibits better performance,

due to: i) higher recovered thermal powers (because of the higher convective heat transfer coefficient of the fluids into the evaporator and the condenser) and ii) lower relative operating machine consumption (3 % against 30 % of the CO_2 configuration), although the s-CO_2 expander enthalpy drops are considerably higher. Concerning the cogenerative performance, instead, the s-CO_2 system exhibits at the same time higher electric efficiency and thermal efficiency, if compared to ORC system, being equal the installed topper gas turbine model. The PES values for s-CO_2 cycle range between 10 % and 22 %. It is interesting to notice that the ORC lower performance is due to the high condensing pressure value, imposed by the thermal user temperature, not affecting instead the s-CO_2 operating pressures, since the s-CO_2 does not present a condensing phase. From the economic point of view, this analysis suggested that higher capital costs are associated to the CO_2. It is due to the larger required sized but especially to the high heat exchangers investment still associated to this component, related to the design and the selection of materials compatible with the high cycle pressures and the strong corrosive behavior of CO_2 at high temperatures. Considering the plant footprint, it cannot be forgotten that the ORC working fluid expands into the ORC turbine at lower density ranges if compared to the CO_2, leading to larger expander machines, even 4 time greater.

Further investigation regarded the identification of the economic optimum for a cogenerative case study, accounting for the influence of the process yearly demand profile and thus of the plant part-load operation. It was noticed that the s-CO_2 system maintains higher part-load performance when working with turbines regulated by means of the VTIT strategy, thus, working with almost constant exhaust flow rate; contrary to the ORC which benefits from working with exhausts temperatures that do not change significantly with respect to the design values. Considering the analyzed scenarios, the high investment costs still associated to the s-CO_2 technology make it not already viable for industrial gas turbines heat recovery applications (no return on the investment), except in the case a high value carbon tax value is applied. The influence of the user profile demand is instead less strong, even if it can be decisive when the investment is uncertain and the net present value close to zero.

Perspectives

Besides to the initial scope, the added value of this work also relies in the identification of novel issues and possibilities identified along the resolution path. In this regard, to the author's point of view, the following remarks and hints may be worthy of future investigations.

Concerning the micro-generation application:

- The modification of the valve timing of the reciprocating piston expander in exam could be implemented and the derived benefit actually tested for different heat source characteristics. However, when designing from scratch new volumetric expander, it is suggested to perform a preliminary analysis to identify the optimal built-in volume ratio depending on the specific application.
- New performant low-GWP fluids could be identified via simulations among fluids and mixtures which: i) work with operating pressures granting the higher possible enthalpy drop at the

expander, and ii) own high viscosity to minimize the leakage at the pump meatus; since more performant according to the results of this work. The experimental evidence, in this case too, would valorize the considerations made in this thesis. High latent heat of vaporization can also improve the performance of a micro-ORC system, since it can allow to recover a large amount of heat at the evaporator. Hydrocarbons whose typically exhibit this characteristic, cannot be used now for tertiary/residential applications because of their high flammability risk, but it cannot be excluded that new materials and design would allow in future to employ this alternative.

- Further investigation could be performed considering a scaling up of the Carnot battery size. Indeed, extrapolating the results of this work, the revenue is expected to increase more than the investment costs with the size, thanks to the scale effect. In this situation it would be more convenient to invest on larger storage and obtain even bigger economic benefit, exploiting more the storage thermal inertia and the heat pump mode, which proved to be not so convenient instead for smaller size.

Concerning the medium to large scale application, instead:

- For the new natural gas compressor stations projects, it would be profitable to design the plant considering since the beginning the installation of an ORC as bottomer cycle of the gas turbines prime movers. To maximize the revenue, turbines regulated by means of variable inlet guide vanes are proved to be the best choice. In those facilities in which is not possible to sell the electric energy surplus to the grid, it could be convenient to employ GT runners of different capacities, allowing a wider margin of regulation of the ORC, so that to fully exploit its potential without waste energy. This aspect is worth to be further investigated in future studies.
- Given its better performance, the s-CO_2 proved to be an advantageous alternative to the ORC for cogenerative applications. Although its cost is still prohibitive, it is not excluded that once the technology will be established, the s-CO_2 may become very competitive in this sector. Thus, it is worth following its advances.

References

[1] S. Quoilin, M. V. D. Broek, S. Declaye, P. Dewallef, and V. Lemort, "Techno-economic survey of Organic Rankine Cycle (ORC) systems," *Renew. Sustain. Energy Rev.*, vol. 22, pp. 168–186, Jun. 2013, doi: 10.1016/j.rser.2013.01.028.

[2] M. Bianchi and A. De Pascale, "Bottoming cycles for electric energy generation: Parametric investigation of available and innovative solutions for the exploitation of low and medium temperature heat sources," *Appl. Energy*, vol. 88, no. 5, pp. 1500–1509, May 2011, doi: 10.1016/j.apenergy.2010.11.013.

[3] H. Ritchie and M. Roser, "CO_2 and Greenhouse Gas Emissions," *Our World Data*, May 2020, Accessed: Sep. 28, 2021. [Online]. Available: https://ourworldindata.org/emissions-by-sector

[4] K. Rahbar, S. Mahmoud, R. K. Al-Dadah, N. Moazami, and S. A. Mirhadizadeh, "Review of organic Rankine cycle for small-scale applications," *Energy Convers. Manag.*, vol. 134, pp. 135–155, Feb. 2017, doi: 10.1016/j.enconman.2016.12.023.

[5] A. Redko, O. Redko, and R. DiPippo, "9 - Industrial waste heat resources," in *Low-Temperature Energy Systems with Applications of Renewable Energy*, A. Redko, O. Redko, and R. DiPippo, Eds. Academic Press, 2020, pp. 329–362. doi: 10.1016/B978-0-12-816249-1.00009-1.

[6] *Thermoflex 29.0. Sudbury, MA, USA: Thermoflow Inc; 2020*.

[7] V. Pethurajan, S. Sivan, and G. C. Joy, "Issues, comparisons, turbine selections and applications – An overview in organic Rankine cycle," *Energy Convers. Manag.*, vol. 166, pp. 474–488, Jun. 2018, doi: 10.1016/j.enconman.2018.04.058.

[8] E. Macchi and M. Astolfi, Eds., *Organic Rankine cycle (ORC) power systems: technologies and applications*. Duxford ; Cambridge, Massachusetts ; Kidlington: Woodhead Publishing is an Imprint of Elsevier, 2017.

[9] F. Campana *et al.*, "ORC waste heat recovery in European energy intensive industries: Energy and GHG savings," *Energy Convers. Manag.*, vol. 76, pp. 244–252, Dec. 2013, doi: 10.1016/j.enconman.2013.07.041.

[10] "Energy_self-consumption__Policy_brief_final.pdf." https://www.interregeurope.eu/fileadmin/user_upload/plp_uploads/policy_briefs/Energy_self-consumption__Policy_brief_final.pdf (accessed Oct. 06, 2021).

[11] B. F. Tchanche, Gr. Lambrinos, A. Frangoudakis, and G. Papadakis, "Low-grade heat conversion into power using organic Rankine cycles – A review of various applications," *Renew. Sustain. Energy Rev.*, vol. 15, no. 8, pp. 3963–3979, Oct. 2011, doi: 10.1016/j.rser.2011.07.024.

[12] J. Bao and L. Zhao, "A review of working fluid and expander selections for organic Rankine cycle," *Renew. Sustain. Energy Rev.*, vol. 24, pp. 325–342, Aug. 2013, doi: 10.1016/j.rser.2013.03.040.

[13] I. H. Bell, J. Wronski, S. Quoilin, and V. Lemort, "Pure and Pseudo-pure Fluid Thermophysical Property Evaluation and the Open-Source Thermophysical Property Library CoolProp," *Ind. Eng. Chem. Res.*, vol. 53, no. 6, Art. no. 6, Feb. 2014, doi: 10.1021/ie4033999.

[14] "Understanding Global Warming Potentials | US EPA." https://www.epa.gov/ghgemissions/understanding-global-warming-potentials (accessed Sep. 29, 2021).

[15] "Regulation (EU) No 517/2014 of the European Parliament and of the Council of 16 April 2014 on fluorinated greenhouse gases and repealing Regulation (EC) No 842/2006," p. 36.
[16] Y. Heredia-Aricapa, J. M. Belman-Flores, A. Mota-Babiloni, J. Serrano-Arellano, and J. J. García-Pabón, "Overview of low GWP mixtures for the replacement of HFC refrigerants: R134a, R404A and R410A," *Int. J. Refrig.*, vol. 111, pp. 113–123, Mar. 2020, doi: 10.1016/j.ijrefrig.2019.11.012.
[17] "Fifth Assessment Report — IPCC." https://www.ipcc.ch/assessment-report/ar5/ (accessed Oct. 20, 2021).
[18] ASHRAE Standards Committee, "Designation and Safety Classification of Refrigerants", [Online]. Available: https://www.ashrae.org/File%20Library/Technical%20Resources/Standards%20and%20Guidelines/Standards%20Addenda/34_2016_g_20180628.pdf
[19] Kenneth and Nichols, "How to Select Turbomachinery For Your Application." Barber Nichols.
[20] M. Imran, M. Usman, B.-S. Park, and D.-H. Lee, "Volumetric expanders for low grade heat and waste heat recovery applications," *Renew. Sustain. Energy Rev.*, vol. 57, pp. 1090–1109, May 2016, doi: 10.1016/j.rser.2015.12.139.
[21] A. Landelle, N. Tauveron, R. Revellin, P. Haberschill, S. Colasson, and V. Roussel, "Performance investigation of reciprocating pump running with organic fluid for organic Rankine cycle," *Appl. Therm. Eng.*, vol. 113, pp. 962–969, Feb. 2017, doi: 10.1016/j.applthermaleng.2016.11.096.
[22] T. Tartière and M. Astolfi, "A World Overview of the Organic Rankine Cycle Market," *Energy Procedia*, vol. 129, pp. 2–9, Sep. 2017, doi: 10.1016/j.egypro.2017.09.159.
[23] M. Bianchi *et al.*, "Feasibility of ORC application in natural gas compressor stations," *Energy*, vol. 173, pp. 1–15, Apr. 2019, doi: 10.1016/j.energy.2019.01.127.
[24] A. Squared, "Introducing the Plug and Play Micro-ORC," *Air Squared Scroll Technology*, Apr. 11, 2018. https://airsquared.com/news/introducing-plug-play-micro-orc/ (accessed Aug. 25, 2021).
[25] "global_gas_report_2018.pdf." https://www.snam.it/export/sites/snam-rp/repository/file/gas_naturale/global-gas-report/global_gas_report_2018.pdf (accessed Aug. 28, 2020).
[26] "Turboden internal communication."
[27] L. Branchini, C. Celis, S. Ruiz, R. Aguilar, A. De Pascale, and F. Melino, "On the Design of an ORC Axial Turbine Based Expander Working As a Mechanical Driver in Gas Compressor Stations," presented at the ASME Turbo Expo 2021: Turbomachinery Technical Conference and Exposition, Sep. 2021. doi: 10.1115/GT2021-01559.
[28] X. Li, B. Xu, H. Tian, and G. Shu, "Towards a novel holistic design of organic Rankine cycle (ORC) systems operating under heat source fluctuations and intermittency," *Renew. Sustain. Energy Rev.*, vol. 147, p. 111207, Sep. 2021, doi: 10.1016/j.rser.2021.111207.
[29] "How A Gas Compressor Station Works | Kimray." https://kimray.com/training/how-gas-compressor-station-works (accessed Oct. 06, 2021).
[30] N. Zaccarelli, N. Rodríguez Gómez, K. Pambour, and R. Lavin, "Towards EUGas-26: The European gas assessment model for EU Directive 2008/14/EC and EU regulation no 994/2010," *Int. Gas Res. Conf. Proc.*, vol. 2, pp. 1198–1206, Jan. 2014.
[31] G. V. P. Varma and T. Srinivas, "Power generation from low temperature heat recovery," *Renew. Sustain. Energy Rev.*, vol. 75, pp. 402–414, Aug. 2017, doi: 10.1016/j.rser.2016.11.005.
[32] L. Tocci, T. Pal, I. Pesmazoglou, and B. Franchetti, "Small Scale Organic Rankine Cycle (ORC): A Techno-Economic Review," *Energies*, vol. 10, no. 4, p. 413, Mar. 2017, doi: 10.3390/en10040413.

[33] A. Landelle, N. Tauveron, P. Haberschill, R. Revellin, and S. Colasson, "Organic Rankine cycle design and performance comparison based on experimental database," *Appl. Energy*, vol. 204, pp. 1172–1187, Oct. 2017, doi: 10.1016/j.apenergy.2017.04.012.

[34] B.-S. Park, M. Usman, M. Imran, and A. Pesyridis, "Review of Organic Rankine Cycle experimental data trends," *Energy Convers. Manag.*, vol. 173, pp. 679–691, Oct. 2018, doi: 10.1016/j.enconman.2018.07.097.

[35] C. Zilio, J. S. Brown, G. Schiochet, and A. Cavallini, "The refrigerant R1234yf in air conditioning systems," *Energy*, vol. 36, no. 10, pp. 6110–6120, Oct. 2011, doi: 10.1016/j.energy.2011.08.002.

[36] Y. Lee and D. Jung, "A brief performance comparison of R1234yf and R134a in a bench tester for automobile applications," *Appl. Therm. Eng.*, vol. 35, pp. 240–242, Mar. 2012, doi: 10.1016/j.applthermaleng.2011.09.004.

[37] A. Mota-Babiloni, J. Navarro-Esbrí, Á. Barragán, F. Molés, and B. Peris, "Drop-in energy performance evaluation of R1234yf and R1234ze(E) in a vapor compression system as R134a replacements," *Appl. Therm. Eng.*, vol. 71, no. 1, pp. 259–265, Oct. 2014, doi: 10.1016/j.applthermaleng.2014.06.056.

[38] Y. Zhao, Z. Qi, J. Chen, B. Xu, and B. He, "Experimental analysis of the low-GWP refrigerant R1234yf as a drop-in replacement for R134a in a typical mobile air conditioning system," *Proc. Inst. Mech. Eng. Part C J. Mech. Eng. Sci.*, vol. 226, no. 11, pp. 2713–2725, Nov. 2012, doi: 10.1177/0954406211435583.

[39] S. Eyerer, F. Dawo, J. Kaindl, C. Wieland, and H. Spliethoff, "Experimental investigation of modern ORC working fluids R1224yd(Z) and R1233zd(E) as replacements for R245fa," *Appl. Energy*, vol. 240, pp. 946–963, Apr. 2019, doi: 10.1016/j.apenergy.2019.02.086.

[40] J. Yang, Z. Ye, B. Yu, H. Ouyang, and J. Chen, "Simultaneous experimental comparison of low-GWP refrigerants as drop-in replacements to R245fa for Organic Rankine cycle application: R1234ze(Z), R1233zd(E), and R1336mzz(E)," *Energy*, vol. 173, pp. 721–731, Apr. 2019, doi: 10.1016/j.energy.2019.02.054.

[41] C. M. Invernizzi, P. Iora, M. Preißinger, and G. Manzolini, "HFOs as substitute for R-134a as working fluids in ORC power plants: A thermodynamic assessment and thermal stability analysis," *Appl. Therm. Eng.*, vol. 103, pp. 790–797, Jun. 2016, doi: 10.1016/j.applthermaleng.2016.04.101.

[42] F. A. Boyaghchi, M. Chavoshi, and V. Sabeti, "Optimization of a novel combined cooling, heating and power cycle driven by geothermal and solar energies using the water/CuO (copper oxide) nanofluid," *Energy*, vol. 91, pp. 685–699, Nov. 2015, doi: 10.1016/j.energy.2015.08.082.

[43] F. Molés, J. Navarro-Esbrí, B. Peris, A. Mota-Babiloni, and C. Mateu-Royo, "R1234yf and R1234ze as alternatives to R134a in Organic Rankine Cycles for low temperature heat sources," *Energy Procedia*, vol. 142, pp. 1192–1198, Dec. 2017, doi: 10.1016/j.egypro.2017.12.380.

[44] N. Yamada, M. N. A. Mohamad, and T. T. Kien, "Study on thermal efficiency of low- to medium-temperature organic Rankine cycles using HFO−1234yf," *Renew. Energy*, vol. 41, pp. 368–375, May 2012, doi: 10.1016/j.renene.2011.11.028.

[45] V. L. Le, M. Feidt, A. Kheiri, and S. Pelloux-Prayer, "Performance optimization of low-temperature power generation by supercritical ORCs (organic Rankine cycles) using low GWP (global warming potential) working fluids," *Energy*, vol. 67, pp. 513–526, Apr. 2014, doi: 10.1016/j.energy.2013.12.027.

[46] A. Giuffrida, "Modelling the performance of a scroll expander for small organic Rankine cycles when changing the working fluid," *Appl. Therm. Eng.*, vol. 70, no. 1, pp. 1040–1049, Sep. 2014, doi: 10.1016/j.applthermaleng.2014.06.004.

[47] Y. Liu, Y. Wang, and D. Huang, "Supercritical CO2 Brayton cycle: A state-of-the-art review," *Energy*, vol. 189, p. 115900, Dec. 2019, doi: 10.1016/j.energy.2019.115900.
[48] M. T. White, G. Bianchi, L. Chai, S. A. Tassou, and A. I. Sayma, "Review of supercritical CO2 technologies and systems for power generation," *Appl. Therm. Eng.*, vol. 185, p. 116447, Feb. 2021, doi: 10.1016/j.applthermaleng.2020.116447.
[49] M. Marchionni, G. Bianchi, and S. A. Tassou, "Review of supercritical carbon dioxide (sCO 2) technologies for high-grade waste heat to power conversion," *SN Appl. Sci.*, vol. 2, no. 4, pp. 1–13, Apr. 2020, doi: 10.1007/s42452-020-2116-6.
[50] A. Zhou, X. s Li, X. Ren, and C. Gu, "Improvement design and analysis of a supercritical CO2/transcritical CO2 combined cycle for offshore gas turbine waste heat recovery," *Energy*, vol. 210, p. 118562, Aug. 2020, doi: 10.1016/j.energy.2020.118562.
[51] A. Yu, W. Su, X. Lin, and N. Zhou, "Recent trends of supercritical CO2 Brayton cycle: Bibliometric analysis and research review," *Nucl. Eng. Technol.*, Aug. 2020, doi: 10.1016/j.net.2020.08.005.
[52] C. S. Turchi, Z. Ma, T. W. Neises, and M. J. Wagner, "Thermodynamic Study of Advanced Supercritical Carbon Dioxide Power Cycles for Concentrating Solar Power Systems," *J. Sol. Energy Eng.*, vol. 135, no. 4, Nov. 2013, doi: 10.1115/1.4024030.
[53] J. Syblik, L. Vesely, S. Entler, J. Stepanek, and V. Dostal, "Analysis of supercritical CO2 Brayton power cycles in nuclear and fusion energy," *Fusion Eng. Des.*, vol. 146, pp. 1520–1523, Sep. 2019, doi: 10.1016/j.fusengdes.2019.02.119.
[54] S. Park, J. Kim, M. Yoon, D. Rhim, and C. Yeom, "Thermodynamic and economic investigation of coal-fired power plant combined with various supercritical CO2 Brayton power cycle," *Appl. Therm. Eng.*, vol. 130, pp. 611–623, Feb. 2018, doi: 10.1016/j.applthermaleng.2017.10.145.
[55] M. Astolfi, D. Alfani, S. Lasala, and E. Macchi, "Comparison between ORC and CO2 power systems for the exploitation of low-medium temperature heat sources," *Energy*, vol. 161, pp. 1250–1261, Oct. 2018, doi: 10.1016/j.energy.2018.07.099.
[56] S. Y. Yoon, M. J. Kim, I. S. Kim, and T. S. Kim, "Comparison of micro gas turbine heat recovery systems using ORC and trans-critical CO2 cycle focusing on off-design performance," *Energy Procedia*, vol. 129, pp. 987–994, Sep. 2017, doi: 10.1016/j.egypro.2017.09.223.
[57] O. Dumont, G. F. Frate, A. Pillai, S. Lecompte, M. De paepe, and V. Lemort, "Carnot battery technology: A state-of-the-art review," *J. Energy Storage*, vol. 32, p. 101756, Dec. 2020, doi: 10.1016/j.est.2020.101756.
[58] O. Dumont, S. Quoilin, and V. Lemort, "Experimental investigation of a reversible heat pump/organic Rankine cycle unit designed to be coupled with a passive house to get a Net Zero Energy Building," *Int. J. Refrig.*, vol. 54, pp. 190–203, Jun. 2015, doi: 10.1016/j.ijrefrig.2015.03.008.
[59] O. Dumont, A. Charalampidis, and V. Lemort, "Experimental Investigation Of A Thermally Integrated Carnot Battery Using A Reversible Heat Pump/Organic Rankine Cycle," *Int. Refrig. Air Cond. Conf.*, May 2021, [Online]. Available: https://docs.lib.purdue.edu/iracc/2085
[60] L. Di Cairano, W. Bou Nader, and M. Nemer, "Assessing fuel consumption reduction in Revercycle, a reversible mobile air conditioning/ Organic Rankine Cycle system," *Energy*, vol. 210, p. 118588, Nov. 2020, doi: 10.1016/j.energy.2020.118588.
[61] S. Ottaviano, "TEST BENCH DEVELOPMENT, EXPERIMENTAL ANALYSIS AND MODELLING OF MICRO-ORGANIC RANKINE CYCLE FOR LOW-GRADE HEAT RECOVERY," Università di Bologna, 2020.
[62] G. Zampieri, "'Closed-cycle plant' U.S. Patent US2016/0032786A1, Feb. 4, 2016," US20160032786A1, Feb. 04, 2016 Accessed: May 05, 2020. [Online]. Available: https://patents.google.com/patent/US20160032786/en

[63] Eric W. Lemmon, Ian H. Bell, Marcia L. Huber, and Mark O. McLinden, *REFPROP 10.0 Standard Reference Database 23*. National Institute of Standards and Technology, Boulder, Colorado, United States.
[64] S. Cao and R. R. Rhinehart, "An efficient method for on-line identification of steady state," *J. Process Control*, vol. 5, no. 6, pp. 363–374, Dec. 1995, doi: 10.1016/0959-1524(95)00009-F.
[65] M. Kim, S. H. Yoon, P. A. Domanski, and W. Vance Payne, "Design of a steady-state detector for fault detection and diagnosis of a residential air conditioner," *Int. J. Refrig.*, vol. 31, no. 5, pp. 790–799, Aug. 2008, doi: 10.1016/j.ijrefrig.2007.11.008.
[66] B. Woodland, J. Braun, E. Groll, and W. Horton, "Experimental Testing of an Organic Rankine Cycle with Scroll-type Expander," *Publ. Ray W Herrick Lab.*, Jul. 2012, [Online]. Available: https://docs.lib.purdue.edu/herrick/52
[67] O. Dumont, R. Dickes, and V. Lemort, "Extrapolability and limitations of a semi-empirical model for the simulation of volumetric expanders," *Energy Procedia*, vol. 129, pp. 315–322, Sep. 2017, doi: 10.1016/j.egypro.2017.09.198.
[68] R. Dickes, O. Dumont, R. Daccord, S. Quoilin, and V. Lemort, "Modelling of organic Rankine cycle power systems in off-design conditions: An experimentally-validated comparative study," *Energy*, vol. 123, pp. 710–727, Mar. 2017, doi: 10.1016/j.energy.2017.01.130.
[69] W. Li, "Simplified steady-state modeling for hermetic compressors with focus on extrapolation," *Int. J. Refrig.*, vol. 35, no. 6, pp. 1722–1733, Sep. 2012, doi: 10.1016/j.ijrefrig.2012.03.008.
[70] L. Molinaroli, C. M. Joppolo, and S. De Antonellis, "A semi-empirical model for hermetic rolling piston compressors," *Int. J. Refrig.*, vol. 79, pp. 226–237, Jul. 2017, doi: 10.1016/j.ijrefrig.2017.04.015.
[71] F. D'Amico *et al.*, "Semi-empirical model of a multi-diaphragm pump in an Organic Rankine Cycle (ORC) experimental unit," *Energy*, vol. 143, pp. 1056–1071, Jan. 2018, doi: 10.1016/j.energy.2017.10.127.
[72] V. Lemort and A. Legros, "12 - Positive displacement expanders for Organic Rankine Cycle systems," in *Organic Rankine Cycle (ORC) Power Systems*, E. Macchi and M. Astolfi, Eds. Woodhead Publishing, 2017, pp. 361–396. doi: 10.1016/B978-0-08-100510-1.00012-0.
[73] D. Ziviani, N. A. James, F. A. Accorsi, J. E. Braun, and E. A. Groll, "Experimental and numerical analyses of a 5 kWe oil-free open-drive scroll expander for small-scale organic Rankine cycle (ORC) applications," *Appl. Energy*, vol. 230, pp. 1140–1156, Nov. 2018, doi: 10.1016/j.apenergy.2018.09.025.
[74] L. C. Mendoza, J. Navarro-Esbrí, J. C. Bruno, V. Lemort, and A. Coronas, "Characterization and modeling of a scroll expander with air and ammonia as working fluid," *Appl. Therm. Eng.*, vol. 70, no. 1, pp. 630–640, Sep. 2014, doi: 10.1016/j.applthermaleng.2014.05.069.
[75] A. Giuffrida, "Modelling the performance of a scroll expander for small organic Rankine cycles when changing the working fluid," *Appl. Therm. Eng.*, vol. 70, no. 1, Art. no. 1, Sep. 2014, doi: 10.1016/j.applthermaleng.2014.06.004.
[76] F. Ayachi, E. B. Ksayer, P. Neveu, and A. Zoughaib, "Experimental investigation and modeling of a hermetic scroll expander," *Appl. Energy*, vol. 181, pp. 256–267, Nov. 2016, doi: 10.1016/j.apenergy.2016.08.030.
[77] A. Giuffrida, "Improving the semi-empirical modelling of a single-screw expander for small organic Rankine cycles," *Appl. Energy*, vol. 193, pp. 356–368, May 2017, doi: 10.1016/j.apenergy.2017.02.015.
[78] V. Vodicka, V. Novotny, J. Mascuch, and M. Kolovratnik, "Impact of major leakages on characteristics of a rotary vane expander for ORC," *Energy Procedia*, vol. 129, pp. 387–394, Sep. 2017, doi: 10.1016/j.egypro.2017.09.249.

[79] Y. Glavatskaya, P. Podevin, V. Lemort, O. Shonda, and G. Descombes, "Reciprocating Expander for an Exhaust Heat Recovery Rankine Cycle for a Passenger Car Application," *Energies*, vol. 5, no. 6, pp. 1751–1765, Jun. 2012, doi: 10.3390/en5061751.

[80] J.-L. Bouvier, V. Lemort, G. Michaux, P. Salagnac, and T. Kientz, "Experimental study of an oil-free steam piston expander for micro-combined heat and power systems," *Appl. Energy*, vol. 169, pp. 788–798, May 2016, doi: 10.1016/j.apenergy.2016.01.122.

[81] W. M. Kays, *Convective heat and mass transfer.*, 4th ed. / W.M. Kays, M.E. Crawford, Bernhard Weigand. Boston: McGraw-Hill Higher Education, 2005.

[82] O. Dumont, A. Parthoens, R. Dickes, and V. Lemort, "Experimental investigation and optimal performance assessment of four volumetric expanders (scroll, screw, piston and roots) tested in a small-scale organic Rankine cycle system," *Energy*, vol. 165, pp. 1119–1127, Dec. 2018, doi: 10.1016/j.energy.2018.06.182.

[83] O. Dumont, R. Dickes, and V. Lemort, "Experimental investigation of four volumetric expanders," *Energy Procedia*, vol. 129, pp. 859–866, Sep. 2017, doi: 10.1016/j.egypro.2017.09.206.

[84] R. Dickes, O. Dumont, L. Guillaume, S. Quoilin, and V. Lemort, "Charge-sensitive modelling of organic Rankine cycle power systems for off-design performance simulation," *Appl. Energy*, vol. 212, pp. 1262–1281, Feb. 2018, doi: 10.1016/j.apenergy.2018.01.004.

[85] *A-to-Z Guide to Thermodynamics, Heat and Mass Transfer, and Fluids Engineering: AtoZ*, vol. F. Begellhouse, 2006.

[86] *MATLAB 2019b*. Natick, Massachusetts, United States: © 1994-2020 The MathWorks, Inc.

[87] M. Bianchi *et al.*, "Experimental analysis of a micro-ORC driven by piston expander for low-grade heat recovery," *Appl. Therm. Eng.*, vol. 148, pp. 1278–1291, Feb. 2019, doi: 10.1016/j.applthermaleng.2018.12.019.

[88] E. S. Menon and P. S. Menon, "Chapter 4 - Pressure Loss through Piping Systems," in *Working Guide to Pumps and Pumping Stations*, E. S. Menon and P. S. Menon, Eds. Boston: Gulf Professional Publishing, 2010, pp. 69–111. doi: 10.1016/B978-1-85617-828-0.00004-4.

[89] L. Liu, J. Ma, and T. Zhu, "Working fluid charge oriented off-design modeling of a small scale Organic Rankine Cycle system," *Energy Convers. Manag.*, vol. 148, pp. 944–953, Sep. 2017, doi: 10.1016/j.enconman.2017.06.009.

[90] "Product Catalogue | European Refrigerants." https://www.honeywell-refrigerants.com/europe/product/tag/all-refrigerants/ (accessed Jun. 18, 2021).

[91] I. H. Bell, P. A. Domanski, M. O. McLinden, and G. T. Linteris, "The hunt for nonflammable refrigerant blends to replace R-134a," *Int. J. Refrig.*, vol. 104, pp. 484–495, Aug. 2019, doi: 10.1016/j.ijrefrig.2019.05.035.

[92] J. Wronski, M. Imran, M. J. Skovrup, and F. Haglind, "Experimental and numerical analysis of a reciprocating piston expander with variable valve timing for small-scale organic Rankine cycle power systems," *Appl. Energy*, vol. 247, pp. 403–416, Aug. 2019, doi: 10.1016/j.apenergy.2019.04.028.

[93] M. Antonelli, A. Baccioli, M. Francesconi, and L. Martorano, "Experimental and Numerical Analysis of the Valve Timing Effects on the Performances of a Small Volumetric Rotary Expansion Device," *Energy Procedia*, vol. 45, pp. 1077–1086, Jan. 2014, doi: 10.1016/j.egypro.2014.01.113.

[94] M. Bianchi *et al.*, "Performance and operation of micro-ORC energy system using geothermal heat source," *Energy Procedia*, vol. 148, pp. 384–391, Aug. 2018, doi: 10.1016/j.egypro.2018.08.099.

[95] Accuvio Sustainability & Corporate Social Responsibility Data Software Solutions, "Annual leakage rate (%) for the refrigeration/air-con/HVAC," *Support*, May 07, 2020.

https://support.accuvio.com/support/solutions/articles/4000040366-annual-leakage-rate-for-the-refrigeration-air-con-hvac- (accessed May 07, 2020).
[96] A. K. Cerutti *et al.*, *Covenant of Mayors for Climate and Energy: default emission factors for local emission inventories : version 2017.* 2017. Accessed: Apr. 23, 2020. [Online]. Available: http://dx.publications.europa.eu/10.2760/290197
[97] "Countries & Regions energy data - IEA," *IEA*. https://www.iea.org/countries (accessed Jun. 26, 2020).
[98] O. Dumont, A. Reyes, and V. Lemort, "Modelling of a thermally integrated Carnot battery using a reversible heat pump/organic Rankine cycle," presented at the ecos conference, Japan, Oct. 2020.
[99] "Solstice® zd (R-1233zd) | European Refrigerants." https://www.honeywell-refrigerants.com/europe/product/solstice-zd/ (accessed Aug. 27, 2021).
[100] V. Lemort, "CONTRIBUTION TO THE CHARACTERIZATION OF SCROLL MACHINES IN COMPRESSOR AND EXPANDER MODES," University of Liège, 2008.
[101] O. Dumont and V. Lemort, "Mapping of performance of pumped thermal energy storage (Carnot battery) using waste heat recovery," *Energy*, vol. 211, p. 118963, Nov. 2020, doi: 10.1016/j.energy.2020.118963.
[102] "University of Liège internal communication."
[103] "bespoke buffer tank supplier uk and europe fast delivery." https://www.thebiomasshut.co.uk/buffer-tank-distributor-uk-and-thermal-stores/renewable-energy--buffer-tanks/ (accessed Sep. 07, 2021).
[104] R. Kurz and S. Ohanian, "Modeling Turbomachinery In Pipeline Simulations," presented at the PSIG Annual Meeting, Oct. 2003. Accessed: Sep. 24, 2021. [Online]. Available: https://onepetro.org/PSIGAM/proceedings/PSIG03/All-PSIG03/PSIG-03A1/2245
[105] "Directive 2004/08/EC of the European Parliament and of the Council, Official Journal of the European Union 21.2.2004, pp. 50–60." https://eur-lex.europa.eu/LexUriServ/LexUriServ.do?uri=OJ:L:2004:052:0050:0060:EN:PDF (accessed Nov. 04, 2020).
[106] "NIST repository - Thermodynamic Properties of Natural Gas and Related Gases." https://pages.nist.gov/AGA8/ (accessed May 06, 2021).
[107] A. Turboden, "Turboden provides the first Direct Heat Exchange Organic Rankine Cycle solution from multiple heat sources."
[108] V. E. Ecofys Weltbank, *State and Trends of Carbon Pricing 2017.* 2017. Accessed: Sep. 23, 2021. [Online]. Available: http://hdl.handle.net/10986/28510
[109] "IEA CO2 Emissions from Fuel Combustion Statistics." OECD.
[110] "IEA – International Energy Agency," *IEA*. https://www.iea.org/data-and-statistics/data-products (accessed Sep. 23, 2021).
[111] D. R. Legates and C. J. Willmott, "Mean seasonal and spatial variability in global surface air temperature," *Theor. Appl. Climatol.*, vol. 41, no. 1–2, pp. 11–21, 1990, doi: 10.1007/BF00866198.
[112] B. A. Hedman, "Waste energy recovery opportunities for interstate natural gas pipelines. Report for Interstate Natural Gas Association of America (INGAA)." Feb. 2008. Accessed: Oct. 13, 2020. [Online]. Available: https://www.ingaa.org/File.aspx?id=6210
[113] "C45," *https://www.solarturbines.com/en_US/products/gas-compressors/c45.html*. https://www.solarturbines.com/en_US/products/gas-compressors/c45.html (accessed Sep. 24, 2021).
[114] R. Kurz, S. Ohanian, and M. Lubomirsky, "On Compressor Station Layout," *Proc. ASME Turbo Expo 2003 Atlanta Ga.*, pp. 1–10, Jan. 2003, doi: 10.1115/GT2003-38019.

[115] R. Kurz, "Optimizing Transient Operation," *17th Pipeline Technology Conference*. https://www.pipeline-conference.com/abstracts/optimizing-transient-operation (accessed Sep. 24, 2021).
[116] R. Kurz and K. Brun, "Gas Turbine Performance - What Makes The Map?," *Turbomach. Pump Symp.*, 2000, doi: 10.21423/R15S95.
[117] H. Huang, D. Peng, Y. Zhang, and Y. Liang, "Research on Load Optimal Distribution Based on Equal Incremental Principle," *J. Comput. Inf. Syst.*, vol. 9, no. 18, pp. 7477–7484, 2013.
[118] D. Beevers, L. Branchini, V. Orlandini, A. De Pascale, and H. Perez-Blanco, "Pumped hydro storage plants with improved operational flexibility using constant speed Francis runners," *Appl. Energy*, vol. 137, pp. 629–637, Jan. 2015, doi: 10.1016/j.apenergy.2014.09.065.
[119] H. P. Loh, J. Lyons, C. W. White, and EG&G Technical Services, Inc., Morgantown, WV (United States), "Process Equipment Cost Estimation, Final Report," DOE/NETL--2002/1169, 797810, Jan. 2002. doi: 10.2172/797810.
[120] F. Crespi, G. Gavagnin, D. Sánchez, and G. S. Martínez, "Analysis of the Thermodynamic Potential of Supercritical Carbon Dioxide Cycles: A Systematic Approach," *J. Eng. Gas Turbines Power*, vol. 140, no. 5, p. 051701, May 2018, doi: 10.1115/1.4038125.
[121] R. K. Bhargava, M. Bianchi, L. Branchini, A. De Pascale, and V. Orlandini, "Organic Rankine Cycle System for Effective Energy Recovery in Offshore Applications: A Parametric Investigation With Different Power Rating Gas Turbines," *Proc. ASME Turbo Expo 2015 Montr. Can.*, p. V003T20A004, Jun. 2015, doi: 10.1115/GT2015-42292.
[122] Y. Ahn, J. Lee, S. G. Kim, J. I. Lee, J. E. Cha, and S.-W. Lee, "Design consideration of supercritical CO2 power cycle integral experiment loop," *Energy*, vol. 86, pp. 115–127, Jun. 2015, doi: 10.1016/j.energy.2015.03.066.
[123] D. D. W. Green and D. M. Z. Southard, *Perry's Chemical Engineers' Handbook, 9th Edition*. McGraw-Hill Education, 2019. Accessed: Nov. 12, 2020. [Online]. Available: https://www.accessengineeringlibrary.com/content/book/9780071834087
[124] N. T. Weiland, B. W. Lance, and S. R. Pidaparti, "sCO2 Power Cycle Component Cost Correlations From DOE Data Spanning Multiple Scales and Applications," presented at the ASME Turbo Expo 2019: Turbomachinery Technical Conference and Exposition, Nov. 2019. doi: 10.1115/GT2019-90493.
[125] M. Astolfi, M. C. Romano, P. Bombarda, and E. Macchi, "Binary ORC (Organic Rankine Cycles) power plants for the exploitation of medium–low temperature geothermal sources – Part B: Techno-economic optimization," *Energy*, vol. 66, pp. 435–446, Mar. 2014, doi: 10.1016/j.energy.2013.11.057.
[126] "Statistics | Eurostat." https://ec.europa.eu/eurostat/databrowser/view/nrg_pc_203/default/table?lang=en (accessed Apr. 19, 2021).
[127] "European Countries with a Carbon Tax | Tax Foundation." https://taxfoundation.org/carbon-taxes-in-europe-2020/ (accessed Apr. 19, 2021).